Phase transitions in ethylene oxide – methyl methacrylate block copolymers

Richardson, Paul H.

Phase Transitions in Ethylene Oxide - Methyl Methacrylate Block Copolymers.

Paul H. Richardson

Graduate Society, 1993.

A thesis submitted to the University of Durham in partial fulfilment of the regulations for the Degree of Doctor of Philosophy.

Phase Transitions in Ethylene Oxide - Methyl Methacrylate Block Copolymers.

Paul H. Richardson Ph.D. 1993.

This thesis describes the methods of anionic polymerisation and characterisation of poly(ethylene oxide) - poly(methyl methacrylate) block copolymers. Several experimental techniques have been used to study the phase transitions in these block copolymers as well as the corresponding binary blends. These techniques have included the following: differential scanning calorimetry, optical microscopy, small angle light scattering, small angle and wide angle x-ray scattering. A major part of this work involved the design, construction and operation of the small angle light scattering technique.

The isothermal crystallisation kinetics of both the block copolymers and blends with high percentages of ethylene oxide component were investigated. The phase behaviour of the block copolymers and the blends was also studied. This involved analysing melting point depression and glass transition data as well as investigating the structural morphology of the polymer systems.

The phase behaviour of the block copolymers and the blends containing intermediate component compositions was observed at temperatures below the melting point temperature of PEO. For two block copolymer systems containing 50% and 55% by weight ethylene oxide, the chemical joint within the block inhibited crystallisation directly from the melt. These block copolymers microphase separated at low temperatures forming microdomains rich in PEO. Upon heating, the PEO microdomains crystallised. A phase diagram incorporating this behaviour as well as the phase behaviour of the blends is presented. The structure from the micron level and below of the phase separated and crystalline regions has also been deduced.

A block copolymer containing 76% ethylene oxide by weight crystallised directly from the melt. The isothermal crystallisation mechanism was very similar to that of the corresponding blend, however, the rate of crystallisation was appreciably slower and the melting point reduced. Comparison of analysed data from several techniques has allowed the contributions to the isothermal crystallisation mechanism to be distinguished.

To My Parents.

Acknowledgements.

Firstly, I would like to thank my supervisor Randal Richards, for his continuous help, encouragement and understanding throughout my postgraduate study. I would also like to take this opportunity to thank Jim Feast, whose efforts, along with Randals, have created a pleasant and rewarding environment to work in.

Numerous friends and colleagues have contributed in many ways to this thesis. I would like to single out a special few. Thanks goes to my friends and colleagues, past and present, who have studied and socialised with me in Durham, namely:
Abdulla Ahmed - the Okey Dokey King, Donald Davison, Richard 'Manager' Towns, Ian 'the computer manager' Hopkinson, Mark 'charger' and Vicki Jones, Steve 'Bolton' Edge, Panagiotis 'PD' Dounis, Ian 'Skidiledee' Jobling, John 'checkmate' Tsibouklis, Gordon 'Trigger' Forrest, John Holland, Gail McClean, John Henderson, The Physics gang - Chris, Harry, Paul, Andy 'Chorley' Brown

This work would not have been possible with out the technical assistance of Gordon Forrest (SEC), the nmr people: Alan Kenwright and Julia Say, the electrical and mechanical workshops: Barry Barker, Neil Holmes and Jim Hodgson, the glass blowers: Ray Hart and Gordon Haswell, and Jimmy Lincoln and Tom Caygill. I would also like to acknowledge the financial support of SERC, ICI (Wilton) and the rewarding meetings with my industrial supervisors: Bill MacDonald, Peter Mills and David Blundell.

I would like to especially thank the close friendship of Stephen 'West Brom' Westwood and the moral support from my family. They have contributed a great deal towards maintaining my sanity throughout the past three years. Finally, I would like to thank Meg Schellenberg for the proof reading of this thesis and for a highly enjoyable summer.

Contents.

Preface - Symbols.

The list below defines briefly the symbols used in the text. For each symbol, an associated parenthesised indication is included to direct the reader the appropiate section:

INTRO -Chapter 1, Introduction.

PEO/PMMA -Chapter 2,

SYN -Chapter 3

DSC -Chapter 4, Differential Scanning Calorimetry.

OM -Chapter 5, Optical Microscopy.

X-RAY -Chapter 6, Wide Angle and Small Angle X-ray Scattering.

SALS -Chapter 7, Small Angle Light Scattering.

3-D -3-dimensional correlation length (X-RAY)

a -characteristic dimension of the scattering unit (SALS)

a -electrical dipole moment (SALS)

a -statistical Kuhn length (INTRO)

a_i -block statistical segment length (INTRO)

a_I -interphase thickness (INTRO)

A -positive constant arising from free volume effects (INTRO)

A -proportionality constant (I_{Vv} 3-D isotropic sphere) (SALS)

A -first intercept of the correlation function with the abscissa (X-RAY)

A_i -peak height (X-RAY)

α -conformational symmetry (INTRO)

α -polarisability (SALS)

α_1 -polarisability in optic axis direction (SALS)

α_2 -polarisability perpendicular to the optical axis direction (SALS)

α_0 -polarisability of a uniform isotropic sphere (SALS)

α_r -polarisability in radial direction (SALS)

α_t -polarisability tangentially to radius direction (SALS)

α_s -polarisability of the surroundings (SALS)

b -coherent scattering length (X-RAY)

b -position in Kratky set-up (X-RAY)

bcc -body-centred cubic (INTRO)

b_o -thickness of a monomolecular layer (OM)

B -constant associated with equation of state theories (INTRO)

B -interaction energy density (INTRO, DSC, OM)

β -angle between optic axis and spherulitic radius (SALS)

c -velocity of light (SALS)

C_1 -constant for PEO, 16,238J mol^{-1} (OM)

C_2 -constant for PEO, 51.6K (OM)

C_p -heat capacity (DSC)

χ -Flory-Huggins interaction parameter (INTRO, PEO/PMMA, DSC, OM)

χ_{eff} -effective interaction parameter (INTRO)

χ_s -interaction parameter at the spinodal point (INTRO)

d -periodicity (INTRO)

d -Bragg spacing (X-RAY)

dn -local deviation in refractive index due to composition fluctuations (SALS)

$d\varepsilon$ -Fourier component of the dielectric constant fluctuation tensor (SALS)

D -microdomain period (INTRO)

D -distortion factor (X-RAY)

DSC -differential scanning calorimetry (INTRO)

δ -solubility parameter (PEO/PMMA)

δ -chemical shift, ppm (SYN)

ΔF^* -activation energy for transport of crystallising units across the melt crystal interface (OM)

ΔG_m -Gibb's free energy of mixing (INTRO)

Δh_{cryst}-enthalpy of crystallisation (DSC)

Δh_{fus} -enthalpy of fusion (DSC)

$\Delta h_{fus,v}$-heat of fusion per unit volume (OM)

$\Delta\varphi^*$ -free energy required to form a critical sized nucleus from the melt (OM)

ΔH_m -enthalpy of mixing (INTRO)

ΔH_μ -heat of fusion per mole of crystalline component (INTRO)

ΔS_m -entropy of mixing (INTRO)

ΔT -undercooling, T_m-T_c (OM)

ΔU_m -internal energy of mixing (INTRO)

ΔV_m -volume change upon mixing (INTRO)

Δw_{12} -energy of formation of an unlike contact pair (INTRO)

E -electrical field (SALS)

EO -ethylene oxide (SYN)

E_s -magnitude of scattered electric field (SALS)

ε -local dielectric constant (SALS)

ε_o -average dielectric constant (SALS)

f -macroscopic volume fraction (INTRO)

f_i -profile function parameter (X-RAY)

f_i -scattering factor of the atom i (X-RAY)

$\bar{f}^2$ -weighted mean-square atomic scattering factor (X-RAY)

fcc -face centred cubic (INTRO)

F -form factor (SALS)

g(f,x) -Debye function (INTRO)

G -spherulitic growth rate (PEO/PMMA, OM)

G -polymer crystal growth rate (OM)

G_o -proportionality constant (OM)

hcp -hexagonal close packed (INTRO)

ϕ -phase factor (SALS)

ϕ_A -local volume fraction of component A (INTRO)

ϕ_i -volume fraction of component i (INTRO)

ϕ_x -volume fraction of component x (SALS)

η -electron density deviations (X-RAY)

H -H=q (X-RAY)

I(q) -scattered intensity (INTRO)

IR -infra-red spectroscopy (PEO/PMMA)

I(s) -x-ray scattered intensity (X-RAY)

I_c -x-ray scattered intensity associated with the crystalline component (X-RAY)

I_s -intensity of scattered light (SALS)

I_{Hv} -scattered intensity with polarisers crossed (SALS)

I_{Vv} -scattered intensity with polarisers aligned (SALS)

$\gamma(x)$ -1-dimensional correlation function (X-RAY)

k -Boltzmann's constant (OM)

K -$(2\pi/\lambda)$ (SALS)

K_n -Avrami rate constant (INTRO, PEO/PMMA, DSC, OM)

$K_{T'}$ -rate constant related to the rate of structural organisation (DSC)

L_i -thickness of lamellar (X-RAY)

L -crystalline lamellar thickness (PEO/PMMA)

L_e -scattering length of one electron (X-RAY)

L_c^m probable distance between the centre of gravity of a crystal and its adjacent amorphous region (X-RAY)

L_c^M -most probable distance between the centres of gravity between two adjacent crystals or lamellar stacks of the same composition (X-RAY)

L_o -Onsager coefficient (INTRO)

LCST -Lower Critical Solution Temperature (INTRO, OM)

λ -wavelength of incident radiation (INTRO, SALS, X-RAY)

m -refractive index of the scattering unit (SALS)

m_i -weight fraction of polymer i (DSC)

M1 -molecular weight of previous polymer from SEC (SYN)

M2 -molecular weight of required polymer (SYN)

MST -microphase separated temperature (INTRO)

MMA -methyl methacrylate (SYN)

M_n -number average molecular weight (PEO/PMMA)

M_w -weight average molecular weight (SYN, DSC)

M_w^m -monomer molecular weight (X-RAY)

μ -azimuthal scattering angle (SALS)

μ -linear absorption factor (X-RAY)

n -Avrami (JMA) exponent (INTRO, PEO/PMMA, DSC, OM)

n -local refractive index (INTRO)

n -number of crystalline peaks (X-RAY)

n_i -number of atoms of type i (X-RAY)

n_o -average refractive index for a homogeneous two component system (SALS)

nmr -nuclear magnetic spectroscopy (INTRO)

N -degree of polymerisation (INTRO)

N_A -Avogadro's number (INTRO, X-RAY)

N_i -number of moles of component i (INTRO)

NIA -narrow interphase approximation (INTRO)

NPL -non-periodic model (INTRO)

N_e^m -number of electrons in one monomer unit (X-RAY)

OBDD -order bicontinuous double diamond (INTRO)

ODT -order disorder transition (INTRO, DSC)

OM -optical microscopy (INTRO)

P -pressure (INTRO)

P_i -peak position angle (X-RAY)

P(Q) -single particle scattering function (X-RAY)

PEO -poly(ethylene oxide) (SYN)

PMMA-poly(methyl methacrylate) (SYN)

Q_i -Gaussian and Cauchy profiles (X-RAY)

θ -polar scattering angle (INTRO, SALS)

θ_{max} -polar scattering angle with maximum intensity (SALS)

q -scattering vector $(4\pi n/\lambda)(\sin[\theta/2])$ (INTRO, SALS)

q_m -value of q at maximum I(q) (INTRO)

R -gas constant (INTRO)

R -spherulitic radius (OM, SALS)

R_∞ -maximum spherulitic radius before truncation (OM)

R(q) -first order rate constant which characterises the ODT (INTRO)

R_g -copolymer radius of gyration (INTRO)

RPA -random phase approximation (INTRO)

r -correlation distance (X-RAY)

ρ -electron scattering density (X-RAY)

ρ_s -sample density (X-RAY)

s -reciprocal lattice vector (X-RAY)

s -$s=q/2\pi$ (X-RAY)

S(q) -sum of the Fourier transforms of the different density-density correlation functions (INTRO)

S(q) -scattering law (S(q=0)=1), correlation of the composition fluctuations in the system (SALS)

S(Q) -interference function (X-RAY)

SALS -small angle light scattering (INTRO)

SANS -small angle neutron scattering (PEO/PMMA)

SAXS -small angle x-ray scattering (INTRO)

SEC -size exclusion chromatography (INTRO)

SSL -strong segregation limit (INTRO)

σ_e -lateral surface free energy per unit area perpendicular to the molecular chain direction (INTRO, PEO/PMMA, OM)

σ_u -interfacial free energy per unit area parallel to the molecular chain direction (OM)

t -transformation time (INTRO)

t permanence or crystallisation time (DSC, OM, SALS, X-RAY)

t -sample thickness (X-RAY)

T -temperature (INTRO, PEO/PMMA)

T' -permanence temperature (DSC, X-RAY)

T_{tr}' -transitional temperature (DSC)

THF -tetrahydrofuran (SYN)

T_1 -nmr relaxation time (PEO/PMMA)

T_c -crystallisation temperature (PEO/PMMA, DSC, OM)

T_g -glass transition temperature (INTRO, PEO/PMMA, DSC, OM)

$T_{g,T}$ -glass transition of a mixed binary system (DSC)

T_m' -observed melting point temperature (PEO/PMMA, DSC, OM)

T_m^o -equilibrium melting point temperature (INTRO, PEO/PMMA, DSC, OM)

$T_{m,PEO}{}^{o}$-equilibrium melting point temperature for pure PEO (INTRO, DSC)

T_{SAXS} -run temperature (X-RAY)

$T_{1/2}'$ -permanence temperature at which half the maximum amount of attainable crystallinity is induced (X-RAY)

U -$(4\pi R/\lambda)(\sin[\theta/2])$ (SALS)

UCST -Upper Critical Solution Temperature (INTRO, OM)

V -volume occupied by the monomer unit (X-RAY)

V1 -volume of initiator required (SYN)

V2 -volume of initiator used for previous synthesis (SYN)

V_i -molar volume of component i (INTRO)

V_o -volume of isotropic sphere (SALS)

$V_{1\mu}$ -molar volume per mole of amorphous polymer (INTRO, DSC, OM)

$V_{2\mu}$ -molar volume per mole of crystalline polymer (INTRO, DSC, OM)

$\overline{V}_i$ -molar volume of polymer i (INTRO)

w -energy of pair interactions (INTRO)

W1 -weight of monomer used for previous synthesis (SYN)

W2 -weight of monomer to be used (SYN)

W_i -peak width at half height (X-RAY)

WAXS -wide angle x-ray scattering (INTRO)

WSL -weak segregation limit (INTRO)

x -scattering angle, 2θ (X-RAY)

x -co-ordinate perpendicular to the layers under investigation (X-RAY)

x_c -crystallinity index of the crystalline phase (DSC)

x_c -degree of crystallinity (X-RAY)

x_{c1} -degree of crystallinity within the lamellar stack (X-RAY)

x_{1L} -degree of crystallinity within the lamellar stack, different method of determination from x_{c1} (X-RAY)

x_t -crystallinity index of the polymer (DSC)

X_c -relative degree of crystallinity (PEO/PMMA)

X_i -concentration dependent coefficients (INTRO)

X_0' -entropic portion of the interaction energy (INTRO)

X_1' -enthalpic portion of the interaction energy (INTRO)

X(t) -property which changes linearly with the degree of transformation and the nucleated growth process (INTRO)

y -value of the correlation function at it's first minimum (X-RAY)

Y -related to the ratio of the surface areas (INTRO)

Y_{ci} -calculated x-ray scattering intensities (X-RAY)

Y_{ei} -experimental x-ray scattering intensities (X-RAY)

$W(q)$ -determinant of $S(q)$ (INTRO)

$\psi(r)$ -order parameter (INTRO)

Ψ -angle between dipole a and vector r extending from the dipole to the observer (SALS)

z -co-ordination number (INTRO)

Chapter 1.

1. Introduction.

1.1. Polymer Blends.

1.1.1. Introduction.

New chemical structures or organisations are not always needed to create a material with new and/or improved properties. In fact it is assumed that few new polymers will attain commercial success in the coming decades. The physical blending of two or more existing polymers is a concept that can be used, and often is, to obtain new products and meet the need for new higher performance engineering thermoplastics, composite matrix material and elastomers. Through blending, a range of materials with desired properties, which may be completely different from those of the blend constituents, can be produced. An obvious added advantage of this approach is that it usually requires little or no capital expenditure relative to the production of new polymers.

1.1.2. Phase Separation in Polymer Blends.

Two concepts that are often incorrectly used in describing polymer blends are miscibility and compatibility. Miscibility is defined as the ability of a system to be mixed on a molecular level to produce one homogeneous phase. This should not be confused with compatibility, which is applied to a blend that is immiscible on the molecular level yet exhibits useful technological properties, e.g. high impact polystyrene (PS contains a dispersed rubbery phase, usually polybutadiene).

Most polymer blends are immiscible forming a two phase material. This result becomes apparent from simple thermodynamic considerations. One of the criteria for miscibility is that the Gibb's free energy of mixing, ΔG_m (constant pressure and temperature) is negative. This is given by equation 1.1.;

$$\Delta G_m = \Delta H_m - T\Delta S_m \qquad (1.1)$$

where ΔH_m is the enthalpy of mixing at constant temperature and pressure, ΔS_m is the entropy of mixing (a positive value of ΔS_m indicates an increase in the randomness of the system) and T is the absolute temperature. ΔH_m is defined as;

$$\Delta H_m = \Delta U_m + P\Delta V_m \qquad (1.2)$$

where ΔU_m is the internal (total) energy of mixing.

As the molecular weight of the polymers in the blend increases, the number of moles, N_i, in the blend becomes very small. Since the change in the entropy upon mixing is directly proportional to N_i (equation 1.3), then ΔS_m is small and positive i.e. favourable for mixing. For non-polar macromolecules, the enthalpy of mixing is expected to be positive, i.e. unfavourable for mixing (see below for an explanation in terms of contact pair interactions, equation 1.6.).

Since the entropy contribution to mixing, $-T\Delta S_m$ is smaller than ΔH_m, then ΔG_m will be positive; this explains the observation that most polymer blends do not mix. However, a polymer blend will be miscible if $-T\Delta S_m > \Delta H_m$ i.e. if ΔH_m is less positive (if the two polymers are very similar chemically and physically) or even negative (as in the case of polar or hydrogen-bonded interactions), at higher temperatures, T, or for lower molecular weights (ΔS_m is larger).

To be able to control the miscibility of polymer blends, it is necessary to be able to estimate the contributions, ΔH_m and ΔS_m. Several approaches to this problem have been proposed and a review of such theories is presented below.

1.1.3. Theoretical Background.

The Flory-Huggins lattice theory[1] is probably the simplest theory that exists for estimating the contributions to ΔG_m. Owing to this simplicity, the fundamental features of phase separation, the phase diagram and phase separation mechanisms will be discussed within this theory's context.

1.1.3.1. Flory-Huggins Lattice Theory.

In terms of the lattice theory of Flory and Huggins,[1,2] as applied by Scott[3] and Tompa[4] to polymer mixtures, the entropy and enthalpy of mixing are given respectively by (1.3):

$$\Delta S_m = -R(N_1 \ln \phi_1 + N_2 \ln \phi_2) \tag{1.3}$$

$$\Delta H_m = RT\chi\phi_1\phi_2 \tag{1.4}$$

where R is the gas constant, N_i is the number of moles and ϕ_i the volume fraction of component i, and χ is the dimensionless interaction parameter which is assumed to be independent of concentration. The Flory-Huggins interaction parameter can be expressed as:

$$\chi = \frac{BV_1}{RT} = \frac{z\Delta w_{12}N_A}{RT} \tag{1.5}$$

where B is an interaction energy density, V_1 is the molar volume of component 1, N_A is Avogadro's number, z is the co-ordination number of the lattice and Δw_{12} is the energy of formation of an unlike contact pair which can be expressed as:

$$\Delta w_{12} = w_{12} - \frac{1}{2}(w_{11} + w_{22}) \qquad (1.6)$$

where w_{12}, w_{11} and w_{22} are the energies of the respective pair interactions. In the case of interactions between non-polar macromolecules w_{12} is usually less than the mean of w_{11} and w_{22} and, according to the geometric mean assumption, is given by $(w_{11} \times w_{22})^{1/2}$. This results in a positive value for ΔH_m as stated earlier.

Consequently, by combining equations 1.1., 1.3. and 1.4., the Gibb's free energy of mixing of two polymers is given by:

$$\Delta G_m = RT(N_1 \ln \phi_1 + N_2 \ln \phi_2) + BV_1\phi_1\phi_2 \qquad (1.7)$$

Systems that phase separate upon heating are said to exhibit a lower critical solution temperature (LCST) (see figure 1.1.). For this case of phase separation, the interaction parameter, χ must be replaced by[5]:

$$\chi = A + \frac{B}{RT} \qquad (1.8)$$

where A is a positive constant arising from free volume effects derived from the equation of state theory (see 1.1.3.4.). Whereas B is always positive, based on the original Flory-Huggins theory (in equation 1.8.) for the equation of state theory, B may be negative and often is. In this situation $\partial^2 \Delta G_m / \partial \phi_1^2$ becomes negative at higher temperatures, i.e., mixing is unfavoured (see figure 1.1).

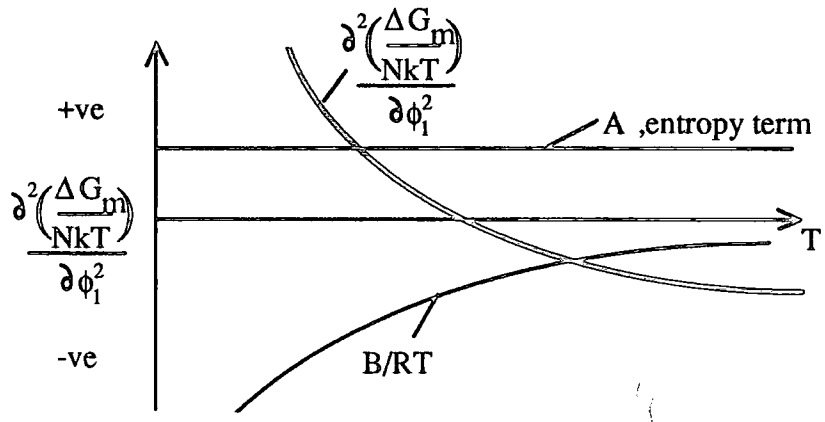

Figure 1.1. Explanation of LCST Behaviour Based on the Equation of State Theories.

On the other hand, a miscible system that phase separates upon cooling is said to possess an upper critical solution temperature, UCST, see figure 1.2.

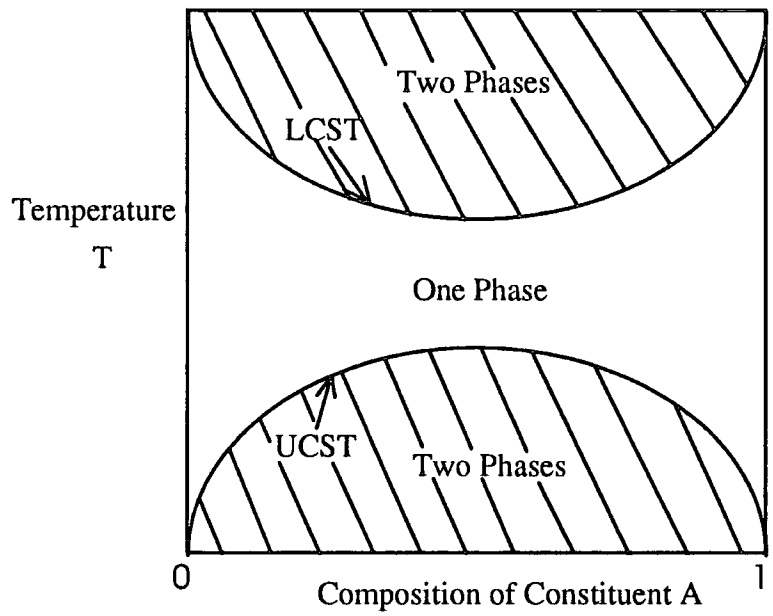

Figure 1.2. Schematic Representation of the Two Classes of Phase Separation for Polymer Blends.

The shape of the phase diagram in figure 1.2. is not typical of all polymer blend systems. Several variations exist, examples of which have been reported elsewhere.[6]

There are three different types of concentration dependence that can be obtained from equations 1.7 and 1.8., depending upon the temperature, T. These are illustrated in figure 1.3.:

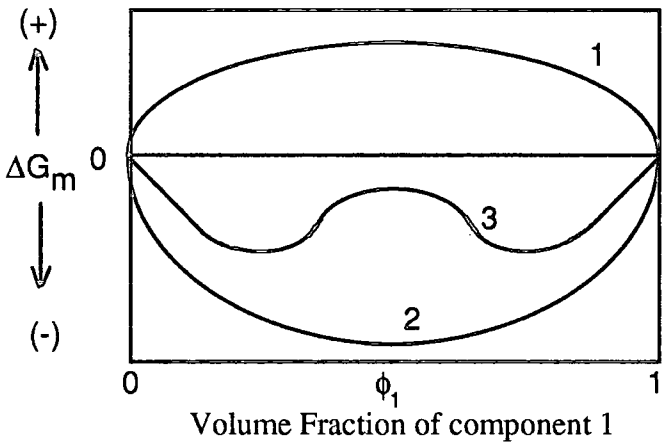

Figure 1.3. The 'Miscibility Gap' for Polymer Blends.

$$1.\ \Delta G_m > 0 \quad \text{and} \quad \frac{d^2 \Delta G_m}{d\phi^2_1} < 0$$

The system is immiscible over the total concentration range.

$$2.\ \Delta G_m < 0 \quad \text{and} \quad \frac{d^2 \Delta G_m}{d\phi^2_1} > 0$$

The system is completely miscible on the molecular level over the total composition range. This is the criterion for miscibility.

3. $\Delta G_m < 0$

As shown in figure 1.2., in the central composition region, the Gibb's free energy of mixing is greater than zero. This results in a so called 'miscibility gap'.

Figure 1.4. illustrates the miscibility gap situation in terms of a composition profile as a function of temperature and the resultant LCST type phase diagram.

At temperature, T_2, where miscibility is observed over the entire composition range, the second differential of ΔG_m with respect to composition is always positive (see equation 1.7. and condition 2).

At temperature T within the region where phase separation occurs (figure 1.4., b)), compositions between ϕ_a' and ϕ_a'' can phase separate to reduce the overall free energy and give two phases of compositions ϕ_a' and ϕ_a''. This occurs at points where a common tangent can be drawn to the curve (not necessarily the minima) where:

$$\frac{\partial(\Delta G_m)_{a'}}{\partial\phi} = \frac{\partial(\Delta G_m)_{a''}}{\partial\phi} \qquad (1.9)$$

Two regimes are distinguishable in the miscibility gap[7]. First, between ϕ_a' and ϕ_s' and between ϕ_a'' and ϕ_s'', a region of metastability occurs. Small fluctuations in composition in these regions raise the free energy and act as a barrier to phase separation. Phase separation is said to occur by a process known as nucleation and growth. To overcome this energy barrier, the mechanism of phase separation is an activated process in which the nuclei formation involves an increase in free energy. Once the nuclei are formed, the growth occurs with an overall decrease in free energy.

Second, between ϕ_s' and ϕ_s'', concentration fluctuations are immediately lower in free energy and phase separation occurs spontaneously by a mechanism known as spinodal decomposition. The spinodal (S in figure 1.4., b)) curve is the loci

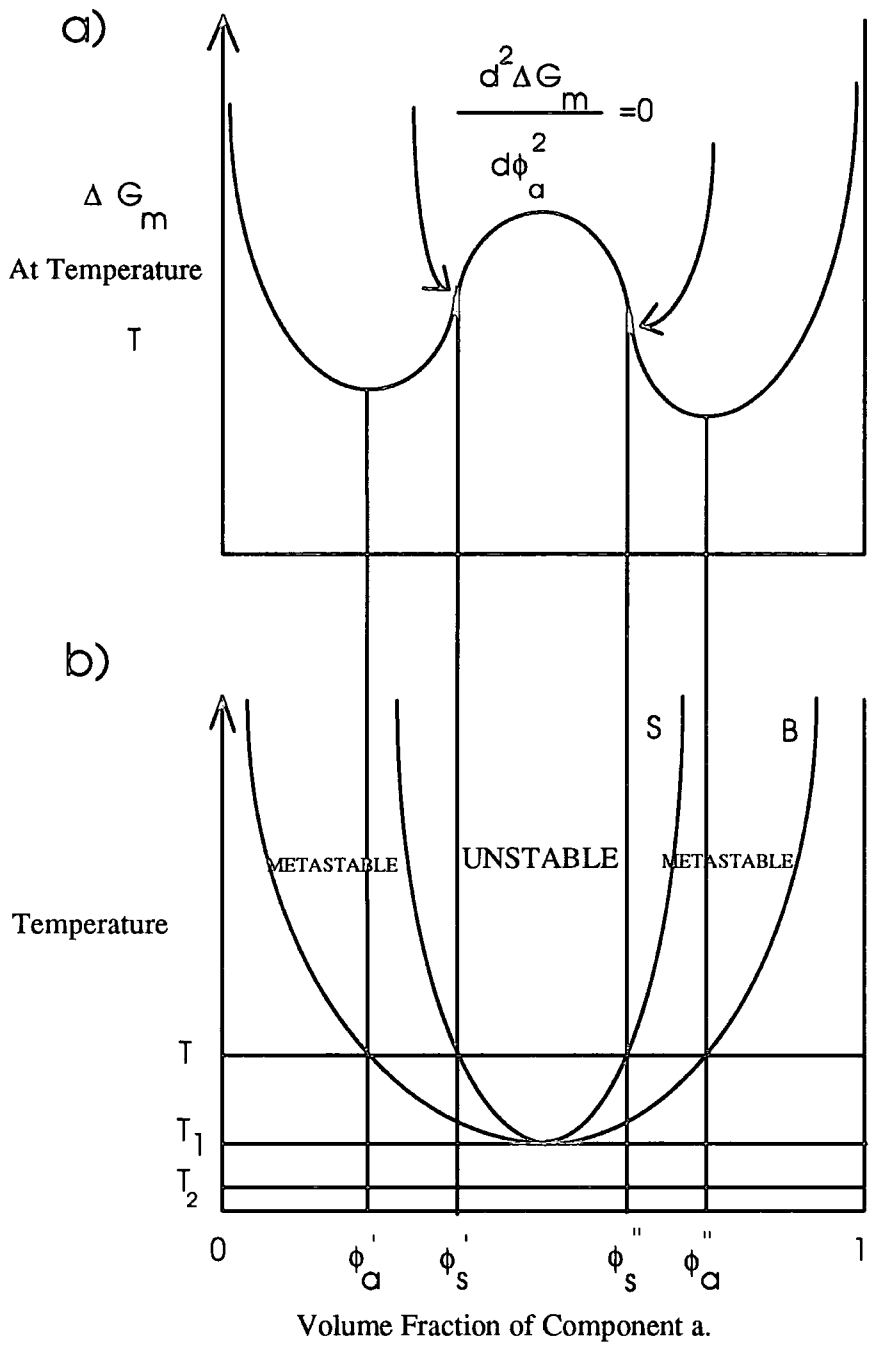

Figure 1.4. The Effect of the Miscibility Gap in the form of a Composition Profile as a Function of Temperature and an LCST Phase Diagram.

of the limits of metastability in the temperature phase diagram and occurs at the points of inflection of the free energy plot where:

$$\frac{\partial^2 \Delta G_m}{\partial \phi^2} = 0 \qquad (1.10)$$

The binodal (B in figure 1.4., b) is the loci of coexisting phase compositions in the temperature phase diagram, i.e., the coexistence curve where the chemical potentials of each component are equal in each phase, and marks the limit of the one phase region.

Temperature T_1 is the critical point where the spinodal and binodal curves meet where:

$$\frac{\partial^2 \Delta G_m}{\partial \phi_A{}^2} = \frac{\partial^3 \Delta G_m}{\partial \phi_A{}^3} = 0 \qquad (1.11).$$

1.1.3.2. Phase Separation Mechanisms.

1.1.3.2.1. Spinodal Decomposition.

In the unstable regime between ϕ_S' and ϕ_S'' in figure (1.4., b), phase separation occurs by a process called spinodal decomposition which involves the spontaneous and continuous growth of one phase within an unstable parent phase. In the early stages, small amplitudes of composition fluctuations of fixed periodicity grow exponentially with time (see figure 1.5., a)). 'Uphill' diffusion occurs where component 1 diffuses from a low concentration region to a low energy, high concentration region. Spinodal decomposition is often characterised by the initial exponential growth with constant periodicity and a morphological texture that is highly interwoven.

The linearised Cahn-Hilliard theory is often applied to describe the kinetics of the early stages of spinodal decomposition[8-12]. This theory, however, has its limitations in that it cannot be applied to the intermediate and late stages of spinodal

decomposition. Figures 1.5. and 1.6.a) illustrate the changing features during spinodal decomposition. The periodicity increases and the growth of the concentration fluctuations tend toward an equilibrium value. Consequently, experimental work[13-15] and successful theoretical extensions of the Cahn Hilliard theory[16-18] have been performed on the later stage regime.

1.1.3.2.2. Nucleation and Growth.

In the metastable regions, ϕ_a' to ϕ_s' and ϕ_a'' to ϕ_s'', phase separation occurs via nucleation and growth. In this activated process the initial formation of the nuclei involves an increase in free energy. Once formed, growth occurs with an overall decrease in free energy (see figure 1.6., b)). The immediate volume around a nucleus of composition, ϕ_a', is anticipated from thermodynamics to be ϕ_a''. Consequently, 'downhill' diffusion occurs from the higher concentration region of ϕ_0 to the lower concentration region surrounding the nucleus of composition ϕ_a'. The concentration of the nucleus, ϕ_a' and the secondary phase, ϕ_a'', remains constant whereas the interface between the two phases moves during the growth process.

Often it is desirable to distinguish between both mechanisms of phase separation to determine the exact positions of the binodal and spinodal curves. Table 1.1. summarises the characteristic features of each mechanism.

Solely from morphological studies, identifying each mechanism can be unreliable since the interwoven texture of spinodal decomposition can break down in the late stages and disperse. A far superior method is to study the kinetics of each process. As mentioned earlier, the early stages of spinodal decomposition is successfully described by the linearised Cahn Hilliard theory. For nucleation and growth, an approach originally derived for crystallisation processes by Johnson, Mehl and Avrami[19,20] can be applied.

Table 1.1. Mechanisms of Phase Separation.

1. Nucleation and Growth.

a) Formation of a more stable nucleus.

b) Two contributions to free energy:

i) work spent in forming the surface and

ii) work gained in forming the interior.

c) Concentration in immediate vicinity of the nucleus is reduced - 'downhill' diffusion (diffusion coefficient is positive).

d) Increase in the droplet size.

e) Requires activation energy, metastable process.

2. Spinodal Decomposition.

a) Initial small amplitude composition fluctuations.

b) Amplitude of wave-like composition fluctuations increases with time.

c) Diffusion is 'uphill' from the low concentration region into the domain (diffusion coefficient is negative).

d) Unstable process: no activation energy required.

e) Phases tend to be interconnected.

a). Early stage.

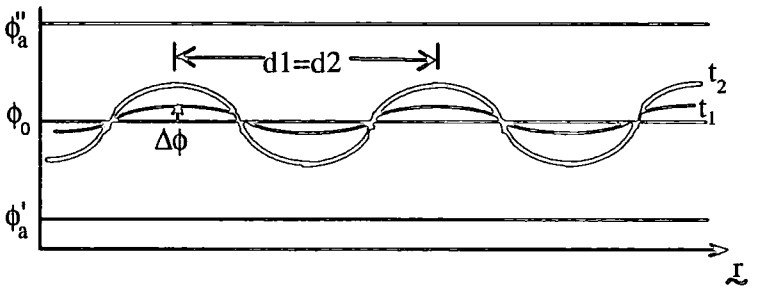

The periodicity is essentially fixed, d1=d2. The amplitude of concentration fluctuations, $\Delta\phi$, increases exponentially with time, $t_2 > t_1$

b). Intermediate stage.

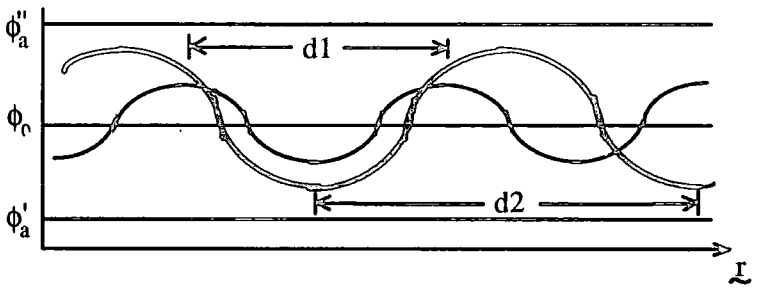

Periodicity increases and there is a non-exponential growth in the amplitude of fluctuation.

c). Late stage.

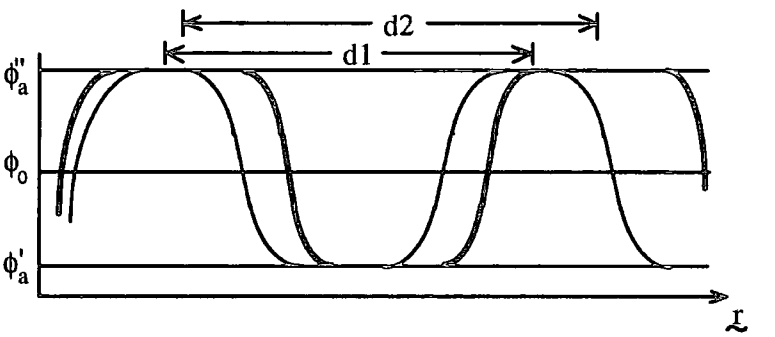

The periodicity continues to increase whereas the amplitude of concentration fluctuation reaches an equilibrium value.

Figure 1.5. The Characteristic Features of Each Stage of Spinodal Decomposition.

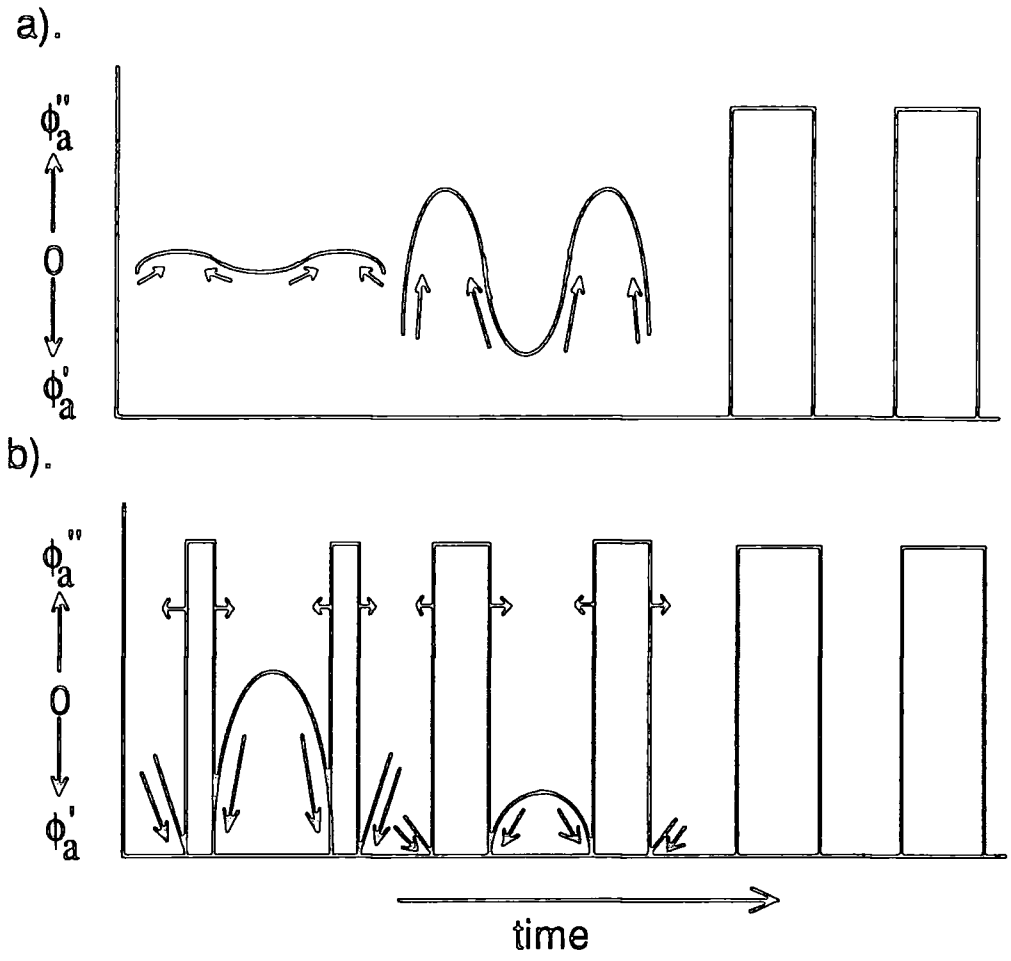

Fig. 1.6. a). Spinodal Decomposition and b). Nucleation and Growth.

1.1.3.3. Phase Separation Kinetics: Nucleation and Growth.

This method provides information about the mechanism of any nucleated growth process of a new phase in a parent matrix, e.g., the isothermal crystallisation of a bulk polymer from its melt and metastable phase separation. The kinetic mechanism is described in terms of the growth geometry, the type of nucleation process and identifies the slowest rate determining step.

The sigmoidal shape illustrated in figure 1.7. is characteristic of any nucleated growth process and has generally been analysed using the Johnson, Mehl and Avrami (JMA) method. This theory[21] provides a relationship between the fraction of polymer transformed as a function of transformation time in the form;

$$X(t) = 1 - \exp\left(-K_n t^n\right) \qquad (1.12)$$

where X(t) is a property of the system which changes linearly with the degree of transformation and the nucleated growth process, e.g., X could be related to the spherulitic radius or scattered depolarised light intensity; K_n contains several constants[22] and is related to the rate of transformation, t is the transformation time at the transformation temperature and n is the JMA exponent. Such analysis is independent of the exact polymer model (the general form is characteristic of any transformation that proceeds by nucleation and growth of a new phase in the parent matrix), and it is possible to fit any transformation isotherm by adjustment of the parameters K_n and n. Since the value of the JMA exponent depends upon the details of the nucleation and growth processes[21], the determined JMA exponent should in principle provide information on the geometry of the growth process, the type of nucleation (instantaneous or homogeneous) and the rate limiting process that controls the elementary transformation event (diffusion or interfacially controlled) (see table 1.2.).

Figure 1.7. X(t) vs. time for a Nucleated Growth Process.

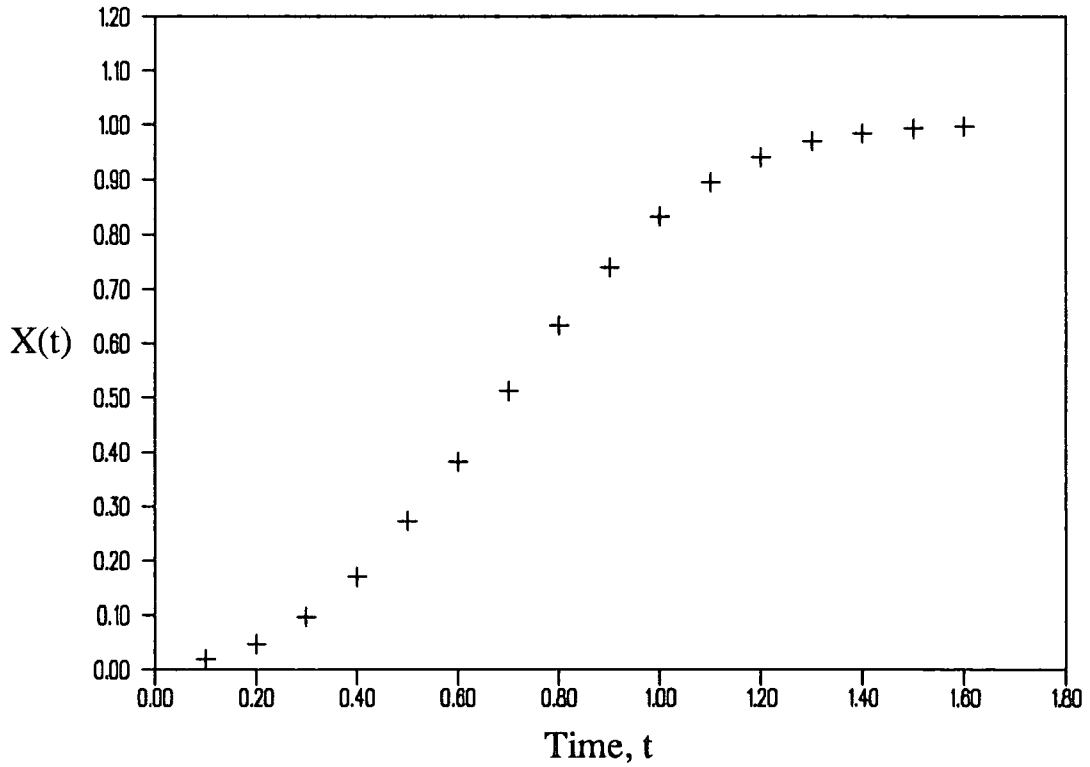

Exponent	Nucleation	Growth Geometry	Growth Control
1/2	Instantaneous	Rod	Diffusion
1	Instantaneous	Rod	Interface
1	Instantaneous	Disc	Diffusion
1 1/2	Instantaneous	Sphere	Diffusion
1 1/2	Homogeneous	Rod	Diffusion
2	Instantaneous	Disc	Interface
2	Homogeneous	Disc	Diffusion
2	Homogeneous	Rod	Interface
2 1/2	Homogeneous	Sphere	Diffusion
3	Instantaneous	Sphere	Interface
3	Homogeneous	Disc	Interface
4	Homogeneous	Sphere	Interface

Table 1.2. Avrami Exponents and their Interpretation.

Instantaneous: Nucleation occurs on existing heterogeneities. Nuclei form simultaneously at the start of the transformation.

Homogeneous: There is a sporadic formation of nuclei. Nucleation occurs at a constant rate throughout the time scale of the experiment in the untransformed parent phase.

Diffusion controlled: The kinetics are controlled by the rate of diffusion of macromolecules to the nuclei.

Interface controlled: The kinetics are controlled by the rate of attachment of macromolecules to the nuclei.

1.1.3.4. Equation of State Theories.

Freeman and Rowlinson[23] observed that many hydrocarbon polymers in solvents of low polarity exhibit an LCST in addition to the more familiar UCST. This was attributed to the proximity of the solvent's vapour/liquid critical point. As a result, Flory[24] presented a new expression for ΔG_m based on the 'equation of state properties' of the pure components following earlier work of Prigogine.[25] This was further elaborated and simplified by Patterson.[26,27]

Somewhat later it was recognised that phase separation in high mass polymer blends was almost always of the LCST type. McMaster[28] evaluated the Prigogine-Flory-Patterson theory and applied it to polymer-polymer mixtures.

The equation of state theory effectively modifies the temperature dependence of χ by the inclusion of a 'free volume term', A (see equation 1.8.). The free volume term, A, is always positive and has an exponential dependence upon temperature.

If χ is negative, then only an LCST is predicted to be present, but if χ is positive and very small, or if the components of the mixture are of moderate molecular mass, then both LCST and UCST may occur.

1.1.3.5. Lattice Fluid Model and Further Developments of the Flory-Huggins Approach.

Sanchez and Lacombe[29,30] modified the original F-H theory to take into account volume changes upon mixing by allowing their lattice model to be compressible. The most important result from the lattice-fluid treatment predicted the temperature and composition dependence of χ for high molecular mass blends.

Following this treatment, Koningsveld et al[31,32] derived the following expression:

$$\chi = X_0 + \frac{X_1}{T} + X_2 T + X_3 \ln T \qquad (1.13)$$

where the various coefficients X_i may depend on concentration.

The concentration dependence of χ arises from the difference in size and shape between segments 1 and 2. Staverman[33] approached this concentration dependence by expressing χ in terms of the ratios of the surface areas of the two interacting segments. For many purposes, the interaction parameter can be approximated by:

$$\chi = X_0' + \frac{X_1'}{T} + Y\phi_2 \qquad (1.14)$$

where X_0' refers to the entropic portion and X_1' to the enthalpic portion of the interaction energy and Y is related to the ratio of the surface areas of segment 1 and 2. This theory predicts a LCST (only) if X_1 or X'_1 are negative, an UCST (only) if X_1 or X'_1 are positive and the values of X_2 and X_3 allow both UCST and LCST in the same system.

The concentration dependence of χ is often not sufficient to account for some of the complex shapes encountered experimentally in actual phase diagrams. Consequently, it is necessary to introduce explicitly the 'compressible-lattice model' which effectively introduces a number of additional parameters.

1.1.3.6. Spin Lattice Models.

De Gennes[34,35] and des Cloizeaux[36] have noted that a system of n-component magnetic spins is analogous with a system of self avoiding polymer chains disposed on a lattice. This model, however, is unable to predict properties dependent on molecular weight and solvent character.

More recently, Freed et al[37] has modified this magnetic lattice model by labelling the spins with an internal symmetry. This enabled the generation of rigorous corrections to the Flory-Huggins theory and their concentration dependence. It also indicated the source of the entropic contribution to the Flory-Huggins interaction parameter, χ.

1.1.4. Crystallinity in Semi-Crystalline/Amorphous Polymer Blends.

Polymer chains must be capable of packing closely together in a regular, parallel array in order for crystallinity to occur. Consequently, the more regular the polymer chain structure, the higher the level of crystallinity possible. This ordering of polymer chains is energetically favourable as there is a lowering of enthalpy as the chains are bound together. However, there is an opposing entropic contribution owing to the associated reduction in possible chain conformations. Crystalline blends are often used commercially as engineering plastics and fibres, owing to their high level of thermal and chemical resistance and mechanical strength.

For an amorphous/semi-crystalline polymer blend, the homopolymer components are either miscible or immiscible. For the immiscible case, the crystalline component crystallises apart from the amorphous fraction, which has no effect on the melting point and crystallisation behaviour of the crystalline component, e.g., polyisobutylene/isotactic polypropylene[38].

For the miscible case, extensive experimental studies have shown that the amorphous component has a dramatic effect on the crystallisation behaviour of the crystalline component. A reduction in the crystalline lamellar thickness and an increase in the interlamellar distance (poly(vinylidiene fluoride)/poly(methyl methacrylate), PVDF/PMMA[39]), decrease in the radial growth rate (poly(vinyl acetate)/PMMA[40], a depression in the equilibrium melting point (see section 1.1.4.3.), a reduction in the degree of crystallinity (poly(ε-caprolactone)/poly(vinyl chloride)[41] and a change in the crystal surface energies[38] have been observed as the fraction of the amorphous component is increased. A number of excellent reviews on the crystallisation behaviour of semi-crystalline/amorphous blends have been presented elsewhere.[5,22,23,42,43,44]

1.1.4.1. Structure of Crystalline Polymers.

Before the 1950's, the fringed micelle model[45-47] was used to explain successfully a wide range of behaviour in semi-crystalline plastics and fibres (see figure 1.8.). In figure 1.8., each chain meanders from crystallite to crystallite, binding the whole mass together.

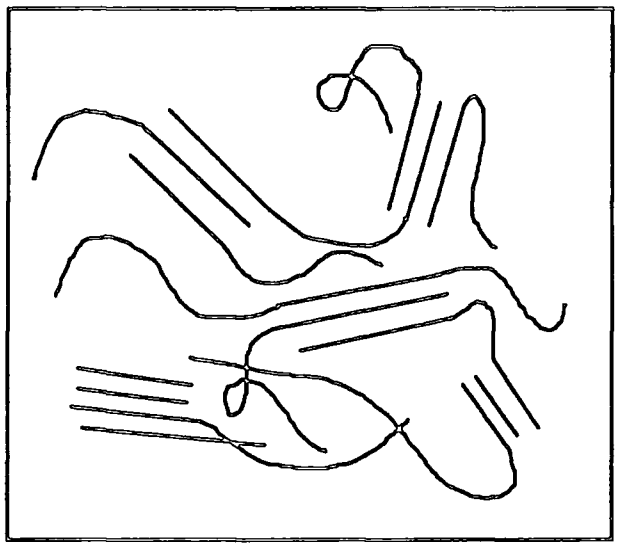

Figure 1.8. Fringed Micelle Model. Linear regions represent crystallinity (ordered polymer chains).

The model was succeeded by the folded chain model[48], see figure 1.9.

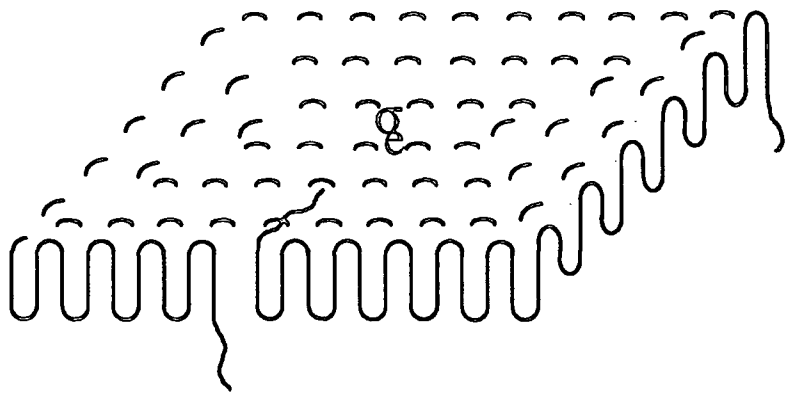

Figure 1.9. Folded Chain Model - adjacent re-entry.

Figure 1.9. shows that with this model, the molecules fold back and forth with hairpin turns along with adjacent re-entry. Combined with the other limiting case, i.e.,

the Switchboard model[49] where the chain re-entry is essentially random, these two models represent the accepted view of the structure of crystalline polymers. This crystalline model is commonly referred to as a lamellar shaped crystal and are practically of the order of 100-200Å thick. In fact a lower crystal thickness limit exists for lamellar crystals because there must be a sufficient amount of free energy of crystallisation to balance out that needed for the formation of the hairpin-like fold.[50] The lateral surface free energy of the crystal, σ_e, is shown in figure 1.9.

1.1.4.2. Morphology.

Whereas dilute solutions form lamellar shaped crystals similar in appearance to the model in figure 1.9., in a concentrated solution, various multi-layered dendritic structures are formed.

The most common micro-structure is a sphere-shaped crystalline structure called a spherulite. Spherulites are composed of individual lamellar crystalline platelets where the flat surface of the lamellae lies perpendicular to the radial direction of the spherulite,[50] see figure 1.10.

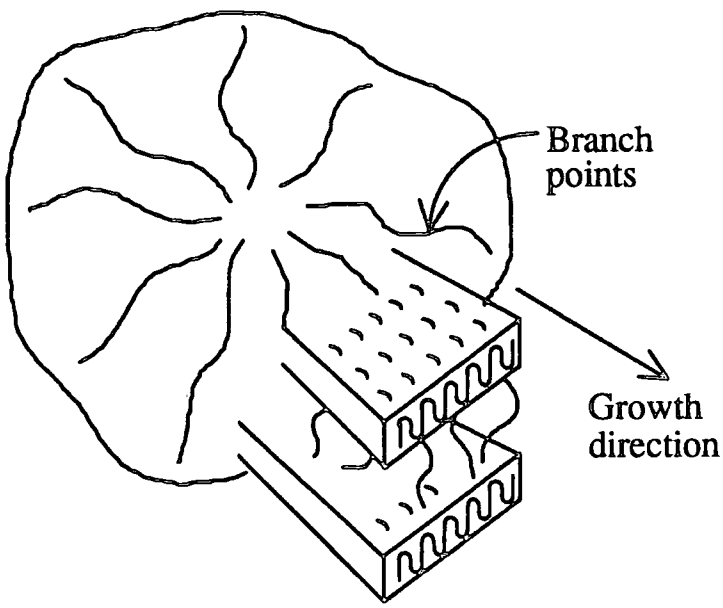

Figure 1.10. Model of Spherulitic Structure.

The interlamellar regions contain the amorphous component, impurities and/or a low molecular fraction of the crystallisable component, as well as tie molecules. These tie molecules bind the adjacent lamellar crystals together and it has been proposed that they are a source of the high mechanical strength that spherulites possess.

Other less common morphologies include axailites[51] and hedrites[52]. These sheaf-like structures are observed during the intermediate stages of spherulitic growth.

Spherulitic sizes range from the micron level to hundreds of microns allowing their detection using light. Consequently, with their crystalline birefringent properties, extinction patterns of spherulites are easily observed when viewed through a optical microscope with crossed polars (see Chapter 5). Typically, a 'Maltese Cross' extinction pattern is observed where the dark extinction arms are centred at the origin of the spherulite and are oriented parallel to the plane of polarisation of the polarisers.

1.1.4.3. Melting Point Depression.

In a miscible amorphous/crystalline blend, the amorphous component acts as a diluent and depresses the equilibrium melting point as well as alters the overall crystallisation rate. If the glass transition temperature of the amorphous component is lower than that of the crystallising component, then the spherulites grow faster. Conversely, if the T_g of the amorphous component is greater than that of the crystallising component, then the rate of crystallisation is retarded,[53] as is the case for poly(ethylene oxide)/poly(methyl methacrylate), PEO/PMMA.

As the fraction of diluent increases, the equilibrium melting point is depressed further. This change in melting point with volume fraction of the amorphous component has been used often to determine the Flory-Huggins interaction parameter, χ, for the blend.[54-56]

Following the thermodynamic treatment by Scott[3] based on earlier work by Flory,[57] a quantitative analysis of the melting point depression has been presented by Nishi and Wang[58] for amorphous/crystalline polymer blends (equation 1.15.):

$$\left[\frac{1}{T_m^{\,o}}-\frac{1}{T_{m,PEO}^{\,o}}\right]=\frac{-RV_{2\mu}}{\Delta H_{2\mu}}\left[\left(\frac{B}{RT_m^{\,o}}\right)v_1^{\,2}+\frac{\ln(1-v_1)}{\overline{V}_2}+v_1\left(\frac{1}{\overline{V}_2}-\frac{1}{\overline{V}_1}\right)\right] \quad (1.15)$$

where $T_m^{\,o}$ is the evaluated equilibrium melting point temperature for the blend, $T_{m,PEO}^{\,o}$ is the equilibrium melting point for the pure crystalline component, $V_{2\mu}$ and $\Delta H_{2\mu}$ are the molar volume and the heat of fusion per mole of the crystalline polymer, $\overline{V}_2$ and $\overline{V}_1$ are the molar volumes of the crystalline and amorphous polymers respectively and v_1 is the volume fraction of the blend. B is the free energy density and is related to the Flory-Huggins interaction parameter by:

$$\chi=\frac{BV_{1\mu}}{RT_m^{\,o}} \quad (1.16)$$

where $V_{1\mu}$ is the molar volume of the amorphous polymer.

The last two terms on the right hand side of equation 1.15 account for entropic contributions to the free energy of mixing. For high molecular weight polymers, $\overline{V}_1$ and $\overline{V}_2$ are large, and so these two terms are negligible. Consequently, equation 1.15 simplifies to:

$$\left[\frac{1}{T_m^{\,o}}-\frac{1}{T_{m,PEO}^{\,o}}\right]=\frac{-RV_{2\mu}}{\Delta H_{2\mu}}\left[\left(\frac{B}{RT_m^{\,o}}\right)v_1^{\,2}\right] \quad (1.17)$$

Thus, χ at $T_m^{\,o}$ can be evaluated form the slope of $(1/T_m^{\,o}-1/T_{m,PEO}^{\,o})$ vs. $v_1^{\,2}$.

Rostami[59] has further developed the Nishi-Wang equation by proposing a model that relates the melting point to the crystal thickness, the excess and combinatorial entropies and enthalpy of mixing of the semi-crystalline polymer with the amorphous one as well as χ.

1.2. Block Copolymers.

1.2.1. Introduction.

Block copolymers consist of blocks of monomeric units which are constitutionally or configurationally different from monomer units in adjacent parts. Several variations on this theme exist ranging from the simplest diblock copolymer - $(A)_n$-$(B)_m$- to random copolymers -(ABBAA)-, graft copolymers, multiblock copolymers and star copolymers[60].

Many synthetic routes to block copolymers exist: anionic, cationic, radical initiation, metathesis, condensation and coupling methods.[61-63] Whilst the number of new routes is increasing, the ability of the synthetic polymer chemist to synthesise block copolymers with a defined molecular weight and architecture is rapidly improving.

Interest in such polymers arises, as with the blends, from the ability to tailor and enhance the properties of two chemically distinct constituents. Commercial examples of this include poly(propylene oxide)-b-poly(ethylene oxide), poly(styrene)-b-poly(ethylene oxide) and poly(styrene)-b-poly(butadiene). Most of the useful properties evolve from the thermodynamic immiscibility between unlike blocks leading to microphase separation and their resultant morphologies. Understanding the physics underlying the microphase separation process is important since this enables the controlling factors to be determined and quantified.

1.2.2. Order-disorder Transition (ODT).

As described in section 1.1., under certain conditions polymer blends phase separate forming domains rich in one component of the blend. These domains are usually of the order of thousands of angstroms. For a block copolymer where the otherwise immiscible homopolymer constituents are chemically joined together, a similar situation occurs. Figure 1.11. illustrates the ODT in a diblock copolymer and a homopolymer blend. As the thermodynamic state of the system changes, in this case by altering the temperature, both systems phase separate into a two phase system. For the case of the diblock copolymer, however, micro-domains are formed as a direct result of the restriction of the molecular connectivity. Typical microdomain sizes are of the order of hundreds of angstroms and the term microphase separation is often applied.

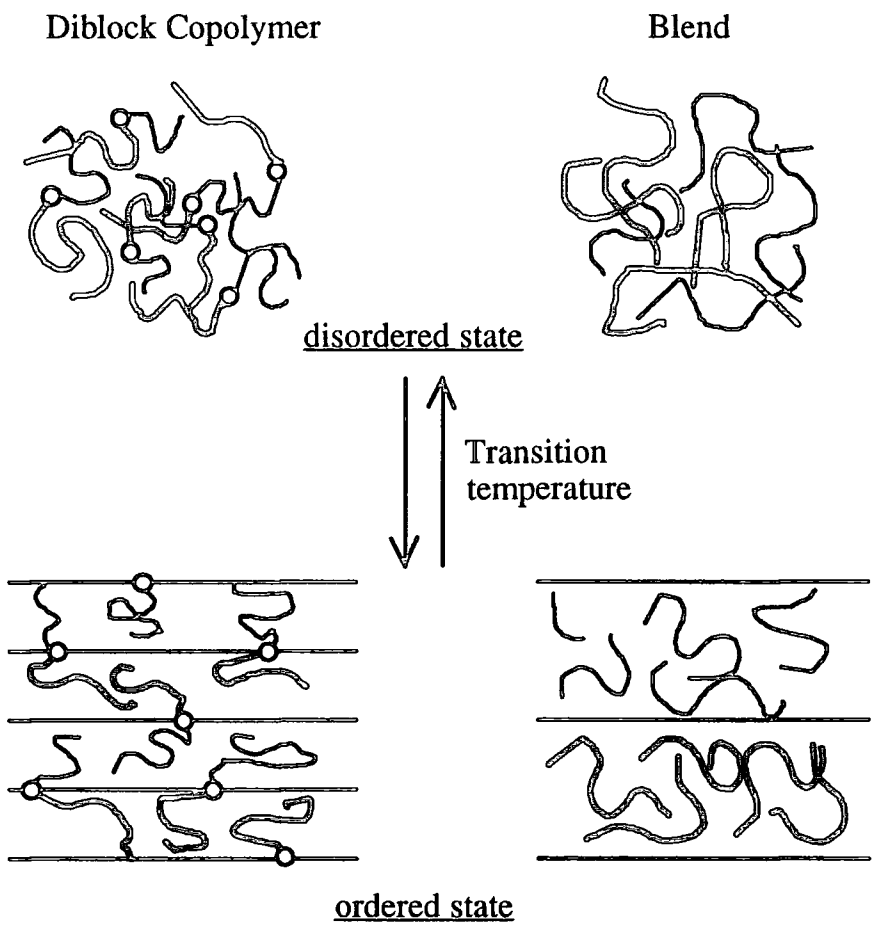

Figure 1.11. ODT for Block Copolymers and Blends.

1.2.3. Microdomain Morphologies.

In the ordered state, primarily dependent upon the relative composition of each constituent in the block copolymer, a wide variety of different morphologies can be obtained. Molau first identified three distinct types of morphology[64]: spherical, cylindrical and lamellae, which was later extended to four by Thomas et al[65] who detected the two tetrapod interpenetrating networks morphology known as the ordered bicontinuous double diamond (OBDD) lattice, see figure 1.12.

For higher molecular weight polymers, the dominant factor involved in the formation of a particular morphology is the drive to minimise the interfacial contact area between the chemical constituents. This leads on to the concept of surfaces having a constant mean curvature, which in turn predicts additional domain morphologies. Recent modulated and perforated lamellar phases have been established near the order-disorder transition[66] and in a recent lecture, Bates[67] et al have detected several additional new phases near the ODT. Bates has related this additional phase complexity to fluctuation effects and the influence of broken conformational symmetry in the block copolymer, $\alpha=a_1/a_2\neq1$ where a_1 and a_2 are the block statistical segment lengths.

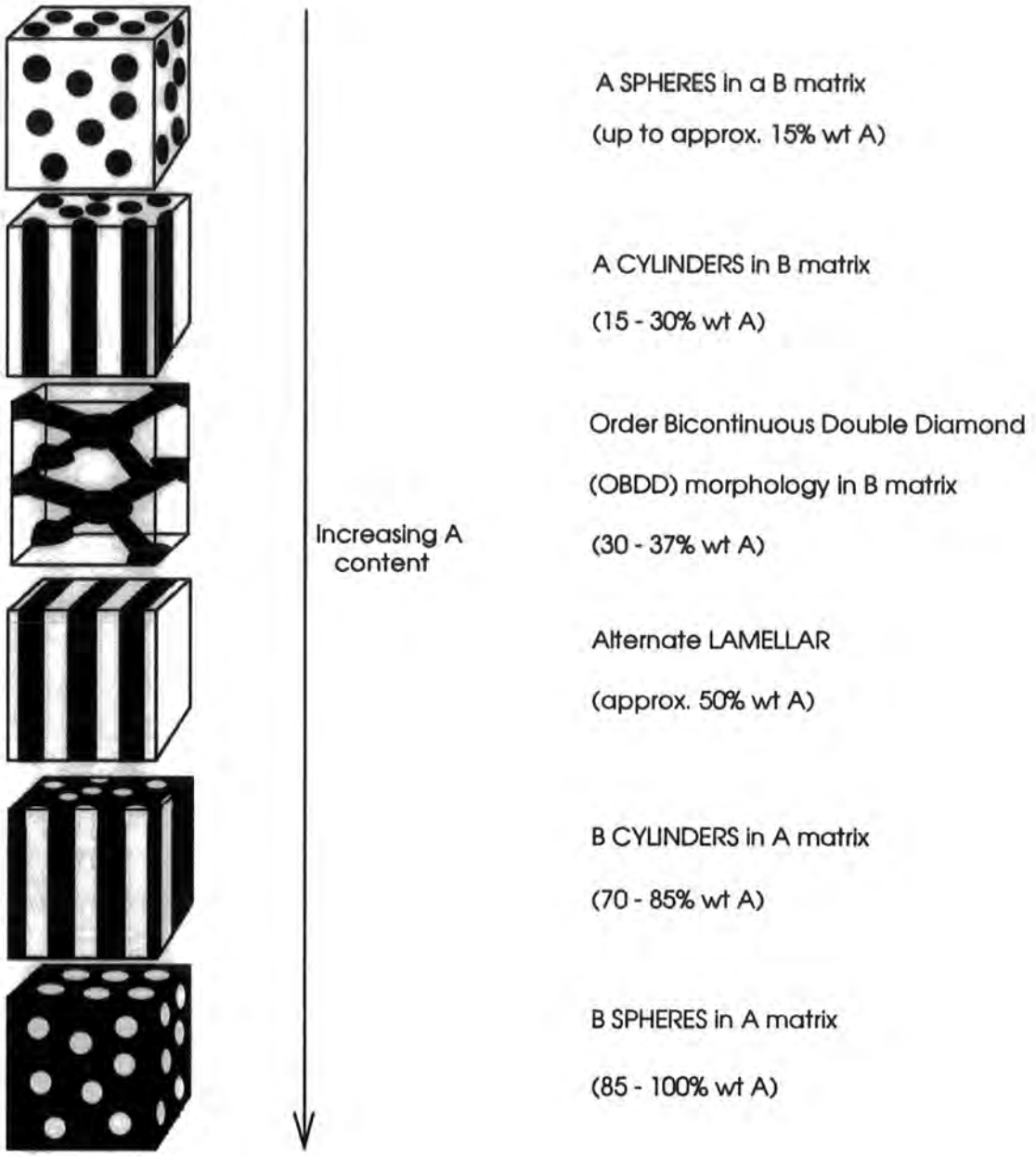

Figure 1.12. Dependence of A-B Diblock Copolymer Morphology on Composition.

1.2.4. Theories of Microdomain Formation.

Several theoretical approaches attributing the different types of morphologies observed and the position of the ODT based upon the thermodynamics of the block copolymer system have been proposed. These approaches, and experimental evidence supporting these theories, have been discussed and summarised in a number of reviews on block copolymers.[61-64] Two limiting regimes exist in the block copolymer phase diagram and are illustrated in figure 1.13.

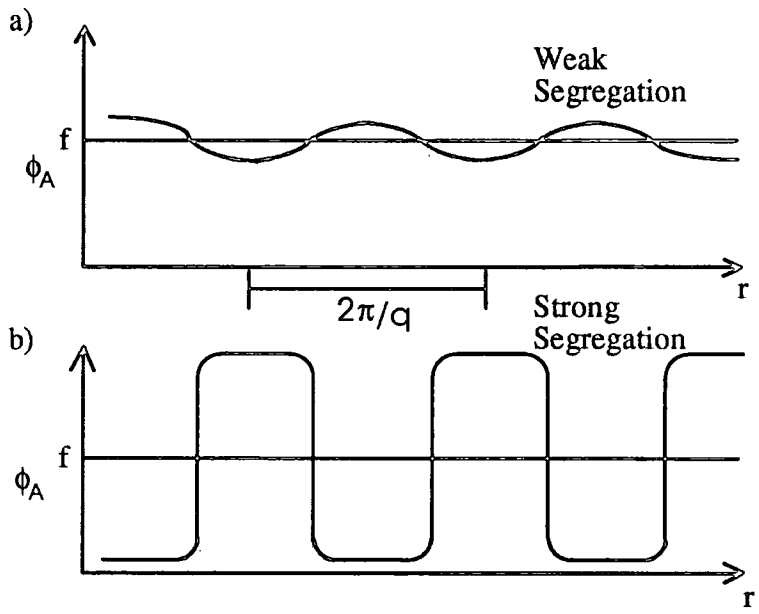

Figure 1.13. Comparison of the One-Dimensional Composition Profiles Characterising the Weak (WSL) and Strong (SSL) Segregation Limits.

In figure 1.13., ϕ_A and f refer to the local and macroscopic A-block volume fractions respectively, and q is the scattering vector, $q=4\pi/\lambda\sin(\theta/2)$, where θ is the polar scattering angle and λ the wavelength of incident radiation.

For the weak segregation limit (WSL), the ordered composition profile changes smoothly from one domain space to the other and is approximately sinusoidal, see figure 1.10., a). In the disordered melt, ($\chi N<<1$), the A-B interactions are sufficiently

weak that the individual chains are unperturbed, however, the connectivity and the incompressibility of the melt lead to a correlation hole[68,69] that is manifested in scattering measurements as a peak corresponding to a fluctuation length scale $D \sim R_g \sim aN^{1/2}$, where R_g is the copolymer radius of gyration and a is a characteristic segment length.

The second limiting regime of phase behaviour is referred to as the strong segregation limit (SSL). This corresponds to the situation of $\chi N >> 10$ where nearly pure A and B microdomains are separated by narrow interfaces, see figure 1.13.b. Here the microdomain period scales as $D \sim aN^{2/3}\chi^{1/6}$. The critical value of χN is $(\chi N_c)=10.495$ for f=0.5 (see equation 1.20). This value increases for other values of f.

Whereas the classification of a particular regime may break down in the ODT region, the proposed theories can be categorised as either WSL or SSL.

1.2.4.1. Strong Segregation Limit.

Numerous authors have advanced theories of the domain structure in block copolymers.[70] One of the earliest statistical theories to describe the equilibrium aspects of microphase separation and the resultant morphologies was proposed by Meier.[71,72] Meier's theory enabled conditions for microphase separation and equilibrium domain size, in solvent free systems for spherical, cylindrical and lamellar morphologies of di- and tri-block copolymers to be predicted in terms of the interaction parameter and molecular characteristics. There are three factors involved in the calculation of the free energy of formation of the microdomain equilibrium morphology:

i) Drive to reduce the interfacial free energy; this is possible by reducing the surface area to volume ratio by increasing the domain size. This is opposed by two entropic factors (ii and iii).

ii) Drive to maintain uniform density; for large domains: unperturbed molecules usually would not be able to reach into the centre of the domain to fill it up. Since the drive to maintain constant density is a strong one, there is a preferential rejection of

those configurations which do not fill the domain centre uniformly, and a preferential weighting of the rarer configurations which do reach further into the centre. Such re-weighting of the chain conformational statistics results in a loss of conformational entropy.

iii) Restriction on the placement of the block copolymer junction at the interfacial area: each block copolymer must have its joint in the interfacial region, otherwise B units would be unfavourably situated in the A phase, causing a penalty in free energy. This effectively results in an entropic limitation to domain growth.

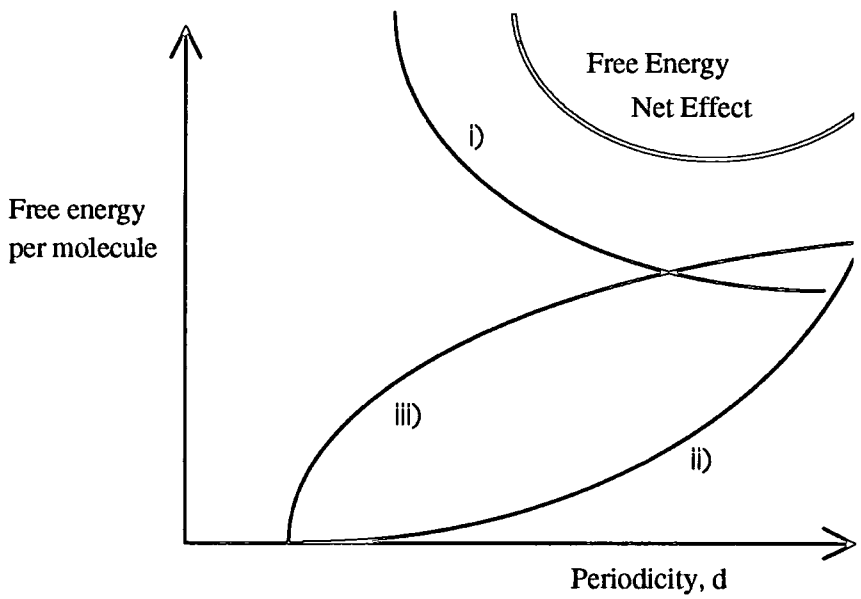

Figure 1.14. Factors Involved in the Free Energy of Formation of Microphase Separation in Block Copolymers.

The equilibrium domain dimensions are obtained by minimising the overall free energy equation and the corresponding value of the periodicity, d is the most stable domain size, see figure 1.14. Thermodynamically, the domain morphology depends strongly upon the relative composition of each component as illustrated in figure 1.15.

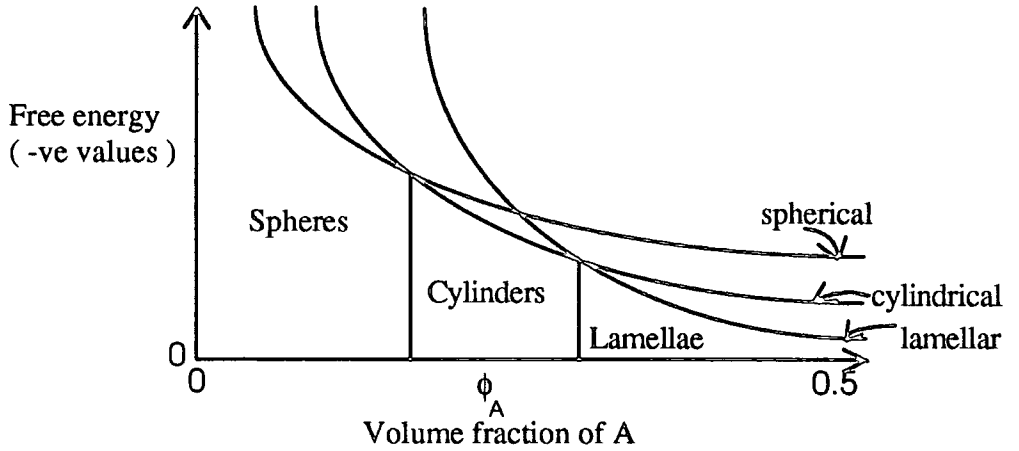

Figure 1.15. Domain Morphology for A-B Type Block Copolymers as a Function of Composition A.

After the publication of Meier's work, many additional and modified theories based upon Meier's original theory were proposed: Inoue et al[73] who concluded that the block segments are preferentially oriented along the direction perpendicular to the interface between the two phases, Leary and Williams[74] who emphasised the importance of the interphase region in their theory and Krigbaum et al.[75,76] More recently Helfand[77] significantly developed Meier's work and presented a statistical thermodynamic theory to predict the size and shape of microdomains in amorphous block copolymers. This theory, often referred to as the narrow interphase approximation (NIA), assumed that the domain interface is small in comparison with the microdomain size and introduced a fourth term involving χ which sets the zero of free energy as the homogeneous phase of the diblock copolymer. The thickness of the interphase, a_I, was given by:

$$a_I = (2 / 6^{1/2})(a / \chi) \qquad (1.18.)$$

where a is the Kuhn statistical segment length and it is assumed that the polymer pair in the block copolymer is symmetric, i.e. $a_A=a_B=a$ and equal densities of A and B phases.

The NIA simplified the expression for the change in free energy, made it more widely applicable and allowed the domain sizes and the inter-domain distance to be obtained by minimisation. The theory was applied to spherical[78], cylindrical[79] and lamellar[80] domain morphologies.

NIA is applicable for block copolymers where the following expression holds:

$$\chi N \geq 20 \qquad (1.19.)$$

where N is the degree of polymerisation (number of monomer units in the polymer chain) of the block.

Further discussion on this strong limit has been provided[81,82] and good experimental agreement with Meier and Helfand's SSL theories for PS-Poly(isoprene) has been observed.[83-86]

Although the NIA simplified Meier's original theory, the practical application of this approach required complex numerical analysis for some systems. Semenov[81] introduced a more soluble classical analogue which was further clarified by Milner et al.[87-89] The solution indicates that the copolymers are stretched non-uniformly as they enter into the microdomains and predicts that chain ends are in excess in the domain interiors.

Ohta and Kawasaki[82,90] more recently derived a SSL field theory based upon a single scalar field describing the composition patterns. A random phase approximation (RPA) for the free energy function was also used. Although this approximation is only valid for weak compositional fluctuations, see section 1.2.4.2., this approach is able to predict the phase diagram and domain periods that are qualitatively similar to those of Helfand and Semenov, with a reduction of the free energy function calculation to a purely geometrical problem.

No theory at present is capable of predicting the existence of the OBDD in the SSL, although an attempt has been made by Anderson and Thomas[91] based upon the approach by Ohta and Kawasaki[81].

1.2.4.2. Weak Segregation Limit.

Leibler[68] derived a mean field theory for this WSL regime based upon the random phase approximation, (RPA), developed by de Gennes[34]. This described the situation of the block copolymer in the single phase melt and predicted the symmetry of the microphase separated structure produced as the ODT (microphase separated temperature, MST) is crossed on cooling in terms of the degree of polymerisation, the Flory-Huggins interaction parameter and the composition of the block copolymer. Three symmetries were predicted: lamellar, hexagonal close packed (hcp), and body-centred cubic (bcc) spheres, see figure 1.16.

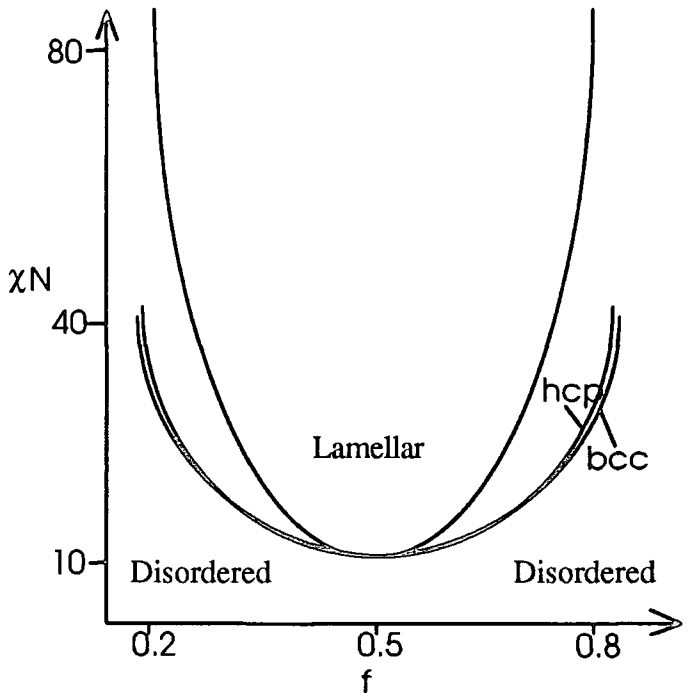

Figure 1.16. Phase Diagram for a Block Copolymer showing the Transition Lines between the Disordered and Various Ordered Phases.

The important product, χN, where N is the number of monomer units, as well as the composition, determines the morphology of the block copolymer, see figure 1.16.

For a block copolymer with composition f=0.5, the critical point of the phase diagram is:

$$\chi N = 10.495 \qquad (1.20.)$$

This is compared to the critical point for a homopolymer blend of the same composition, where:

$$\chi N = 2 \qquad (1.21.)$$

This suggests that at the same temperature, assuming A and B from the relation $\chi=A+B/T$, are the same in both copolymer and homopolymer blend, a diblock copolymer would be homogeneous $\{(\chi N)<(\chi N_c)\}$ while the corresponding homopolymer would phase separate $\{(\chi N)>(\chi N_c)\}$, in agreement with the experimental work of Krause et al[92] and Hoffman et al[93].

Leibler's theory has been described in detail elsewhere,[94] and only some of the more relevant characteristics will be described here.

Leibler introduced an order parameter, $\psi(r)$, which describes the average deviation of the local monomer number density from the uniform system. This parameter is related to the density-density correlation functions, S(q) which in turn is related to the scattered intensity, I(q):

$$\langle|\psi(q)|\rangle^2 \propto S(q) \propto I(q) \qquad (1.22.)$$

Using the RPA, he provided the following general expression for a molten diblock copolymer:

$$I(q) \approx \left[\frac{S(q)}{W(q) - 2\chi}\right]^{-1} \qquad (1.23.)$$

where S(q) is the sum of the Fourier transforms of the different density-density correlation functions and W(q) is the determinant of the same terms:

$$S(q) = S_{AA}(q) + S_{BB}(q) + 2S_{AB}(q) \qquad (1.24.)$$

$$W(q) = S_{AA}(q)S_{BB}(q) - S_{AB}{}^2(q) \qquad (1.25.)$$

For a linear A-B diblock copolymer:

$$S_{AA}(q) = Ng(f,x) \qquad (1.26.)$$

$$S_{BB}(q) = Ng(1-f,x) \qquad (1.27.)$$

$$S_{AB}(q) = \frac{N}{2}[g(1,x) - g(f,x) - g(1-f,x)] \qquad (1.28.)$$

where g(f,x) is the Debye function:

$$g(f,x) = \frac{2[fx + \exp(-fx) - 1]}{x^2} \qquad (1.29.)$$

and $x=q^2Rg^2$, $Rg^2=Na^2/b$ where a is the Kuhn statistical length and Rg is the radius of gyration of an ideal chain with N monomers.

At high values of q, the monomer density fluctuations are like those of an ideal chain and I(q) decreases as $1/q^2$. At low q, the intensity decreases as a result of the systems incompressibility. The net result is a peak at intermediate q and has been described as the 'correlation hole' effect, as stated earlier.[34] Consequently, the wavelength of the dominant mode of the thermal fluctuations and the spinodal point, χ_S, for the system can be determined from the following expressions:

$$\xi = \frac{2\pi}{q_m} \tag{1.30.}$$

$$I(q_m)^{-1} \approx \frac{S(q)}{W(q) - 2\chi_s} = 0 \tag{1.31.}$$

where q_m is the value of q at which I(q) becomes a maximum and S(q)/W(q) becomes a minimum, and χ_S is the Flory-Huggins interaction parameter at the spinodal point. The magnitude of the intensity maximum is determined from the value of N, the width reflects the influence of χ and the position depends upon Rg (moves to lower q as the radius of gyration increases)[93]. It is interesting to note that at the spinodal point, the scattered intensity for a copolymer is infinite and becomes discontinuous, whereas for the equivalent homopolymer mix, the scattered intensity is finite (intensity is infinite at q=0).

Experimental evidence supporting this mean field theory have been reported.[95,96] It is worth noting at this point that experimental work on block copolymers is often limited by the range in χN afforded by accessible temperatures. This has been overcome by adding modest amounts of neutral solvent, with no preference to the constituents in the copolymer, and replacing χ with an effective interaction parameter, χ_{eff}, which is proportional to the concentration of copolymer. As shown by Fredrickson and Leibler[97], caution must be taken in using this 'dilution approximation' since it neglects several aspects of the physics of such solutions. They

noted that there is a tendency for a neutral, good solvent to accumulate at the interfaces of the microdomains.

A major flaw appears however in the predicted transitions between different ordered states which has not been observed experimentally. This can be attributed to the fact that Leibler's mean field theory does not take into account compositional fluctuations. These fluctuations were included by Fredrickson and Helfand[98] which modifies the phase diagram illustrated in figure 1.16., providing direct windows accessing the lamellar and hexagonal ordered phases rather than going through the bcc phase. Additionally, the critical point of the phase diagram is now first order with respect to the degree of polymerisation of the diblock copolymer:

$$(\chi N)_c = 10.495 + (41.022 / N^{1/3}) \qquad (1.32.)$$

These corrections, however, are only applicable to copolymer systems with relatively high molecular weights, $N>>10^4$.

Similar analyses to Leibler's theory have been performed based upon different mathematical models.[99] The resultant phase diagram is qualitatively very similar, differences arising in the values of χN for the transition regions. Extensions to the theory have also been reported,[100-104] where Benoit et al,[102] Mori et al[103] and Whitmore and Noolandi[104] have dealt with mixtures of homopolymers and block copolymers.

Recently, Semenov[105] has suggested that the sides of the phase diagram (figure 1.16.), i.e. ϕ_A or $\phi_B<<0.5$, are far more complicated than is predicted by Leibler's and Fredrickson and Helfand's theories. He postulated the existence of a spherical micellar phase close to the ODT in the disordered phase. This phase becomes more concentrated in micelles as χN is increased leading onto a phase transition at which the micelles order into a macro-lattice with fcc symmetry (at the ODT). Subsequent first order structural transitions into hexagonal and bcc phases are also predicted.

The microphase separation kinetics have been described by a time dependent Ginzburg-Landau approach by Hashimoto.[106] If the copolymer melt is quenched from a higher temperature to a lower temperature within the one phase, homogeneous region, the growth of the scattering intensity with time is given by:

$$I(q,t) = I(q,0)\exp(2R(q)t) \qquad (1.33.)$$

where

$$\mathrm{R(q)} = \mathrm{L_0 q^2(-S(q)^{-1})} \qquad (1.34.)$$

and L_0 is the Onsager coefficient connecting the diffusive flux of copolymer molecules to the local chemical potential. R(q), a first order rate constant which characterises the disorder-order transition, can therefore be determined by monitoring the variation in scattered intensity with time. The values of $R(q)/q^2$ with q^2 depend upon five terms: L_0, Rg, N, ϕ_A and ϕ_B, and χ_{eff} (the effective interaction parameter). The effect of these parameters on $R(q)/q^2$ vs. q^2 have been described elsewhere.[93]

This approach is similar to one that has been applied to the description of demixing in polymer blends.[9,107]

1.2.5. Crystallinity in Block Copolymers.

1.2.5.1. Introduction.

The aspects described in section 1.1.4. on the crystallinity in polymer blends are also applicable to block copolymers. The restrictive chemical bond between blocks, however, alters the scale on which crystallisation occurs. The crystallisation regions are confined by the domain size of the block copolymer (if microphase separated), and are usually only of the order of hundred's of Å's in size.

For microphase separated crystalline/amorphous copolymers, the amorphous co-units are either excluded or located within the crystalline lattice.

1.2.5.2. Excluded Amorphous Co-units.

A variety of crystallisable block copolymers where the amorphous fraction is excluded from the crystallite have been examined. The poly(ethylene)-b-polystyrene (PEO-b-PS) system has attracted wide spread interest.[108-112] If the volume fraction of PEO is sufficiently large so that in the melt a PEO matrix or lamellar domains are formed, then upon crystallisation, spherulitic textures with fibrous features are observed.[113] The basic crystalline morphology is sandwich-like, with layers of PS regularly spaced between crystalline layers of folded PEO chains, however, some unusual morphologies have been observed. Square shaped crystals with spirals for a diblock copolymer of PEO-b-PS[114,115] where this morphology becomes less ordered as the fraction of PS increases have been reported. When the volume fraction of PS is large enough to form a PS matrix in the melt, then the PEO crystallises within the disperse phase without any rearrangement of the matrix.[116] Other experimental work has been reported for polyamides,[117,118] polypeptides[119,120] and polyesters.[121]

Following the work by Flory,[122] Mandelkern[123] proposed a theory to estimate the fraction of crystallisable units that are crystalline in copolymers where the amorphous co-unit is excluded from the crystalline lattice. This theory predicted a dependency of the melting point of the copolymer on the sequence arrangement of

1.2.5. Crystallinity in Block Copolymers.

1.2.5.1. Introduction.

The aspects described in section 1.1.4. on the crystallinity in polymer blends are also applicable to block copolymers. The restrictive chemical bond between blocks, however, alters the scale on which crystallisation occurs. The crystallisation regions are confined by the domain size of the block copolymer (if microphase separated), and are usually only of the order of hundred's of Å's in size.

For microphase separated crystalline/amorphous copolymers, the amorphous co-units are either excluded or located within the crystalline lattice.

1.2.5.2. Excluded Amorphous Co-units.

A variety of crystallisable block copolymers where the amorphous fraction is excluded from the crystallite have been examined. The poly(ethylene)-b-polystyrene (PEO-b-PS) system has attracted wide spread interest.[108-112] If the volume fraction of PEO is sufficiently large so that in the melt a PEO matrix or lamellar domains are formed, then upon crystallisation, spherulitic textures with fibrous features are observed.[113] The basic crystalline morphology is sandwich-like, with layers of PS regularly spaced between crystalline layers of folded PEO chains, however, some unusual morphologies have been observed. Square shaped crystals with spirals for a diblock copolymer of PEO-b-PS[114,115] where this morphology becomes less ordered as the fraction of PS increases have been reported. When the volume fraction of PS is larger enough to form a PS matrix in the melt, then the PEO crystallises within the disperse phase without any rearrangement of the matrix.[116] Other experimental work has been reported for polyamides,[117,118] polypeptides[119,120] and polyesters.[121]

Following the work by Flory,[122] Mandelkern[123] proposed a theory to estimate the fraction of crystallisable units that are crystalline in copolymers where the amorphous co-unit is excluded from the crystalline lattice. This theory predicted a dependency of the melting point of the copolymer on the sequence arrangement of

crystallisable units in the copolymer chain and not directly on composition. Experimental results on the melting points of copolyesters[124,125] supported this prediction, however, conflicting experimental results for poly(ethylene terephthalate)-b-poly(butylene terephthalate) block copolymers were also reported.[126] The level of crystallinity predicted was often lower than that found experimentally. This was ascribed to the more significant influence of the crystalline/amorphous interfacial structure owing to the relatively small crystallite thicknesses. A further theoretical development of this excluded model for a copolymer system has recently been proposed by Goldbeck-Wood.[127] He extended a Sadler-Gilmer model,[128] and introduced an additional entropy term in the free energy and melting point depression relationships to describe the copolymer crystal. This model is more applicable when non-equilibrium effects (defects) are significant, as often is the case experimentally, and a stronger melting point depression was predicted than for Mandelkern's theory.[123]

1.2.5.3. Included Amorphous Co-units.

For the latter case, where the amorphous co-unit is incorporated within the crystal lattice, the situation is less clear. This is the situation often encountered for multiblock copolymers where the crystalline unit sequence along the copolymer chain is small.[129] Limited experimental results[130-132] have shown that the crystalline domains are irregularly shaped, 20-150Å's in size and have relatively large diffuse boundaries where there is partial mixing of the amorphous and crystallisable co-units. More recently[133], the non-periodic model (NPL) has been successfully employed to account for the often unexpected large level of crystallinity in random copolymers e.g. poly(vinyl chloride). In this model, adjacent multiblock copolymers chains are ordered in a parallel array to maximise inter-chain amorphous co-unit contacts as well as crystalline co-unit contacts. This development should lead on to a greater understanding of crystallinity in random copolymers.

1.3. Project Aims.

The aim of this research was to study the crystallisation and phase behaviour of a block copolymer whose constituent homopolymers are miscible as a blend, namely poly(ethylene oxide)-b-poly(methyl methacrylate). Such a system has not been studied previously, and should provide general rules which are applicable to other miscible crystallisable block copolymer systems.

A range of block copolymers with various PEO content have been synthesised and the following techniques have been used to study the physical properties of these blocks: size exclusion chromatography (SEC), differential scanning calorimetry (DSC), optical microscopy (OM), nuclear magnetic resonance spectroscopy (nmr) and wide angle and small angle x-ray scattering (WAXS and SAXS). To provide a direct comparison with the PEO-b-PMMA block copolymers, blends of the two homopolymers have been investigated also.

A major part of this project involved the design, construction and operation of a small angle light scattering (SALS) apparatus to study thin, solid polymer films. This technique has also been used to study the phase behaviour of the synthesised PEO-b-PMMA block copolymers.

1.4. References.

1. Flory, P.J., J.Chem.Phys., 1941, 9, 660; J.Chem.Phys., 10, 51, 1942.
2. Huggins, M.L., J.Chem.Phys., 1941, 9, 440; Ann. N.Y. Acad. Sci., 43, 1, 1942.
3. Scott, R.L., J.Chem.Phys., 17, 279, 1949.
4. Tompa, H., Trans. Faraday Soc., 45, 1142, 1949.
5. Nishi, T., CRC Critical Reviews in Solid State and Materials Science, 12, 329, 1984.
6. Sanchez, I.C., Vol. 1, Chapt. 3, p.130 in 'Polymer Blends', Paul, D.R., Newman, S., (Eds.), Academic Press, Inc., 1978.
7. Olabisi, O., Robeson, L.M., Shaw, M., Section 2.2, Polymer-Polymer Miscibility, Academic Press, 1979.
8. Cahn, J.W., Trans. Metall. Soc. AIME, 242, 166, 1968.
9. Cahn.J.W., J.Chem.Phys., 42, 93, 1965.
10. Cahn, J.W., Hilliard, J.E., J.Chem.Phys., 31, 688, 1959.
11. Nishi, T., Wang, T.T., Kwei, T.K., Macromolecules, 7, 227, 1975.
12. McMaster, L.P., Adv. Chem. Ser., 142, 43, 1975.
13. Snyder, H.L, Meakin, P., J. Chem. Phys., 79, 5588, 1983.
14. Hashimoto, T., Itakura, M., Hasegawa, H., J. Chem. Phys., 85, 6118, 1986.
15. Hashimoto, T., Itakura, M., Shimidzu, N., J. Chem. Phys., 85, 6773, 1986.
16. Binder, K., J. Chem. Phys., 79, 6387, 1983.
17. De Gennes, P.G., J. Chem. Phys., 72, 4756, 1980.
18. Pincus, P., J.Chem. Phys., 75, 1996, 1981.
19. Johnson, W.A. and Mehl, R.F., Trans. AIME, 135, A16, 1939.
20. Avrami, M., J.Chem.Phys., 1103, 7, 1939; 212, 8, 1940; 177, 9, 1941.
21. Shultz,J., Chapt. 9, 'Polymer Materials Science', Prentice Hall, Englewood Cliffs, New Jersey, 1974.
22. Sperling, L.H., 'Introduction to Physical Polymer Science', 2nd Ed., Wiley-Interscience, 1992.

23. Freeman, P.I., Rowlinson, J.S., Polymer, 1, 20, 1960.

24. Flory, P.J., Discuss. Faraday Soc., 49, 7, 1949.

25. Prigogine, I. (with Mathot, V. and Bellemans), 'The Molecular Theory of Polymer Solutions', North Holland, Amsterdam, 1957.

26. Patterson, D., J.Poym.Sci., Part C., 16, 3379, 1968.

27. Patterson,D., Macromolecules, 2, 672, 1969.

28. McMaster, L.P., Macromolecules, 6, 760, 1973.

29. Sanchez, I.C., Lacombe, R.H., J.Phys.Chem., 80, 2352, 1976.

30. Lacombe, I.C., Sanchez, I.C., J.Polym.Sci., Polym. Phys. Lett. Ed., 15, 71, 1977.

31. Koningsveld, R., Kieintjens, L.A. and Lablans-Vinck, A.M., Ber. Bunsenges Phys.Chem., 89, 1234, 1985.

32. Kleintjens, L.A. and Lemstras, P.G. (Eds.), 'Integration of Fundamental Polymer Science and Technology', Elsevier, New York, 1986.

33. Staverman, A.J., Recl.Trav.Chim.Pays-Bas, 56, 885, 1937.

34. De Gennes, P.G., 'Scaling Concepts in Polymer Physics', Cornell University Press, Ithaca, New York, 1979.

35. De Gennes, P.G., Phys. Lett. A., 38, 339, 1972.

36. Des Cloizeaux, J., J.Phys. (Les Ullis, Fr.), 36, 281, 1975.

37. Freed, K.F., J.Phys.A., Math. Gen., 18, 871, 1985.

38. Martuscelli, E., Polym.Eng.Sci>, 24, 563, 1984.

39. Nishi, T, Wang, T.T., Macromolecules, 8, 909, 1975.

40. Hay, J.N., Br.Polym.J., 3, 74, 1971.

41. Ong, C.J., Price, F.P., J.Polym.Sci., Polym.Symp., 63, 45, 1978.

42. Rostami, S., Chapt.3 in 'Multicomponent Polymer Systems', Miles, I.S., Rostami, S., (Eds.), Longman Group UK Ltd., 1992.

43. Mandelkern, L., Chapt.11, and Vaughan, A.S., Bassett, D.C., Chapt.12, in 'Comprehensive Polymer Science', Vol.2, Allen, G. and Bevington, J.C., (Eds.), Pergamon Press, 1989.

44. Chow, T.S., Macromolecules, 23, 333-337, 1990.

45. Statton, W.O., J.Polym.Sci., 20C, 117, 1967.

46. Herrmann, K. and Gerngross, O., Kautschuk, 8, 181, 1932.

47. Herrmann, K., Gerngross, O. and Abitz, W., J.Phys.Chem., 10, 371, 1930.

48. Hoffman, J.D., Davis, G.T. and Lauritzen Jr., J.I., in 'Treatise on Solid State Chemistry, Vol.3., Crystalline and Noncrystalline Solids', Hannay, N.B., Ed., Plenum, New York, Chap. 7, 1976.

49. Flory, P.J., J.Am.Chem.Soc., 84, 2857, 1962.

50. Bovey, F.A., Chapt.5 in 'Macromolecules: An Introduction to Polymer Science', Academic Press, 1979.

51. Bassett, D.C., Keller, A. and Mitsuhashi, S., J.Polym.Sci., A1, 763, 1963.

52. Geil, P.H. p.579-585 in 'Growth and Perfection of Crystals', Doremus, R.H., Roberts, B.W. and Turnball, D., (Eds.), Wiley, N.Y., 1958.

53. Martuscelli, E., 'Multicomponents Polymer Blends Symposium', Capri, Italy, May, 1983.

54. Kwei, T.K. and Frisch, H.L., Macromolecules, 11, 1267, 1978.

55. Plans, J., MacKnight, W.J. and Karasz, H.E., Macromolecules, 17, 810, 1984.

56. Walsh, P.J., Rostami, S and Singh, B.V., Makromol. Chem., 186, 145, 1985.

57. Flory, P.J., 'Principles of Polymer Chemistry', Cornell University Press, Ithaca, NY, 1953.

58. Nishi, T. and Wang, T.T., Macromolecules, 8, 909, 1975.

59. Rostami, S., Polymer, 31, 899, 1990.

60. Bates, F.S., Fredrickson, Ann. Rev. Phys. Chem., 41, 525-557, 1990.

61. Noshay, A., McGrath, J.E., 'Block Copolymers Overview and Critical Survey', Academic Press, New York, 1977.

62. Morton, M.J., 'Anionic Polymerisation: Principles and Practice', Academic Press, London 1983.

63. Riess, G., Block copolymers in 'Encyclopaedia of Polymer Science and Engineering', 2nd Edn., Wiley, New York, 1985.

64. Molau, G., in 'Block Copolymers', Agarwal, S.L., (Eds), Plenum, New York, 1970.

65. Thomas, E.L., Alward, D.B., Kinning, D.J., Martin, D.C., Handlin, D.L., Fetters, L.J., Macromolecules, 19, 2197, 1986.

66. Hamley, I.W., Koppi, K.A., Rosedale, J.H., Bates, F.S., Almdal, K., Mortensen, K., Macromolecules, submitted.

67. Bates, F.S., Polymer Conference, Robinson College, University of Cambridge, 20-22 July, 1993.

68. De Gennes, P.G., p.62-64, 'Scaling Concepts in Polymer Physics', Ithaca, Cornell Univ. Press, 1979.

69. Leibler, L., Macromolecules, 13, 1602, 1980.

70. Folkes, M., Keller, A., in 'Physics of Glassy polymers', Hawards, R.N., (Ed.), Applied Science Publishers, 1973.

71. Meier, D.J., J.Polym. Sci., Part C., 26, 81, 1969.

72. Meier, D.J., Polym. Prepr. Am. Chem. Soc., Div. Polym. Chem., 15, 171, 1974.

73. Inoue, T., Soen, T., Hashimoto, T. and Kawai, H., J. Polym. Sci., A-2, 7, 1283, 1969.

74. Leary, D. and Williams, M., J. Polym. Sci., B, 8, 335, 1970; J. Polym. Sci., Polym. Phys. Ed., 11, 345, 1973; 12, 265, 1974.

75. Krigbaum, W., Yazgan, S. and Tolbert, W., J. Polym. Sci., Polym. Phys. Ed., 11, 551, 1973.

76. Boehm, R. and Krigbaum, W., J. Polym. Sci., C, 54, 153, 1976.

77. Helfand, E., Wasserman, Z.R., Chapt. 4 in 'Developments in Block Copolymers', Goodman I (Ed.), Applied Science Publishers, Barking, 1982.

78. Helfand, E., Wasserman, Z.R., Macromolecules, 11, 960, 1978.

79. Helfand, E., Wasserman, Z.R., Macromolecules, 13, 994, 1980.

80. Helfand, E., Wasserman, Z.R., Macromolecules, 9, 879, 1976; Helfand, E., Macromolecules, 8, 552, 1975.

81. Semenov, A.N., Sov. Phys., JETP, 61, 733, 1985.

82. Ohta, T., Kawasaki, K., Macromolecules, 19, 2621, 1986.

83. Richards, R.W., Thomason, J.L, Macromolecules, 16, 982, 1983.

84. Richards, R.W., Adv. Polym. Sci., 71, 1, 1985.

85. Hashimoto, T., Fujimura, M., Kawai, H., Macromolecules, 13, 1660, 1980.

86. Hashimoto, T., Shibayama, M., Kawai, H., Macromolecules, 13, 1237, 1980.

87. Milner, S.T., Witten, T.A., Cates, M.E., Europhys. Lett., 5, 413, 1988.

88. Milner, S.T., Witten, T.A., Cates, M.E., Macromolecules, 22, 853, 1988.

89. Milner, S.T., Witten, T.A., Cates, M.E., Macromolecules, 21, 2610, 1988.

90. Kawasaki, K., Ohta, T., Kohrogui, M., Macromolecules, 21, 2972, 1988.

91. Anderson, D.M., Thomas, E.L., Macromolecules, 21, 3221, 1988.

92. Krause, S., Dunn, D.J., Seyed-Mozzaffari, A., Biswas, A.M., Macromolecules, 10, 786, 1977.

93. Hoffman, M., Kampf, G., Kramer, H., Pampus, G., Adv. Chem. Ser., 99, 351, 1971.

94. Connell, J.G., Ph.D. Thesis University of Strathclyde, Vol. 1, p.69-76, 1989.

95. Mori, K., Hasegawa, H., Hashimoto, T., Polym. J., 17, 799, 1985.

96. Connell, J.G., Richards, R.W., Macromolecules, 23, 766, 1990.

97. Fredrickson, G.H., Leibler, L., Macromolecules, 22, 1238, 1989.

98. Fredrickson, G.H., Helfand, E.J., Chem. Phys., 87, 697, 1987.

99. Olivera de la Cruz, M., Sanchez, I., Macromolecules, 19, 2501, 1986.

100. Leibler, L., Benoit, H., Polymer, 22, 195, 1981.

101. Ijichi, T., Hashimoto, T., Polym. Comm., 29, 135, 1988.

102. Benoit, H., Hadzioannou, G., Macromolecules, 21, 1449, 1988.

103. Mori, K., Tanaka, H., Hashimoto, T., Macromolecules, 20, 465, 1987.

104. Whitmore, M.D., Noolandi, J., Macromolecules, 18, 2486, 1985.

105. Semenov, A.N., Macromolecules, 22, 2849, 1989.

106. Hashimoto, T., Macromolecules, 20, 465, 1987.

107. Binder, K., J. Chem. Phys., 75, 1966, 1981.

108. Gervais, M. and Gallot, B., Makromol. Chem., 171, 157, 1973.

109. Thomas, H.R. and O'Malley, J.J., Macromolecules, 12, 323, 1979.

110. O'Malley, J.J., Thomas, H.R. and Lee, G.M., Macromolecules, 12, 996, 1979.

111. Shimura, Y. and Hatekeyama, T., J.Polym.Sci., Polym.Phys.Ed., 13, 653, 1975.

112. Hirata, E., Ijitzu, T., Seon, T., Hashimoto, T and Kawai, T., Polym.Prepr., Am.Chem.Soc., Div. Polym. Chem., 15, 177, 1974.

113. Crystal, R.G., Erchardt, P.F., and O'Malley, J.J., p.179 in 'Block Copolymers', Aggarwal, S.L. (Ed.), Plenum Press, New York, 1970.

114. Kovacs, A.J., Lotz, B., Kolloid Z.Z.Polym., 97, 209, 1966.

115. O'Malley, J.J., Crystal, R.G., Erhardt, P.F., p.163 in 'Block Copolymers', Aggarwal, S., Ed., Plenum Press, New York, 1970.

116. Lotz, B. and Kovacs, A.A., Polym.Prepr., Am.Chem.Soc., Div.Polym.Chem., 10, 820, 1969.

117. Petit, D., Jerome, R. and Teyssie, Ph., J.Polym.Sci., Polym. Chem. Ed., 17, 2903, 1979.

118. Hergenrother, W.L. and Ambrose, R.J., J.Polym. Sci.,Polym. Chem. Ed., 12 2613, 1974.

119. Hayashi, T. Chapt.4 in 'Developments in Block Copolymers - 2', Goodman, I, (Ed.), Elsevier Applied Science, London, 1985.

120. Nakajima, A., Kugo, K. and Hayashi, T., Macromolecules, 12, 845, 1979.

121. Van Berkel, R.W.M., de Graaf, S.A.G., Huntjens, F.J. and Vrouenraets, C.M.F., Chapt.7 in 'Developments in Block Copolymers - 1', Goodman, I, (Ed.), Applied Science, London, 1982.

122. Flory, P.J., Trans. Faraday Soc., 51, 848, 1955.

123. Mandelkern, L., p.387 Chapt. 11 in 'Comprehensive Polymer Science', Vol.2, Allen, G. and Bevington, J.C., (Eds.), Pergamon Press, 1989.

124. Coffey, D.H. and Meyrick, T.J., Proc. Rubber Techno. Conf., 3rd, 170, 1954.

125. Kenney, J.F., Polym.Eng.Sci., 8, 216, 1968.

126. Misra, A. and Garg, S.N., J.Polym.Sci., Polym.Phys.Ed., 24, 983, 1986.

127. Goldbeck-Wood, G., Polymer, 33, 4, 778, 1992.

128. Sadler, D.M. and Gilmer, G.H., Phys. Rev. Lett., 56, 1708, 1986.

129. Reiss, G., p.235-434 in 'Block Copolymers', Vol. 2.

130. Sorrano, M., MacKnight, W.J., Thomas, E.L. and Ottino, J.M., Polymer, 28, 1667-1674, 1987.

131. Droescher, M., Bandara, U. and Schmidt, F.G., Macromol. Chem. Phys. Suppl., 6, 107, 1984.

132. Tyagi, D., J.L., Webster, D.C., McGrath, J.E. and Wilkes, G.L., Polymer, 29, 833, 1988.

133. Windle, A., 'Crystallisation of Random Copolymers', at The Polymer Conference, Cambridge, 20-22 July, 1993.

Chapter 2.

Poly(ethylene oxide)/Poly(methyl methacrylate) (PEO/PMMA) Blends - Literature Review.

2.1. Introduction.

2.1.1. Poly(ethylene oxide).

PEO is a thermoplastic of low toxicity and high melt viscosity. It is hydrophilic, semi-crystalline (T_m^o is approximately 338K depending upon molecular weight), has a low glass transition temperature of approximately 208K and is miscible with a variety of formulations e.g. poly(propylene oxide)[1], poly(vinyl naphthalene)[2]. Commercially it is used in cosmetic formulations, dental adhesives, detergents and contact lens solutions.[1]

2.1.2. Poly(methyl methacrylate).

PMMA is also a thermoplastic, but is hydrophobic and in its glassy state, (T_g=398K for atactic PMMA), has a high resistance to wear and chemical attack and possesses excellent optical properties. In industry, because of its hardness and relatively high T_g, it tends to be used to manufacture shaped objects. Rigid applications include glazing materials, biomedical appliances and optical applications. Non-rigid applications include coatings, textiles, paper and oil additives[3].

The potential for a blend of these two homopolymers with tailored properties is consequently enormous. Scientific and industrial interest in semicrystalline miscible blends has been gaining significant momentum over the last few years and a market growth of 9% annually has been predicted until 1996[4].

Until now PEO/PMMA blends have found application in paints, forming hydrophilic/hydrophobic pigment carrying latexes in aqueous solutions and as blend based

polymer electrolytes[5]. As high-performance and engineering thermoplastics usually contain a certain level of crystallinity to provide high temperature stability and environmental resistance, it is therefore important to know the effect upon the crystallisation of a semicrystalline polymer when it is blended with an amorphous polymer with which it has favourable interactions. Consequently, there has been much study using a wide variety of physical techniques on the crystalline phase behaviour of poly(ethylene oxide)/poly(methyl methacrylate) blends.

For the purpose of this chapter, PMMA will denote atactic and syndiotactic poly(methyl methacrylate) only. The influence of isotactic PMMA blended with PEO will be treated separately, (section 2.3.3.).

2.2. Methods of Analysis.

2.2.1. Optical Microscopy.

A slight depression of the equilibrium melting point has been observed as the PMMA concentration is increased.[6-9,14,16] This has been attributed to favourable interactions between the homopolymer pairs suggesting miscibility at temperatures above the melting point temperature. The Flory-Huggins interaction parameter, χ, at temperature T has been evaluated from the determined equilibrium melting point temperatures, T_m^o, using the Nishi-Wang equation,[38] see table 2.1..

PEO/PMMA M_w	χ	Temperature, T (K)
20,000/110,000	-1.93	349
100,000/110,000	-0.35	349
365,000/93,600	-0.131	333
4,000,000/93,600	-0.139	333

Table 2.1.. Evaluated Flory-Huggins Interaction Parameter for PEO/PMMA Blends using Optical Microscopy.

From the Nishi-Wang plot, Martuscelli[16] observed a non-negligible entropic contribution to the mixing of the two polymers. Russell et al,[14] however, has attributed the observed melting point, T_m', depression to changes in the surface free energies of the crystalline lamellae, an increase in the number of crystalline defects and, or a change in the crystalline structure. Consequently, along with the assumptions inherently present in the determination of the equilibrium melting point, T_m^o, and its dependence upon temperature scanning rate and the annealing time at the crystallisation temperature, T_c, they concluded

that χ=0. A more desirable method to determine T_m^o was suggested. This involved determining the crystalline lamellae thickness, L, as a function of T_c using small angle x-ray scattering, SAXS, followed by extrapolation to infinite L. This publication also summarised the T_m^o values for various molecular weights of PEO from earlier studies.

Martuscelli et al[9] observed a non-linear T_m' dependence on T_c at low undercooling and attributed this to lower critical solution temperature, LCST, type phase behaviour[39] at temperatures close to the melting point temperature. Such non-linear behaviour , however, was later attributed to the more probable cause of morphological and kinetic effects[52] as stated by the same author four years later.[16]

For blends containing <40% by weight of amorphous PMMA, the polymer system crystallises forming a well defined spherulitic, X-type Maltese cross morphology when viewed under crossed polars. This indicates that the crystalline axes within the spherulite are aligned parallel or perpendicular to the radial direction,[40,41] it was observed that this texture became more feather-like and less ordered as the concentration of PMMA increased,[16] and the growth rates were linear and decreased dramatically as the concentration of PMMA increased and the crystallisation temperature decreased.[8,9,15,16] The linear growth rate along with the observation of no significant dark regions denoting high concentrations of amorphous material[9,16] when viewed under crossed polars, suggests the amorphous PMMA component is incorporated in interlamellar regions within the crystalline spherulite. The spherulitic growth rate was faster for a specific T_c, for blends containing a lower molecular weight PEO component.[16]

Several authors have studied the isothermal crystallisation kinetics using the values obtained for the spherulitic growth rate, G and T_m^o and a modified version of the Turnbull-Fisher equation[8,15-17](see Chapter 5 for a more detailed desription of this approach). The lateral surface free energy for the crystalline species, σ_e, has been evaluated for various molecular weights and compositions, see table 2.2.

Composition (w/w) PEO/PMMA	PEO (20,000) PMMA (110,000)	PEO (100,000) PMMA (110,000)	PEO (4,000,000) PMMA (93,600)
100/0	23.6	25	18.8 independent of composition
90/10	10.8	17.8	
80/20	11.2	15.8	
70/30	9.1	14.7	
60/40	-	14.6	

Table 2.2. Lateral Surface Free Energy, σ_e (mJm^{-2}), for PEO/PMMA Blends.

An increase in σ_e with increasing molecular weight of PEO is observed and has been attributed to an extension of the crystal/isotropic liquid like interphase owing to an increase in entanglement and knotting of chains in the initial melt as the molecular weight increases preventing the attainment of the equilibrium interphase.[42] The lateral surface free energy also increases as the concentration of PMMA decreases. Martuscelli et al[8,16] have proposed an explanation for this observation in terms of an overriding increase in the entropy of folding as the proportion of PMMA content increases. This is due to the formation of loops on the surface of the PEO lamellae crystals.

Russell et al[14] have developed a new phenomenological theoretical treatment for G for the case of an amorphous/crystalline blend. The rate of spherulitic growth is described by a kinetic equation that incorporates co-operative diffusion, crystalline lamellae thickness, free energy of formation of secondary nuclei and the Flory-Huggins interaction parameter, χ. Whereas this approach in principle is more theoretically correct for PEO/PMMA, the modified Turnbull-Fisher equation is based on a homopolymer system, difficulties arise owing to its complexity and the fact that the rate equation derived is dimensionally incorrect.

Additional work using optical microscopy on PEO/PMMA blends has involved studying the influence of tacticity of the PMMA component[10,17] and the crystallisation process under high pressure.[12] Atactic and syndiotactic PMMA both acts as diluents, retarding the spherulitic growth rate and depressing the observed melting point temperature. This is in contrast to isotactic PMMA which has no effect on G and T_m'. John et al,[17] explained this observation in terms of i-PMMA/PEO immiscibility. For blends under high pressure (500MPa), the degree of T_m' depression is smaller, blends with higher PMMA concentrations (70% by weight) are able to crystallise and it was observed that the PEO crystallises separately from the PMMA.[12] They ascribed these observations to phase separation during to crystallisation.

2.2.2. Differential Scanning Calorimetry, DSC.

Differential scanning calorimetry has been used to study the crystallisation kinetics and phase behaviour of PEO/PMMA blends.[8,9,14,16,18-21,23]

By monitoring the heat of crystallisation, the relative degree of crystallinity, X_c, and the overall isothermal crystallisation kinetics have been analysed[8,16]. The degree of crystallinity was found to decrease with an increase in the PMMA concentration and a decrease in T_c.[16] This suggests the PMMA component is incorporated within the spherulite and more PMMA is trapped as the level of undercooling increases. Evaluated overall isothermal rate constants, K_n, based upon the Johnson/Mehl/Avrami, (JMA), equation[43], show a decrease with increasing PMMA concentration and increasing crystallisation temperature[8,16]. The Avrami exponents tend to increase with PMMA concentration and decrease as the overall molecular weight increases, see table 2.3.

The values of the exponent are scattered around an average value of 2.5 which relates to homogeneous nucleation, spherical growth geometry and diffusion controlled isothermal crystallisation.[44] Further work by Addonizio et al[20] have studied the non-isothermal crystallisation of the polymer blend.

Composition (w/w)	PEO (100,000) PMMA (110,000)[16]	PEO (4,000,000) PMMA (936,000)[24*]
100/0	2.6	1.9
90/10	2.6	2.0
80/20	2.5	2.1
70/30	2.8	2.3
60/40	3.1	2.7

Table 2.3. Evaluated Avrami Exponents for PEO/PMMA Blends.

(* from depolarised light microscopy data).

The Flory-Huggins interaction parameter has been evaluated from T_m^o values by two sets of authors.[18,21] Assman et al[18] observed two distinct gradients for plots of the observed melting point versus crystallisation temperature, the slope of highest gradient being at lower undercooling. Consequently, two χ values were evaluated, χ=-1.76 for higher crystallisation temperatures and χ=-0.177 for lower T_c. They ascribed this non-linear T_m' depression behaviour over the whole range of T_c to the kinetic dependence of the morphology of the blends. Such non-linear T_m behaviour has also been observed by Martuscelli et al.[8] They attributed this to a more perfect crystalline phase (higher T_m') at lower undercooling (higher T_c) owing to molecular fractionation and preferential dissolution of smaller and/or more defective molecules of the crystallisable component into the uncrystallised/amorphous phase. Liberman[23] evaluated χ=-0.157 at 333K, again suggesting miscibility at this temperature.

Li et al's work[21] on the observed melting points for various compositions of PEO/PMMA yielded some interesting conclusions. They observed constant T_m' values for blends of low PEO concentrations (40-60% w/w) and postulated that the crystallisation process occurs together with phase separation, the phase separation

proceeding to completion prior to the slower crystallisation for these lower PEO concentrated blends.

The glass transition temperature, T_g, can provide useful information regarding the miscibility of a polymer system. Single T_g's which agreed well with Fox[45] and Pochan[46] analyses for miscible systems were observed for high PMMA concentrations (>70%).[9,23] For compositions containing a low PMMA concentration, a single but constant T_g value has been detected using DSC at approximately 228K.[18,21] Assman[18] attributed this to phase separation which is supported by Li's[21] observation of a second T_g which is masked by the melting endotherm but detected by a shift in the baseline. For compositions around 50% w/w, the situation is less clear. Assman[18] observed two T_g's for 75-80% w/w PMMA, and a single T_g for compositions up to 60% PMMA, whereas Li[21] observed two T_g's for concentrations of PMMA >50%. Owing to the repeated presence of two glass transition temperatures, this suggests that two different phases are present, probably due to phase separation of the UCST type. However, it important to realise that difficulties arise in determining the T_g for these compositions because the expected values are at temperatures which are invariably masked by the melting endotherm.

2.2.3. Small Angle X-ray Scattering, SAXS and Small Angle Neutron Scattering, SANS.

Using SAXS measurements, Silvestre et al[13] deduced that the superstructure of the blends is influenced not only by composition but also by the configuration of PMMA used. For the case of atactic PMMA and syndiotactic PMMA, the structure consists of PEO crystalline lamellae separated by amorphous and transition regions containing PEO and PMMA, whereas for the isotactic PMMA/PEO system, it consists of alternate crystalline and amorphous lamellae of PEO with the isotactic PMMA segregated in interfibrillar regions. For atactic PMMA Cimmino et al[37] not only evaluated the crystalline lamellae thickness as a function of crystallisation temperature, but also deduced

that the lamellae thickness was independent of composition. They also supported the amorphous PMMA/crystalline PEO two phase lamellar structure model.

By comparing SAXS and SANS measurements, Russell et al[14] showed unequivocally that the amorphous PMMA is incorporated between the crystalline PEO lamellae. They also suggested the interaction parameter between PEO and PMMA is quite small based on the observation of a relatively constant crystalline lamellae thickness as a function of composition. SAXS measurements indicated a diffuse-phase boundary of approximately 20Å. This was ascribed to an interfacial region at the surface of the PEO crystals from which the amorphous PMMA is excluded. This region represented a volume over which the order from the crystal is lost.

Earlier work by Ito et al[26] using SANS evaluated the χ value to be quite large and negative for mixtures of PEO/PMMA. This value was found to be independent with temperature but became more positive as the percentage of PMMA increased (at 80% by weight PMMA, χ was positive). This composition dependence of χ suggest that the entropic rather than enthalpic interactions are dominant.

2.2.4. Depolarised Light Microscopy.

Calahorra et al[24] studied the crystallisation kinetics of PEO/PMMA using depolarised light microscopy based on the JMA approach[43]. Again, they observed atactic PMMA acting as a diluent, lowering the rate of crystallisation as the concentration of PMMA increased. Avrami exponents close to 2 were evaluated which increased as the concentration of PMMA increased.

2.2.5. Electron Spin Resonance, ESR.

Shimada et al[27] detected an upper critical solution temperature (UCST) at 341K for an isotactic PMMA (M_n=5,000)/PEO (M_n=6,000) system. This was deduced from

two spectral components with different rates of motion - the 'fast' and 'slow' components are attributed to nitroxide radicals trapped in the PEO-rich and PMMA-rich regions respectively.

2.2.6. ^{13}C Nuclear Resonance Spectroscopy, NMR.

At 333K and 363K, using ^{13}C nmr, Martuscelli et al[28] monitored T_1 relaxation times for various PMMA/PEO compositions. T_1 of PEO was found to monotonically decrease with increasing PMMA indicating the commensurate reduction in mobility of the PEO. These observations were accounted for by assuming that at 333K and 363K the two polymers were miscible.

2.2.7. Infra-red Spectroscopy, IR.

Ramana et al[29] observed the presence of a blend component as well as the pure homopolymers components using IR spectroscopy measurements. They concluded along with theoretical work, that the PEO/PMMA system was weakly miscible. Li et al[21] observed a PEO conformation change with composition where the number of trans sequence for PEO increased with increasing PMMA content. This supports Ramana's[29] work where the PEO more favoured helical structure (gauche conformation)[32] changes to a co-planar structure (trans dominant) owing to PMMA interactions.

2.2.8. Theoretical Analysis.

Using the results from IR measurements and the application of group theory upon blending, PMMA forces the PEO molecule to change from the helical (7/2) structure of PEO[32] to a planar zig-zag structure[30]. By considering the relative atomic charge distribution for each homopolymer and their relative structures, Ramana et al[29] concluded that for both ideal isotactic and syndiotactic PMMA/PEO blends, strong polar attractive interactions were sterically improbable. This stems from the presence of both attractive

and repulsive forces having their origin in the carbonyl group of PMMA. Thus the interactions are very weak and quite possibly of the magnitude of van der Waals type, indicating the miscibility of PEO/PMMA is more 'physical' than 'chemical'. Silvestre et al[13] also applied this atomic charge method to isotactic PMMA/PEO and syndiotactic PMMA/PEO blends. Their result also indicated weak miscibility for both tacticities which were in disagreement with their SAXS results suggesting immiscibility for the isotactic PMMA/PEO system. Thus, they speculated that the difference in mixing behaviour was partly due to differences in free-volume contributions and thermal expansivities between the various tactic forms of PMMA.

Several approaches have been used to predict the phase behaviour of PEO/PMMA blends.[28,30,33-36] From the similarity in their solubility parameters (δ=38.67$J^{1/2}cm^{-3/2}$ for PMMA, δ=35.97$J^{1/2}cm^{-3/2}$ for PEO (amorphous) and, δ=44.32$J^{1/2}cm^{-3/2}$ for PEO (crystalline)), this approach predicts the blend of PEO/PMMA to be miscible in the melt.[28,30] A more extensive approach was used by Cimmino et al[33] who applied a simplified version of the corresponding states theorem of Prigogine[47,48] for a polymer-liquid system (Patterson's theory).[49,50] They found that this approach predicted miscibility in the liquid state from 273K to 473K and a lower critical solution temperature (LCST) at 623K±70K. Privalko et al[34] studied the composition, temperature and pressure dependences of thermodynamic characteristics for the melts of blends of PEO/PMMA and treated the experimental data in terms of the Sanchez-Lacombe equation of state theory.[51] This predicted a weak temperature dependence of χ and the presence of a high LCST.

Chow et al[36] extended the well known Nishi Wang equation for the melting point depression of miscible polymer blends to include the effect of crystalline morphology, i.e., the melting depression arises not only from polymer-polymer interaction, but also from the change in the crystal thickness or perfection. They applied this approach to PEO/PMMA blends and found that the negative Flory-Huggins interaction parameter tends to a smaller value and the thickness of lamellae thins as the concentration of the diluent increases.

Thus, the polymer mixture becomes less compatible as the concentration of PEO is reduced in this miscible polymer blend.

2.3. Summary and Conclusions.

Figure 2.1. below represents schematically a summary of the accumulated literature data and the author's own interpretation for PEO/PMMA blends in the form of a phase diagram.

2.3.1. Phase Behaviour.

A vast amount of experimental data using a variety of experimental techniques indicate that PEO/PMMA are weakly miscible at temperatures close to the melting point of PEO. Numerous investigations have evaluated the Flory-Huggins interaction parameter, χ, ranging from -0.13 to -1.93, along with theoretical treatments predicting a small negative value for χ, which is weakly temperature dependent. A strong composition dependence of χ has also been observed, becoming more positive as the concentration of PMMA increases, suggesting that the favourable interactions are entropically driven. This miscible one phase region tends to cover all temperatures above T_m^o up to the degradation temperature at 573K, see figure 2.1. No experimental data has supported any LCST behaviour at these higher temperatures but such a phase boundary has been theoretically predicted at 623±70K. For temperatures below 338K, the situation becomes far more complex, as additional factors such as crystallisation of the PEO component and the mobility of the miscible system come into play.

A single glass transition temperature indicating miscibility has been observed for high PMMA concentrations, but for blends containing a higher proportion of PEO, frequently two T_g 's have been observed. For the middle composition range (40-60% PEO), the experimental results are at times inconsistent. This inconsistency cannot be wholely attributed to variations in molecular weight, polydispersity and experimental variations such as thermal histories. This implies that additional processes as well as crystallisation are present. Taking into account the observed non-linear T_m' behaviour for

this composition range and the temperature and composition dependence of χ, a possible explanation lies in a UCST type phase boundary at temperatures below the depressed melting point temperature, see the crossed hatch region in diagram 2.1. Combined with the crystallisation of the PEO component both processes are critically balanced giving rise to the observed experimental inconsistencies.

The observation of a constant T_g for higher PEO concentrations is more likely to be attributed to crystallisation forming crystalline lamellae of relatively constant PEO composition (80% by weight of PEO). This is supported by SAXS data of a constant crystalline lamellar long period as a function of composition.

The thermodynamic state of a blend of PEO/PMMA can also be altered by changing the pressure. An increase in pressure effectively forces the polymer blend to be less miscible, thus reducing the diluent effect of PMMA.

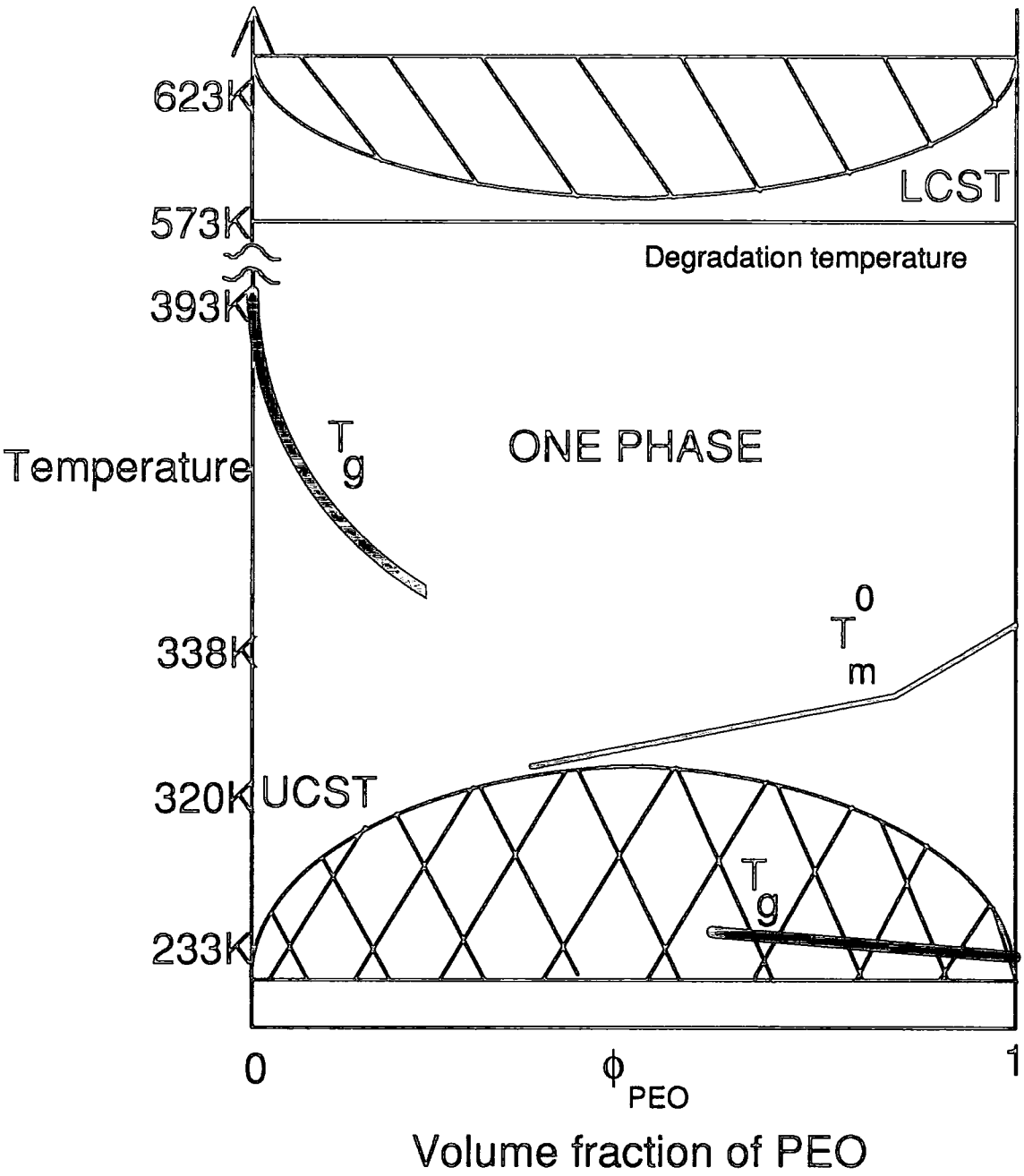

Figure 2.1. Schematic Representation of a Phase Diagram for PEO/PMMA Blends.

2.3.2. Crystallisation.

Poly(methyl methacrylate) acts as a diluent, depressing the equilibrium melting point, reducing the rate of spherulitic growth and the degree of crystallinity. Since PMMA has a higher glass transition temperature than PEO, the associated reduction in chain mobility as the PMMA composition increases also contributes to a reduction in the overall rate of crystallisation. The non-linear behaviour at low undercooling can be ascribed to a variety of kinetic effects such as crystalline morphology, crystalline defects, the influence of different annealing times and scanning rates, and molecular fractionation. These effects contribute to the broad range of values obtained for χ evaluated using the Nishi/Wang approach[52]. For compositions >50% of PEO, the blend crystallises forming an X-type Maltese cross morphology when viewed under crossed polars which becomes less ordered as the concentration of diluent increases. The spherulitic growth rates are linear, which, supported by SAXS evidence of increasing amorphous lamellae thickness with increasing PMMA content, indicate that PMMA is incorporated within the interlamellar regions of the crystalline spherulite. The crystallisation process was found to be homogeneously nucleated (constant nucleation rate throughout), have a spherical growth geometry and was diffusion controlled i.e. the JMA exponent, $n \approx 2.5$.[43] As the concentration of PMMA increases, n also increases and based on two different molecular weight studies, n also increases as the overall molecular weight of the blend decreases implying a change in the crystallisation mechanism. Little is known of the specific polymer-polymer interactions between PEO and PMMA, however, the PMMA diluent alters the favoured 7/2 helical structure of PEO to one that is zig-zag planar (trans dominated). The lateral surface free energy of the crystal ranges from 9-25mJm^{-2}, increasing as the concentration of PMMA increases and the combined molecular weight increases. A diffuse phase boundary on the crystal surface of width approximately 20Å's has been detected. This region contains no PMMA component and it represents a volume where the crystalline order of the PEO crystalline lamellae is lost.

2.3.3. Tacticity.

As previously stated, in the above text, PMMA (without any reference to its tacticity) refers to atactic and syndiotactic conformations only. For isotactic PMMA/PEO blends, fundamental differences in the physical characteristics of the blend have been observed owing to the blends immiscibility. Thus, isotactic PMMA does not act as a diluent and a UCST value of 341K has been detected for a low molecular weight blend of these two components. This behaviour is not predicted from group theory or atomic charge methods, which has lead theorists to propose the origin of immiscibility lies in free volume and/or thermal expansivity effects.

2.4. References.

1. Booth, C. and Pickles, C.J., J.Polym.Sci., Polym.Phys.Ed., 11, 595, 1973.
2. Rembaum, A., Moacanin, J. and Cuddihy, E., Adv.Chem.Ser., 48, 159, 1965.
3. Consise Encyclopaedia of Polymer Science and Engineering, Kroschwitz, J.I., (Ed.), Wiley-Interscience, 1990.
4. Kossoff and Associates, 'The future of Polymer Alloys - III, 1987.
5. Florjanczyk, Z., Such, K., Wieczorek, W., J. of Macromol. Sci., Pure Appl. Chem., A29(10), 853-863, 1992.
6. Cortazar, M.M., Calahorra, M.E. and Guzmán, G.M., Eur. Polym. J., Vol.18, p.165-166, 1982.
7. Martuscelli, E., Silvestre, C., Addonizio, M.L. and Amelino, L., Makromol. Chem., 187, 1557, 1986.
8. Martuscelli,E., Poly. Eng. and Science, Vol. 24, No.8, 563-586, 1984.
9. Martuscelli, E., Demma, G., in Polymer Blends: Processing, Morphology and Properties, Martuscelli, E., Palumbo, R. and Kryszewski, M., Eds., Plenum, New York, 1980.
10. Cimmino, S., Di Pace, E., Martuscelli, E., Silvestre, C., Makromol. Chem., Rapid Commun., 9, 261-265, 1988.
11. Li, X., Wang, Y., Yang, Y., Acta Polymerica Sinica, No.1, 75, 1987.
12. Nakafuku, C., Toyonaga, N., Polymer, 33, No.11, 2370-2375, 1992.
13. Silvestre, C., Cimmino, S., Martuscelli, E., Karasz, A.L. and MacKnight, W.J., Polymer, 28, 7, 1987.
14. Alfonso, G.C., Russell, T.P., Macromolecules, 19, 1143-1152, 1986.
15. Calahorra, E., Cortazar, M., Guzmán, G.M., Polymer, Vol. 23, Aug. 1322-1327, 1982.
16. Martuscelli, E., Pracella, M., Yue, W.P., Polymer, Vol. 25, Aug 1097-1106, 1984.

17. John, E., Ree, T., J. Polym. Sci.: Part A: Polym. Chem., Vol. 28, 385-398, 1990.

18. Assman, K., Schneider, H.A., J.of Thermal Analysis, 35, 459-468, 1989.

19. Makhija, S., Pearce, E.M., Kwei, T.K., J.of Polym. Sci.: Part A: Polym. Chem., Vol. 30, 2693-2698, 1992.

20. Addonizio, M.L., Martuscelli, E., Silvestre, C., Polymer, 28, 183-188, 1987.

21. Li, X., and Hsu, S.L., J. of Polym. Sci., Polym. Phys., Vol 22, 1331-1342, 1984.

22. Hoffman, D.M., Ph.D. Thesis, University of Massachusetts, 1979.

23. Liberman, S.A., De S. Gomes, A., Macchi, E.M., J. of Polym. Sci.: Polym. Chem., 22, 2809-2815, 1984.

24. Calahorra, E., Cortazar, M., Guzmán, G.M., Polymer Commun., Vol. 24, July p.211-213, 1983.

25. Russell, T.P., Ito, H., Wignall, G.D., Macromolecules, 21, 1703-1709, 1988.

26. Ito, H., Russell, T.P., Wignall, G.D., Macromolecules, 20, 2213-2220, 1987.

27. Shimada, S., Kashima, K., Hori, Y., Kashiwabara, H., Macromolecules, 23, 3769-3772, 1990.

28. Martuscelli, E., Demma, G., Rossi, E. and Segre, A.L., Polymer Commun., 24, 266-267, 1983.

29. Ramana Rao, G., Castiglioni, C., Gussoni, M., Zerbi, G., Martuscelli, E., Polymer, Vol. 26, 811-820, 1985.

30. Sanchez, I.C., in Polymer Blends, Paul, D.R. and Newman, S., Eds., Academic, New York, p.135, 1978.

31. Miyazawa, T., J.Chem.Phys., 35, 693, 1961.

32. Flory, P.J., Statistical Mechanics of Chain Molecules, Wiley, New York, p.166, 1969.

33. Cimmino, S., Martuscelli, Silvestre, C., Polymer, Vol.30, 393-398, 1989.

34. Privalko, V.P., Petrenko, K.D., Lipatov, Yu.S., Polymer, Vol.31, 1277-1287, 1990.

35. Petrenko, K.D., Privalko, V.P. and Lipatova, Yu.S., Polymer, Vol. 31, 1283-1287, 1990.

36. Chow, T.S., Macromolecules, 23, 333-337, 1990.

37. Cimmino, S., Di Pace, E., Martuscelli, E., Silvestre, C., Makromol. Chem., 191, 2447-2454, 1990.

38. Nishi, T., Wang, T.T., Macromolecules, 8, 909, 1975.

39. Kwei, T.K., Wang, T.T., Chapt. 4 in 'Polymer Blends', Paul D.R., Newman, S., Ed., Vol. 1, Academic Press, 1978.

40. Samuels, R.J., J. Polym. Sci., Part A-2, 9, 2165-2246, 1971.

41. Haudin, J.M., Chapt. 4 in 'Optical Properties of Polymers', Meeten, G.H., Ed., Elsevier, London, 1986.

42. Mandelkern, L., 363-414 Comprehensive Polymer Science, Vol.2, eds. G.Allen and J.C.Bevington, Pergamon Press, 1989.

43. Avrami, M., J. Chem. Phys., 7, 1103, 1939; 8, 212, 1940; 9, 177, 1941.

44. Shultz, J., Chapt. 9 'Polymer Materials Science', Prentice Hall, Englewood Cliffs, New Jersey 1974.

45. Fox. T.G., Bull., Am., Phys., Soc., 1, 123, 1956.

46. Pochan, J.M., and Crystal, R.G., in 'Dielectric Properties of Polymers', p.313, (Ed., Karasz, F.E.), Pleum, New York, 1972.

47. Prigogine, I., Bellemans, A. and Mathot, V., Chapt. 16, 'The Molecular Theory of Solutions', North-Holland, Amsterdam, 1957.

48. Eichinger, B.E. and Flory, P.J., Trans., Faraday, Soc., 64, 2035, 1968.

49. Saeki, S., Konno, S., Kuwahara, N., Nakata, M. and Kaneko, M., Macromolecules, 6, 246, 1973.

50. Saeki, S., Konno, S., Kuwahara, N., Nakata, M. and Kaneko, M., Macromolecules, 7, 521, 1974.

51. Sanchez, I.C. and Lacombe, R.H., J.Phys.Chem., 80, 2353, 1976.

52. Runt, J.P., Barron, C.A., Zhang, X-F, Kumar, S.K., Macromolecules, 3466-3468, 24, 1991.

Chapter 3.

Poly(ethylene oxide) - Poly(methyl methacrylate) Block Copolymers PEO-b-PMMA.

3.1. Synthesis.

3.1.1. Introduction.

Poly(ethylene oxide)- Poly(methyl methacrylate) block copolymers, PEO-b-PMMA, were synthesised using high vacuum anionic polymerisation methods and diphenyl methyl potassium as the anionic initiator. This technique provides a controlled, convenient route for the preparation of well defined polymers in terms of molecular weight, polydispersity and tacticity.

3.1.2. Synthetic Approaches to PEO-b-PMMA.

Various approaches to the synthesis of poly(ethylene oxide)- poly(methyl methacrylate) block copolymers have been investigated, all involving the use of high vacuum anionic polymerisation methods along with a suitable anionic initiator. The so called conventional approach involving the anionic initiation of ethylene oxide (EO) monomer by 'living' poly(methyl methacrylate) (PMMA) macro anions has been commonly utilised. This synthetic route, however, is not without its faults. Low EO conversion along with the possibility of side reactions between the 'living' PEO chain and the alkyl ester group of the block causing formation of inhomogeneous block copolymers have been reported by Suzuki et al,[1,2] Garg et al[3,4] and Seiler et al.[5]

Alternative non-conventional approaches involving reverse sequential addition of the comonomers have proven to be no better. Suzuki et al[1,2] have synthesised PEO-b-PMMA by initiating methyl methacrylate (MMA) with the alkali metal salts of PEO prepared by metalation of PEO oligomers bearing hydroxyl, amine or methyl isobutyrate end groups. This successful approach, however, is limited in its application since only block copolymers with low molecular weight PEO may be synthesised.

Garg[3,4] and Ulbricht[6] were successful in substituting the oxoanions with living PEO macro anions. Higher molecular weight block copolymers with a high degree of PEO monomer conversion were prepared, however, difficulties arose in obtaining homogeneous (non-grafted) PEO-b-PMMA block copolymers. Garg[4] noted that 20% of EO was pinned onto the PMMA section of the block, forming a grafted block copolymer and attributed this to the fact that not all of the 'living' and dormant precursor PEO ends were able to start to copolymerise immediately with PMMA. Similar grafting using this synthetic approach of MMA addition to 'living' PEO has also been observed by Vinogradova et al.[9] Transfer and termination reactions[6,9] associated with the PMMA component could not be prevented since the polymerisation of PMMA had to occur above 293K owing to the low solubility of PEO sequences in THF as PMMA is normally polymerised at 195K. The presence of transesterification reactions were also noted for this less conventional synthetic approach[6,9]. Additional work in this area has focused upon the effect of the PEO chain length upon the tacticity of PMMA[7] along with the synthesis of PEO with poly(tert-butyl methacrylate) (PtBMA)[6,7,8]. MMA was replaced by tBMA since PtBMA is less sensitive to side reactions and this ester does not transesterify under basic conditions to the same extent as MMA.

To summarise, no ideal synthetic approach for the formation of reasonably high molecular weight, low polydispersity PEO-b-PMMA block copolymers exists. It was decided to use the 'conventional' approach using diphenyl methyl potassium as the anionic initiator. This approach minimises the extent of grating reactions and transesterification, and facilitates the formation of high molecular weight block copolymers. By understanding the limitations associated with this approach, this synthetic procedure has been fully optimised for PEO-b-PMMA (see 3.1.8.).

3.1.3. Vacuum Line.

The vacuum line used for this synthesis is illustrated in figure 3.1.

The following list of specifications applied:

Standard tubular glass main manifold fitted with three valved o-ring/sleeve connections allowing for the attachment of various sub-manifold combinations.

Each sub-manifold had a further three outlets fitted with either o-ring/sleeve or ball/socket type joints.

Apiezon N type grease was used on all joints to maintain a high vacuum.

The Young's taps, OS teflon seals and the 10mm diameter tubular glassware used were supplied from Young's Scientific Glassware, Acton, England.

Vacuum was achieved by a combination of an Edwards roughing rotary pump model E2195 ($6x10^{-2}$ torr) with an Edwards backing diffusion pump model 63 (10^{-6} to 10^{-7} torr). This system was purchased from Edwards High Vacuum, Crawley, Sussex.

3.1.4. Preparation Of Reagents.

Anionic synthesis requires the extremely rigorous preparation of glassware and reagents in terms of cleanliness, purity and dryness. The presence of even trace amounts of impurity can readily lead to premature termination of a polymerisation.

3.1.4.1.Methyl Methacrylate, MMA, (Aldrich M5,590-9).

Methyl methacrylate, when supplied, contained 10ppm hydroquinone monomethyl ether. This was removed by separate repeated washings with 10% aqueous sodium hydroxide and distilled water solutions. The monomer was then dried over calcium chloride, distilled under reduced pressure and then placed on the vacuum line in a $250cm^3$ round bottomed flask over ground calcium hydride and a magnetic follower. Owing to the light sensitive nature of this monomer, which would induce polymerisation, the flask was covered with aluminium foil to exclude light.

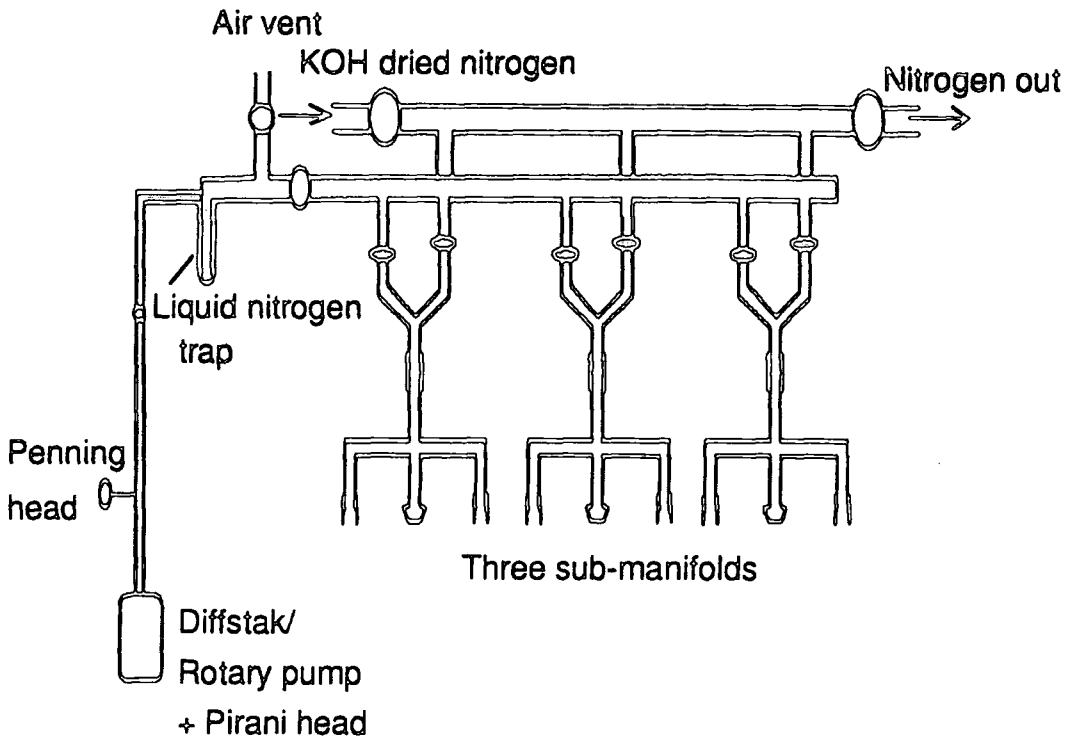

Figure 3.1. Vacuum line used for the anionic synthesis of PEO-b-PMMA.

3.1.4.2.Ethylene Oxide, EO, (Fluka 03901).

Extreme caution was taken with this monomer owing to its highly volatile nature (b.pt.=286.2K) and toxicity at room temperature. As supplied, it was transferred under vacuum into a round bottomed flask fitted with a Young's tap. The flask was cooled by liquid nitrogen and contained ground calcium hydride and a magnetic stirrer, (see figure 2.2., flask B). The flask and contents were then transferred immediately to the vacuum line. Prior to polymerisation, further drying and purification of the EO monomer were required using sodium mirrors (see 3.1.8.).

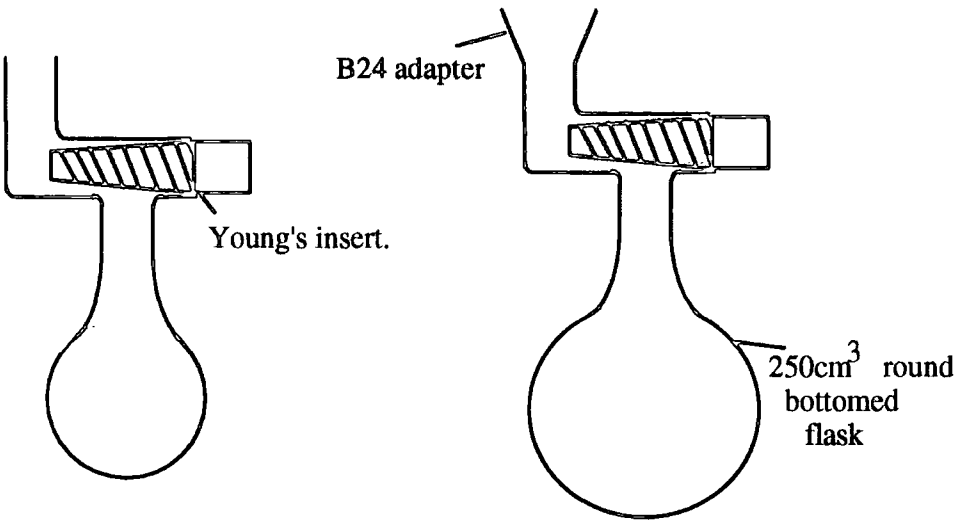

Flask A - transfer monomers. Flask B - Transfer and store EO.

Figure 2.2. Flasks.

3.1.4.3. Tetrahydrofuran, THF, (Aldrich 17,881-0).

THF was vacuum distilled to remove any inhibitor, refluxed and dried over freshly squeezed sodium wire and a few crystals of benzophenone in a 500cm^3 flask. This resulted in a dark, ink-blue coloured solution. The addition of benzophenone was necessary to prevent the formation of peroxides in the uninhibited THF. The flask and contents, plus a magnetic follower, were then connected to the vacuum line. Prior to its use, THF, like all liquid reagents and solvents, was degassed thoroughly to remove any dissolved gases (impurities) from the liquid, by means of freeze-thaw cycles on the vacuum line. The reagent was freezed by immersing the flask in liquid nitrogen, opening the appropriate Young's tap connecting the flask to the vacuum line, and pumping down upon the frozen material. This was followed by isolation of the flask, thawing the reagent and stirring using a magnetic follower for several hours. This was repeated many times until the material was thoroughly degassed.

3.1.5. Preparation of the Glassware.

All glassware was washed with permanganic acid prior to first use and then subsequently washed with chloroform and methanol between syntheses. Immediately before synthesis, the reaction flask was dried with a heat gun to remove any absorbed water and cleaned thoroughly with a living solution of polystyryl lithium in benzene under reduced pressure (figure 3.3.). This solution, which had been prepared earlier, consisted of a small quantity of styrene monomer dissolved in benzene, anionically polymerised (but not terminated) by the injection of a few microlitres of 2.5M n-butyl lithium initiator (Aldrich 23,070-7). This bright orange coloured solution was stored in a small side arm flask attached to the reaction flask (figure 2.3.).

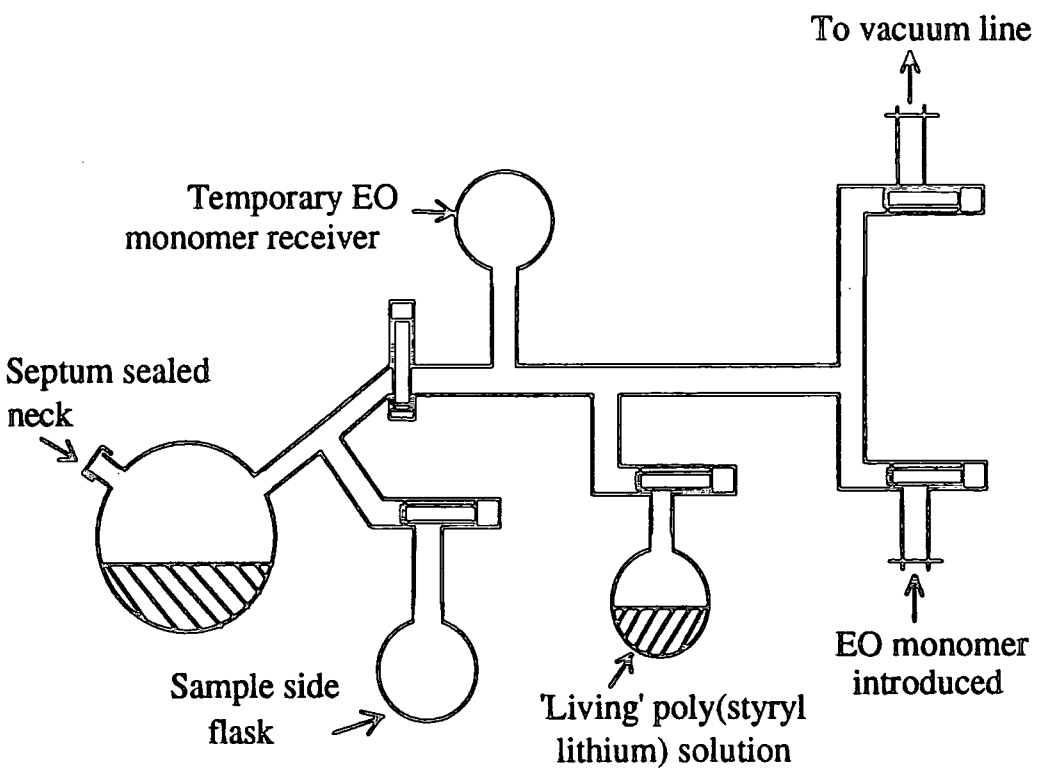

Figure 3.3. Reaction Flask used for the Synthesis of PEO-b-PMMA.

3.1.6. Synthesis of the Diphenyl Methyl Potassium Initiator.

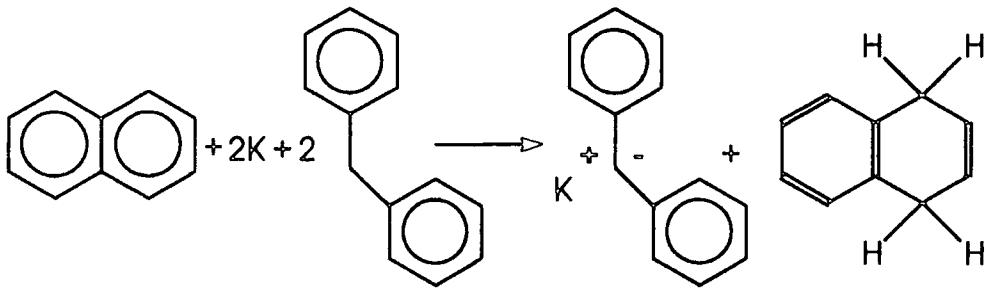

For the synthesis above, the following molar ratios of reactants were used: naphthalene (0.25), diphenylmethane (0.66) and potassium (1.0). This ensured complete conversion of the naphthalene present. Dried distilled tetrahydrofuran (THF) ($80cm^3$) and naphthalene (Aldrich 14,714-1) were placed in a clean, three necked round bottom flask under a dry nitrogen atmosphere, which was cooled at 273K in an ice bath whilst stirring. Potassium was added slowly, which resulted in the formation of a dark green coloured reaction mixture along with the evolution of heat. The reaction flask's contents were then stirred for three hours until most of the potassium had reacted, after which diphenylmethane (Aldrich 24,007-9) dissolved in THF($40cm^3$) was added dropwise. After stirring for a further two hours, the initiator present appeared as a dark red/purple solution. This was then decanted from the solid excess potassium and stored in a rubber septum sealed storage bottle under nitrogen in a dark cupboard.

3.1.7. Calibration of Initiator.

Several samples of poly(methyl methacrylate) of different molecular weights were synthesised using known quantities of initiator and monomer (see section 3.1.8. for the synthetic procedure). The actual molecular weights were determined using size exclusion chromatography (SEC) in THF solvent. An average value for initiator efficiency was determined from which the amount of initiator required for

polymerisation of PMMA with a specific molecular weight could be calculated from the following expression,(3.1):

$$V2 = V1 \times \frac{M1}{M2} \times \frac{W2}{W1} \qquad (\mu l) \qquad (3.1).$$

where:

V2 - volume of initiator required (μl).

V1 - volume of initiator used for previous synthesis.

M1 - molecular weight of previous polymer from SEC.

M2 - molecular weight of required polymer.

W1 - weight of monomer used for previous synthesis.

W2 - weight of monomer to be used.

3.1.8. Polymerisation of the Block Copolymer, PEO-b-PMMA.

The polymerisation of this block copolymer was carried out in the reaction flask shown in figure 3.3.. Reagents were transferred by molecular distillation under high vacuum with the receiver vessel immersed in liquid nitrogen or liquid air.

The first step in the polymerisation of PEO-b-PMMA involves the polymerisation of PMMA. After weighing the empty evacuated flask (figure 3.2, flask A), approximately 8 grams of MMA monomer were added and the flask re-weighed. The monomer was then transferred to the main section of the reaction flask, which contained enough THF to make an approximately 10% v/v solution of monomer (too little THF and the reaction mixture becomes too viscous during polymerisation). The reaction flask was then immersed in a dry ice/acetone bath (195K), and the polymerisation was initiated by the rapid injection of an appropriate volume according to the molecular weight desired of a solution of diphenyl methyl potassium through a subseal gas tight septum. Initiation was accompanied by the evolution of heat, an

increase in viscosity and the presence of a faint yellow/orange coloured solution. The reaction flask was then allowed to stand for 2-3 hours at 195K to complete polymerisation. At this stage, the PMMAs that were prepared in order to calibrate the initiator, were terminated by the rapid injection of approximately 100ml of degassed methanol. The methanol having been previously degassed using a dry nitrogen purge. The polymers were then precipitated out into methanol, filtered using a glass sintered filter and then dried under vacuum at 308K for two days.

For the defined synthesis of PEO-b-PMMA, a small amount of the 'living' anionic PMMA was isolated in the side arm of the reaction flask (figure 3.2.) in order to determine the molecular weight of the PMMA component in each block copolymer. Whilst the PMMA was left to polymerise fully at 195K, EO monomer was dried and purified using a sodium mirror technique. For this, a small pellet of freshly cut sodium was added to a flask (flask type A in figure 3.2.), which was subsequently evacuated on the vacuum line. The sodium was melted by local heating with an air/gas torch flame. Once vaporised, the metal condensed uniformly, completely covering the cooler inner surfaces of the flask with a thin layer of sodium. Sufficient EO monomer was then distilled into the sodium mirrored flask and shaken to ensure good contact with the fresh sodium mirror. This process was repeated until the monomer no longer tarnished the sodium surface. A known amount of monomer was then obtained by distillation into the flask A (figure 3.2.), which had previously been dried and weighed. The known amount of E.O. monomer was transferred to the temporary receiver flask of the reaction flask (figure 3.3.), thawed and then added rapidly to the 'living' PMMA/THF solution and shaken. The reaction mixture was allowed to warm up slowly to room temperature overnight, and then heated at 248K for 4 days. Polymerisation was accompanied with the formation of a yellow coloured solution. The reaction was terminated with approximately 100ml of degassed glacial acetic acid, precipitated into approximately 500ml of n-hexane, filtered and dried under vacuum at 308K for 2 days.

3.2. Characterisation.

3.2.1. Size Exclusion Chromatography, SEC.

The molecular weight characteristics of each block copolymer were determined by size exclusion chromatography using chloroform as a solvent and with three gel columns (10^5, 10^3, and 100 Å pore size with 5μm gel beads), a Waters differential refractometer (Model R401) and a Waters pump (Model 590), calibrated with polystyrene standards. The PMMA homopolymers were dissolved in THF prior to SEC measurement (THF was not used for the block copolymers owing to precipitation after 24 hours). Two sets of PMMA homopolymers were measured. The first set's results were used to calibrate the initiator, and the second to determine the molecular weight of the MMA component of the block copolymer.

Table 3.1. lists the molecular characteristics of each of the block copolymers synthesised. For those block copolymers not in bold face in table 3.1., the size exclusion chromatogram appeared bimodal in shape, suggesting the presence of homopolymer owing to termination reactions during polymerisation. The block copolymers in bold type, however, displayed unimodal chromatograms. These block copolymers were synthesised using a new batch of initiator. This batch was three times more efficient (in terms of volume of initiator used) than that initiator used for the other block copolymers. That is, the same volume of this new initiator produced a polymer with a molecular weight three times greater than a polymer polymerised using the old batch of initiator. This suggests the less efficient initiator contained impurities which prematurely terminated polymer chains during the polymerisation of the block copolymer, yielding unwanted PEO homopolymer and broadening of the molecular weight distribution.

The unwanted PEO homopolymer was removed by Soxhlet extraction. Initially, a variety of solvents were tested. These included 1-chlorobutane, cyclohexanol at 348K (theta temperature for PMMA), n-propanol and tetrochloromethane. However, all of these listed solvents dissolved not only the

homopolymer, but also the block copolymer. The polymers were recovered from these solvents by substitution of methanol (approximately six washings) and then chloroform (approximately three washings) using a rotary evaporator, followed by precipitation into hexane. Water proved to be successful as a Soxhlet solvent in removing pure PEO homopolymer from the block copolymer.

It was noted that one of the block copolymers (BC76) which contained 76% w/w EO completely dissolved in water forming a blue, opalescent solution. This suggests the formation of a stable micelle structure and warrants further investigation.

Subsequent ^{1}H and ^{13}C nmr spectroscopy on the Soxhlet extraction indicated the presence of pure homopolymer PEO. The molecular weight characteristics were again determined for each block copolymer after soxhlet extraction using chloroform SEC. The chromatograms were now unimodal in shape and table 3.1. lists the SEC results for all of the block copolymers synthesised, along with the percentage of ethylene oxide (w/w) present in each block copolymer as determined from ^{1}H nmr spectroscopy (see 3.2.2.).

3.2.2. ^{1}H and ^{13}C nmr Spectroscopy.

A proton and carbon 13 nmr spectrum was recorded for each PEO-b-PMMA block copolymer. The solvent used was deuterated chloroform and a 200MHz Gemini nmr spectrometer was used to record the spectra. Fig.3.4.a and b shows the respective ^{1}H and ^{13}C NMR spectra for one of the block copolymers synthesised (BC31).

The 200 MHz ^{1}H nmr spectra shows resonances of the methylene protons of PEO (δ=3.64) and of the methoxy protons of PMMA (δ=3.59) (see insert in figure 2.4.). The proportion of PEO and PMMA in the block copolymers was calculated from the ratio of the integral intensities of these resonances and compared with the theoretically calculated composition (see table 3.1.). As shown in table 3.1, a range of block copolymers with varing weight percent of EO were synthesised. The percentage of ethylene oxide monomer that actually polymersied to form the block copolymer was

constant, 25 -30%. It is assumed that the remaining 70% either formed homopolymer PEO or remained unreacted.

The relative intensities of the absorptions of the methoxy and α-methyl protons for PMMA are essentially the same indicating the absence of transesterification reactions as reported by Suzuki et al.[2]

The tacticity of the MMA component of the block copolymer was determined from the relative ratios of the methyl peaks close to 1.0 ppm in the ^{1}H nmr spectra (see figure 2.4). Syndiotactic methyl has an associated nmr peak at 0.8 ppm, atactic at 1.0 ppm and isotactic at 1.2 ppm. The tacticity was constant for all of the block copolymers synthesised and was found to be mainly atactic (50% tactic, 30% syndiotactic, 20% isotactic).

An attempt was made to detect the presence of the block copolymer interface using conventional ^{13}C nmr. This nmr peak associated with this interface proved to be too small to detect using this conventional method, however spectroscopic evidence to support the block character of the block copolymer comes from the observation that the spectrum of PMMA is identical to that for the block copolymer. If the copolymer was a random copolymer, then these two spectra would not be identical.

3.2.3. Solubility.

All the block copolymers were soluble in methanol and insoluble in water (with the exception of BC76). Since homopolymer PEO is soluble in both of these solvents and homopolymer PMMA is insoluble in both of these solvents, this suggests that the constituent polymers are chemically bonded together. If they were not bonded together, then the PEO fraction would dissolve in either the methanol or water solvent.

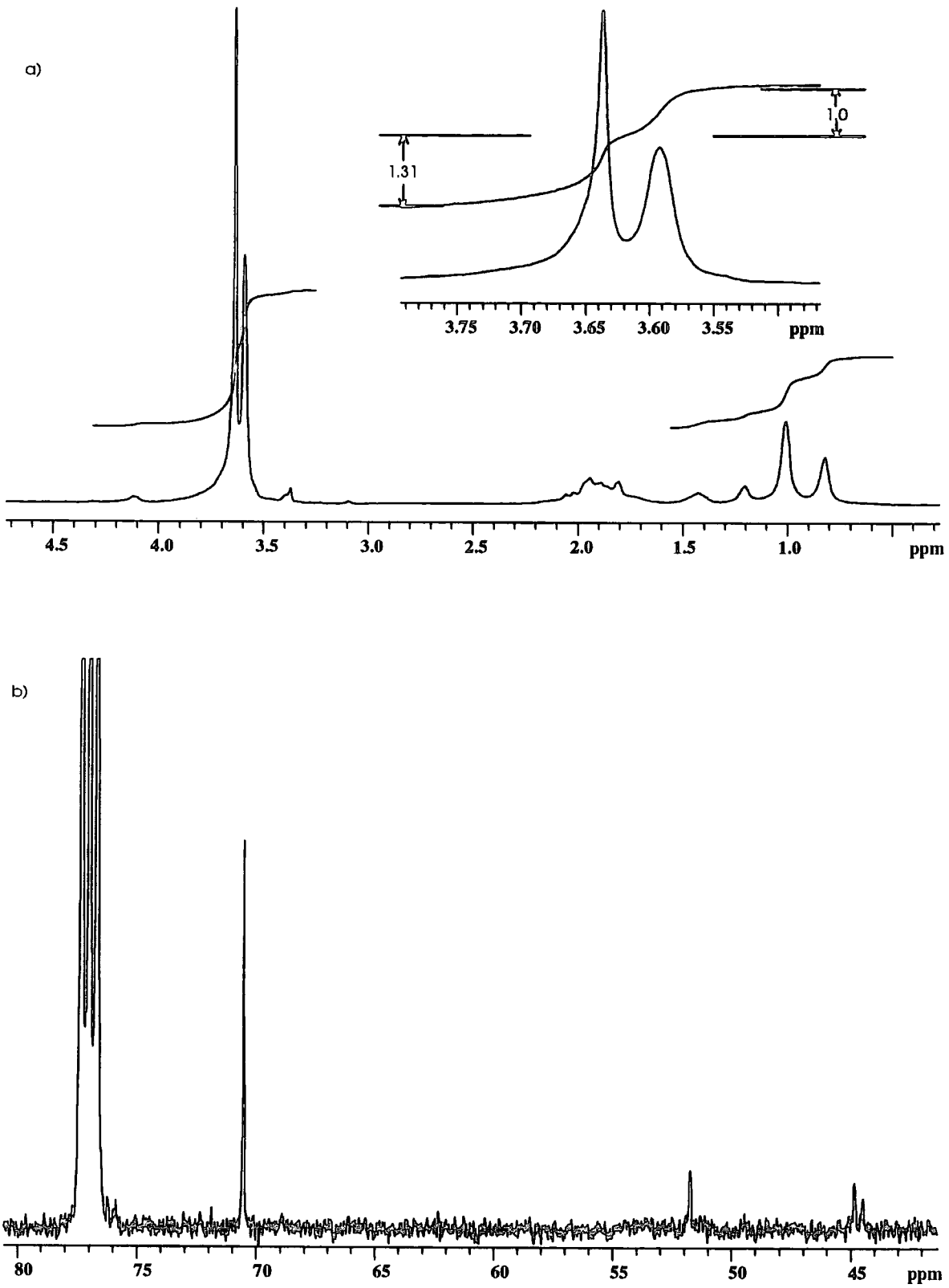

Figure 2.4. a) ^{1}H and b) ^{13}C nmr Spectra for BC31.

PEO-b-PMMA	M_n* (total)	M_w/M_n* (total)	M_n** (PMMA)	M_w/M_n** (PMMA)	% E.O. (w/w)
BC76	18,100	1.46	20,100	1.08	76.0
BC55	17,900	1.28	18,800	1.10	54.5
BC50	16,900	1.91	19,900	1.60	49.5
BC38	12,400	1.86	19,600	1.95	37.6
BC31	9,600	5.50	23,800	1.45	31.3
BC30	11,300	4.04	11,000	1.70	29.7
BC22	40,200	1.08	14,500	1.00	22.4
BC16	12,300	2.64	23,000	1.60	16.2
BC14	42,100	1.08	53,500	1.01	14.3
BC9	12,600	3.10	23,300	1.65	10.0
BC9	15,500	3.50	18,100	1.26	9.9
BC5	11,400	2.47	18,900	1.67	4.7
BC4	11,200	2.45	22,000	1.65	4.0

Table 3.1. Molecular Characteristics of the Poly(ethylene oxide) - Poly(methyl methacrylate) Block Copolymers, PEO-b-PMMA.

* = $CHCl_3$ solvent SEC, ** = THF solvent SEC.

The relative molecular weight of the PMMA component is high in comparison to that of the block owing to the different solvents used for SEC (different hydrodynamic radii).

Throughout the rest of this thesis, the encoding listed in table 3.1. will be used to denote the PEO-b-PMMA block copolymer in question.

3.3. Poly(ethylene oxide) / Poly(methyl methacrylate) Blends, PEO/PMMA.

The homopolymers, poly(ethylene oxide), PEO, and poly(methyl methacrylate), PMMA, were commercially supplied by Polymer Laboratories (Essex Road, Church Stretton, U.K.) (see table 3.2).

Homopolymer	M_n	M_w/M_n
PEO	18,600	1.06
PMMA	22,200	1.07

Table 3.2. Molecular Characteristics of Poly(ethylene oxide) / Poly(methyl methacrylate) PEO/PMMA Blends.

The molecular characteristics of the above homopolymers are very similar to those of the synthesised block copolymers, and so provide a direct comparison for the following work where the block copolymer is compared to the corresponding blend.

3.4. Conclusion.

A range of block copolymers with varying percentages of ethylene oxide incorporation were successfully synthesised. The molecular weight of the PMMA component was maintained constant at approximately 20,000 (M_n) (with the exception of BC14), and the tacticity was mainly atactic (50% tactic, 30% syndiotactic, 20% isotactic).

The relative intensities of the absorptions of the methoxy and α-methyl protons for PMMA were essentially the same indicating the absence of transesterification reactions as reported by Suzuki et al[2].

An attempt was made to detect the presence of the block copolymer interface using conventional ^{13}C nmr. This nmr peak associated with this interface proved to be too small to detect using this conventional method.

Evidence to support the block character of the block copolymer came from the observation that the spectrum of PMMA was identical to that for the block copolymer.

3.5. References.

1. Suzuki, T., Murakai, Y., Takegami, Y., Polymer J., 12, 183, 1980.
2. Suzuki, T., Murakami, Y., Tsuji, Y., Takegami, Y., J.Polym.Sci., Polym. Lett. Ed., 14, 675, 1976.
3. Garg, D., Höring, S., Ulbricht, J, Makromol. Chem, Rapid Commun., 5, 615, 1984.
4. Garg, D., Thesis, TH Merseburg, 1985.
5. Seiler, E., Fahrenbach, G., Stein, D., Ger. Pat. 2237954, BASF AG, 1972; Chem. Abstr. 81, 13978x, 1974.
6. Reuter, H., Berlinova, I.V., Höring, S., Ulbricht, J., Eur. Polym. J., 7, 673, 1991.
7. Reuter, H., Höring, S., Ulbricht, J., Makromol. Chem. Suppl, 15, 79-84, 1989.
8. Wang, J., Varshney, S.K., Jerome, R., Teyssie, P., J. Polym. Sci., Part A: Polym. Chem., Vol.30, 2251-2261, 1992.
9. Vingradova, L.V., Sgonnik, V.N., Ilina, A.A., Dotcheva, D.T., Tsvetanov, Ch.B., Macromolecules, Vol.25, No.25, 6733-6738, 1992.

Chapter 4.

4. Differential Scanning Calorimetry.

4.1. Principles of Operation.

4.1.1. Introduction.

Differential scanning calorimetry, DSC, is extensively used in the area of polymer science and its principle of operation is based upon the ability of the technique to detect thermal changes within the sample. This change is evaluated by monitoring the electrical input supplied to the sample to maintain the same temperature as that of a reference cell (empty sample vessel). Several other modes of operation exist based on the same theme.

4.1.2. Mode of Operation.

DSC measurements were performed using a power compensation designed Perkin-Elmer DSC7, linked to a Perkin-Elmer TAC7/PC Instrument Controller and a Dell PC. Indium and zinc standards were used for calibration and a Perkin-Elmer Controlled Cooling Accessory was used for low temperature work. The powdered polymer samples, approximately 8mg, were sealed in aluminium sample pans, (Perkin Elmer, kit no. 0219-0062), and an empty sealed aluminium pan was used as a reference cell. For melting point and glass transition temperature determination, the scanning rate was 10Kmin^{-1} and the DSC head was continuously purged using dry nitrogen.

4.1.3. Glass Transition Temperature, T_g.

A stepwise increase in the heat capacity, C_p, of a polymeric system represents a complex summation of conformational and vibrational effects. A large change in C_p is observed when the rigid carbon backbone relaxes and becomes mobile. The

temperature of this physical change from a hard, glassy state to one that is rubbery is called the glass transition temperature, T_g.

The size and temperature of this endothermic transition is inherently dependent upon the chemical structure and molecular weight characteristics of the polymer. Generally, any structure that reduces chain mobility (i.e., side groups) will increase the T_g. The glass transition temperature also increases with increasing molecular weight tending towards a limiting value at 10^4-10^5 M_w.

The glass transition temperature is normally determined by the onset point, or the intersection of the initial straight line and the transition region, or at the point of inflection of the transition region, see figure 4.1.

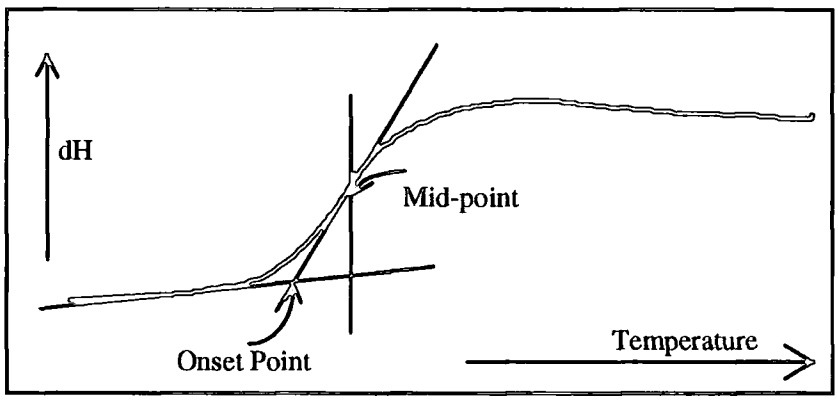

Figure 4.1. Schematic Representation of a Glass Transition Temperature.

To optimise the measurement of the T_g using DSC, it is advisable to cool the sample from above the T_g and acquire data at a low scanning rate. If the measurement is performed by heating through the transition temperature, the kinetic nature of the glass transition is often dominant. Sudden expansions and/or contractions occur in the transition region resulting in an endothermic peak which can mask the true T_g temperature.

Glass transition temperatures are often used in polymer science as a tool to detect the miscibility of a polymeric system. For binary systems, blends or copolymers,

observation of a single T_g whose value is intermediate between the T_g of the component homopolymers reflects miscibility on a molecular level[1,2]. For systems that are immiscible, two T_g's are observed at temperatures close to those expected for the constituent homopolymers. For real systems, this situation is not always so clearly defined. Intermediate and multiple T_g's are sometimes seen but a detailed analysis is difficult and several unanswered questions concerning miscibility and detectability of T_g in domains that maybe of molecular dimensions still exists. For domains that contain less than fifty carbon-carbon bonds, the technique is unable to detect any change in the specific heat of the domain.

4.1.4. Crystallinity.

DSC measurements can be used to monitor crystallisation in polymers if it is assumed that the heat of crystallisation or heat of fusion is directly related to the degree of crystallinity present.

The melting point endotherm is relatively broad and for the DSC instrument used in this work, it is represented as a peak lying above the constant thermal background. This broadness often results in two melting point temperature values being quoted i.e., the onset and peak temperatures. Conversely, an inverted peak below the constant background line represents a crystallisation exotherm (see figure 4.6.).

4.2. Experimental Procedures.

4.2.1. Glass Transition Temperature.

For each block copolymer listed in table 4.1., the blends and PEO, the glass transition temperatures, T_g, were determined by cooling from 423K at a scanning rate of $10Kmin^{-1}$. Any thermal history present in the polymeric samples was removed by annealing at 423K for 10 minutes prior to performing the DSC measurement.

Difficulties arose in detecting glass transition temperatures for systems containing >40% EO owing to crystallisation exotherms and melting endotherms masking the glass transition temperature region as well as the inherently low magnitude of the T_g for PEO. Consequently, it was often necessary to perform several DSC runs for these higher EO fraction polymer systems.

4.2.2. Melting Points.

4.2.2.1. Unannealed Samples.

Prior to any thermal treatment, the melting point of the blends were determined at a scanning rate of $10Kmin^{-1}$. These blends had been precipitated from 5% w/w chloroform solutions into methanol, and dried under vacuum at 303K for 3 days.

4.2.2.2. Equilibrium Melting Points.

The equilibrium melting point was determined for BC76, BL60, BL70, BL80, BL90 and PEO. Each polymer sample was annealed at 423K for 10 minutes to remove any thermal history, and quenched at the controlled rate of $100Kmin^{-1}$ to a series of crystallisation temperatures ranging from 305K to 323K. After allowing the polymer samples to crystallise fully for 60 minutes at the crystallisation temperature, the apparent melting point temperature, T_m', was determined by acquiring data at a scanning rate of $10Kmin^{-1}$ from the crystallisation temperature to 423K.

4.2.3. Isothermal Crystallisation.

Approximately 10mg of each sample was annealed at 423K for 10 minutes, and then quenched to a specific crystallisation temperature at the controlled rate of $100Kmin^{-1}$. The crystallisation exotherm, Δh_{fus}, was monitored as a function of time at various crystallisation temperatures using the Perkin-Elmer isothermal crystallisation software package.

A series of crystallisation temperatures, T_c, were investigated ranging from 308K to 315K (1K increments) for BC76 and from 305K to 323K for the blends and PEO.

4.2.4. Phase Separation in BC50 and BC55.

Individual block copolymer samples of BC50 and BC55 were annealed at 423K for 10 minutes, and then quenched at the controlled rate of $100Kmin^{-1}$ to a series of 'permanence' temperatures, T' (231K to 245K for BC50 and 250K to 260K for BC55). The samples were held at these temperatures for various permanence times, t, ranging from 0.5 minute to 120 minutes, and then data ~~was~~ were subsequently acquired at a scanning rate of $10Kmin^{-1}$ from each permanence temperature to 423K. The subsequent enthalpy of fusion per gram of PEO was determined as a function of time, t, at various permanence temperatures, T', for both BC50 and BC55. Figure 4.2 illustrates a schematic representation of the thermal programme used.

A few additional DSC experiments were performed on BC30, and also with lower quenching rates from 423K to T' ($2Kmin^{-1}$) for BC50 and BC55.

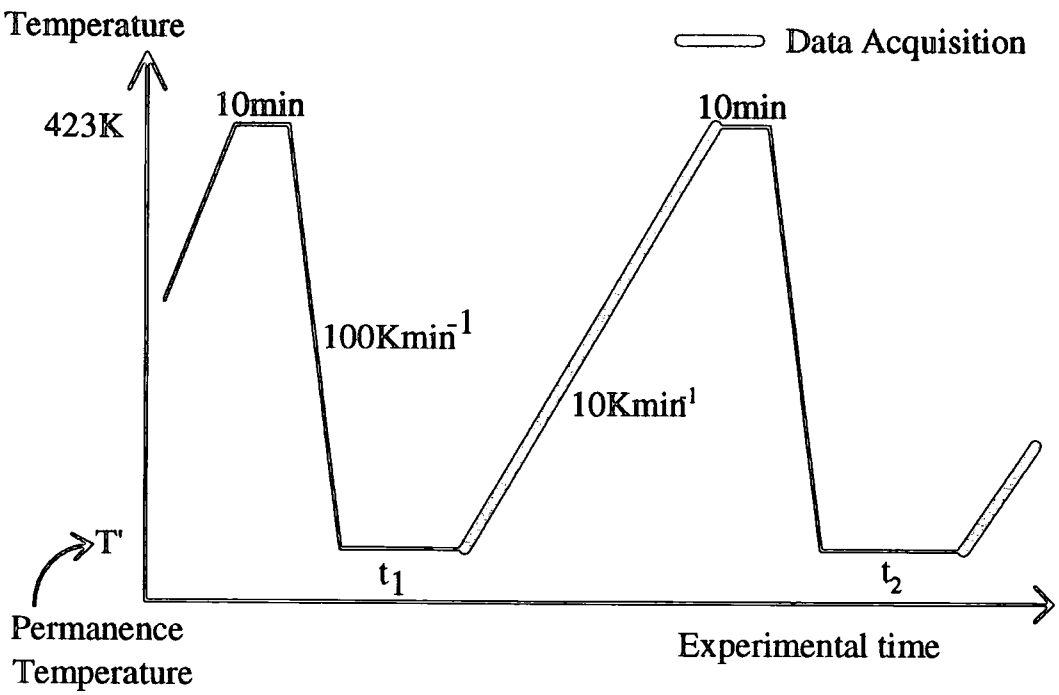

Figure 4.2. Schematic Representation of the Thermal Treatment for BC50 and BC55.

4.3. Results.

4.3.1. Glass Transition Temperature.

The T_g's experimentally observed for the block copolymers and for the blends (including PEO) are listed in tables 4.1. and 4.2. respectively. Expected values as obtained from Pochan[1] and Fox[2] analyses (see p.102) for a miscible system have also been listed.

PEO-b-PMMA	% E.O. (w/w)	Expt. T_g (K)	Fox T_g (K)	Pochan T_g (K)
BC76	76.0	-	235	243
BC55	54.5	267	266	279
BC50	49.5	208,273	273	288
BC38	37.6	307±9, 390	295	311
BC31	31.3	243.5, 327	308	322
BC30	29.7	244	307	321
BC22	22.4	328	331	345
BC16	16.2	335±1	344	356
BC14	14.3	355	353	363
BC9	10.0	235, 365	362	369
BC9	9.9	231, 372	362	369
BC5	4.7	379±2	378	380
BC4	4.0	376	380	385

Table 4.1. Experimentally Determined Glass Transition Temperatures for PEO-b-PMMA Block Copolymers and the Expected Single T_g from Fox and Pochan Analyses Assuming the Polymer System is Miscible.

PEO/PMMA Blends	Expt. T_g (K)	Fox T_g (K)	Pochan T_g (K)
PEO	208	208	208
BL90	235	219	222
BL80	240	230	236
BL70	241	242	252
BL60	323±5	256	268
BL50	230±4	272	286
BL40	240±4	290	305
BL30	315±3	311	325
BL20	336	334	347
BL10	362	361.5	369
PMMA	394	398	398

Table 4.2. Experimentally Determined Glass Transition Temperatures for PEO and PEO/PMMA Blends and the Expected Single T_g from Fox and Pochan Analyses Assuming the Polymer System is Miscible.

Those values with an associated error term represent mean experimentally determined glass transition temperatures. The error associated with the remaining T_g's is ±4K.

4.3.2. Melting Points.

4.3.2.1. Unannealed Samples.

Table 4.3. lists the peak melting point temperatures (error term = ±0.2K) and the heats of fusion for the unannealed blends.

Polymer	Peak T_m (K)	ΔH_{fus} (J/g of PEO)
PEO	337.4	171.7
BL90	336.4	166.0
BL80	334.5	162.3
BL70	337.1	155.8
BL60	333.6	144.3
BL50	333.9	132.9

Table 4.3. Apparent Melting Point Temperatures and Enthalpies of Fusion for the Unannealed PEO/PMMA Blends.

4.3.2.2. Equilibrium Melting Points.

The Hoffman-Weeks[3] plots (see figures 4.3.), display the apparent melting point temperatures, T_m' versus crystallisation temperature, T_c, for BC76, BL60, BL70, BL80, BL90 and PEO. Extrapolation of T_m' to $T_m'=T_c$ gave the equilibrium melting point, T_m^o (error term - ±0.2K), for each polymer system, see table 4.4.

Sample	Equilibrium Melting Point, T_m^o (K)
PEO	343.5
PEO/PMMA (90/10) BL90	342.9
PEO/PMMA (80/20) BL80	341.0
PEO/PMMA (70/30) BL70	341.6
PEO/PMMA (60/40) BL60	341.7
PEO-b-PMMA (76/24) BC76	339.2

Table 4.4. Equilibrium Melting Points for PEO, BC76 and the Blends.

Figure 4.3. Hoffman/Weeks plot to evaluate the Equilibrium Melting Point, T_m^o

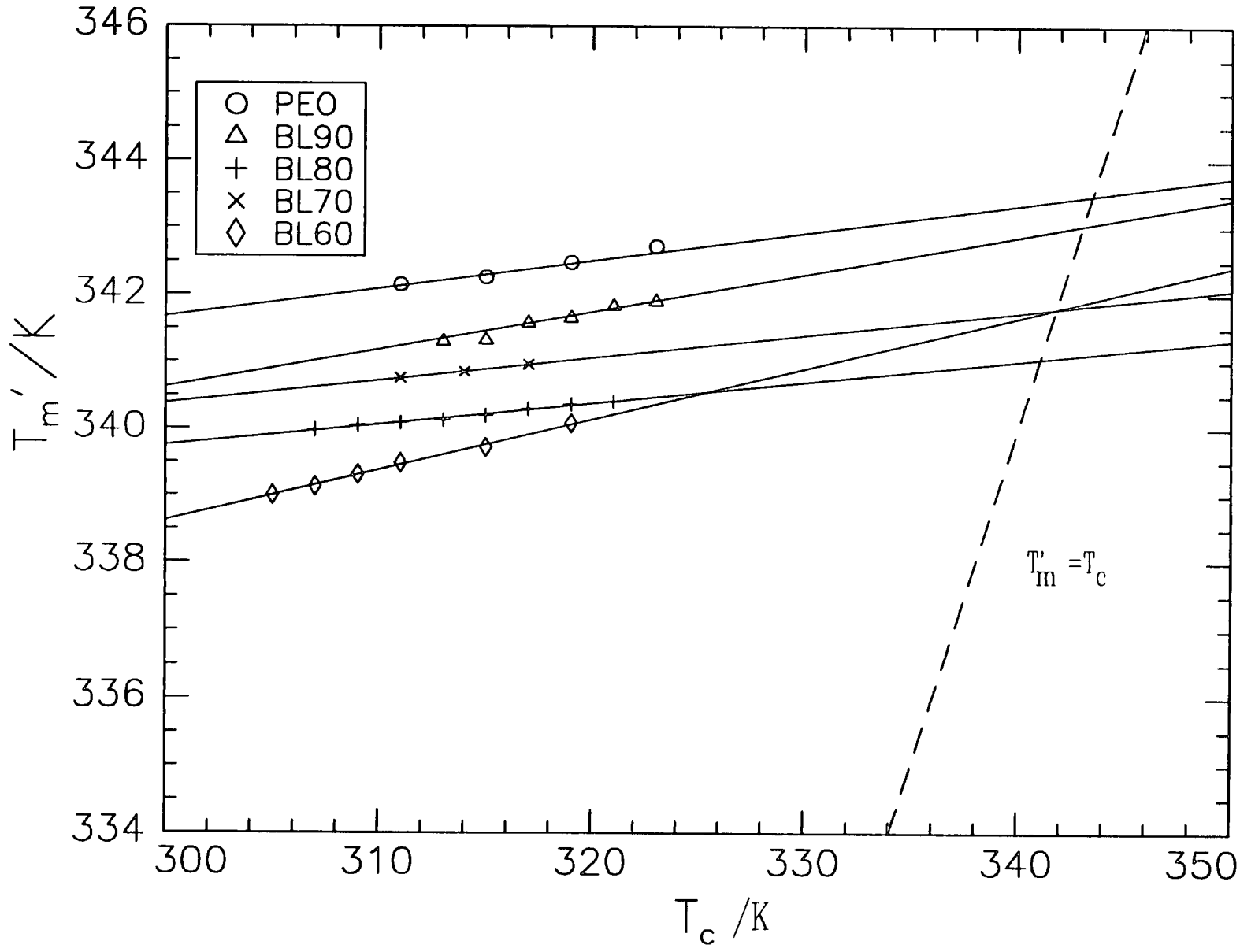

4.3.3. Isothermal Crystallisation.

Figure 4.4 shows the DSC thermograms obtained from the isothermal crystallisation of BC76 at various crystallisation temperatures and figure 4.5 compares the isothermograms for BL80 and BC76 at T_c=313K. The area under each curve represents the heat of crystallisation of the polymer sample, Δh_{cryst}. It is evident that the rate of crystallisation of the block copolymer is appreciably slower than that of the blend.

The heat of crystallisation per gram of PEO present after the polymer has fully crystallised, $\Delta h_{cryst,t=\infty}$ (error term = ±1J/g), the crystallinity index values of the blends and BC76, x_t, and of the PEO phase present, x_c, are reported in table 4.5. The enthalpy of crystallisation for 100% crystalline PEO was taken from the literature to be 199.7J/g.[4]

Polymer System	$\Delta h_{cryst,t=\infty}$ (J/g of PEO)	x_t	x_c
PEO	171.7	0.86	0.86
BL90	162.1	0.73	0.81
BL80	150.4	0.60	0.75
BL70	142.3	0.51	0.73
BL60	107.7	0.33	0.54
BC76	138.3	0.53	0.69

Table 4.5. Overall Crystallinity Index, x_t, and Crystallinity Index of the PEO Phase, x_c, for Various Blend Compositions and BC76.

No variation in $\Delta h_{cryst,t=\infty}$ as a function of crystallisation temperature, T_c, was observed. Consequently, the values for $\Delta h_{cryst,t=\infty}$ presented in table 4.5 were averaged over all the crystallisation temperatures studied.

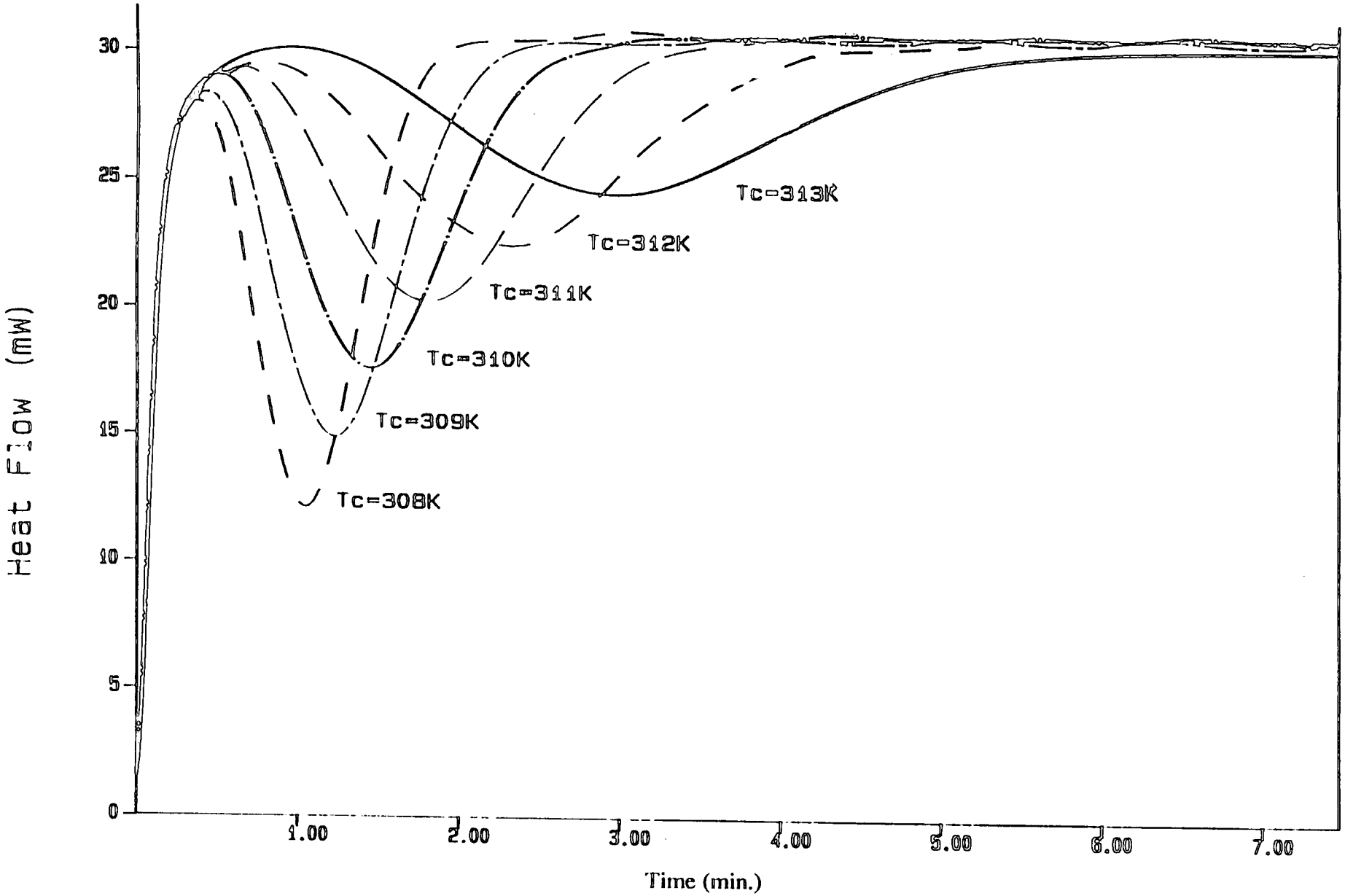

Figure 4.4. Isothermal Crystallisation of BC76 at various Crystallisation Temperatures.

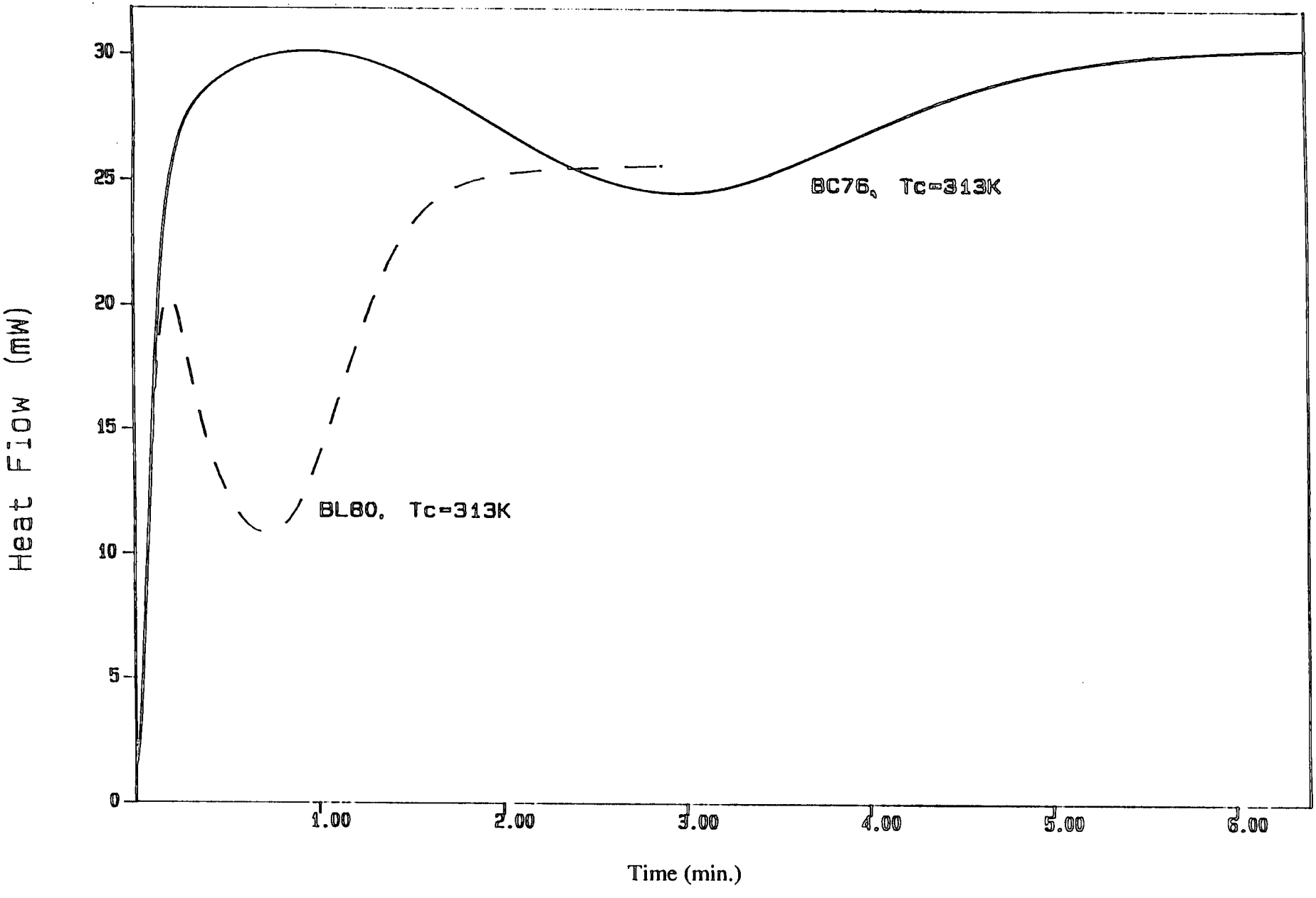

Figure 4.5. Comparison of the Isothermograms for BL80 and BC76 at T_c=313K.

4.3.4. Phase Separation in BC50 and BC55.

Figure 4.6. shows a typical DSC scan after a sample of BC55 which has been thermally treated as described earlier, i.e., the polymer was quenched at 100Kmin^{-1} to T'=253K, held at this temperature for t=10minutes, and then heated at a scanning rate of 10Kmin^{-1}. The thermogram clearly shows a crystallisation exotherm, Δh_{cryst}, followed by a melting endotherm, Δh_{fus}. As shown in figure 4.6., the magnitude of both of these transitions (area under the peaks) were approximately the same (the enthalpies reported in figure 4.6. are in units of J per gram of polymer used).

The heats of fusion, Δh_{fus}, per gram of ethylene oxide present in the sample, the crystallinity index values of the block copolymers, x_t, and of the PEO phase present, x_c versus permanence time, t, for various permanence temperatures, T', for BC55 and BC50 are listed in tables 4.6. to 4.15. The crystallinity indices, x_c and x_t were calculated using the value of Δh_{fus}=199.7J/g for 100% crystalline PEO.

For temperatures below 235K for BC50 and 250K for BC55, the permanence time required to induce the maximum amount of crystallinity attainable at the crystallisation temperatures was very short. The maximum Δh_{fus} attainable was 20J/g of EO for BC50 and 68J/g of EO for BC55. Direct comparison of the apparent melting points of BC50 and BC55 with the corresponding blend showed a 6K decrease in T_m' for the former with respect to the latter. No correlation in T_m' with permanence temperature for both block copolymers was observed.

For lower cooling rates (2Kmin^{-1}) from the 'thermal history removal temperature', 423K, to T', it was observed that permanence temperatures higher than those observed for the 100Kmin^{-1} quenching rate were able to induce crystallinity in BC50 and BC55.

BC30 also exhibited similar crystallisation behaviour to that of BC50 and BC55 at permanence temperatures close to 243K. However, the maximum Δh_{fus} was only 3J/g of EO and so deemed too small to perform a series of DSC runs with varying permanence temperatures, T', and times, t.

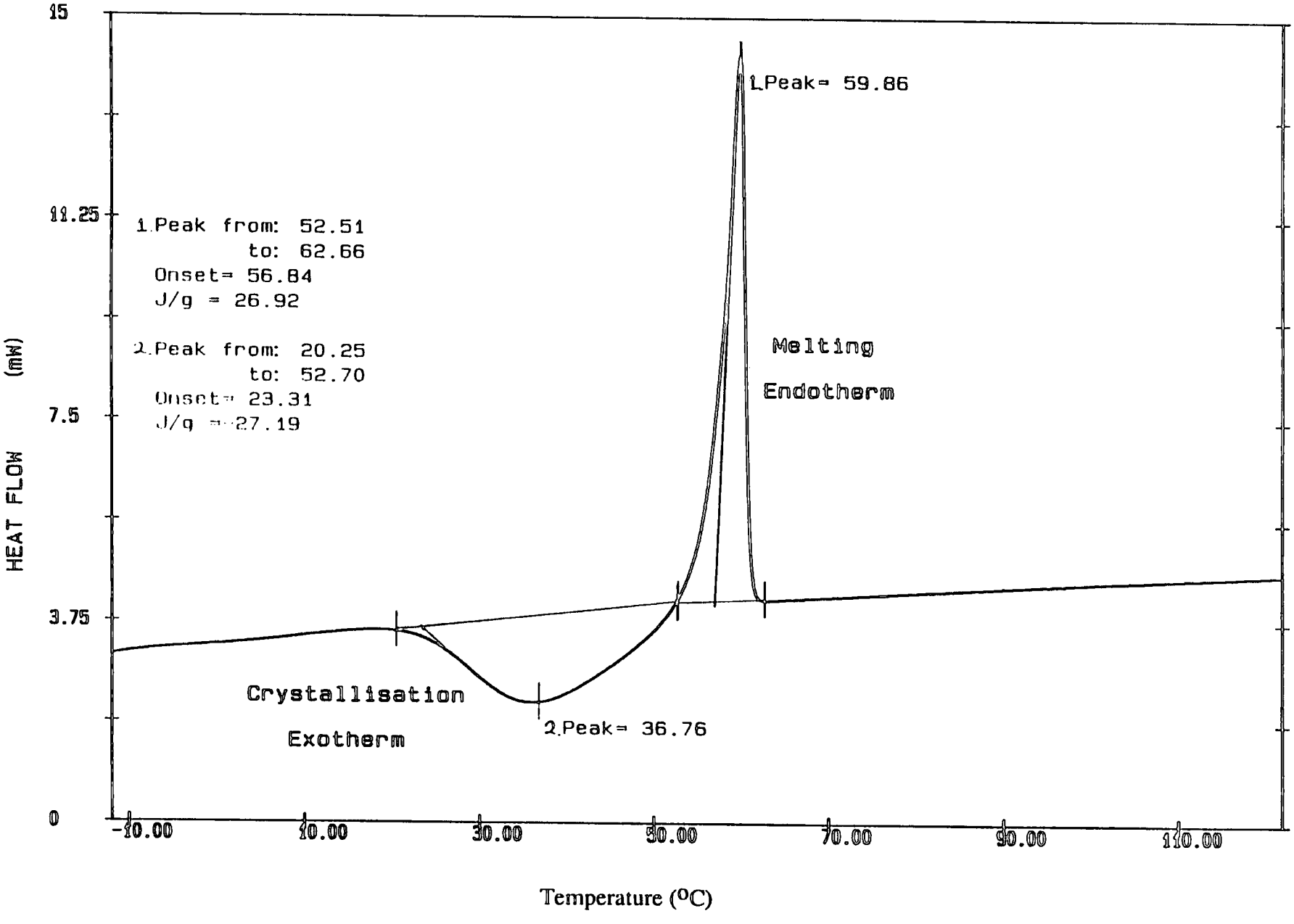

Figure 4.6. DSC Thermogram of BC55, T=253K and t=10 minutes.

Time, t(min.)	Δh_{fus} (J/g of EO)	x_t	x_c
0.25	4.31	0.021	0.042
1	6.53	0.033	0.066
1.5	7.64	0.038	0.076
2	8.08	0.040	0.080
4	10.16	0.051	0.102
8	11.89	0.060	0.120
47	18.16	0.091	0.182

Table 4.6. Induced Heat of Fusion vs. Permanence Time at T'=231K for BC50.

Time,t (min.)	Δh_{fus} (J/g of EO)	x_t	x_c
0.07	1.74	0.009	0.018
0.25	2.55	0.013	0.026
0.5	3.43	0.017	0.034
0.75	3.98	0.020	0.040
1	4.73	0.024	0.048
1.5	5.59	0.028	0.056
2	6.08	0.030	0.060
3	7.25	0.036	0.072
5	8.57	0.043	0.086
10	10.85	0.054	0.108
40	13.76	0.069	0.138

Table 4.7. Induced Heat of Fusion vs. Permanence Time at T'=235K for BC50.

Time, t (min.).	Δh_{fus} (J/g of EO)	x_t	x_c
0.05	1.15	0.006	0.012
0.33	2.12	0.011	0.022
0.87	3.15	0.016	0.032
1	3.55	0.018	0.036
1.37	4.57	0.023	0.046
1.87	4.77	0.024	0.048
3.87	6.42	0.032	0.064
10.87	8.63	0.043	0.086
57	13.05	0.065	0.130

Table 4.8. Induced Heat of Fusion vs. Permanence Time at T'=239K for BC50.

Time, t(min.)	Δh_{fus} (J/g of EO)	x_t	x_c
0.25	0.32	0.002	0.004
0.5	0.54	0.003	0.006
0.75	0.75	0.004	0.008
1	1.04	0.005	0.010
1.33	1.4	0.007	0.014
1.5	1.52	0.008	0.016
2	1.72	0.009	0.018
3	2.2	0.011	0.022
5	2.81	0.014	0.028
10	4.63	0.023	0.046
16	4.99	0.025	0.050
32	6.61	0.033	0.066
60	9.79	0.049	0.098

Table 4.9. Induced Heat of Fusion vs. Permanence Time at T'=242K for BC50.

Time,t (min.)	Δh_{fus} (J/g of EO)	x_t	x_c
0.25	.06	0.0003	0.0006
1.3	0.4	0.002	0.004
2.9	1.05	0.005	0.010
5	1.45	0.007	0.014
7	1.76	0.009	0.018
14	3.47	0.017	0.034
31	3.78	0.019	0.038
40	4.85	0.024	0.048
81.5	6.55	0.033	0.066

Table 4.10. Induced Heat of Fusion vs. Permanence Time at T'=245K for BC50.

Time,t (min.)	Δh_{fus} (J/g of EO)	x_t	x_c
0	21.4	0.107	0.195
0.25	30.82	0.154	0.280
0.5	39.96	0.200	0.364
1	45.44	0.227	0.413
4.75	53.16	0.266	0.484
45	59.67	0.299	0.544
143	63.33	0.317	0.576

Table 4.11. Induced Heat of Fusion vs. Permanence Time at T'=250K for BC55.

Time,t (min.)	Δh_{fus} (J/g of EO)	x_t	x_c
0	2.24	0.011	0.020
0.5	14.4	0.072	0.131
0.75	19.34	0.097	0.176
1.5	25.82	0.129	0.235
5	41.31	0.209	0.380
10	48.74	0.244	0.444
20	51.51	0.258	0.469
45	55.54	0.278	0.505

Table 4.12. Induced Heat of Fusion vs. Permanence Time at T'=253K for BC55.

Time,t (min.)	Δh_{fus} (J/g of EO)	x_t	x_c
1	2.85	0.014	0.025
2	5.11	0.026	0.047
4	8.53	0.043	0.078
8	15.15	0.076	0.138
16	21.27	0.107	0.195
33	25.02	0.125	0.227
72	36.35	0.182	0.331

Table 4.13. Induced Heat of Fusion vs. Permanence Time at T'=256K for BC55.

Time,t (min.)	Δh_{fus} (J/g of EO)	x_t	x_c
1	1.78	0.009	0.016
2	2.71	0.014	0.025
3	4.13	0.021	0.038
6	7.84	0.039	0.071
12	10.24	0.051	0.093
30	16.65	0.083	0.151
100	33	0.165	0.300

Table 4.14. Induced Heat of Fusion vs. Permanence Time at T'=258K for BC55.

Time,t (min.)	Δh_{fus} (J/g of EO)	x_t	x_c
1	1.05	0.005	0.009
2	1.36	0.007	0.013
11	3.16	0.016	0.029
35	5.36	0.027	0.049
55	8.45	0.042	0.076
114	11.56	0.058	0.105

Table 4.15. Induced Heat of Fusion vs. Permanence Time at T'=260K for BC55.

4.4. Analysis and Discussion.

4.4.1. Glass Transition Temperature.

Two different analyses for the correlation of the T_g of a mixed amorphous system are presented below:

Pochan Analysis[1]:

$$\ln T_{g,T} = m_1 \ln T_{g,1} + m_2 \ln T_{g,2} \qquad (4.1.)$$

Fox Analysis[2]:

$$\frac{1}{T_{g,T}} = \frac{m_1}{T_{g,1}} + \frac{m_2}{T_{g,2}} \qquad (4.2.)$$

where $T_{g,T}$ is the glass transition temperature of the mixed binary system, $T_{g,1}$ and $T_{g,2}$, and m_1 and m_2, are the glass transition temperatures and volume or weight fractions of the pure homopolymer components, respectively. Systems which obey the above relationships indicate that intimate mixing on the molecular level is present. The Fox analysis is in fact a simplified form of the Pochan analysis. Contrary to Pochan, Fox assumed that any change in free volume of the polymer blend is independent of the glass transition temperature.

Figures 4.7 and 4.8 show a plot of the experimental T_g's for the block copolymers and the blends respectively along with the predicted single T_g for a miscible system based upon the Pochan and Fox analyses (see tables 4.1 and 4.2).

As previously stated, difficulties were present in detecting the glass transition temperatures for the higher EO fraction polymers using differential scanning calorimetry (no clear T_g was observed for BC76). For the lower EO fraction block copolymers, however, a single T_g was detected for the majority of the block

Figure 4.7. Glass Transition Temperature vs. Volume Fraction of PEO for PEO-b-PMMA Block Copolymers.

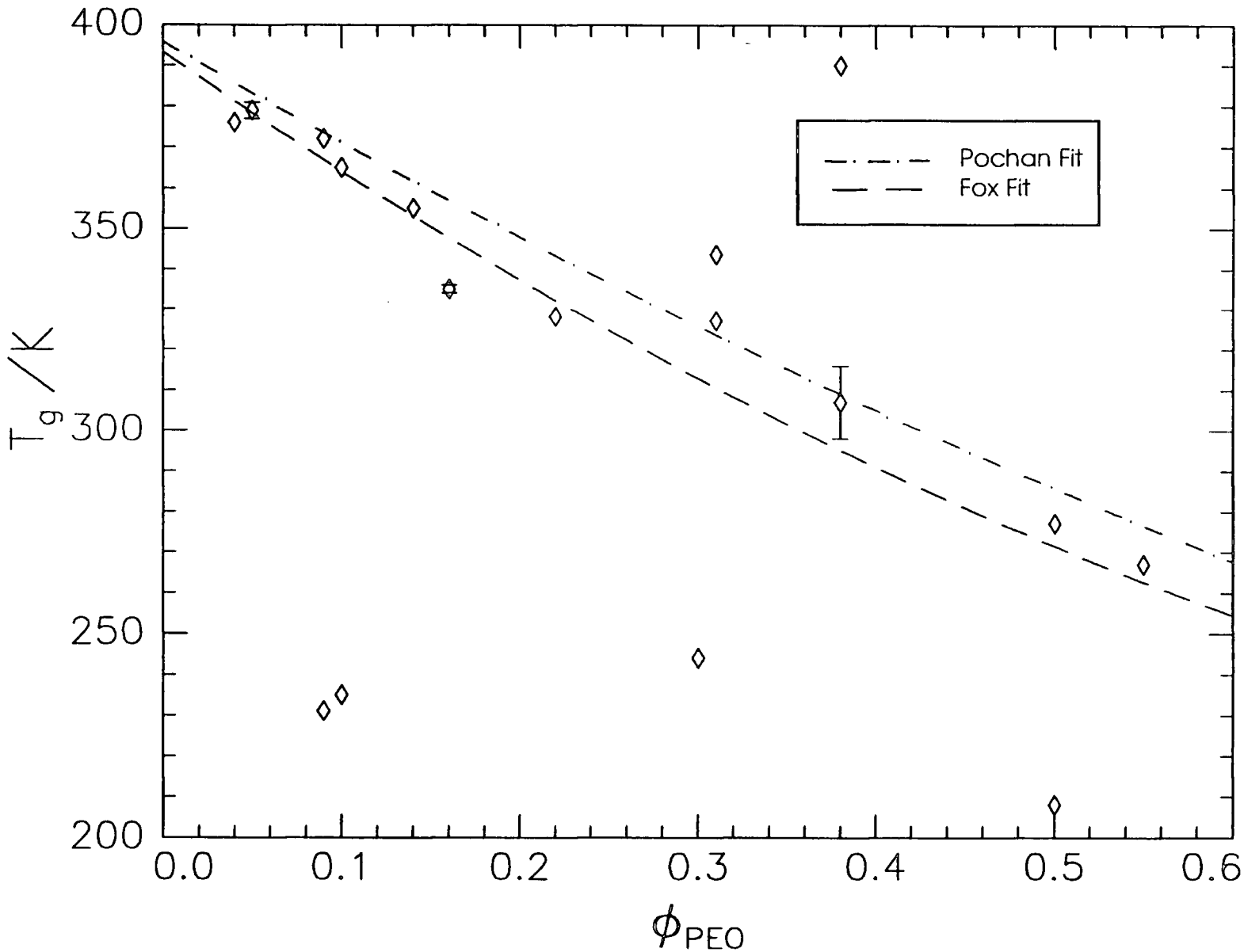

Figure 4.8. Tg vs. Volume Fraction of PEO for the Blends.

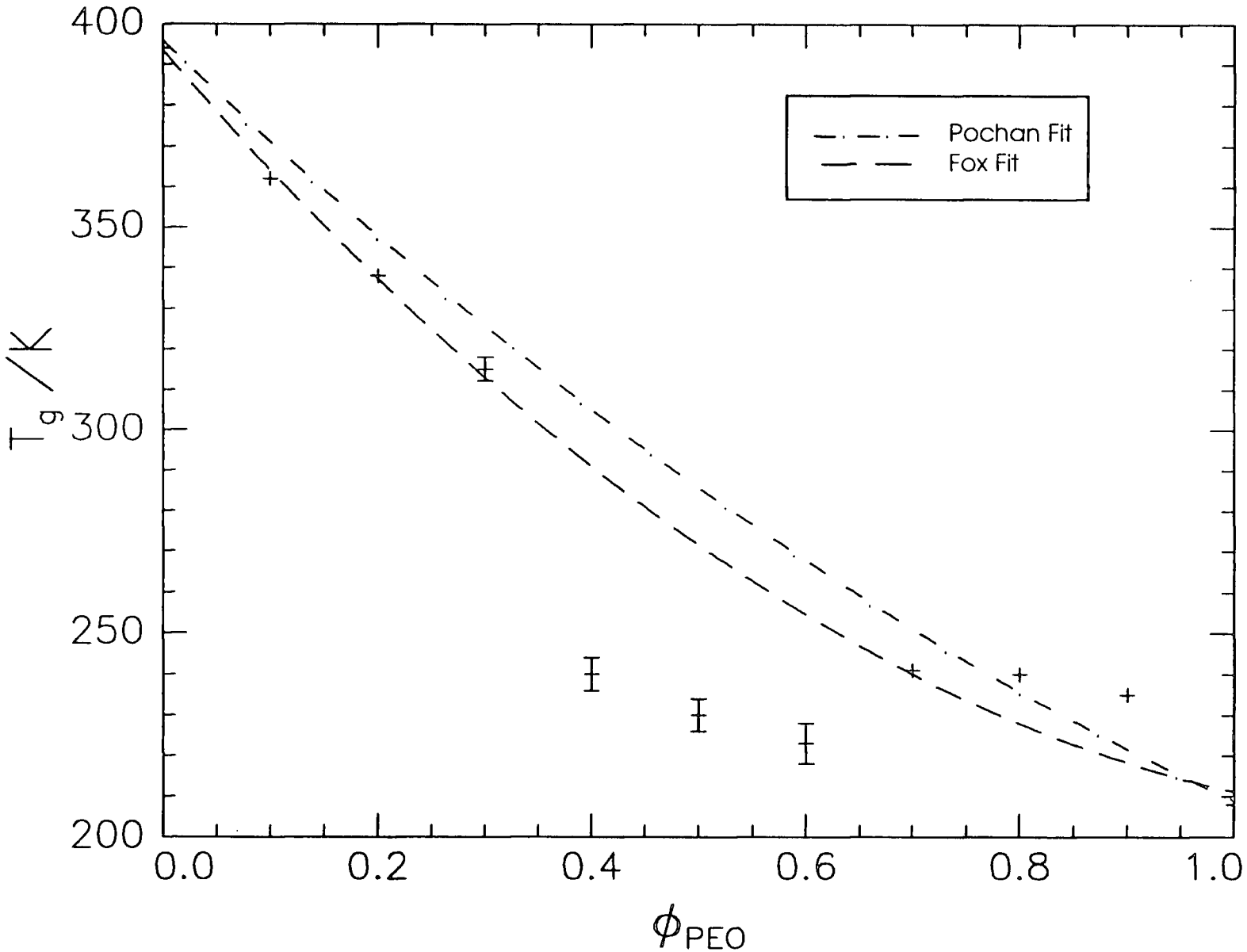

copolymers which agreed well with the Pochan and Fox analyses indicating miscibility on a molecular level (see figure 4.7). For a few block copolymers, additional glass transition temperatures along with the 'miscible' T_g were detected. These extra glass transition temperatures were similar in value to those expected for the constituent homopolymers, indicating that domains rich in PEO and PMMA were present. Consequently, this suggests that the block copolymers are only weakly miscible and that the associated single phase is thermodynamically close to a ODT temperature. This results in kinetic effects becoming more dominant, which when coupled with large local concentration fluctuations, may produce systems with areas of phase separated microdomains. This explains the observation of multiple T_g's for some and not other block copolymers.

For the blends, however, single T_g's were detected over the whole composition range. For compositions less than 40% of PEO, excellent agreement with the Fox analysis was found (see figure 4.8). For compositions >40% PEO the T_g remained at a reasonably constant value of 235±5K. This is in agreement with earlier observations by other investigators (see section 2.3.1.), and can be attributed to the glass transition of crystalline lamellae with constant PEO composition (80% by weight).

4.4.2. Melting Points

4.4.2.1. General Observations.

For both the unannealed and annealed blends, a depression in the melting point was observed as the concentration of PMMA increased. It is interesting to note the irregular, larger than expected value of T_m' for BL70. After precipitation, BL70 appeared denser and more crystalline than the other blends and so the higher T_m' value can be ascribed to this denser morphological state of the blend.

The equilibrium melting point for BC76 was approximately 2K smaller than that T_m^0 for the corresponding blend. This suggests that due to the restrictive chemical joint in the block copolymer, either one, two or all three of the following are

plausible reasons for this lower equilibrium melting point temperature than the corresponding blend: a lower degree of crystallinity, thinner crystalline lamellae and/or lower EO incorporation in the crystalline lamellae.

There appears to be a large discrepancy in the melting point temperatures between the unannealed and annealed blends. It is unlikely that this difference is wholely due to the different thermal histories of the blends. Thus it is attributed to an error with instrument calibration. Although an error in the calibration of the temperature of the DSC head alters the relative melting point temperatures of the unannealed and annealed blends, this does not effect the relative melting point depression values used to determine the Flory-Huggins interaction parameter (see section 4.4.2.2).

4.4.2.2. Flory-Huggins Interaction Parameter for the Unannealed and Annealed Blends.

Using equations 1.15-1.17 developed by Scott[5] and Nishi and Wang,[6] the Flory-Huggins interaction parameter, χ, was evaluated from the melting point depression of the unannealed and annealed blends. The values 85.6cm^{3}mol^{-1}, 38.9cm^{3}mol^{-1} and 8786 Jmol^{-1} were used for $V_{1\mu}$, the molar volume of the amorphous polymer, $V_{2\mu}$ and $\Delta H_{2\mu}$, the molar volume and the heat of fusion per mole of the crystalline polymer, respectively.[7] χ at T_m^o was evaluated form the slope of $(1/T_m^o - 1/T_{m,PEO}^o)$ vs. v_1^2, see figure 4.9.

For the unannealed blends, B=-5.33Jcm^{-3} and χ=-0.16 (337.4K) and for the annealed blends, B=-2.66Jcm^{-3} and χ=-0.08 (343.5K). Both χ values indicate that the solvent cast, unannealed and annealed blends are miscible and are similar in magnitude to values of the interaction parameter determined elsewhere (see section 2.3.1).

As shown in figure 4.9, the intercept is far from zero, and this shift from the origin is greater for the solvent cast, unannealed blends. This suggests that non-negligible entropic effects occur during the mixing of the polymers, and are more dominant for the unannealed blends. This deviation form the origin as well as the

Figure 4.9. Nishi/Wang Plot to Evaluate χ for PEO/PMMA Blends.

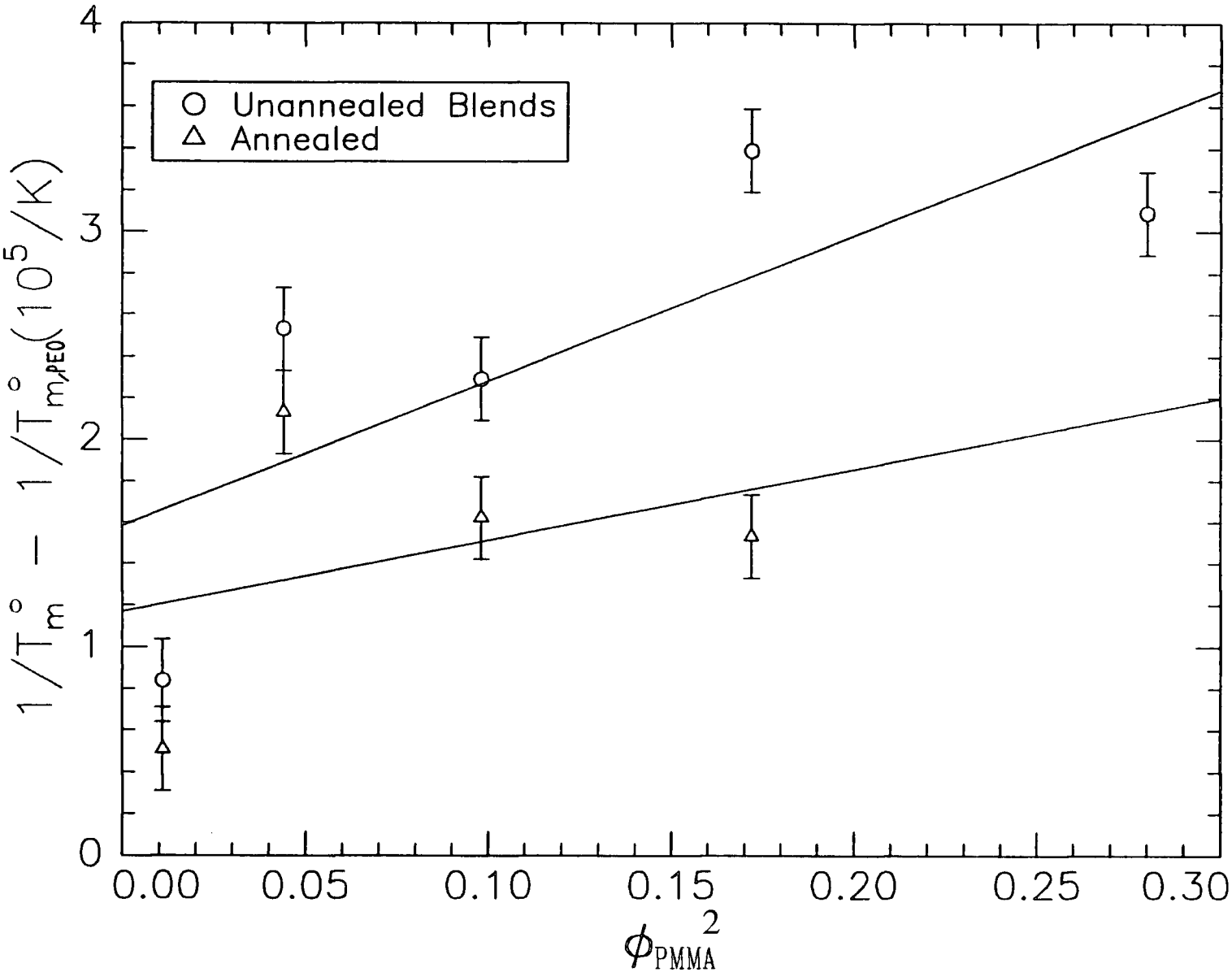

relatively poor linear fits in figure 4.9 may also be due to inadequacies of the Flory-Huggins theory to describe the melting behaviour of such polymer-polymer systems and errors involved in the determination of the equilibrium melting point temperatures, T_m^o. Such errors in the determination of T_m^o are strongly dependent upon kinetic and morphological factors as reported by Runt et al[8]. However, the slopes for the Hoffman/Weeks plots as a function of blend composition in figure 4.3. are relatively constant. Since the magnitude of these gradients are related to a morphological factor, then it is deduced that there is a negligible contribution to any error in T_m^o from morphological factors.

4.4.3. Crystallinity.

For all of the PEO/PMMA blends studied, the heat of crystallisation, Δh_{cryst}, is larger for the unannealed blends than for the annealed blends. An explanation for this difference lies in the relative chain mobility between a solution and the melt. In a solvent, the polymer chains have greater chain movement and so are able to order more effectively, resulting in a higher level of crystallinity when precipitated as a solid.

For the blends, both x_t and x_c decrease with increasing PMMA concentration. This trend can be accounted for by assuming that the relative amount of PMMA trapped in interlamellar regions of the PEO spherulites increases with increasing PMMA concentration. As a consequence, the spherulites should appear to be less ordered (see chapter 5). A similar variation in x_t and x_c have been observed by Martuscelli[9].

The values associated with BC76 are similar in magnitude to the blend BL70. This also suggests that the relative amount of PMMA trapped in interlamellar regions of PEO spherulites is larger for the block copolymer than the corresponding blend.

4.4.4. Isothermal Crystallisation.

The isothermal crystallisation process was analysed on the basis of the JMA equation:

$$X(t) = 1 - \exp(-K_n t^n) \qquad (4.6)$$

where X(t) is a property of the system which changes linearly with the degree of transformation accompanied with the crystallisation process. X is related to the degree of crystallinity which is derived from the enthalpy of crystallisation using the following expression:

$$1 - X(t) = \frac{\Delta h_{cryst,t=\infty} - \Delta h_{cryst,t}}{\Delta h_{cryst,t=\infty} - \Delta h_{cryst,t=0}} \qquad (4.7)$$

where $\Delta h_{cryst,t=\infty}$ is the enthalpy of crystallisation after the polymer has fully crystallised and $\Delta h_{cryst,t}$ is the heat of crystallisation after time t. Zero time was taken to be the instant when the temperature reached T_c i.e. no induction time. The Avrami analysis and the JMA exponent have been described in more detail in section 1.1.3.

Figures 4.10. to 4.15. shows the Avrami analysis of the enthalpy of crystallisation data for BC76, PEO and the blends, BL90, BL80, BL70, BL60, respectively. The constant slopes for each T_c indicate a constant value for n and the intercept with the y axis gives a measure of the rate of isothermal crystallisation, $\log K_n$. For some crystallisation temperatures, the Avrami analysis at long times characteristically departed from the initial linear dependence owing to the enhancement of error as $\Delta h_{cryst,t}$ approaches $\Delta h_{cryst,t=\infty}$ (see figures 4.10. to 4.15.). Consequently, for these cases, the linear fits were strongly weighted towards the

Figure 4.10. Avrami Analysis for BC76.

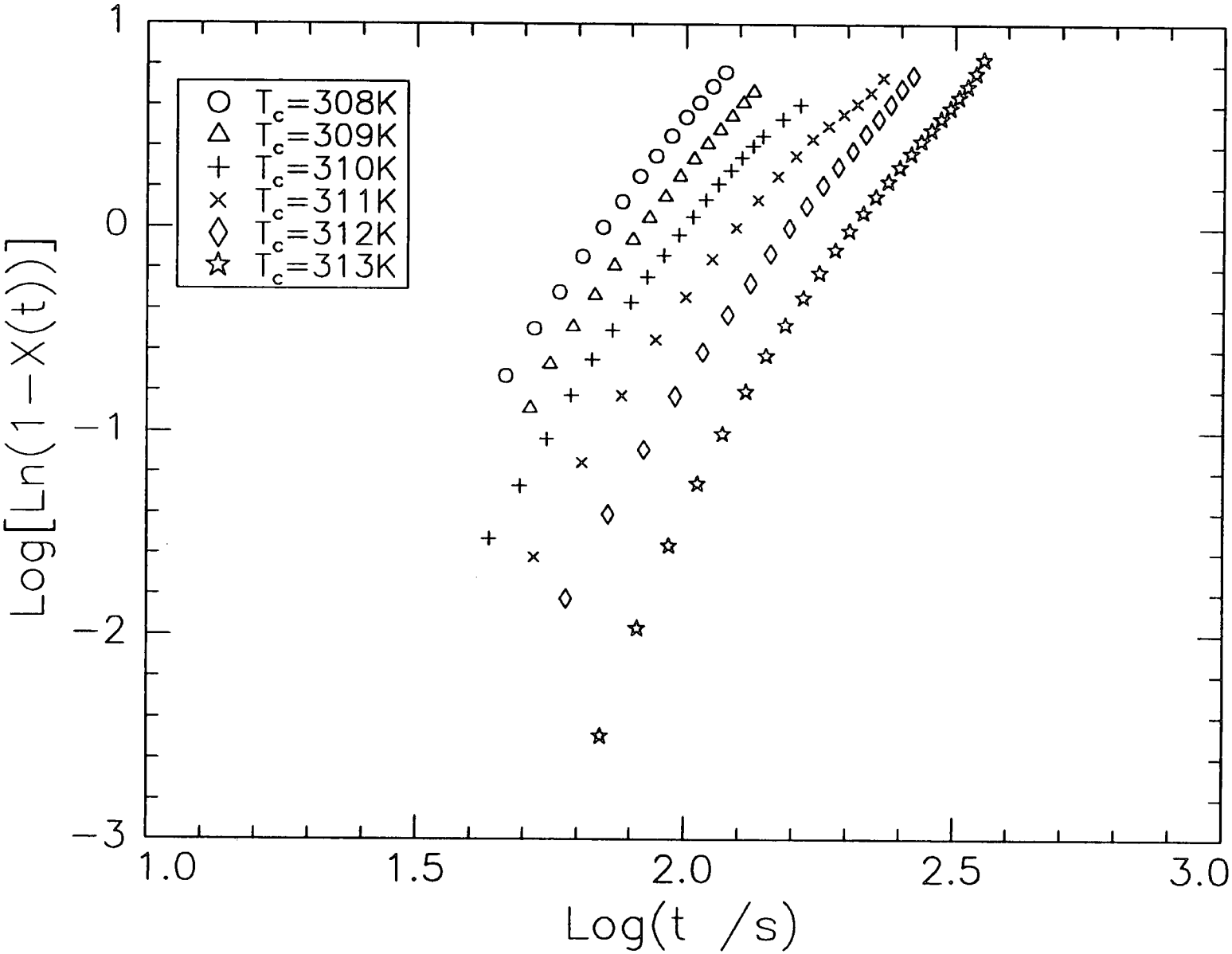

Figure 4.11. Avrami Analysis for PEO.

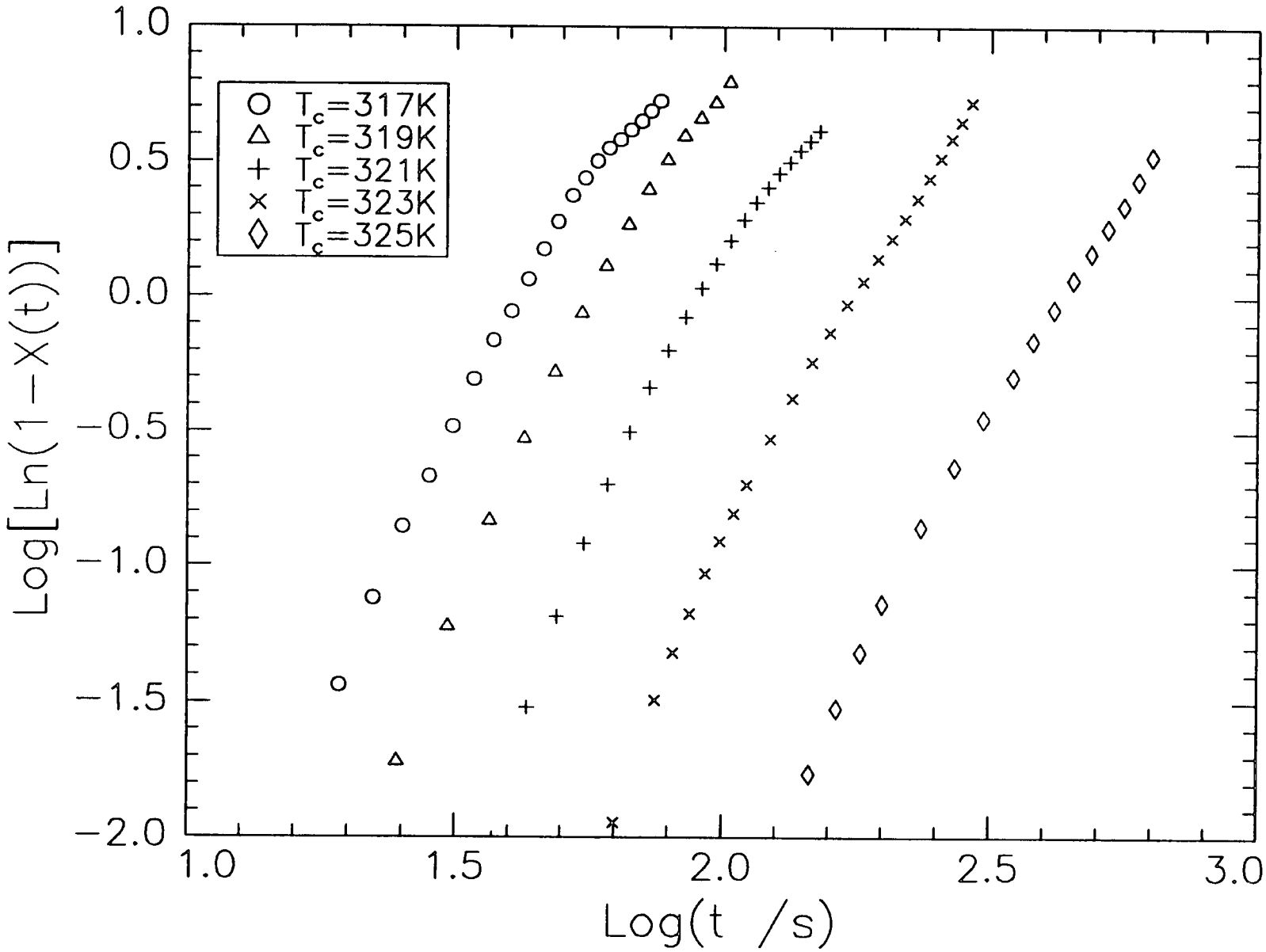

Figure 4.12. Avrami Analysis for BL90.

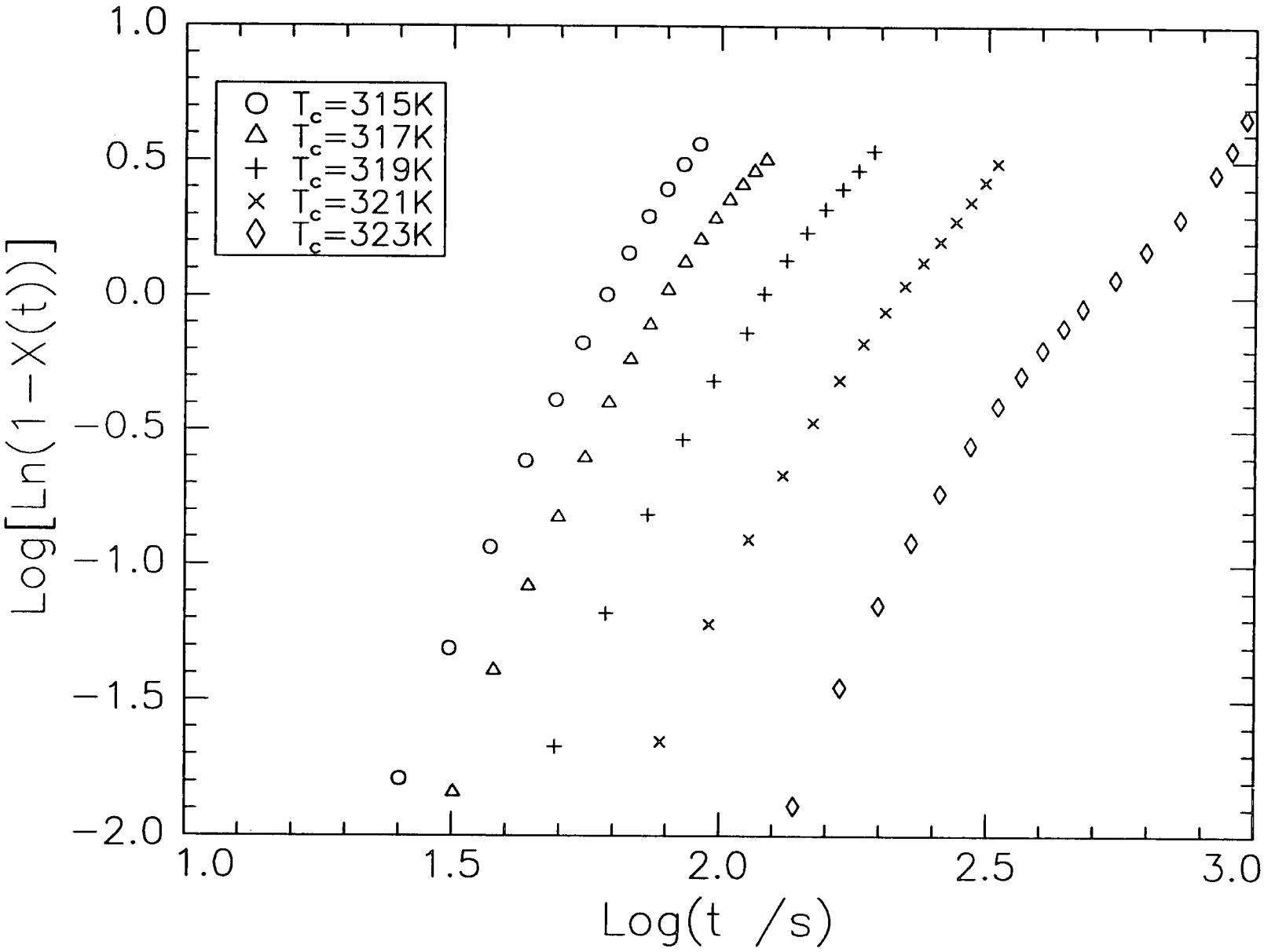

Figure 4.13. Avrami Analysis for BL80.

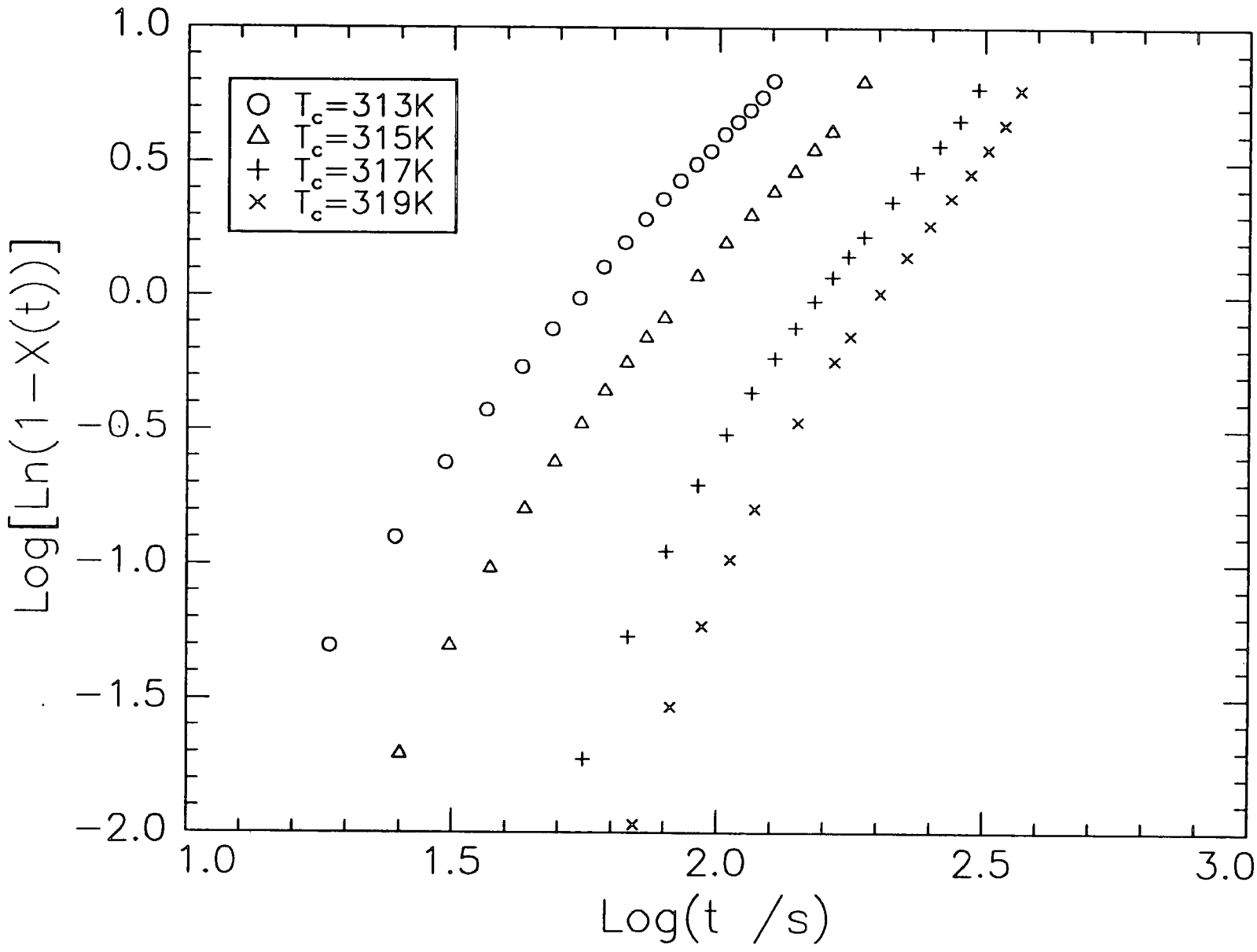

Figure 4.14. Avrami Analysis for BL70.

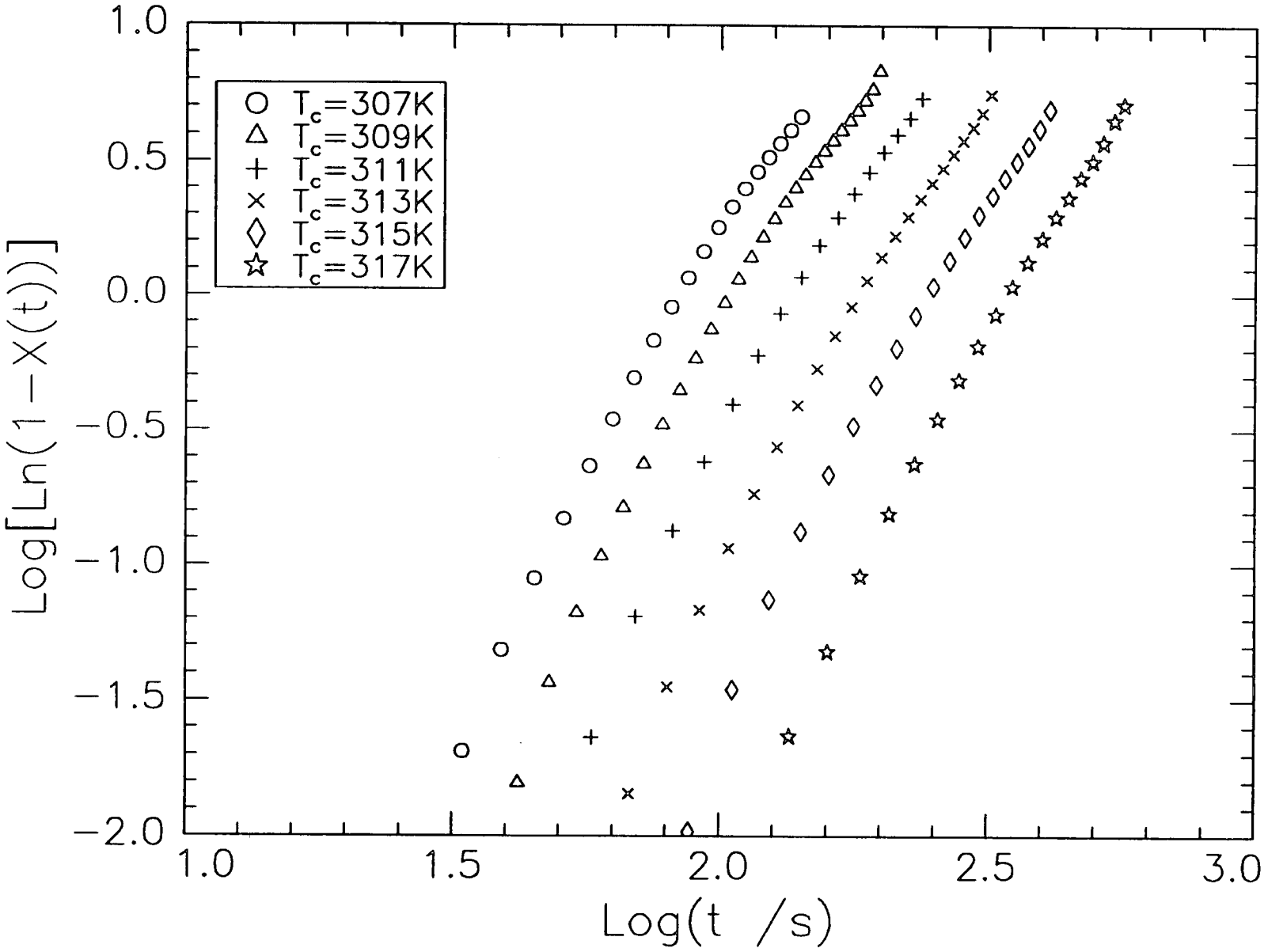

Figure 4.15. Avrami Analysis for BL60.

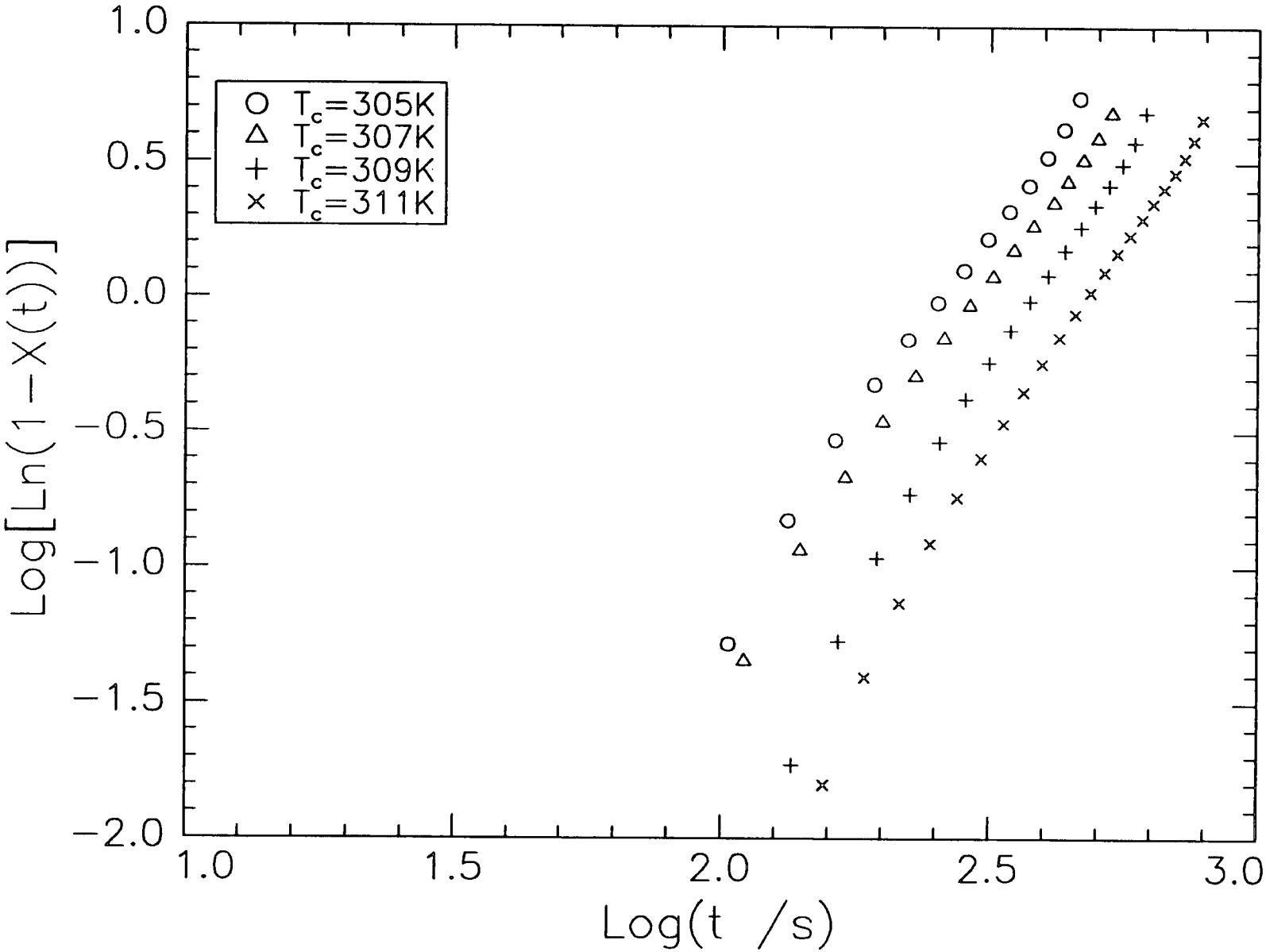

intermediate data points of the Avrami plots. Tables 4.16. and 4.17. list the determined values of n (error term = ±0.2) and $\log K_n$ for the PEO/PMMA blends and PEO, and for BC76 respectively. The peak times listed in tables 4.16. and 4.17. are the times at which the rate of transformation is at a maximum and give an indication on the overall rate of crystallisation (see figure 4.16).

	T_c (K)	Log K_n	n	Peak time (s)
PEO	325	-9.35	3.57	344
	323	-8.84	3.97	149
	321	-7.59	3.89	76
	319	-7.12	4.04	51
	317	-6.21	3.84	36
PEO/PMMA (90/10), BL90	323	-9.73	3.71	320
	321	-8.16	3.52	170
	319	-7.81	3.74	100
	317	-7.42	3.91	68
	315	-6.97	3.89	55
PEO/PMMA (80/20), BL80	321	-10.1	3.88	364
	319	-9.31	3.93	156
	317	--8.74	3.85	116
	315	--7.99	3.79	62
	313	--7.45	3.77	43
PEO/PMMA (70/30), BL70	317	-10.14	4.01	87
	315	-8.66	3.63	76
	313	-8.77	3.89	56
	311	-8.25	3.87	46
	309	-8.17	4.06	36
	307	-7.50	3.90	27
PEO/PMMA (60/40), BL60	311	-9.39	3.67	125
	309	-8.77	3.41	106
	307	-6.66	2.69	80
	305	-6.18	2.56	73

Table 4.16. Evaluated Avrami Parameters for PEO and the Blends.

Figure 4.16. Evaluated Peak Times (s) vs. Crystallisation Temperature for PEO, the Blends and BC76.

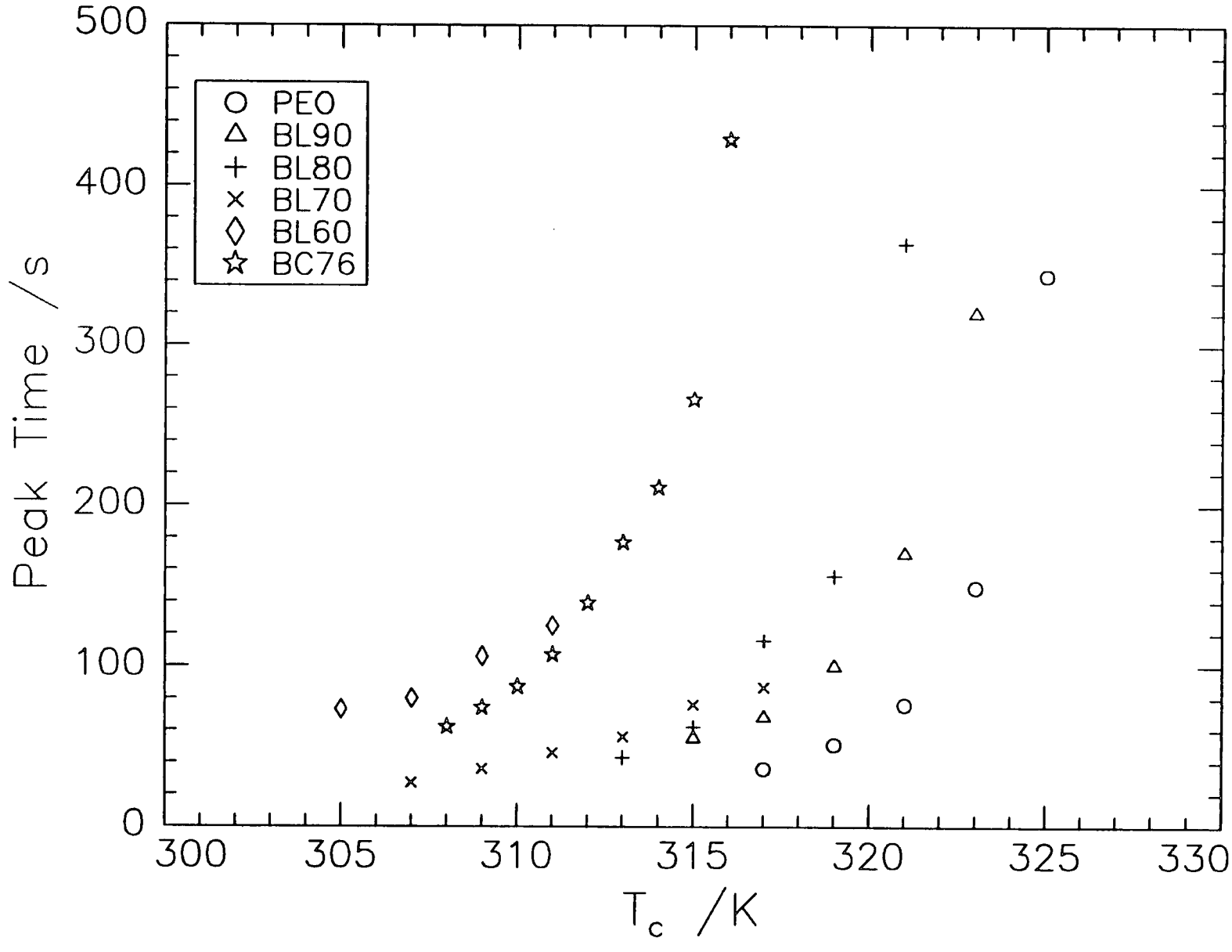

PEO-b-PMMA (76/24) BC76	T_c(K)	Log K_n	n	Peak time (s)
	316	-10.90	4.03	429
	315	-9.63	3.85	266
	314	-8.97	3.75	211
	313	-8.94	3.86	177
	312	-8.33	3.79	139
	311	-7.96	3.79	107
	310	-7.66	3.83	87
	309	-7.19	3.74	74
	308	-6.81	3.68	62

Table 4.17. Evaluated Avrami Parameters for BC76.

No discernible difference between the block copolymer and the blends in the average value of n exists. For BC76, n=3.8 ± 0.2 and for the blends, n=3.8 ± 0.2. With reference to table 1.2., these values of n suggest that the isothermal crystallisation process for BC76 and PEO/PMMA blends has an associated JMA exponent close to 4. This relates to sphere growth geometry, interfacially controlled rate of attachment and homogeneous nucleation. For the blends, no variation in n with PMMA concentration was observed, however, a slight decrease in n with decreasing crystallisation temperature was detected. A similar but more significant trend in n for PEO/PMMA blends was observed by Calahorra et al[10]. Table 4.18. compares the evaluated JMA exponents for the blends with other exponent values from the literature.

As shown in table 4.18, a clear trend with molecular weight is observable. The JMA exponent increases as the overall molecular weight of the PEO/PMMA blend decreases. This can be attributed to a change in the kinetics of the crystallisation mechanism where the rate determining step is now the rate of attachment of macromolecules to the nuclei, i.e., interfacially controlled. As the molecular weight decreases, the polymers become more mobile and consequently their rate of diffusion increases. Thus, the rate of attachment of crystallisable units to the crystalline interface is now the slowest step.

PEO/PMMA (w/w)	PEO(M_n18.6K)[a] PMMA(M_n22.2K)	PEO(M_w100K)[b] PMMA(M_w110K)	PEO(M_w4000K)[c] PMMA(M_w93.6K)
100/0	3.8 ± 0.2 *independent of composition*	2.6	1.9
90/10		2.6	2.0
80/20		2.5	2.1
70/30		2.8	2.3
60/40		3.1	2.7

Table 4.18. Comparison of JMA Exponents with Varying Molecular Weight for PEO/PMMA Blends.

[a] present work from DSC data.

[b] Ref 9, from DSC data.

[c] Ref 10, from depolarisation microscopy measurements.

The evaluated rate constant, K_n, decreases markedly with PMMA concentration and as the degree of undercooling decreases (see figure 4.17). The value of K_n for BC76 is approximately two orders of magnitude smaller at a specific crystallisation temperature than that for the corresponding blend, BL80. Irregular values in K_n (and n) for BL60 at low crystallisation temperatures, however, were evaluated (see table 4.16.). A plausible explanation for this irregularity is the presence of additional processes such as phase separation, which are in competition with the crystallisation process. Other experimental evidence supporting such this explanation for this intermediate blend composition range have been reported elsewhere (see Chapter 2).

Figure 4.17. Log K_n vs. Crystallisation Temperature for PEO, the Blends and BC76.

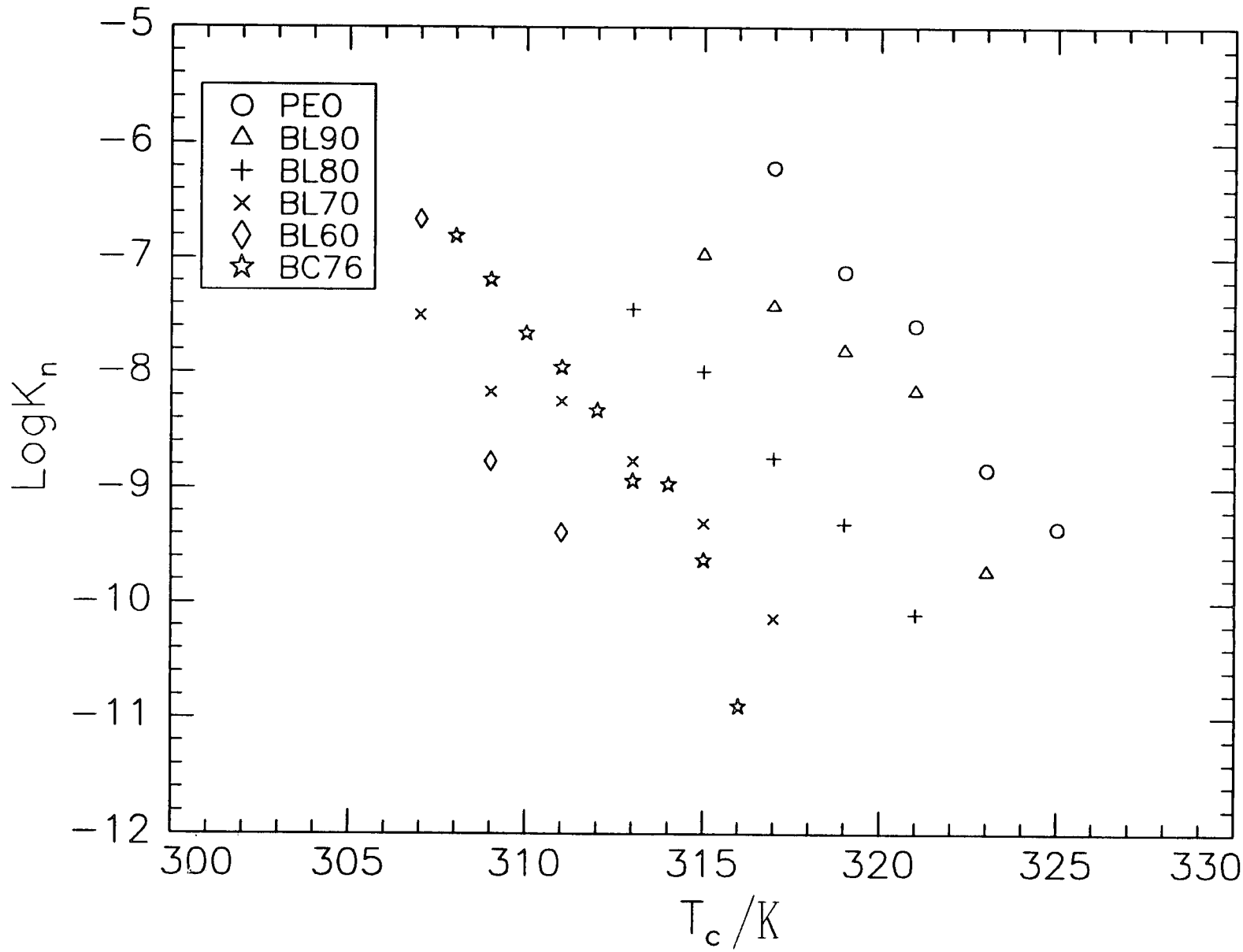

4.4.5. Phase Separation.

As stated in section 4.3.4., the magnitude of the crystallisation exotherm and the melting endotherm were very similar for each individual DSC thermogram. This indicates that all of the crystallinity associated with the melting endotherm crystallised during the temperature range of the crystallisation exotherm Thus, no crystallisation occurred at the low permanence temperatures, T'.

The level of induced crystallisation, which is represented in tables 4.6 to 4.15 as two crystallinity indices, decreased as the permanence temperature increased. This indicates that the amount of structural organisation at T' which induces the subsequent crystallisation at higher temperatures when BC50 or BC55 are heated, increases as T' decreases over the range of permanence temperatures studied. The maximum crystallinity attainable for both block copolymers was appreciably lower than that for the corresponding blend, 10% for BC50 and 34% for BC55. This indicates a highly disordered crystalline structure for these two block copolymers. A possible reason for the large difference in the maximum crystallinity between BC50 and BC55 may be due to the larger distribution in molecular weight for BC50 (see table 3.1.). The number of adjacent chains with equal lengths which are able to order is subsequently reduced.

For all of the permanence temperatures investigated, the amount of induced crystallisation (equivalent to Δh_{fus}) varied exponentially with permanence time, t, levelling off towards a constant value at longer times, $\Delta h_{fus,t=\infty}$, see figures 4.18 and 4.19. The shape of the induced crystallisation with permanence time is characteristic of nucleation and growth of a new phase in a parent matrix phase (see section 1.1.3.3.). Consequently, analysis of this structural organisation at these low temperatures, T', was based upon the Avrami analysis of nucleation and growth. Similar to the analysis of the isothermal crystallisation of BC76 and the blends (see section 4.4.3), the parameter, X(t) was defined as:

Figure 4.18. Induced Enthalpy of Crystallisation vs. Permanence Time at various Permanence Temperatures, T', for BC50.

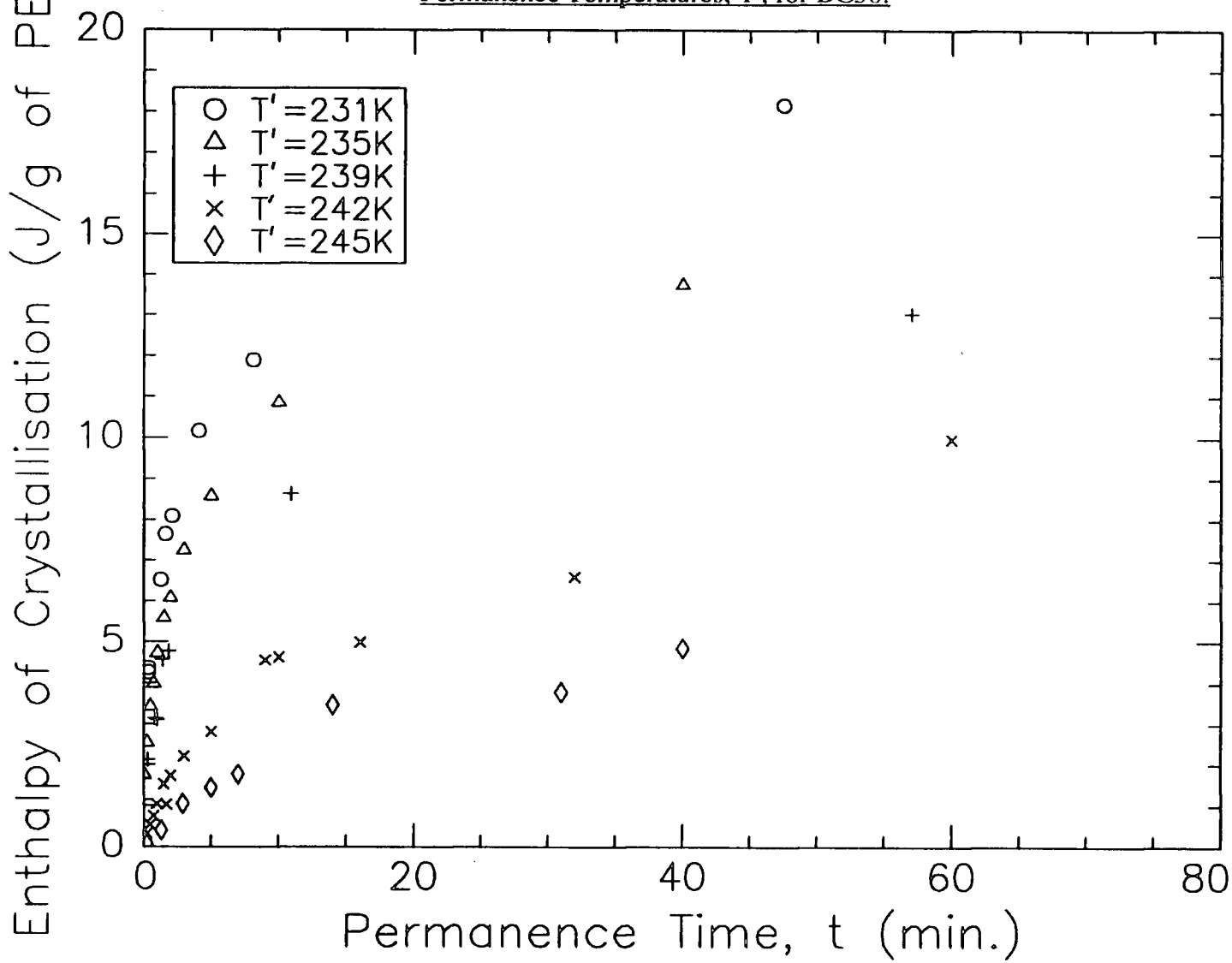

Figure 4.19. Induced Enthalpy of Crystallisation vs. Premanence Time at various Permanence Temperatures, T', for BC55.

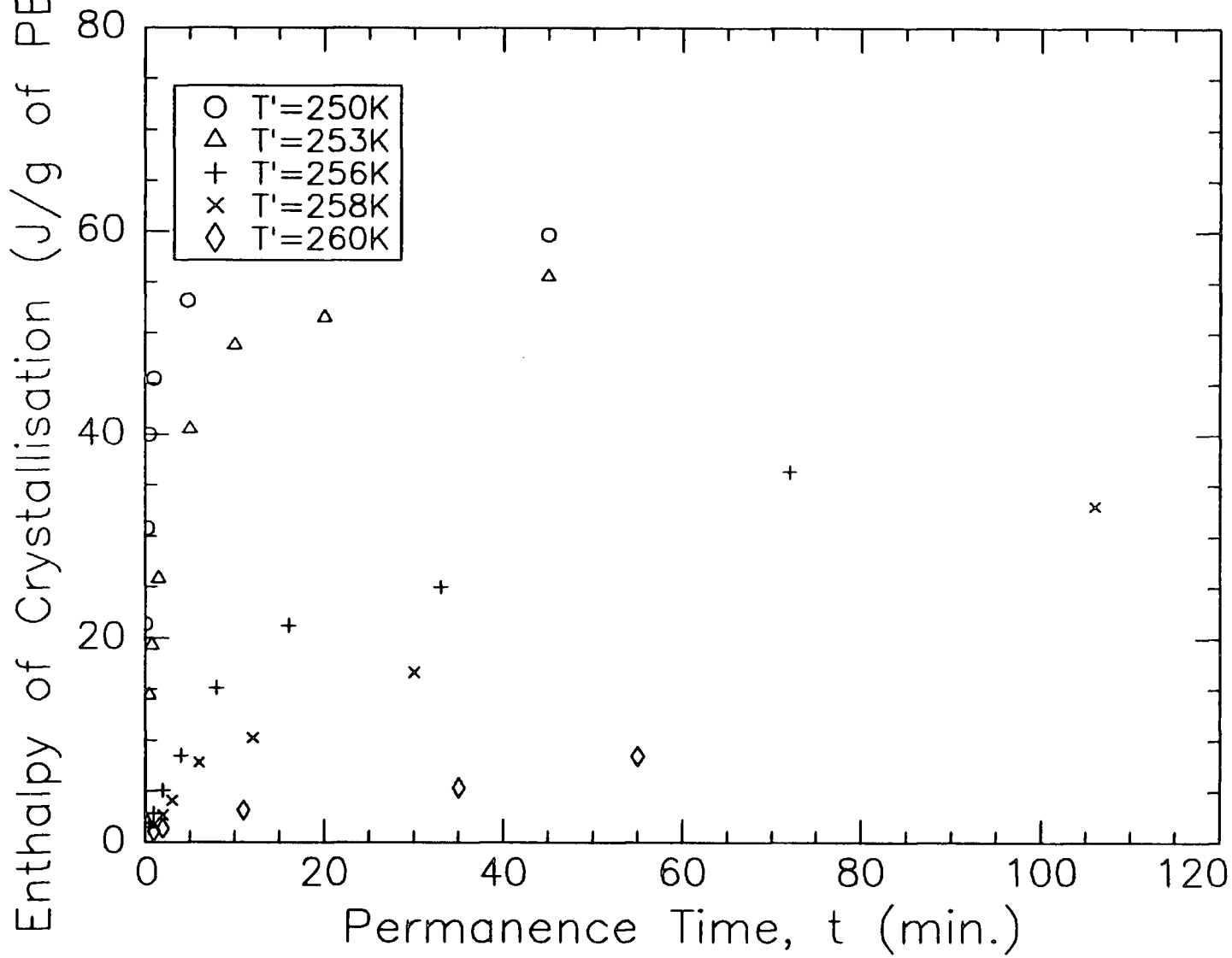

$$X(t) = \frac{\Delta h_{fus,t}}{\Delta h_{fus,t=\infty}} \qquad (4.8)$$

where $\Delta h_{fus,t}$ is the heat of fusion after time t at T' and $\Delta h_{fus,t=\infty}$ is the maximum heat of fusion after $t=\infty$ at T'. X(t) was then fitted to the following Avrami equation:

$$X(t) = 1 - \exp(-K_{T'} t^n) \qquad (4.9)$$

where t is the permanence time, $K_{T'}$ is a rate constant related to the rate of structural organisation at T' which induces the monitored crystallinity and n is the JMA exponent describing the phase separation process at T' (see table 1.2).

A plot of log(-ln(1-X(t))) versus log t is shown in figures 4.20. and 4.21. for BC50 and BC55 respectively, from which $K_{T'}$ and n were determined from the y axis intercept and the gradient respectively, see tables 4.19. and 4.20. Excellent agreement between the data and the JMA equation as obtained, as illustrated by the linear fits in figures 4.18. and 4.19. This supports the conclusion that the phase separation at the permanence temperatures, T', is governed by a nucleation and growth mechanism.

T' (K)	n	Log $K_{T'}$
245	0.84	-1.26
242	0.72	-1.07
239	0.53	-0.55
235	0.50	-0.45
231	0.44	-0.45

Table 4.19. Evaluated JMA Parameters for BC50.

Figure 4.20. Avrami Analysis of the Nucleation and Growth Phase Separation for BC50.

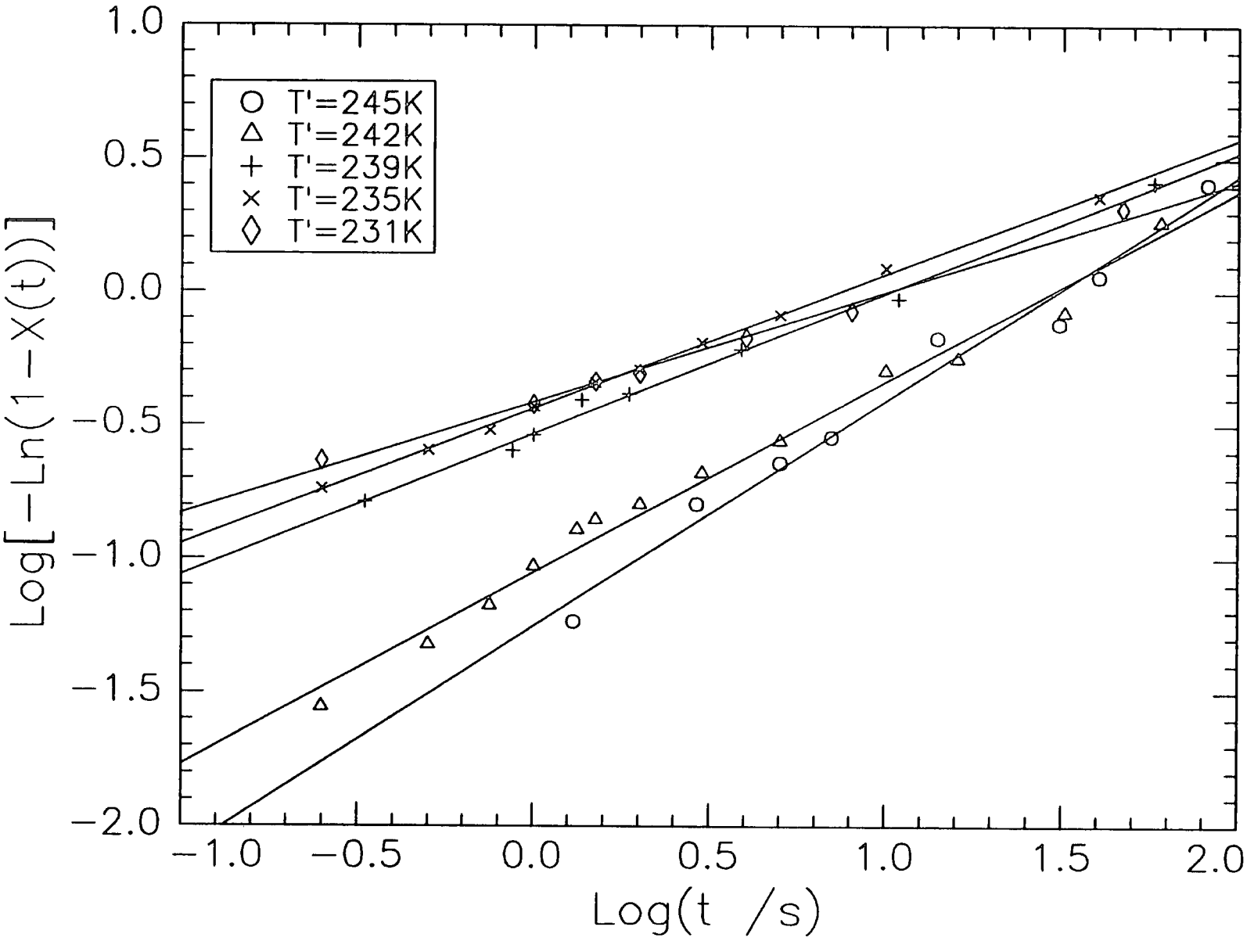

Figure 4.21. Avrami Analysis of the Nucleation and Growth Phase Separation for BC55.

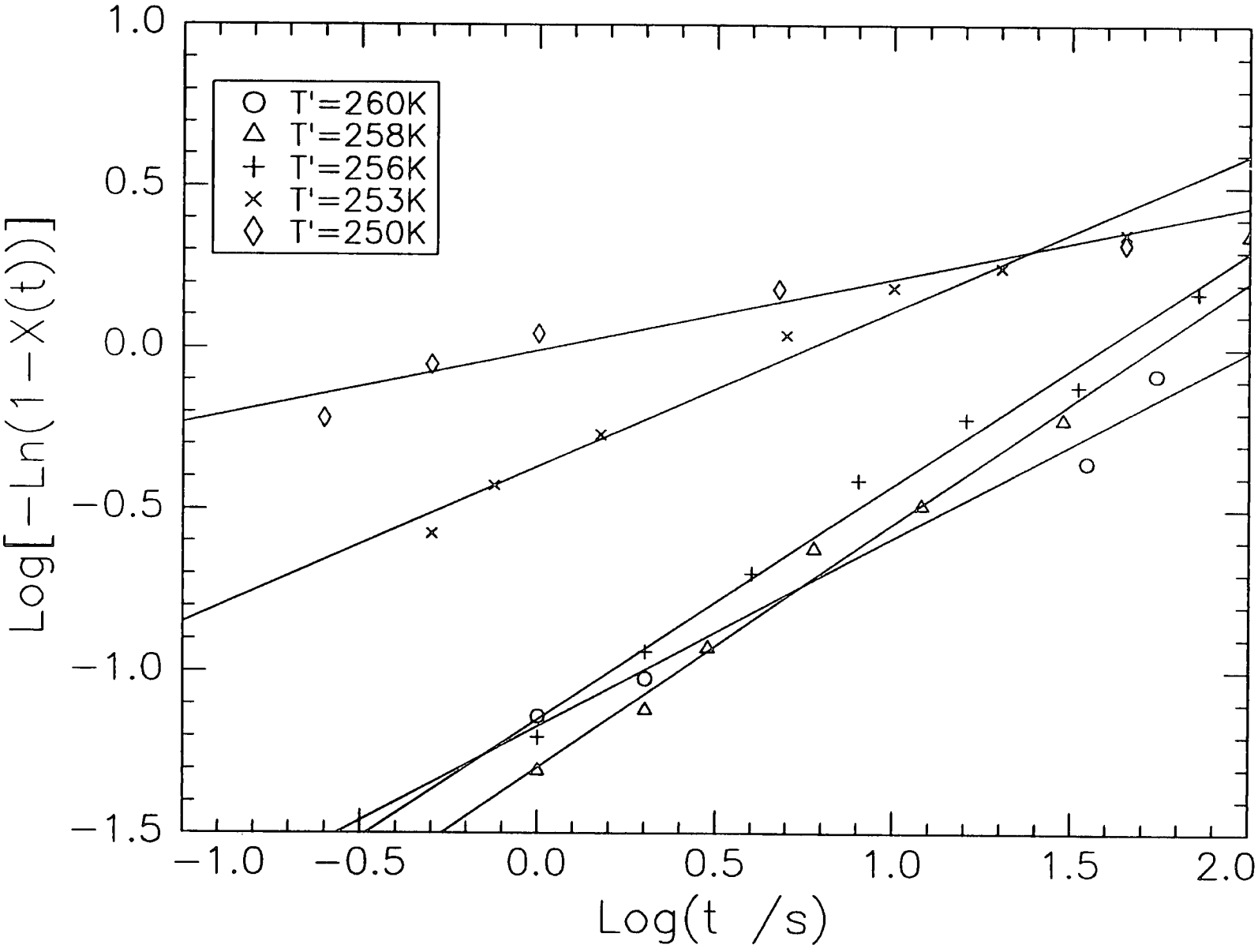

T'(K)	n	Log $K_{T'}$
260	0.63	-1.19
258	0.81	-1.32
256	0.74	-1.24
253	0.52	-0.34
250	0.26	0.036

Table 4.20. Evaluated JMA Parameters for BC55.

For both BC50 and BC55, the JMA exponent decreases with permanence temperature, T', from a value just below 1 to approximately 0.5. These JMA exponent values represent a nucleation and growth mechanism that is instantaneously nucleated, diffusion controlled with a growth geometry that is disc-like, tending towards a geometrically more complex rod-like shape as T' decreases. The instantaneous nature of nucleation is characteristic of nucleation and growth, and owing to the relatively low degree of chain mobility expected at these low permanence temperatures, it is anticipated that the rate determining step would be diffusion controlled. This low level of mobility also explains the shape of growth geometries obtained. The polymer chains are unable to form domains of lowest conformational free energy, i.e., spheres. This kinetic restriction is enhanced as T' decreases, lowering the level of chain mobility, and consequently yielded higher energy, geometrically more complex growth geometries, i.e., rod-like shapes.

Figure 4.22. illustrates the change in $\log K_{T'}$ as a function of permanence temperature. A transitional temperature, T_{tr}', in the rate of phase separation is evident for both block copolymers. For BC50, T_{tr}'=240.5K and for BC55, T_{tr}'=254K. This temperature, T_{tr}', does not represent the phase boundary. It is simply defined as the temperature at which the change in the rate of phase separation is highest, and will be used later (see chapters 6 and 8).

Figure 4.22. Log K_n vs. Permanence Temperature, T' for BC50 and BC55.

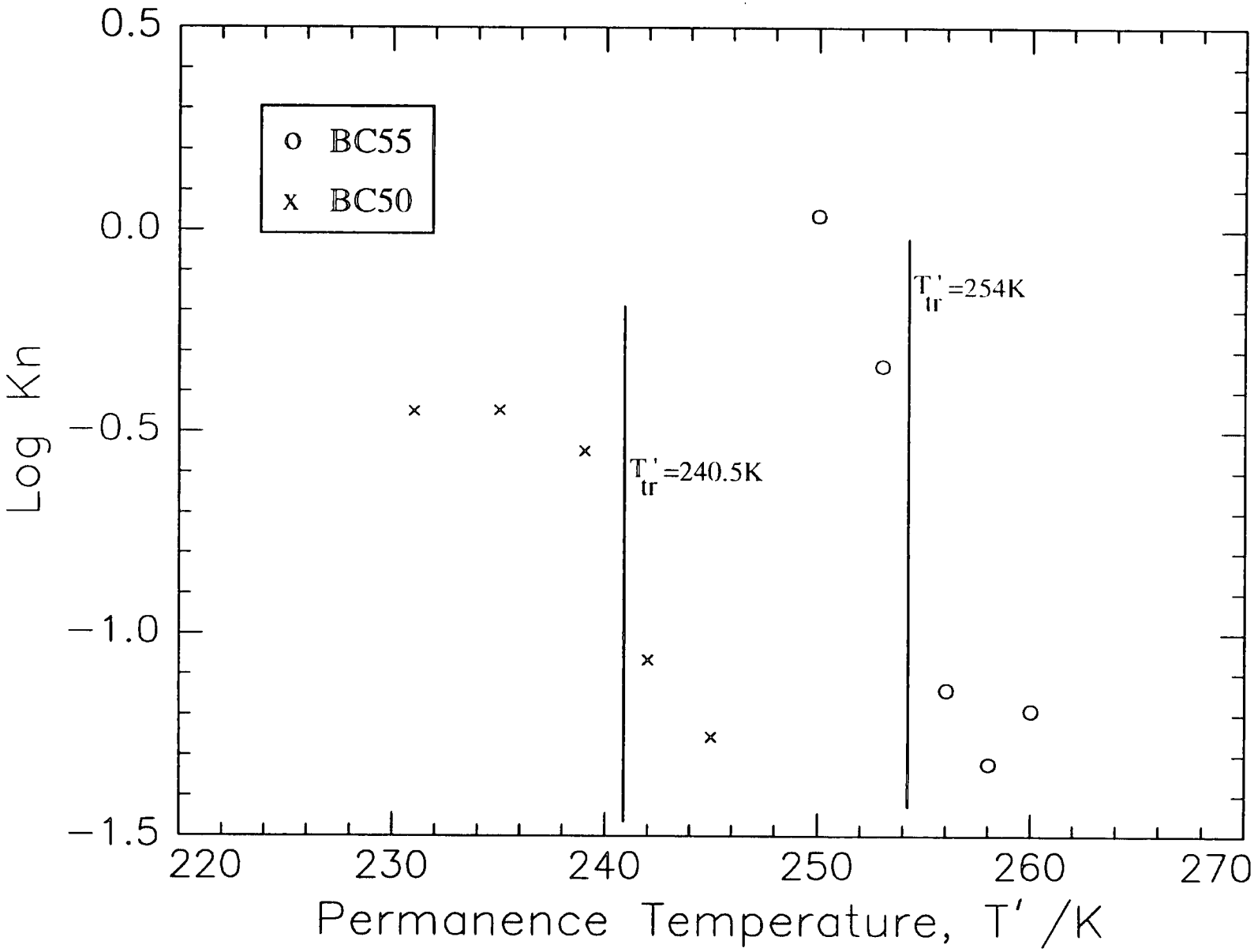

For temperatures less than 253K for BC50 and less than 265K for BC55, no induced crystallisation due to phase separation was detected. These temperatures are below the phase boundary temperature for BC50 and BC55, respectively. For those temperatures studied where $T'<T_{tr}'$, the rate of phase separation levelled off at a constant value of $K_{T'}$. This suggests that the increased quench depth into the two phase region is cancelled out by a reduction in the polymer chain mobility.

4.5. Conclusions.

4.5.1. PEO/PMMA Blends.

Experimental evidence supporting miscibility over the whole composition range for the poly(ethylene oxide)/poly(methyl methacrylate) blends studied in this work was found. Single glass transition temperatures for higher PMMA concentration blends were observed, which agreed well with those predicted by Fox for a miscible system on a molecular level. For lower PMMA fraction blends, again a single T_g was detected, however, this temperature remained at a constant value reflecting the T_g for 80% by weight crystalline lamellae. Further evidence for the diluent nature of the amorphous fraction based upon apparent and equilibrium melting point depression, and the decrease in the crystallinity indices x_t and x_c, as the concentration of PMMA increased was observed. Analysis of the melting point depression using the well known Nishi-Wang equation yielded a low negative interaction parameter (χ=-0.16 for the unannealed blends and χ=-0.08 for the annealed blends) indicating miscibility at temperatures close to the melt temperature of PEO. These values closely resemble previous values of χ for PEO/PMMA blends by other investigators (see chapter 2).

From the Avrami analysis of the isothermal crystallisation of the blends, the evaluated rate constant decreased as the concentration of PMMA increased and as the crystallisation temperature decreased. In fact the PMMA retards the crystallisation of PEO to such an extent that no re-crystallisation was observed for blends containing less than 40% PEO fraction by weight. A reasonably constant value for the JMA exponent of 3.8±0.2 was determined for all blend compositions (with the exception of BL60). This equated to an isothermal crystallisation mechanism of spherical growth geometry, nucleation that occurred throughout the crystallisation process at a constant rate (homogeneous nucleation) and an interfacially controlled rate determining step.

The irregular Avrami parameters for BL60 were attributed to the presence of a UCST-type phase boundary at the crystallisation temperatures studied. Other

investigators have proposed a similar explanation for the rather unusual crystalline behaviour observed for the intermediate blend composition range.

4.5.2. PEO-b-PMMA Block Copolymers.

In accordance with the Fox and Pochan analyses, single T_g's were detected. However, the presence of additional T_g's associated with phases rich in either homopolymer suggests that the block copolymers are only weakly miscible.

Whereas BC76 contained sufficient PEO to crystallise directly when cooled to temperatures below the melt, this was not true for BC55, BC50 and BC30. For these block copolymers, thermal treatment was necessary to induce crystallinity. From the DSC data and subsequent analysis, it was deduced that BC55 and BC50 phase separated according to a nucleation and growth mechanism at relatively low temperatures forming micodomains rich in PEO. The PEO chains did not crystallise at these low temperatures, but were present in a 'supercooled' state. Upon heating, the PEO chains in the PEO rich microdomains become mobile enough to crystallise and then melt. The mechanism of phase separation at the permanence temperatures was determined from an Avrami analysis of the induced crystallisation by monitoring the heat of fusion as a function of time at various permanence temperatures. The nucleation was instantaneous, the growth diffusion controlled and the growth geometry was disc-like changing to rod-like at lower permanence temperatures. The microphase separation temperature (MST) was found to be slightly greater than T_{tr}', 240.5K for BC50 254K for BC55, at a quenching rate of 100Kmin^{-1} to T'. For lower cooling rates to T' (2Kmin^{-1}), the expected increase in T_{tr}' and consequently MST due to the increased sensitivity (lower response time) of the system to permanence temperature was observed.

As the thermal routes to crystallisation for BC76 compared to BC55 and BC50 were different, it is not surprising to find that the degrees of crystallinity and the apparent melting points for these two sets of block copolymers were different. Even though BC76 contains over 20% more PEO by weight than BC55 and BC50, this

difference does not account for the appreciably higher crystallinity values (53% for BC76 compared to 34% and 10% for BC55 and BC50 respectively), and a 4K larger apparent melting point temperature. Consequently, it can be deduced that the crystalline regions for BC55 and BC50 are far more disordered than those for BC76.

4.5.3. Blends vs. Block Copolymers.

BC76 and the blends exhibit similar crystallisation behaviour. The polymers crystallise directly when cooled to temperatures below the melt according to the same crystallisation mechanism; spherical growth geometry where the nucleation is homogeneous and the spherulitic growth is diffusion controlled. The chemical joint connecting the constituent homopolymers in BC76, however, dramatically reduces the rate of crystallisation and lowers the melting point temperature by 2K. This reduced rate of crystallisation can be explained using an approach used by Donth et al.[11] They showed the necessity for mobile free crystallisable chain ends during crystallisation. Since the block copolymer has only one free chain end compared to two for the blends, the rate of crystallisation for BC76 is lower.

The thermal treatment necessary to induce crystallisation for BC55 and BC50 was not needed for BL60. However, this blend composition displayed some unusual crystallisation features which were ascribed to the presence of phase separation processes competing with crystallisation. Therefore, it can be concluded that for both the blend and the block copolymers at these intermediate compositions, phase separation processes are present at low temperatures. In the case of the block copolymers, the crystallisation has been retarded to such an extent that a composition 'window' has been created, where the polymers can be quenched into a metastable region without the block copolymers crystallising. It was not possible to distinguish at what temperatures the order-disorder transition occurred for both the blend and the block copolymers. However, for a blend and a block copolymer with the same fraction of PEO and the same molecular weight distributions, a higher ODT temperature for the

block copolymer would be expected, owing to a decrease in entropy of mixing caused by the restrictive nature of the chemical joint (see chapter 1).

4.6. References.

1. Pochan, J.M., Beatty, C.L. and Pochan, D.F., Polymer, 20, 879, 1979.
2. Fox, T.G., Bull. Am. Phys. Soc., 2, 123, 1956.
3. Hoffman, J.D. and Weeks, J.J., J. Res. Nat. Bur. Stand., Sect. A, 66, 13, 1962.
4. Wunderlich, B., <A> V, 1, Table IV, 1, 'Macromolecular Physics', Academic Press, New York, 1973.
5. Scott, R.L., J.Chem.Phys., 17, 279, 1949.
6. Nishi, T. and Wang, T.T., Macromolecules, 8, 909, 1975.
7. Van Krevelen, D.W., 'Properties of Polymers', Elsevier, New York, 1976.
8. Runt, J., Gallagher, K.P., Polym. Commun., Vol. 32, No.6, 180-182, 1991.
9. Martuscelli, E., Pracella, M. and Yue, W.P., Polymer, 25, 1097, 1984.
10. Calahorra, E., Cortazar, M., Guzmán, G.M., Polymer Commun., 24, 211, 1983.
11. Donth, E., Kretzschmar, Schulze, G., Garg., D., Höring, S. and Ulbricht, J., Acta Polymerica, 38, 261, 1987.

Chapter 5.

5. Polarised Light Microscopy.

5.1. Introduction.

This chapter describes the study of the isothermal spherulitic growth rates of the block copolymer BC76, the blends, BL60, BL70, BL80, BL90 and PEO, and their melting point behaviour. The Flory-Huggins interaction parameter, χ, has been evaluated from melting point depression data for the PEO/PMMA blend. The crystallisation mechanism is determined for each polymer specimen using the JMA analysis and the spherulitic growth rates have been related to a theoretically determined rate, from which values for the lateral surface free energy of the crystal as a function of composition have been calculated.

5.2. Principles of the Technique.

Commonly, semi-crystalline polymers crystallise from the melt forming macromolecular entities known as polymeric spherulites (see 1.1.3.). As viewed using a polarising optical microscope under crossed polars, in their simplest form, spherulites appear as circular birefringent areas showing a dark extinction pattern in the shape of a Maltese cross, of which one arm is aligned with the plane of polarisation of the polariser and the other arm is aligned with the plane of polarisation of the analyser. On rotation of the specimen, this pattern remains stationary showing that the spherulite has either radial or tangential circular symmetry.

These observations can be accounted for by a model in which identical birefringent units radiate symmetrically in all directions from the centre of the spherulite. Where these units are parallel to the plane of polarisation of either of the polars, extinction occurs and the final observation shows these extinction regions as a cross.

Polarised microscopy can be used to monitor the growth rates of spherulites over a length scale which is commensurate with the wavelength of visible light (3-1000's μms). Upon melting the birefringence of the crystalline regions disappears resulting in complete extinction when viewed through crossed polars. Thus, a value associated with the melting point temperature of semi-crystalline polymers can also be obtained using polarised light microscopy.

5.3. Experimental.

5.3.1. Apparatus.

Polymer samples were viewed through an Olympus B061 optical microscope under crossed polars. The image was acquired by a JVC KY-F30 3CCD video camera, displayed on a Sony KX-14CP1 colour monitor and recorded using a JVC HR-S5000EK super VHS video recorder onto super VHS video tapes. A Linkam VTO 232 video text overlay facility was also present and colour prints were obtained using a Sony Color Video Printer Up-5000P. A Linkam THM600 hotstage together with a Linkam CS196 Cooling System and a Linkam TMS 91 temperature controller enabled the polymer samples to be cooled (water or liquid nitrogen as coolant) or heated over a temperature range of 120K to 873K at rates of 0.2 to 110Kmin^{-1}.

5.3.2. Sample Preparation.

Thin films (approx. 4μm thick) of BC76, each of the blends and PEO were cast onto glass cover slips at room temperature from 5%w/w chloroform solutions. After allowing the solvent to evaporate slowly in air, the films were annealed at 303K under vacuum for 48 hours to remove all traces of solvent.

5.3.3. Isothermal Crystallisation.

The sample was placed on the Linkam hotstage on the Olympus optical microscope. The polymer film was covered by a second cover slip, and heated to 423K for 10 minutes to remove any thermal history. The sample was then quenched at the controlled rate of 100Kmin^{-1} to selected crystallisation temperatures, T_C. The subsequent growth of crystalline species after quenching was viewed between crossed polars and recorded by the video camera. The growth rate G, G = dR/dt (R = radius of the spherulite), was determined by measuring the radius of the spherulite as a function of time during the isothermal crystallisation process. The spherulitic radius was measured directly from the video recorded image and knowledge of the

magnification. Values of T_c ranged from 289K to 315K for the block copolymer and from 289K to 323K for each of the blends and PEO. For each crystallisation temperature, at least five growth rates were determined for each sample and the average growth rate is reported here.

5.3.4. Melting Point Determination.

The sample was held at each isothermal crystallisation temperature for 60 minutes. The apparent melting point temperature, T_m', was then determined by heating the specimen at a rate of $10Kmin^{-1}$ and noting the temperature at which birefringence associated with the presence of crystalline species completely disappeared.

5.4. Results.

Figure 5.1 shows a typical micrograph for the isothermal crystallisation of BC76 at 305K. The positive Maltese cross extinction pattern is evident (45^{o} to the meridian), indicating perpendicular or parallel orientation of the crystalline molecular axis with respect to the spherulitic radius[1,2]. There was no distinct difference between the spherulitic textures of the blends and the block copolymer. A reduction in the number of nucleation sites and consequently a reduction in the number of spherulites formed was observed as T_c increased. As a consequence, since the spherulites were volume filling, upon truncation the observed maximum spherulitic radius increased, ranging from 100μm to 1000μm (T_c=289K to 315K), as T_c increased. For all crystallisation temperatures, the radius length was far greater than the thickness of the films under investigation. Thus, owing to this restriction imposed in the growth direction orthogonal to the film surface, the spherulites were disk shaped As the amount of PMMA component increased for the blends, the morphological texture became more open and less ordered, see figure 5.2. For BC76, the blends and PEO, the apparent melting point, T_m', decreased with T_c, additionally for the blends, a decrease in T_m' was observed as the amount of PMMA present increased, (see tables 5.1. and 5.2.). A decrease of 2-3K in T_m' is observed for BC76 with respect to the corresponding blend.

Figures 5.3. and 5.4. shows plots of the spherulitic radius, R, against time, t, at each crystallisation temperature for BC76. For all temperatures, the spherulitic radius increased linearly with time. It was observed that for high T_c, at very long times of isothermal crystallisation, the growth rate decreased. Furthermore, the induction time for nucleation became more protracted for higher values of T_c. For a given T_c, all of the spherulites did not nucleate instantaneously (sporadic nucleation); however, once nucleated each spherulite grew at the same growth rate, G. As descibed in section 5.5.4., the time at T_c, t, was initiated when the spherulite under analysis was first observed.

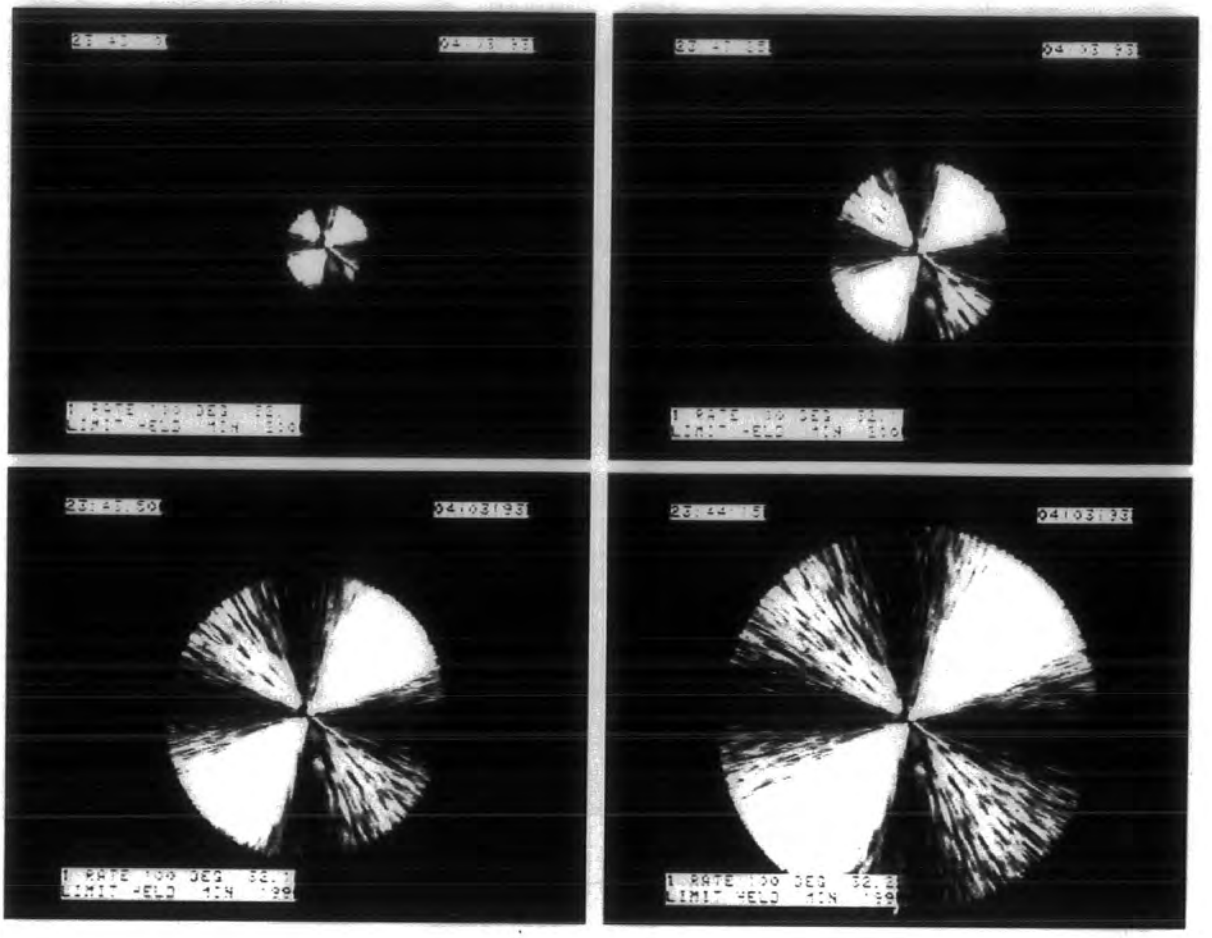

Figure 5.1. Isothermal Spherulitic Growth of BC76 at 305K.

Scale

200µm

Key.

a) b)

c) d)

a). Isolated spherulite after t=20s at T_c=305K.
b). Isolated spherulite after t=45s at T_c=305K.
c). Isolated spherulite after t=70s at T_c=305K.
d). Isolated spherulite after t=95s at T_c=305K.

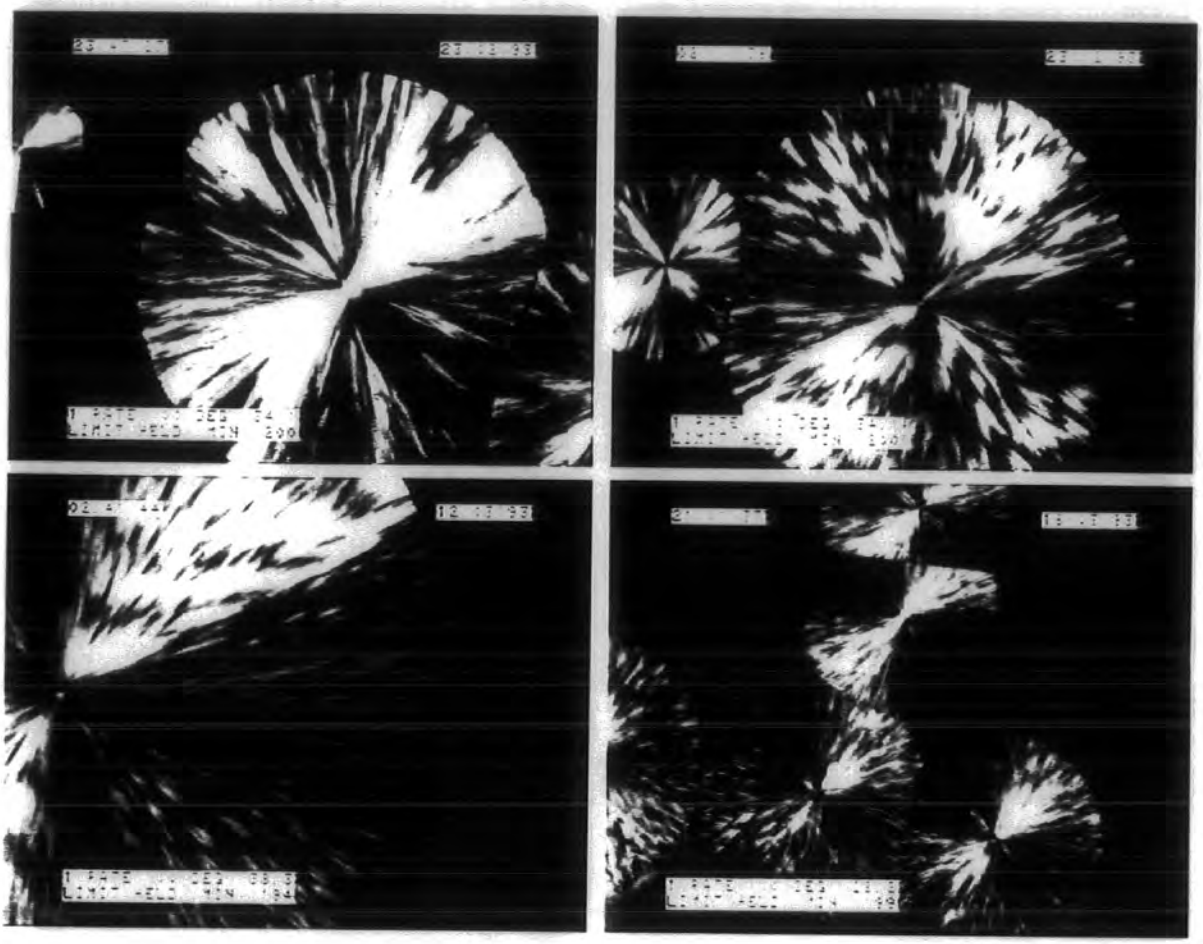

Figure 5.2. Morphological Textures for a series of PEO/PMMA Blends.

Scale

200μm

Key.

a) b)

c) d)

a). BL90 at T_c=307K.
b). BL80 at T_c=307K.
c). BL70 at T_c=311K.
d). BL60 at T_c=301K.

Figure 5.3. Spherulitic Radius vs. Time at various Crystallisation Temperatures for BC76.

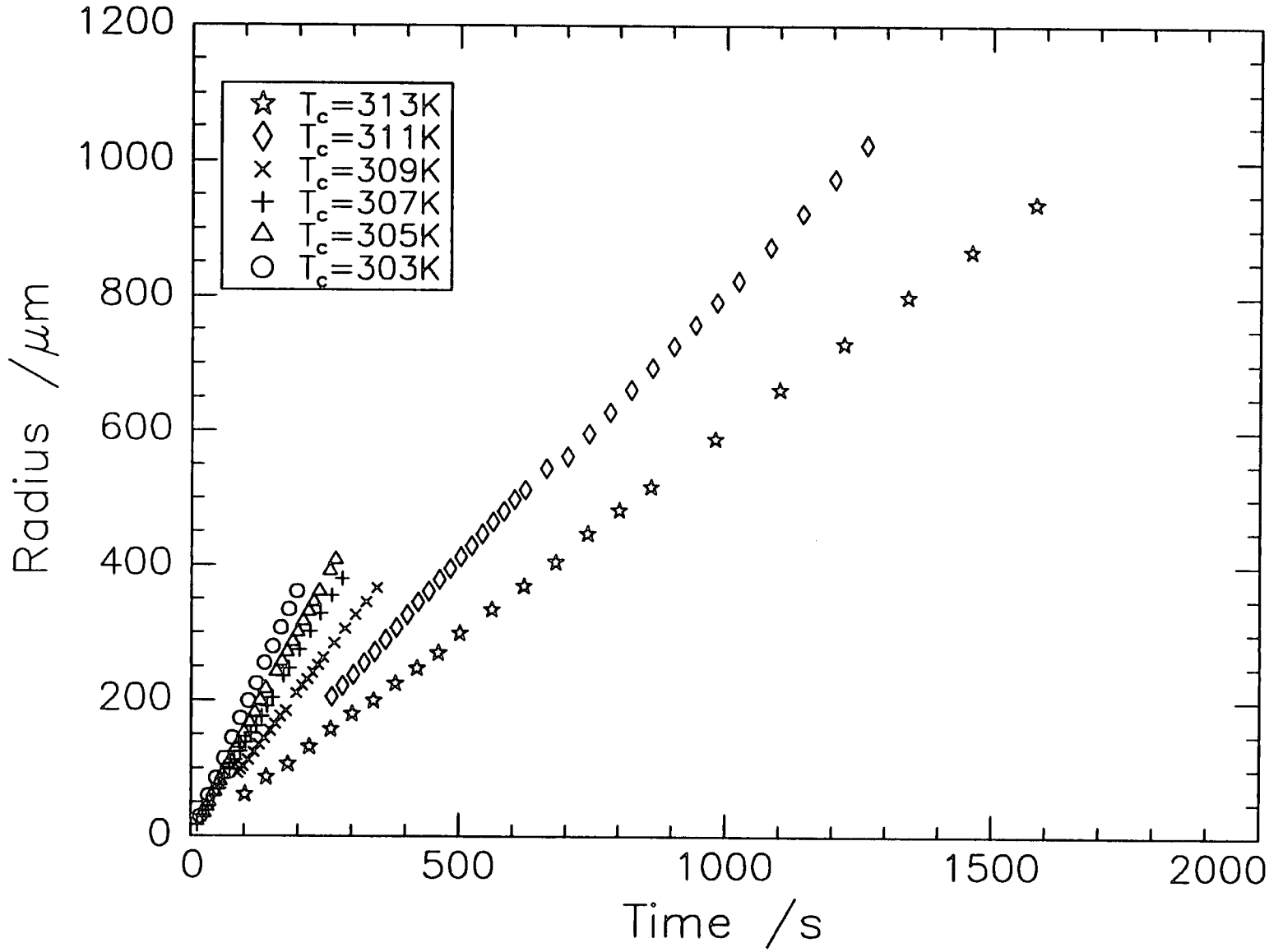

Figure 5.4. Spherulitic Radius vs. Time at various Crystallisation Temperatures for BC76.

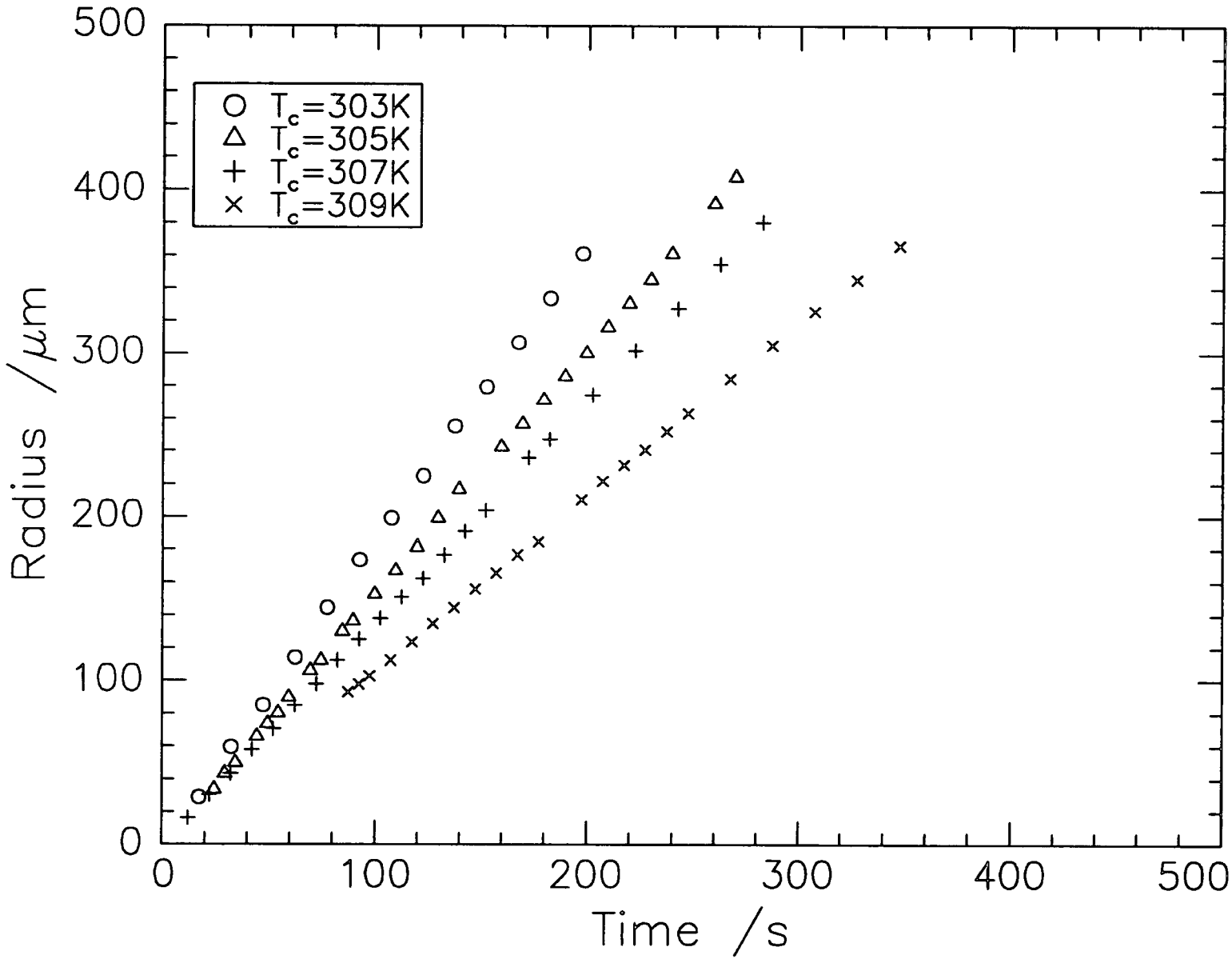

The spherulitic growth rate, G, was determined from the gradient of the spherulitic radius, R vs. t. Figure 5.5 shows the spherulitic growth rate, G, against crystallisation temperature for BC76 and a series of blends. Table 5.1 and table 5.2 list the values of calculated G (2% error) and the observed apparent melting point, T_m' (±0.05), for each T_c for BC76, the blends and PEO.

	T_c (K)	T_m' (K)	Log K_n	n	G (μm min^{-1})
PEO-b-PMMA (76/24) BC76	315	328.9	-7.15	2.34	16.1
	313	328.5	-6.36	2.24	35.7
	311	328.1	-6.88	2.27	48.5
	309	327.05	-5.98	2.44	62.4
	307	326.9	-5.23	2.21	77.4
	305	326.75	-4.87	2.19	92.6
	303	326.75	-4.67	2.21	111.8
	301	326.75	-3.87	2.10	143.5
	299	326.8	-3.85	2.37	170.9
	297	326.95	-3.37	2.34	198.0
	295	327.0	-3.45	2.38	210.7
	293	327.0	-2.76	2.24	235.7
	291	327.0	-2.70	2.33	248.5
	289	327.0	-2.61	2.39	270.3

Table 5.1. Observed Melting Points, Spherulitic Growth Rates and Evaluated Avrami Parameters for BC76.

Figure 5.5. Spherulitic Growth Rate, G, vs. Crystallisation Temperature, Tc.

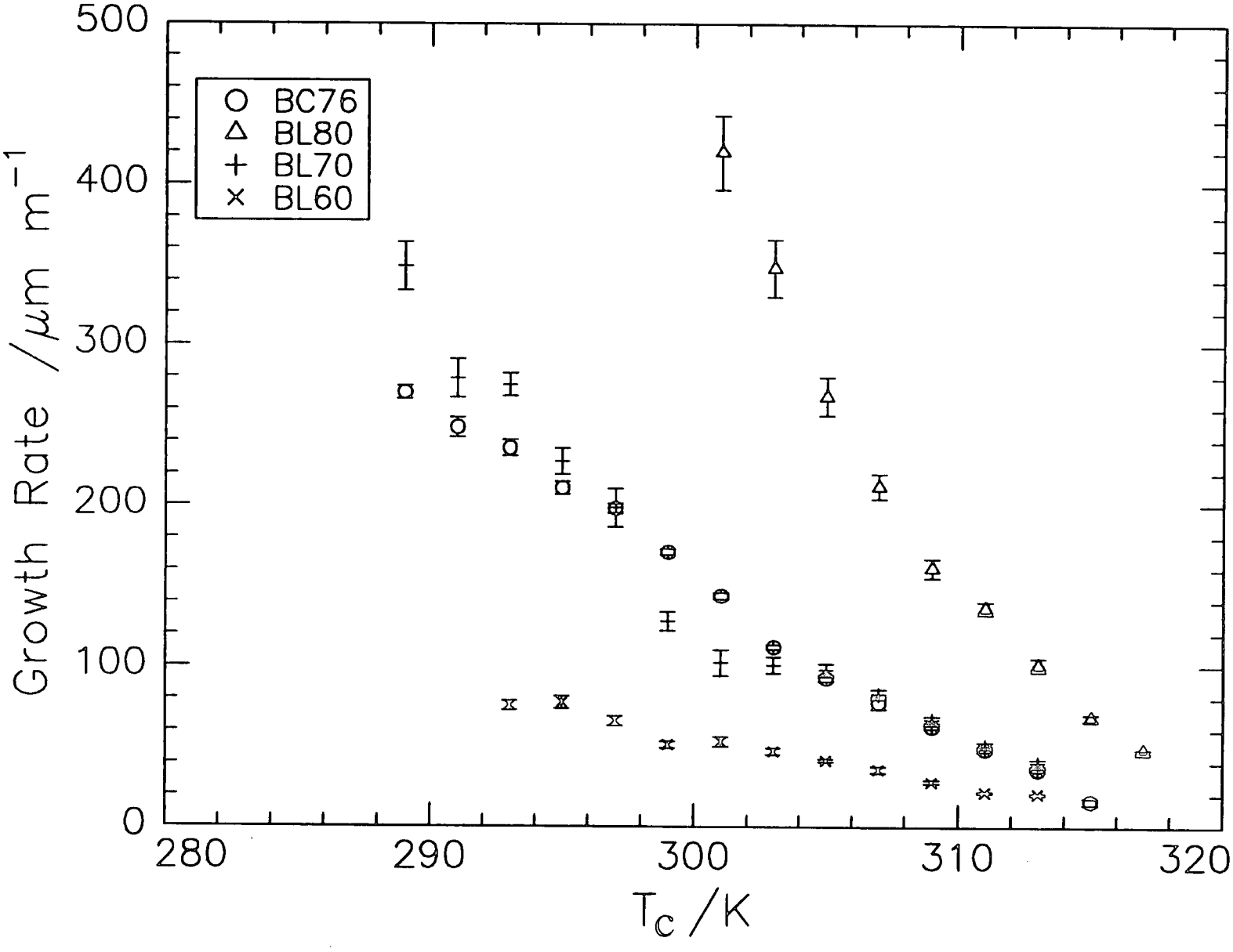

	T_c (K)	T_m' (K)	Log K_n	n	G ($\mu m\, min^{-1}$)
PEO	323	333.85	-	-	-
	321	333.7	-5.09	2.39	122.3
	319	332.1	-3.80	2.30	374
	317	331.6	-2.88	2.11	891
	315	331.2	-2.55	2.28	1,480
	313	331.1	-	-	2,120
	311	331.05	-	-	2,670
	309	330.9	-	-	3,170
PEO/PMMA (90/10)BL90	315	328.95	-4.64	2.14	103
	313	329.9	-4.87	2.37	232
	311	328.4	-3.99	2.21	268
	309	328.55	-3.77	2.44	336
	307	328.6	-3.39	2.22	494
	305	328.2	-3.09	2.24	640
	303	328.7	-3.05	2.22	600
	301	328.3	-2.72	2.44	807
PEO/PMMA (80/20)BL80	317	330.5	-6.03	2.40	47.6
	315	330.05	-5.44	2.30	68.1
	313	330.4	-5.01	2.57	101.2
	311	330.15	-4.42	2.26	136
	309	328.8	-4.32	2.16	161
	307	328.5	-3.71	2.18	212
	305	328.35	-2.77	1.83	268
	303	327.95	-2.88	2.33	348
	301	327.6	-2.70	2.43	420

Table 5.2.a). Observed Melting Points, Spherulitic Growth Rates and Evaluated Avrami Parameters for PEO, BL90 and BL80.

Error term n = ±0.2

PEO/PMMA (70/30)BL70	313	329.9	-5.75	2.16	40.2
	311	329.85	-5.55	2.10	50.7
	309	329.7	-5.10	2.07	66.8
	307	329.75	-4.72	2.01	82.8
	305	329.4	-4.35	2.00	97.9
	303	329.3	-4.69	2.14	100.7
	301	329.5	-4.29	2.29	102.2
	299	329.25	-4.26	2.28	128
	297	328.45	-3.39	2.04	198
	295	328.85	-3.87	2.44	227
	293	328.55	-3.02	2.25	275
	291	328.5	-2.99	2.07	279
	289	328.5	-2.77	2.15	349
PEO/PMMA (60/40)BL60	313	327.45	-6.55	2.21	20.6
	311	327.3	-6.08	2.35	21.5
	309	326.6	-5.46	2.26	28.1
	307	326.8	-5.15	2.13	35.7
	305	326.9	-4.99	2.25	41.5
	303	326.65	-5.32	2.21	47.0
	301	326.5	-4.63	2.26	53.1
	299	327.0	-4.96	2.46	51.0
	297	327.3	-4.38	2.23	65.8
	295	327.7	-4.51	2.44	77.4
	293	327.8	-4.37	2.41	75.6
	291	329.3	-5.74	2.39	22.9
	289	329.9	-5.34	2.05	17.5

Table 5.2.b). Observed Melting Points, Spherulitic Growth Rates and Evaluated Avrami Parameters for BL70 and BL60.

Figure 5.6. Hoffman/Weeks plot to evaluate the Equilibrium Melting Point Temperature, T_m^o.

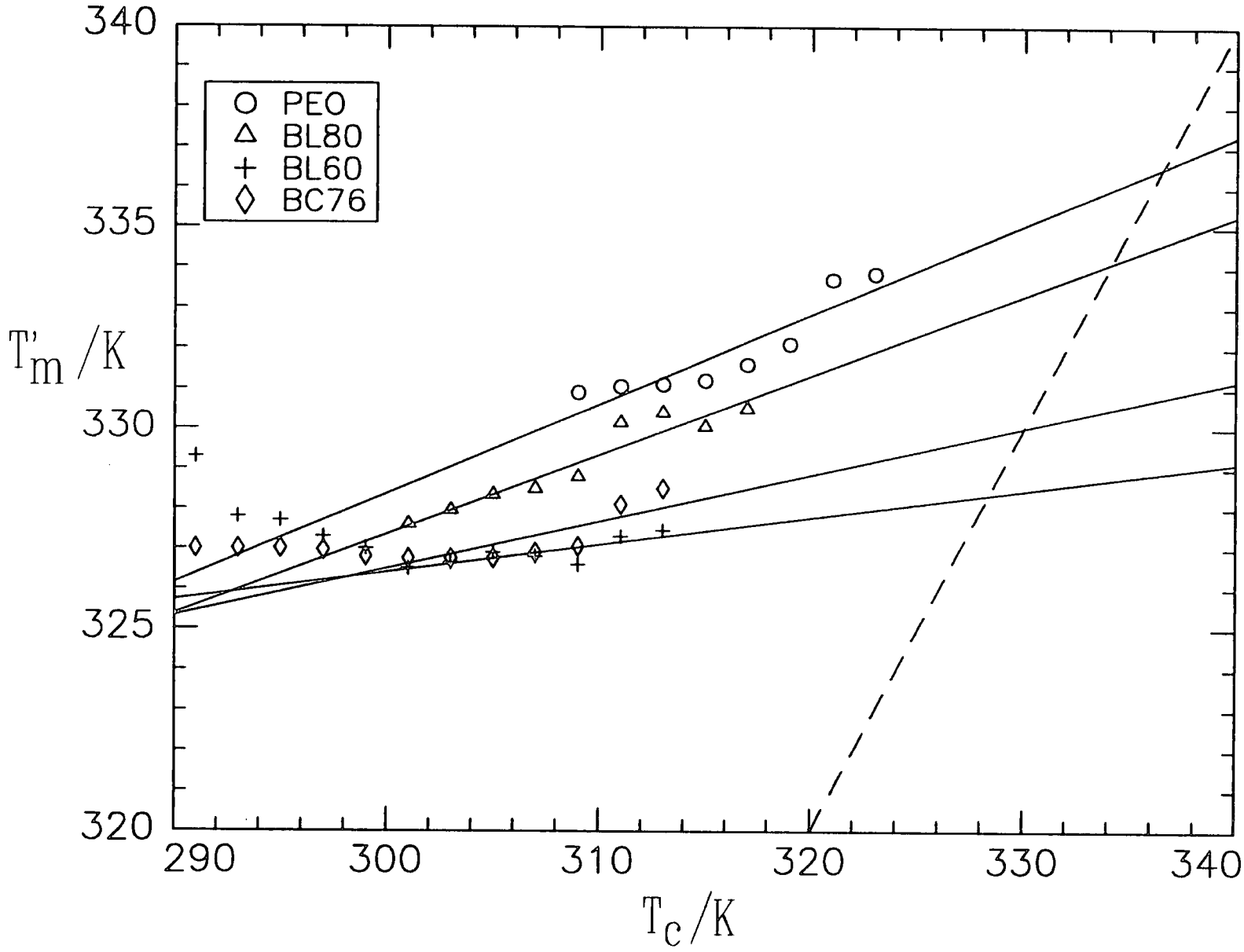

5.5. Analysis and Discussion.

5.5.1. Melting Point Depression.

As noted earlier, the apparent melting point temperature decreases as the amount of diluent (PMMA) increases. This melting point depression was analysed by first evaluating the equilibrium melting point temperature, T_m^o using a Hoffman/Weeks plot,[3] figure 5.6.

The equilibrium melting point temperatures for each polymer system were evaluated by extrapolating the observed T_m' values to the line $T_m'=T_c$ (see table 5.3). As noted by Runt and Gallagher,[4] the determined T_m^o may be strongly dependent upon kinetic and morphological factors. It was anticipated that these effects were minimised by quenching the polymer to the desired crystallisation temperature, allowing the polymer to fully crystallise (60 minutes at T_c) and scanning at a constant rate. It is interesting to note that there is a decrease in the gradient of the Hoffman/Weeks plots in figure 5.6. as the concentration of the PMMA component increases. Since the magnitude of the gradient is related to a morphological factor,[14] then this variation reflects the change in crystalline spherulitic morphology as observed through crossed polars using optical microscopy (see figure 5.2.).

Sample	Equilibrium Melting Point, T_m^o (K)
PEO	336.5
PEO/PMMA (90/10) BL90	332.6
PEO/PMMA (80/20) BL80	333.4
PEO/PMMA (70/30) BL70	331.4
PEO/PMMA (60/40) BL60	328.5
PEO-b-PMMA (76/24) BC76	330.8

Table 5.3,. Equilibrium Melting Points for PEO, BC76 and the Blends.

As described in chapter 4 (section 4.4.2.2.), the Flory-Huggins interaction parameter,[5,6] χ at T_m^o can be evaluated form equations 5.1 and 5.2 by plotting $(1/T_m^o - 1/T_{m,PEO}^o)$ vs. v_1^2 (PMMA is component 1), see figure 5.7.

$$\left[\frac{1}{T_m^{\,o}} - \frac{1}{T_m^{\,o},_{PEO}}\right] = \frac{-V_{2\mu}}{\Delta H_{2\mu}}\left[\left(\frac{B v_1^{\,2}}{R T_m^{\,o}}\right)\right] \qquad (5.1)$$

$$\chi = \frac{B V_{1\mu}}{R T_m^{\,o}} \qquad (5.2)$$

From the gradient of figure 5.7, B was found to be -17.1 Jcm^{-3} from which a value of -0.52 was calculated for χ at the equilibrium temperature of 336.5K. This value implies a miscible system at temperatures close to the melting point temperature. Similar behaviour for PEO/PMMA blends has been reported elsewhere, see chapter 2.

It is interesting to note the unusual T_m' behaviour for BL60 at low crystallisation temperatures. Here, T_m' undergoes a relatively large increase and continues to increase as T_c decreases, see figure 5.8. The higher T_m' values at lower T_c suggests the presence of additional phase behaviour. A higher T_m' reflects a more ordered and/or thicker lamellar crystalline regions. This leads on to the possible explanation that the polymer blend, BL60, has undergone an upper critical solution temperature (UCST) phase transition (see 1.1.3.) at these low crystallisation temperatures, increasing the local concentration of PEO prior to crystallisation.

As reported in chapter 2, similar observations have been noted elsewhere. For PMMA (M_w=110K)/ PEO (M_w = 20K) blends, Martuscelli[7] observed non-linear T_m' depression at low crystallisation temperatures and attributed this to liquid-liquid type phase separation which he incorrectly attributed to lower critical solution temperature (LCST) behaviour. Similar non-linear observations for plots of T_m' versus volume

Figure 5.7. Nishi-Wang plot to Evaluate the Flory-Huggins interaction parameter for PEO/PMMA Blends.

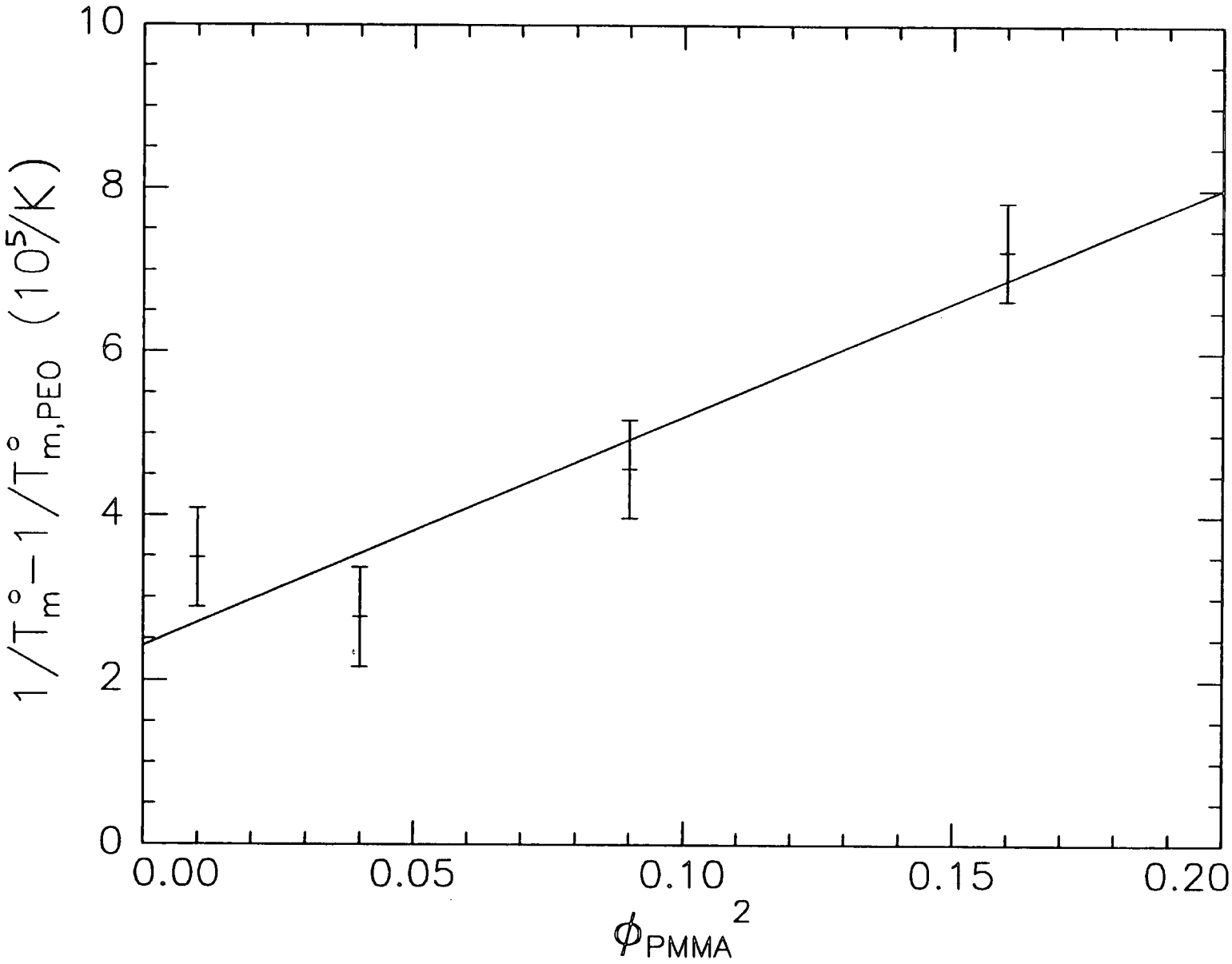

Figure 5.8. Apparent Melting Point Temperature, T'_m vs. Crystallisation Temperature for BL60.

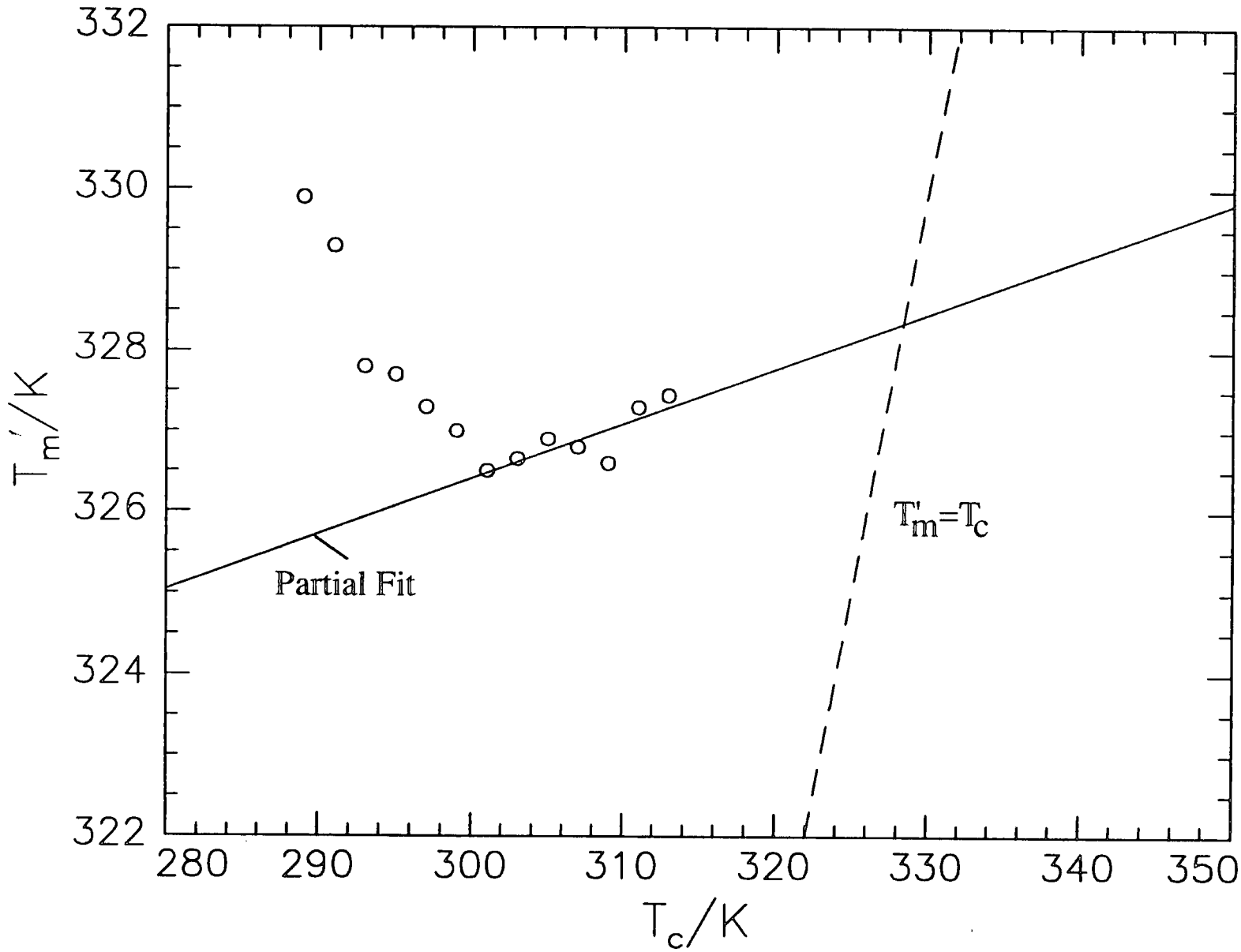

fraction of the non-crystallisable component have been reported for blends of isotactic polypropylene with polyisobutylene and ethylene-propylene-diene terpolymers.[8] Thus, based on the conclusions reached in chapter 2, it is reasonable to believe that liquid-liquid phase separation takes place in competition with crystallisation for blends containing intermediate percentages of PEO at these low crystallisation temperatures. This proposed phase behaviour has a dramatic effect on the observed melting point temperature. This conclusion is supported by work by Li and Hsu[9] who suggested UCST type phase separation to explain the observation of two glass transition temperatures for compositions containing PEO concentrations of ≤50%, and by Calahorra et al[10] who observed a complicated growth pattern for PEO/PMMA blends containing 60% PEO.

5.5.2. Growth Rates and Morphology.

The isothermal crystallisation behaviour of the blends was found to be very similar to that previously investigated, see chapter 2. The observed linear growth rate with time implies that the concentration of PMMA at the tips of the radial lamellae does not change. It has been suggested that this implies that the rejected non-crystallisable PMMA is trapped between the growing fibrils of the spherulite. This suggestion is supported by the observation of less regular, more feather-like morphology as the amount of PMMA in the blend is increased, figure 5.2. For high crystallisation temperatures, at very long times of isothermal crystallisation, this linear growth rate decreases due to the growth, becoming more dependent on the amount of locally available PEO and consequently, dependent upon the diffusion of the crystallisable PEO fraction[11] to the crystallisation site. Crystal growth is now under a concentration gradient formed near the growth front due to segregation of the diluent and can be interpreted in terms of the Cahn theory.[12]

There is no distinct difference in the crystalline morphologies of the block copolymer and the corresponding blend. However, the rate of crystallisation of the block copolymer is considerably reduced (3-4 fold decrease in G at a specific T_c for

BC76 with respect to BL80, figure 5.5) and the melting point is reduced (approximately 2-3K). Donth et al[13] have shown the necessity for mobile free crystallisable ends during crystallisation. This approach can be applied here to explain the dramatic reduction in the rate of crystallisation of BC76 which has only one free mobile chain end.

In comparison to work carried out by Martuscelli et al[14] on higher molecular weight blends of PEO/PMMA, the spherulitic growth rates determined here are systematically higher for these lower molecular weight systems. It is worth noting that the crystallisation temperatures studied in this paper are appreciably lower than those in previous studies.[7,10,14-17]

5.5.3. Avrami Analysis of the Isothermal Crystallisation of BC76 and the Blends.

The isothermal crystallisation process was analysed on the basis of the JMA equation (see 1.1.3.3.):

$$X(t) = 1 - \exp(-K_n t^n) \qquad (5.3)$$

where X(t) is a property of the system which changes linearly with the degree of transformation accompanied with the crystallisation process (e.g., X could be related to the spherulitic radius or scattered depolarised light intensity), K_n contains several constants and is related to the rate of crystallisation, t is the transformation time at the crystallisation temperature and n is the JMA exponent.

Here X(t) was calculated using the following expression and is related to the volume of crystallised material:

$$1 - X(t) = \frac{\left[R_\infty^2 - R_t^2\right]}{\left[R_\infty^2 - R_0^2\right]} \qquad (5.4)$$

where R(t) is the spherulitic radius at time t, R_0 is the size of the spherulitic radius at time=0 (the instant Tc is reached) and R_∞ is the maximum spherulitic radius before truncation. The volume of a disk, and so X(t) (see equation 5.4) is proportional to the square of the disk radius, multiplied by its thickness. Since the radius of the spherulite is much greater than the film thickness, the disk thickness is assumed to be constant. For each spherulite measured, the times t were stet so that t=0 once the spherulite was nucleated i.e. at R=0. This shift in the values of t, is equivalent to the instantaneous crystallisation of each spherulite, contrary to experimentally observation of sporadic nucleation. By using this artificial instantaneous crystallisation, the evaluated JMA exponent, n, no longer depended upon any contribution from the 'type of nucleation'.[18] Consequently, for this analysis, n is dependent upon just two factors (see Table 5.4).

Exponent	Growth Geometry	Growth Control
1/2	Rod	Diffusion
1	Rod	Interface
1	Disc	Diffusion
1 1/2	Sphere	Diffusion
2	Disc	Interface
3	Sphere	Interface

Table 5.4. JMA Exponents and their Interpretation for Optical Microscopy.

Diffusion controlled: The kinetics are controlled by the rate of diffusion of macromolecules to the nuclei.

Interface controlled: The kinetics are controlled by the rate of attachment of macromolecules to the nuclei.

Figures 5.9.-5.13 plots 1-X(t) in the form suggested by the Avrami analysis for a series of crystallisation temperatures for BC76 and the blends: BL90, BL80, BL70 and BL60, respectively.

Tables 5.1 and 5.2 list the Avrami exponents and rates of crystallisation ($LogK_n$) evaluated for BC76, PEO and the blends respectively. A large uncertainty in the value of the JMA exponent exists since a small change in the slope of the Avrami plot results in a relatively large change in n. The error for each Avrami exponent was 0.2. An additional feature of this Avrami analysis is that at long times the data tend to fall away from the initial linear dependence owing to the enhancement of error as R_t approaches R_∞.

There is no distinct difference between the block copolymer and the blends in the average value of the JMA exponent. For BC76, $n = 2.2 \pm 0.2$ and for the blends, $n = 2.2 \pm 0.2$. These exponents suggest, within experimental error and the limits of this analysis, that the isothermal crystallisation process has a disc growth geometry and the initial stage of crystallisation is kinetically controlled by the rate of attachment of crystallisable units to the crystalline interface, see table 5.4. The deviation away from the integer value may reflect a less perfect geometry. Within the limits of this analysis, no variation in n with PMMA concentration or crystallisation temperature was observed.

Analogous to the spherulitic growth rates, the isothermal crystallisation rate constant determined for BC76 was appreciably smaller than that for the corresponding blend for a particular crystallisation temperature, and also decreased as T_c decreased. (see figure 5.14). The rate constant for the blends decreases markedly as PMMA content increases (see figure 5.15.) owing to an increase in viscosity (higher T_g), plus a decrease in the number of nuclei present and the interaction between the PEO and PMMA chains,[19] have been cited as cases for this decreased rate. This is in agreement with thermodynamic considerations of compatible blends, where both the nucleation and crystallisation growth rates are reduced by the presence of a non-crystallisable component.[19] The kinetic rate constant, K_n, contains several constants and

Figure 5.9. Avrami Analysis for BC76.

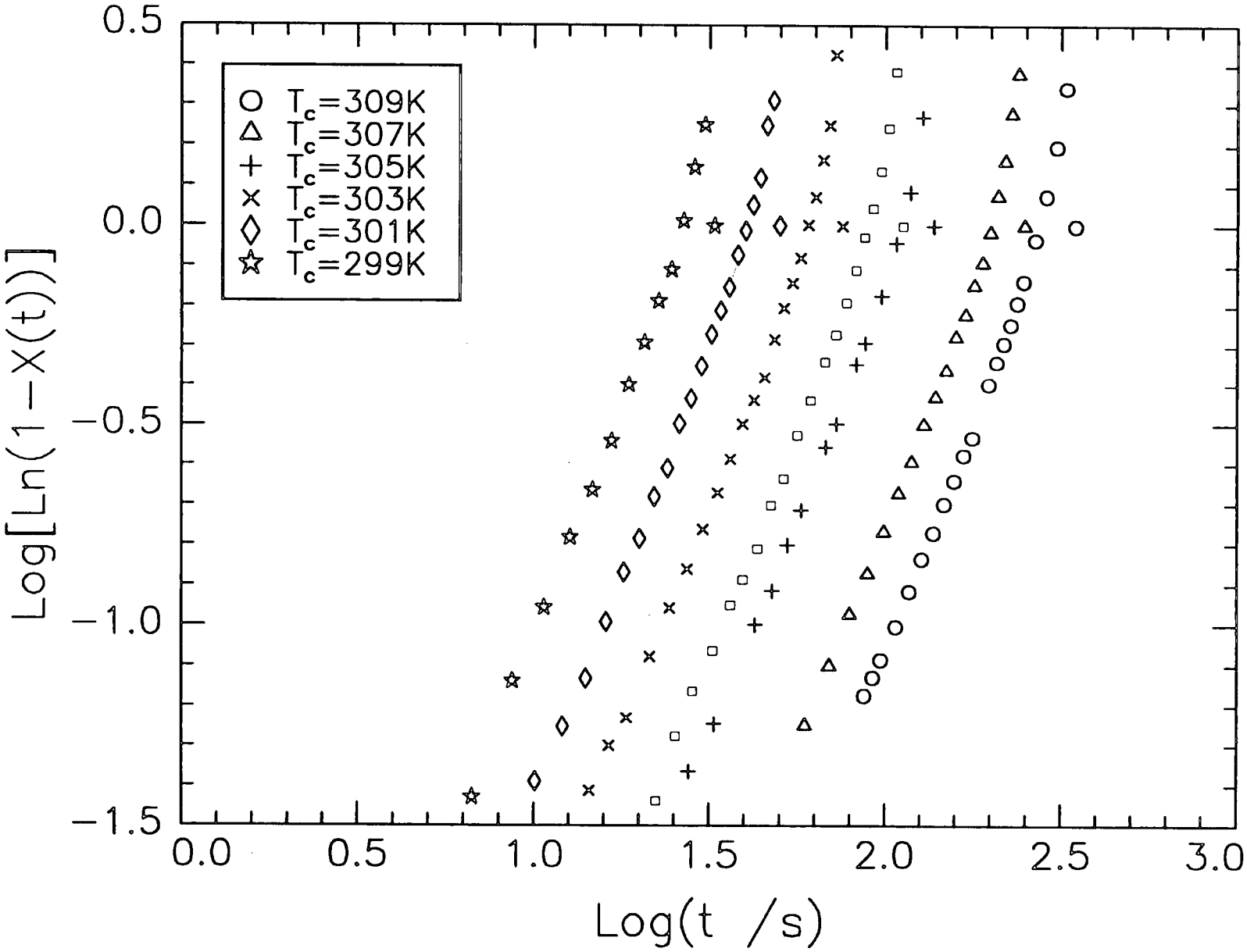

Figure 5.10. Avrami Analysis for BL90.

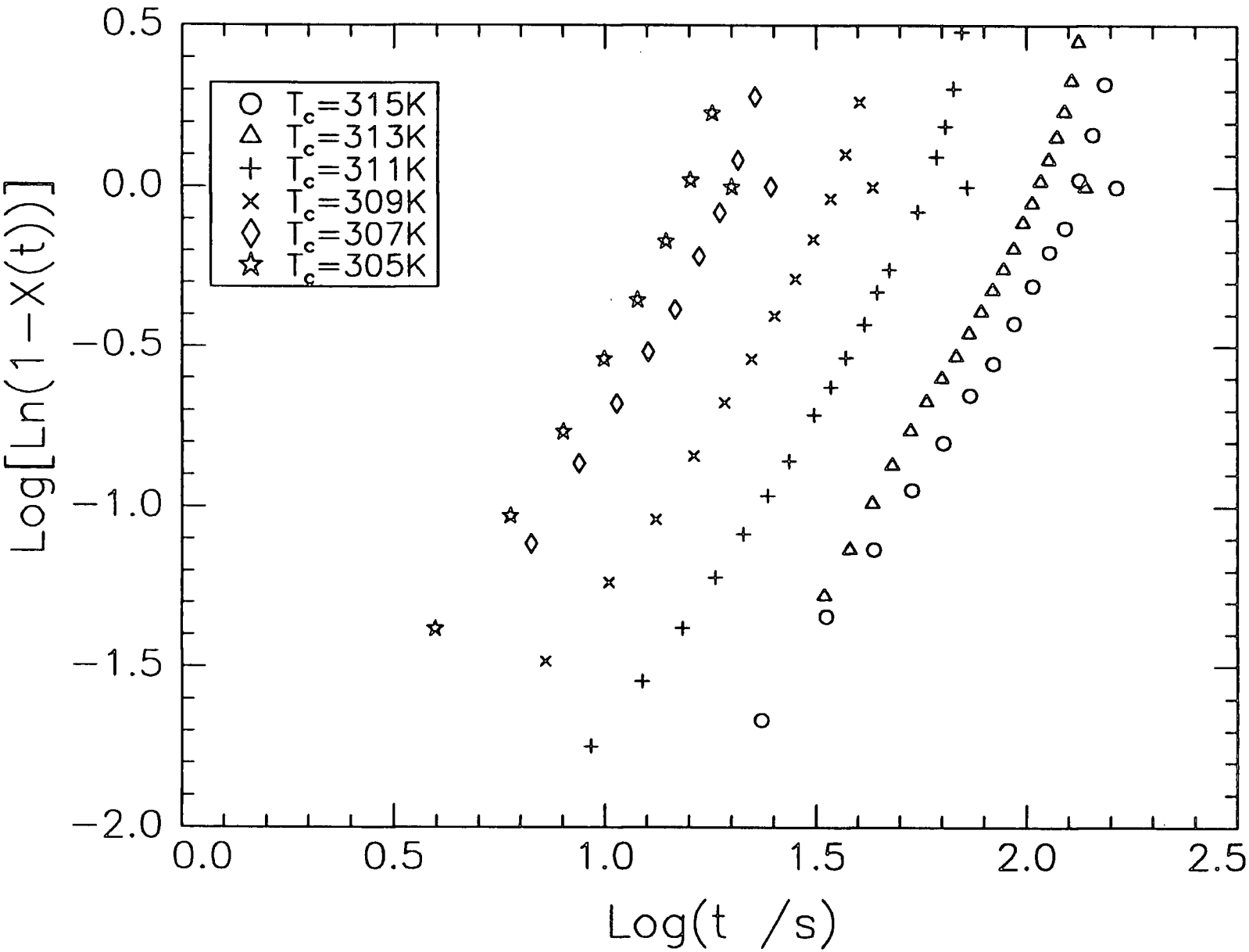

Figure 5.11. Avrami Analysis for BL80.

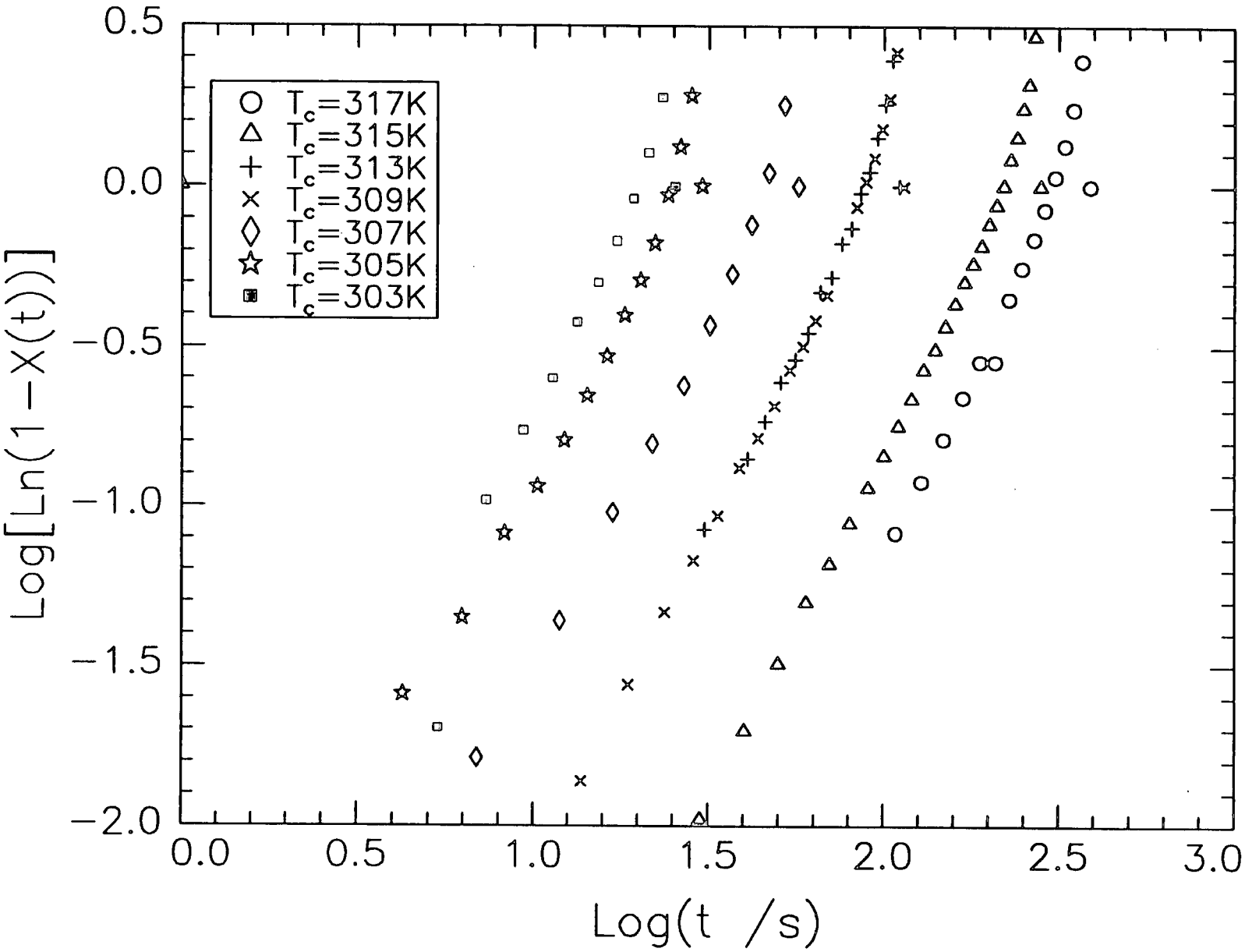

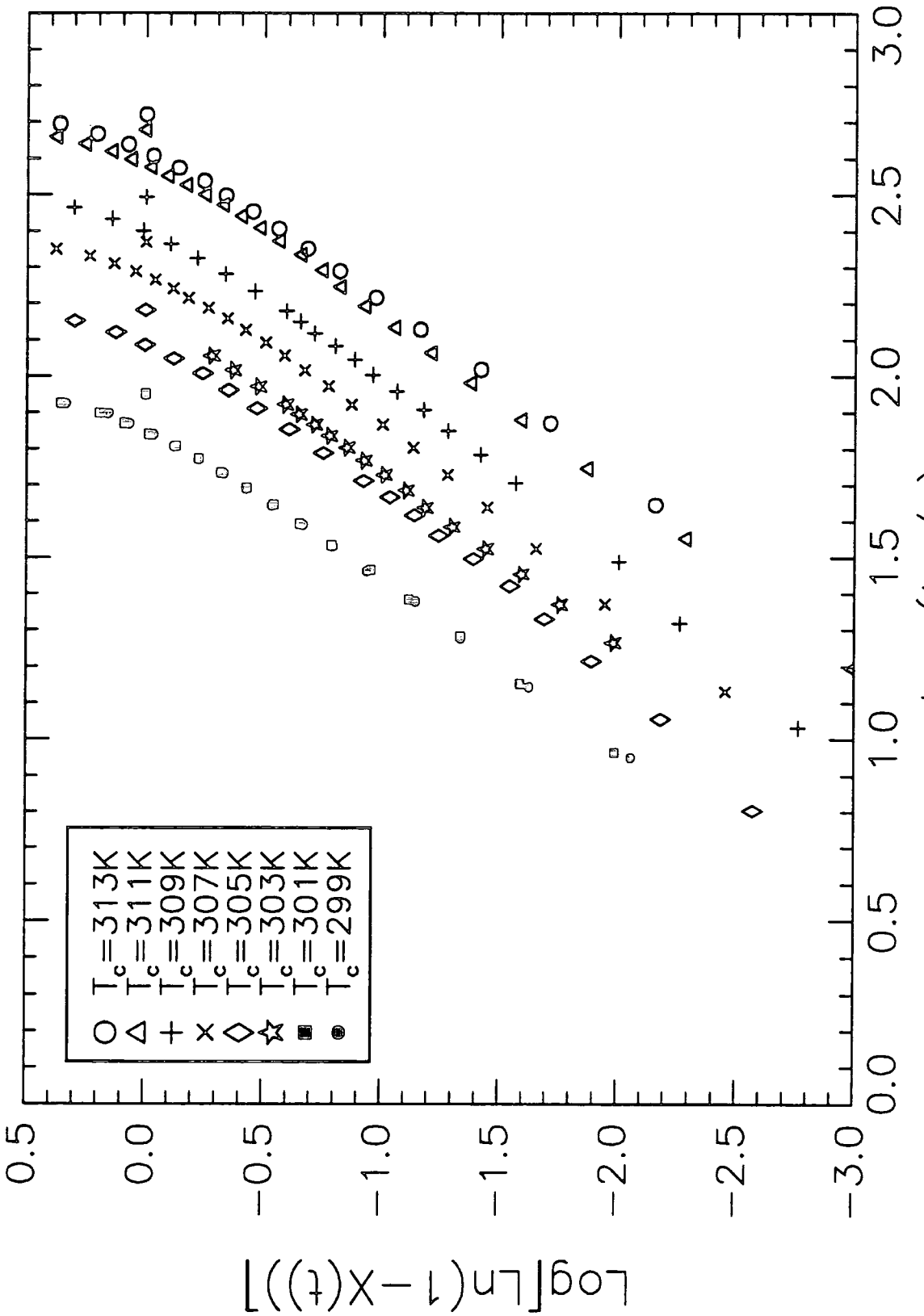

Figure 5.12. Avrami Analysis for BL70.

Figure 5.13. Avrami Analysis for BL60.

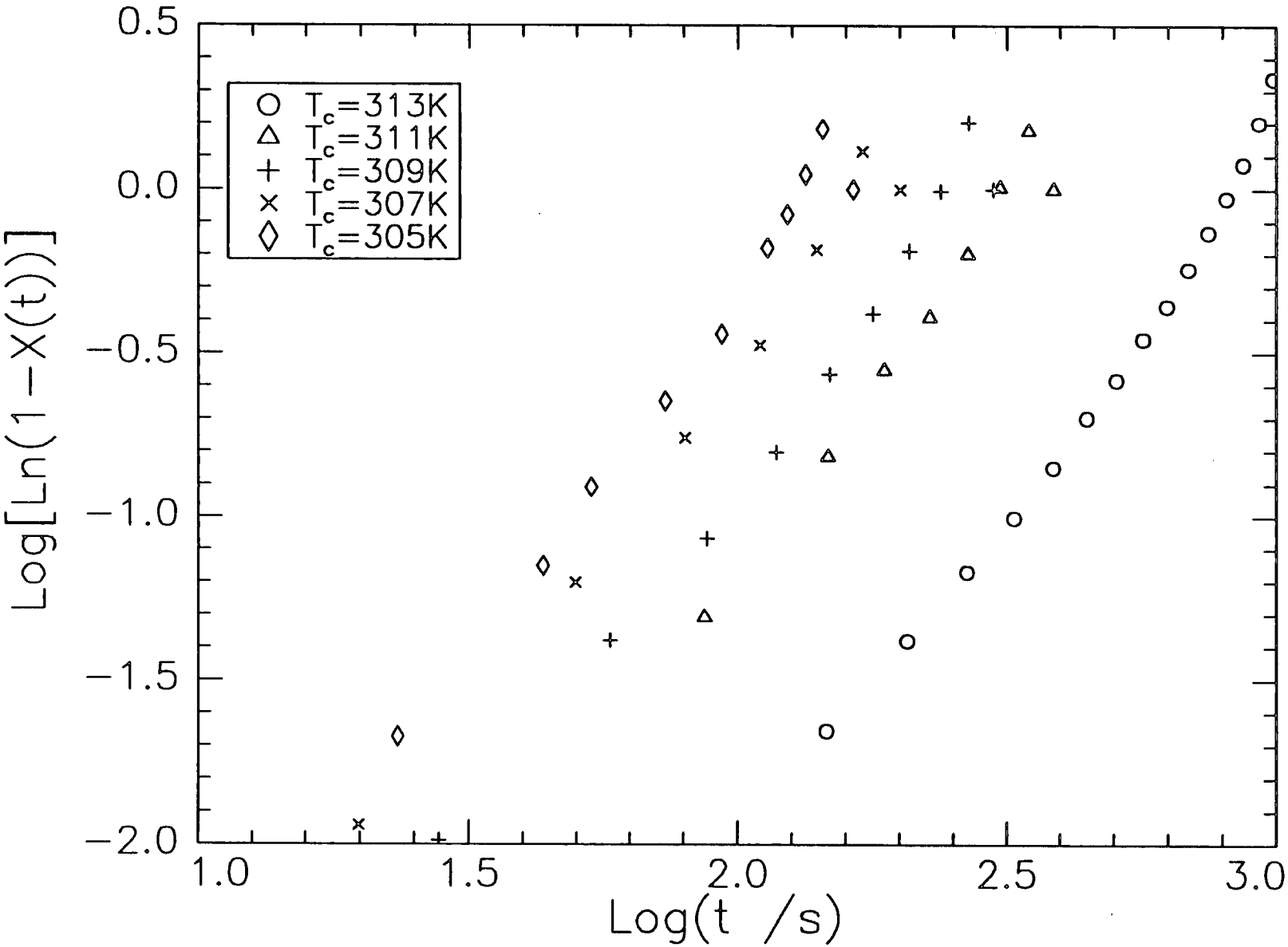

Figure 5.14. Log Kn vs. Tc for BC76 and BL80.

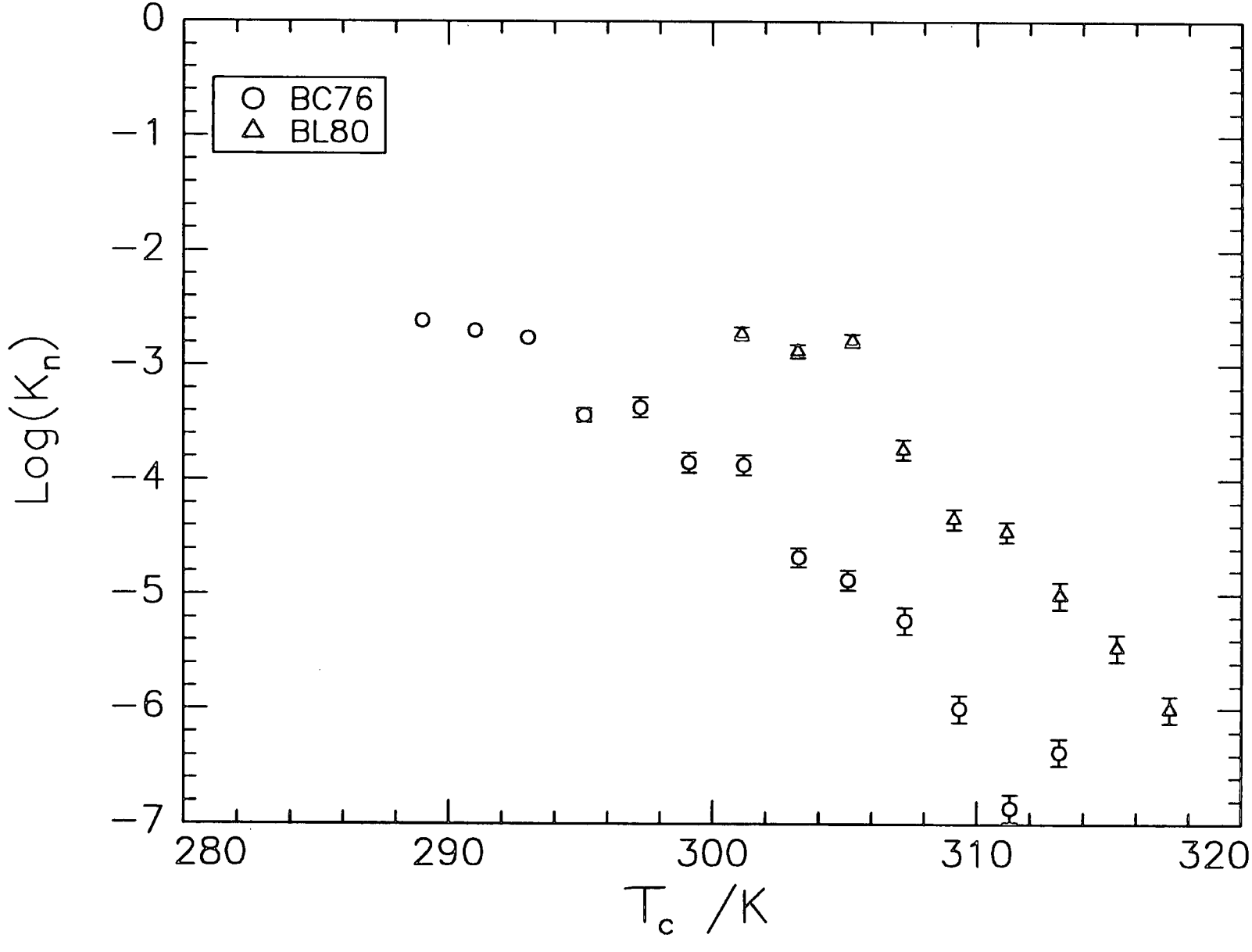

Figure 5.15. Log Kn vs. Crystallisation Temperature for PEO, the Blends and BC76.

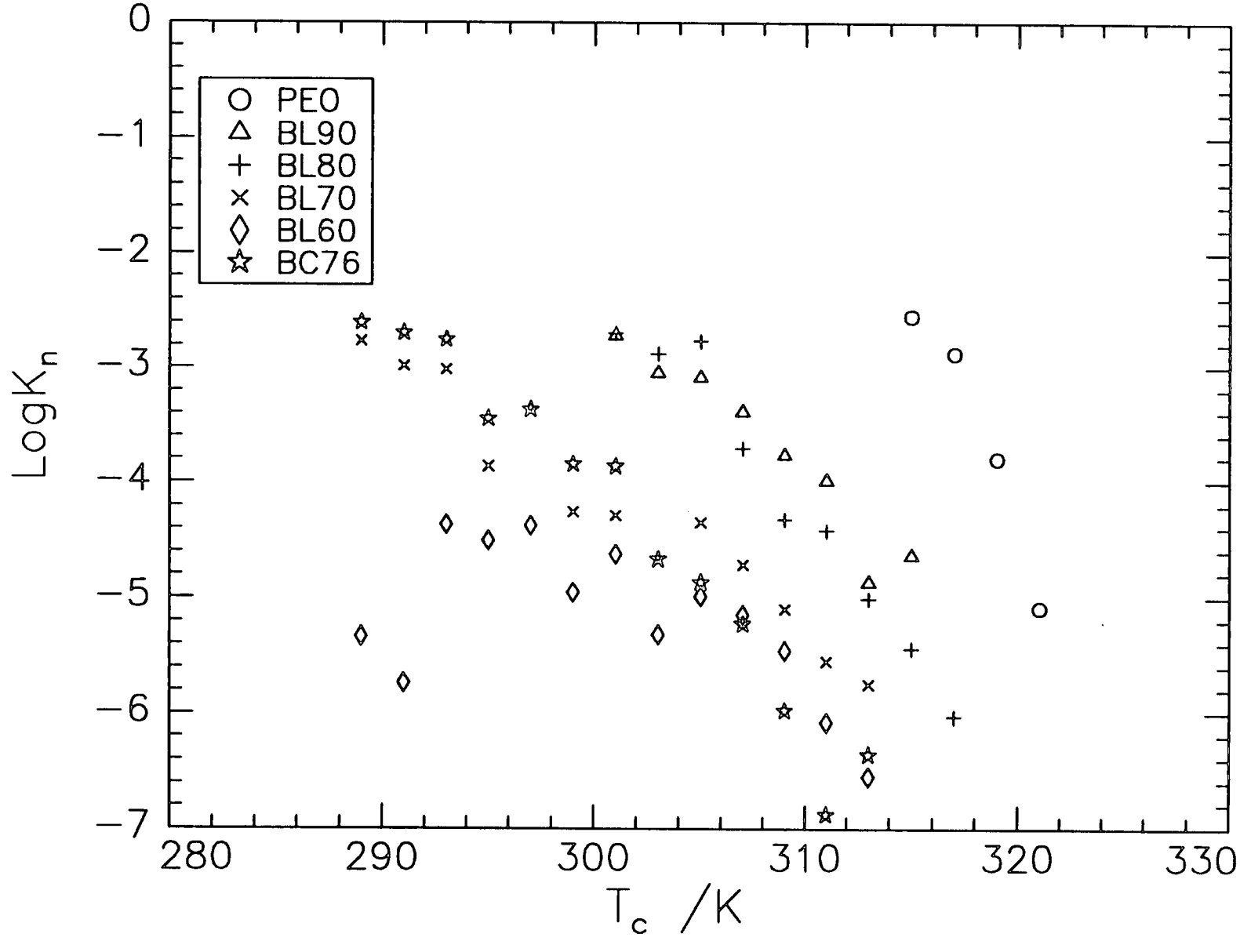

parameters. The number and type of these parameters which contribute to K_n depends upon the value of the JMA exponent.[20]

5.5.4. Evaluation of the Lateral Surface Free Energy of a Crystallite, σ_e.

The lateral surface free energy of a crystallite, σ_e, for BC76 and the blends has been evaluated by the following method. Assuming that crystallisation is by a single mechanism, the polymer crystal growth rates, G, can be described in terms of the classical rate equation[21]:

$$G = v_2 G_0 \exp\left[\frac{-\Delta\varphi^*}{kT_c}\right]\exp\left[\frac{-\Delta F^*}{kT_c}\right] \qquad (5.5)$$

where k is Boltzmann's constant, $\Delta\varphi^*$ is the free energy required to form a critical sized nucleus from the melt, ΔF^* is the activation energy for transport of crystallising units across the melt crystal interface, and G_0 is a constant for low values of ΔT (T_m-T_c). The pre-exponential factor, G_0, is multiplied by the PEO volume fraction v_2, because the rate of nucleation is proportional to the concentration of crystallisable units. ΔF^* can be estimated from the William-Landel-Ferry[22] expression for the temperature dependence of viscosity, from which equation 5.6 was derived[23]:

$$\Delta F^* = \frac{C_1 T_c}{C_2 + T_c - T_g} \qquad (5.6)$$

where C_1 and C_2 are constants for PEO (17,238J mol^{-1} and 51.6K respectively)[24,25] and T_g is the glass transition temperature of the blend or block copolymer. A single T_g was observed for PEO concentrations below 40% w/w where the PEO crystallisation exotherm did not inhibit the observation of the T_g using DSC (see chapter 4). These

values were intermediate between those of the pure components and agreed well with calculated values obtained from the Fox equation.[31] Consequently, for BC76 and for the blends with higher PEO content, the T_g used was calculated from the Fox equation.

For polymer-diluent mixtures, an additional term must be included $\Delta\varphi^*$ to obtain the free energy required to form a critical sized nucleus.[23] This additional term, containing $\ln(v_2)$, represents the probability of selecting the required number of crystalline sequences from a mixture with polymer volume fraction v_2. For a two-dimensional nucleus, $\Delta\varphi^*$ can be expressed as[23]:

$$\frac{\Delta\varphi^*}{kT} = \left[\frac{-4b_o\sigma_u\sigma_e T_m'}{kT\Delta h_{fus,v}(T_m' - T_c)}\right] + \left[\frac{2\sigma_u T_m' \ln(v_2)}{b_o\Delta h_{fus,v}(T_m' - T_c)}\right] \quad (5.7)$$

where σ_u and σ_e are the interfacial free energies per unit area parallel and perpendicular, respectively, to the molecular chain direction, b_0 is the thickness of a monomolecular layer, $\Delta h_{fus,v}$ is the heat of fusion per unit volume and T_m' is the melting point of the crystalline phase in the mixture.

The growth rate can then be expressed by the following equation[23,26]:

$$G = v_2 G_0 \exp\left[\frac{-17,238}{R(51.6 + T_c - T_g}\right] \times \exp\left[\left[\frac{-4b_o\sigma_u\sigma_e T_m'}{kT\Delta h_{fus,v}(T_m' - T_c)}\right] + \left[\frac{2\sigma_u T_m' \ln(v_2)}{b_o\Delta h_{fus,v}(T_m' - T_c)}\right]\right] \quad (5.8)$$

Rearranged:

$$\ln G - \ln(v_2) + \frac{17{,}238}{R(51.6 + T_c - T_g)} - \frac{2\sigma_u T_m' \ln(v_2)}{b_o \Delta h_{fus,v}(T_m' - T_c)} = \ln G_0 - \frac{4 b_o \sigma_u \sigma_e T_m'}{k T_c \Delta h_{fus,v}(T_m' - T_c)} \quad (5.9)$$

Hence by plotting α vs. $T_m'/T_c(T_m' - T_c)$ for BC76 and the blends, where

$$\alpha = \ln G - \ln(v_2) + \frac{17{,}238}{R(51.6 + T_c - T_g)} - \frac{2\sigma_u T_m' \ln(v_2)}{b_o \Delta h_{fus,v}(T_m' - T_c)} \quad (5.10)$$

linear fits were obtained as shown in figures 5.16. and 5.17. From the slope of these lines, the lateral surface free energy of a crystallite, was evaluated using the relations $\sigma_u = 0.1 b_o \Delta h_{fus,v}$[27] , $\Delta h_{fus,v} = 2.13 \times 10^2 Jcm^{-3}$,[28] and $b_o = 4.65 \times 10^{-8} cm$.[29]

Russell et al[30] have developed a new phenomenological theoretical treatment for G for the case of an amorphous/crystalline blend. This approach incorporates co-operative diffusion, crystalline lamellae thickness, free energy of secondary nuclei and the Flory-Huggins interaction parameter, χ, into a kinetic equation describing the spherulitic growth rate. Whereas this equation deals with these additional aspects which are important when describing G for an amorphous/crystalline blend, it has not been used for this analysis since it is dimensionally incorrect. Further work is required in this area.

In figure 5.18., the values of σ_e obtained by the 'classical' method are plotted against the volume fraction of PEO for BC76 and the PEO/PMMA blends. There is no distinct difference in the value of σ_e for BC76 with that of the corresponding blend. This suggests the chemical joint between PEO and PMMA at the crystal interface does not significantly extend the crystal/isotropic interphase. The lateral

Figure 5.16. Lateral Surface Free Energy determination for BC76, PEO and Bl80.

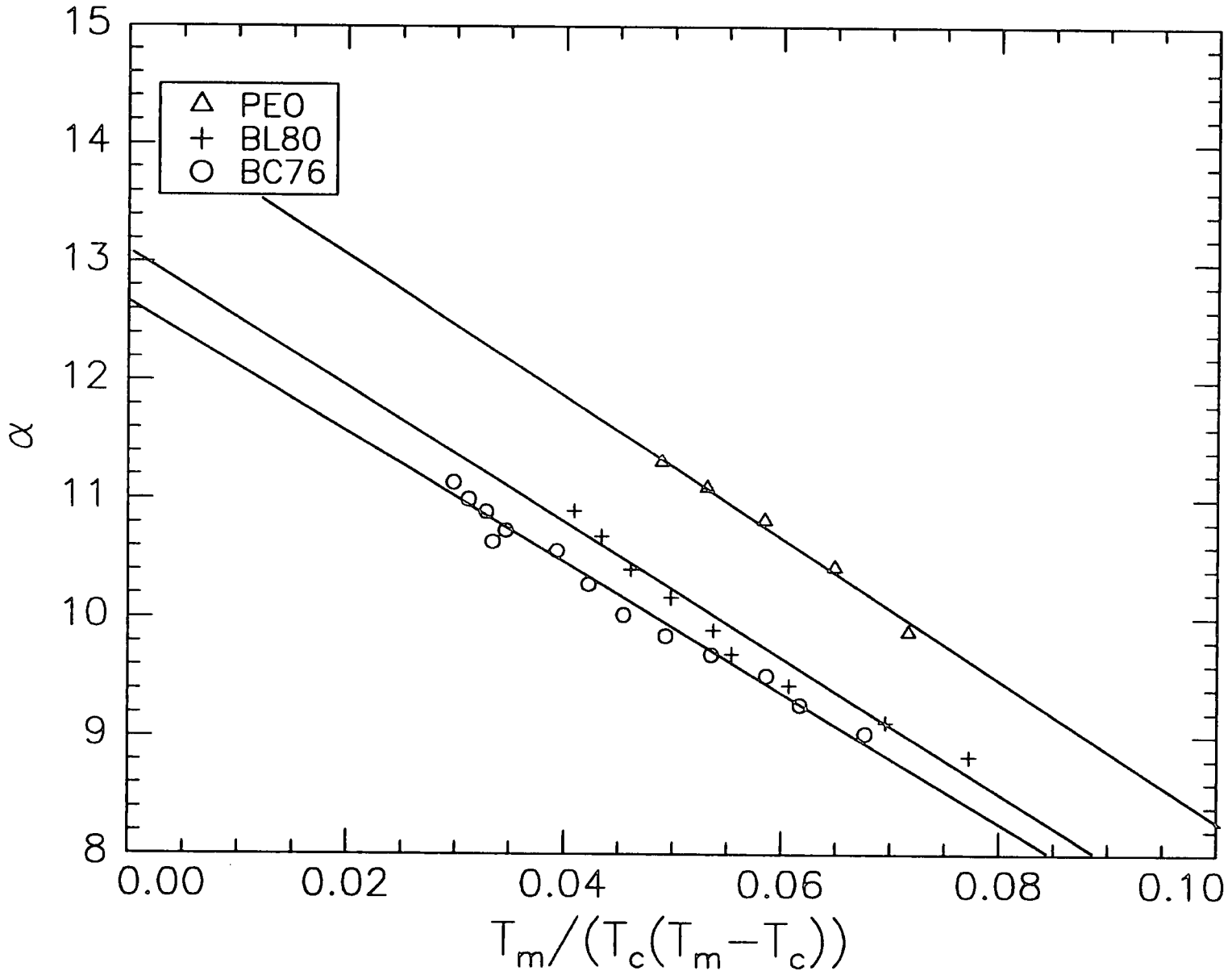

Figure 5.17. Lateral Surface Free Energy determination for BL90, BL70 and B160.

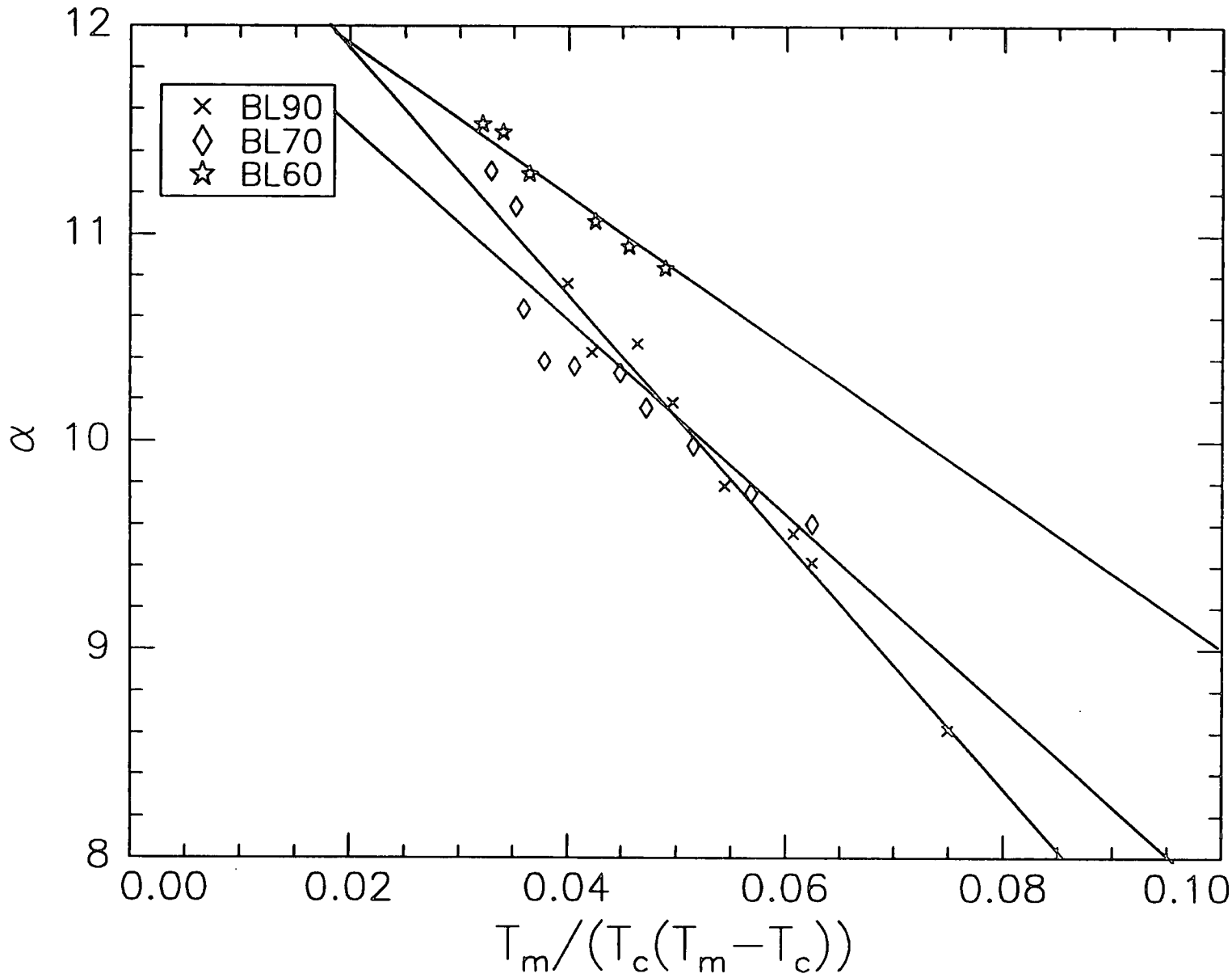

Figure 5.18. Lateral Surface Free Energy vs. Volume Fraction of PEO for PEO, BC76 and Blends.

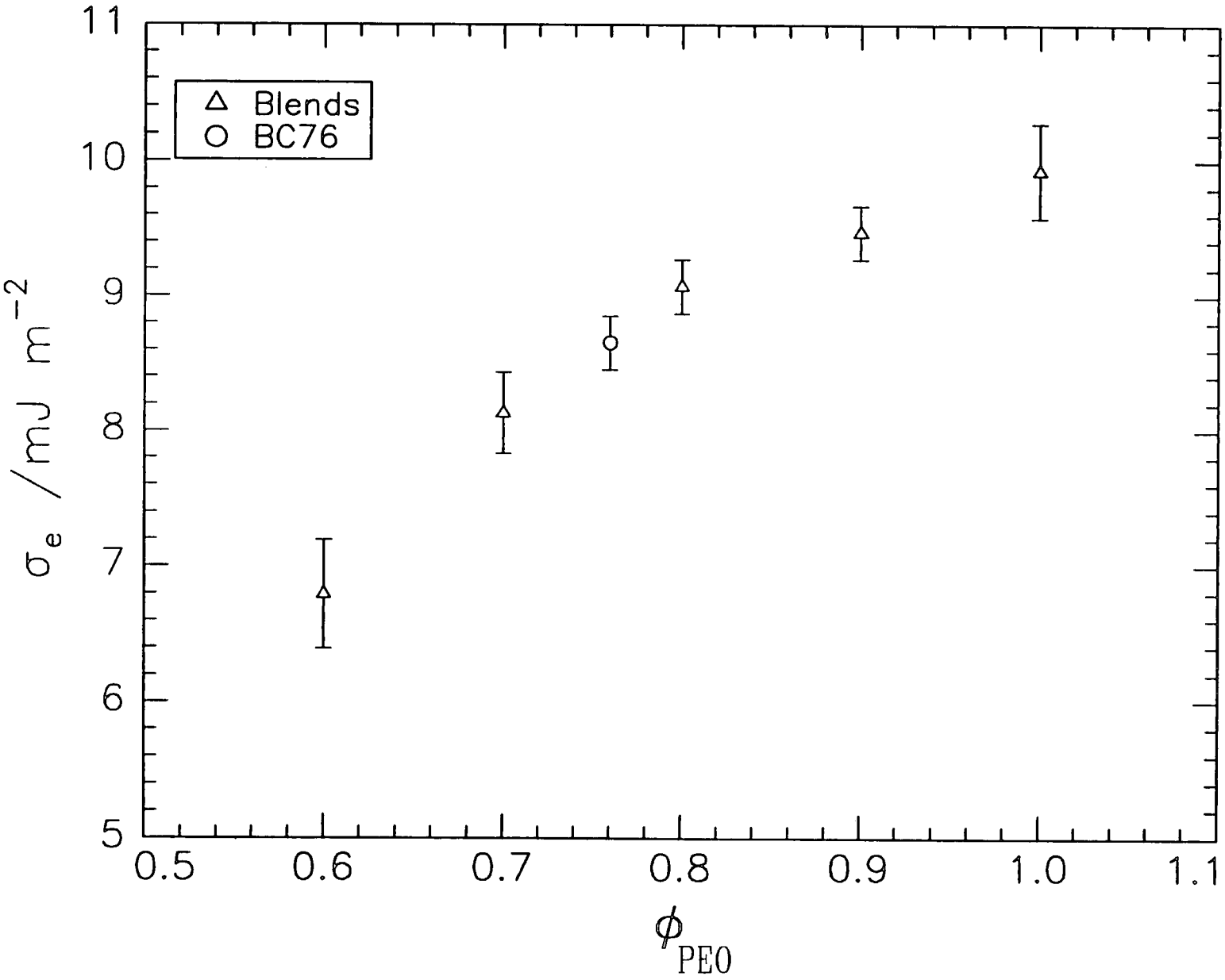

surface free energy decreases with increasing PMMA content. Martuscelli et al[14] proposed an explanation for this observation in terms of an overriding increase in the entropy of folding as the proportion of PMMA content increases. During crystallisation, entanglements between PMMA and PEO favour the formation of loops on the surface of the PEO lamellar crystals. The subsequent increase in the entropy of folding overwhelms any increase in surface enthalpy resulting in a decrease in σ_e as the PMMA content increases. In contrast, Wang and Nishi[32] attributed the decrease in σ_e to changes in the viscosity of the melt and in T_g. Whether one or both explanations are correct, the observed decrease in σ_e is small and it is important to note that a slight change in the gradient for figures 5.16 and 5.17 has a dramatic effect on σ_e.

The observed decrease in σ_e with increasing PMMA concentration is in contradiction to results reported by Calahorra[17] for a higher molecular weight system of PEO/PMMA blends, and Ong and Price[26] for poly (ε-caprolactone)/poly (vinyl chloride), PCL/PVC, blends, where the lateral surface free energies, σ_e, are virtually independent of composition.

By contrast, the lateral surface free energy displays a marked dependence on the combined molecular weight of the blend. Table 5.5, lists σ_e values for PEO/PMMA blends with differing molecular weights as determined by other workers, (see chapter 2).

An increase in σ_e is observed as the overall molecular weight of the blend increases. This is attributed to an extension of the crystal/isotropic liquid like interphase owing to an increase in entanglement and knotting of chains in the initial melt as the molecular weight increases[33] preventing the attainment of the equilibrium interphase. The concomitant increase in σ_e tends towards a limiting value for very high molecular weights.

PEO/ PMMA (w/w)	PEO(M_n18.6K)[a] PMMA(M_n22.2K)	PEO(M_w20K)[b] PMMA(M_w110K)	PEO(M_w100K)[c] PMMA(M_w110K)	PEO(M_w4000K)[d] PMMA(M_w93.6K)
100/0	9.9±0.3	23.6	25	18.8 *independent of composition*
90/10	9.5±0.3	10.8	17.8	
80/20	9.1±0.3	11.2	15.8	
70/30	8.1±0.4	9.1	14.7	
60/40	6.8±0.4	-	14.6	

Table 5.5. Lateral Surface Free Energies (mJm^{-2}) of Folding, σ_e, of PEO Crystals for PEO/PMMA Blends of varying Molecular Weight.

[a] Present work.

[b] Ref. 7, (corrected evaluation of σ_e).

[c] Ref. 14, (corrected evaluation of σ_e).

[d] Ref. 17.

The pre-exponential factor G_0,which is related the type of crystallisation mechanism, depends upon the blend composition and the value obtained for BC76 is slightly smaller than that for the corresponding blend. G_0 for PEO is appreciably higher than the blends and BC76, which in turn tend to have a parabolic relation with v_2 in agreement with Martuscelli[14] (see figure 5.19). The value for PEO is in excellent agreement with those obtained by Godovsky[29], $1.5<G_0x10^6<2$ cm s^{-1}, and the values for BC76 and the blends are only slightly smaller than the theoretically determined range for homopolymers[22], $5<G_0x10^5<8$ cm s^{-1}.

Figure 5.19. Ln G_o vs. Volume Fraction of PEO for PEO, BC76 and Blends.

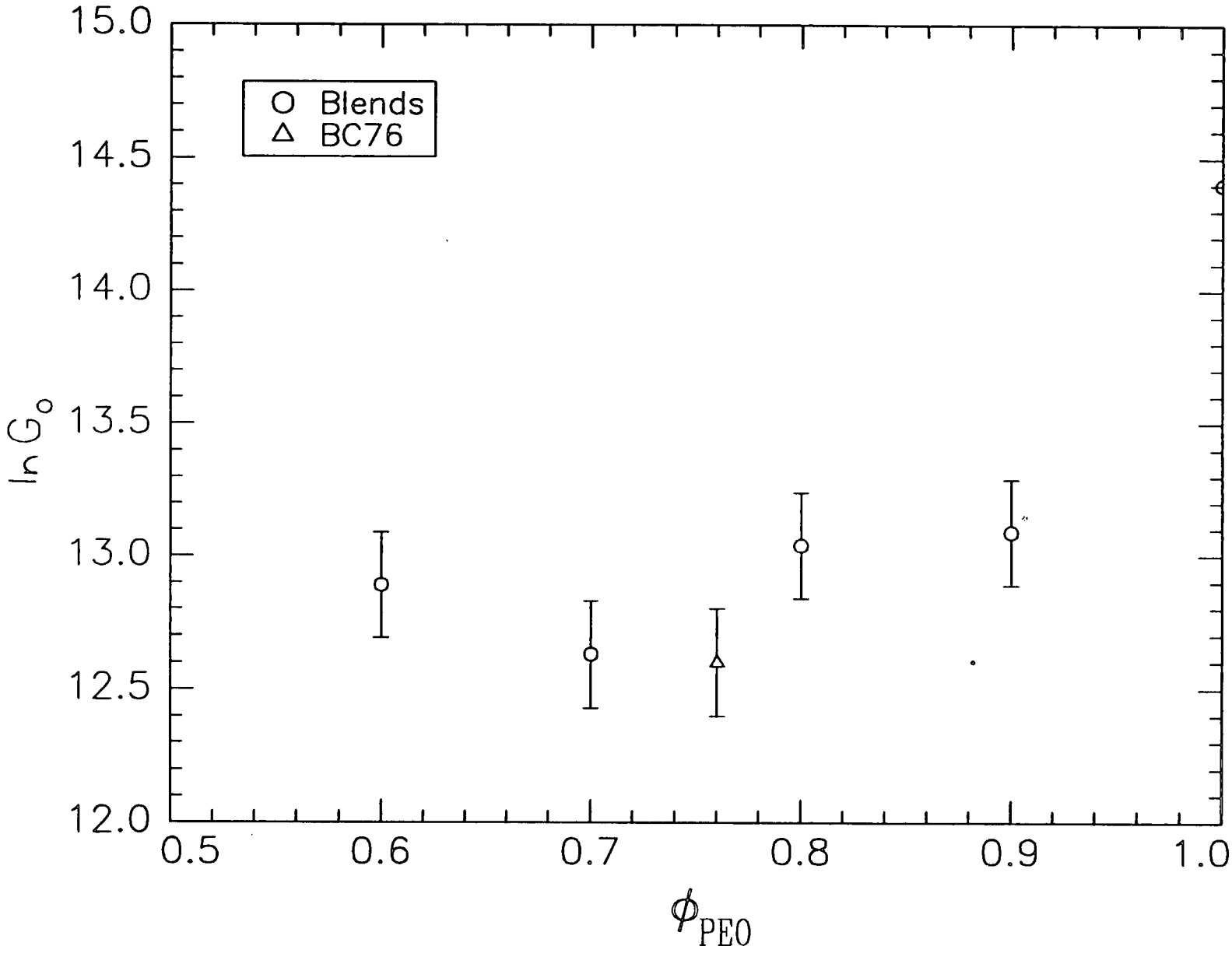

5.6. Conclusions.

A three to four fold decrease in the rate of isothermal crystallisation and a 2-3K reduction of the equilibrium melting point is observed in a linear block copolymer, PEO-b-PMMA, containing 76% (w/w) of PEO, in comparison to the corresponding blend. However, no appreciable variation in the lateral surface free energy perpendicular to the molecular chain direction in the PEO crystal, σ_e, or the value of the JMA exponent in both block and homopolymer blend was observed.

As found by previous investigators (see chapter 2), the amorphous PMMA component acts as a diluent, lowering the observed melting point, increasing the crystalline disorder within the spherulite and decreasing the rate of isothermal crystallisation. A Flory-Huggins interaction parameter value of -0.52 was determined from the equilibrium melting point depression associated with the PEO/PMMA blends. This indicated that the blends are strongly miscible at temperatures close to the melting point of PEO (336K).

The dependence of growth rate of spherulites upon temperature for both the block copolymer and the blends is qualitatively similar to that found in the homopolymer. A disc growth geometry was observed and the initial stage of crystallisation was found to be kinetically controlled by the rate of attachment of crystallisable units to the crystalline interface using a 'modified' Avrami analysis.

5.7. References.

1. Samuels, R.J., J. Polym. Sci., Part A-2, 9, 2165-2246, 1971.
2. Haudin, J.M., Chapt. 4 in 'Optical Properties of Polymers', G.H.Meeten, Ed., Elsevier, London, 1986.
3. Hoffman, J.D. and Weeks, J.J., J. Res. Nat. Bur. Stand., Sect. A, 66, 13, 1962.
4. Runt, J., Gallagher, K.P., Polym. Commun., Vol. 32, No.6, 180-182, 1991.
5. Scott, R.L., J.Chem.Phys., 17, 279, 1949.
6. Nishi, T. and Wang, T.T., Macromolecules, 8, 909, 1975.
7. Martuscelli, E., Demma, G., in 'Polymer Blends: Processing, Morphology and Properties', Martuscelli, E., Palumbo, R. and Kryszewski, M., Eds., Plenum, New York, 1980.
8. Martuscelli, M., Silvestre, C. and Abate, G., Polymer, 23, 229, 1982.
9. Li, X. and Hsu, S.L., J. Polym. Sci. Polym. Phys. Ed., 22, 1331, 1984.
10. Calahorra, E., Cortazar, M., Guzmán, G.M., Polymer Commun., 24, 211, 1983.
11. Okado, T., Saito, H. and Inoue, Macromolecules, 23, 3865, 1990.
12. Cahn, J.W., p.681 'Crystal Growth'; Peiser, H.S., Ed.; Pergamon, New York 1967.
13. Donth, E., Kretzschmar, Schulze, G., Garg., D., Höring, S. and Ulbricht, J., Acta Polymerica, 38, 261, 1987.
14. Martuscelli, E., Pracella, M., Yue, W.P., Polymer, 25, 1097, 1984.
15. Martuscelli,E., Poly. Eng. and Science, 24, 8, 1984.
16. Cimmino, S., Di Pace, E., Martuscelli, E., Silvestre, C., Makromol. Chem., Rapid Commun., 9, 261, 1988.
17. Calahorra, E., Cortazar, M., Guzmán, G.M., Polymer, 23, 1327, 1982.
18. Shultz, J., Chapt. 9 'Polymer Materials Science', Prentice Hall, Englewood Cliffs, New Jersey, 1974.
19. Gornick, F. and Mandelkern, L., J.Appl.Phys., 33, 907, 1962.

20. Sperling, L.H., p.234, 'Introduction to Physical Polymer Science', (2nd Ed.), Wiley-Interscience, 1992.

21. Turnbull, D. and Fisher, J.C., J. Chem. Phys., 17, 71, 1949.

22. Mandelkern, L., J. Appl. Phys., 26, 443, 1955; p.273 in 'Crystallisation of Polymers', McGraw-Hill, New York, 1964.

23. Boon, J. and Azcue, J.M., J. Polym. Sci. A-2, 6, 885, 1968.

24. Wunderlich, B., Macromolecular Physics, Vol. 2, 'Crystal Nucleation, Growth, Annealing'; Academic, New York, 1976.

25. Williams, M.L., Landel, R.F. and Ferry. J.D., J. Am. Chem. Soc., 77, 379, 1955.

26. Ong, C.J. and Price, F.P., J. Polym. Sci. C, 63, 59, 1978.

27. Hoffman, J.D., Soc. Plast. Eng. J., 4, 315, 1964.

28. Van Krevelen, D.W., 'Properties of Polymers', Elsevier, New York, 1976.

29. Godovsky, Y.K., Slonimsky, G.L. and Garbar, N. M. J. Polym. Sci. C, 38, 1, 1972.

30. Alfonso, G.C., Russell, T.P., Macromolecules, 19, 1143-1152, 1986.

31. Fox, T.G., Bull. Am. Phys. Soc., 2, 123, 1956.

32. Wang, T.T. and Nishi, T., Macromolecules, 10, 421, 1977.

33. Mandelkern, L., p.363-414 Comprehensive Polymer Science, Vol. 2, eds. G. Allen and J.C. Bevington, Pergamon Press, 1989.

Chapter 6

Wide Angle and Small Angle X-ray Scattering.

6.1. Introduction.

The basic principles governing the scattering and diffraction of these different electromagnetic waves are very similar to those for light scattering. The difference lies in the wavelength and the mode of interaction. The scattering of x-rays occurs as a result of interaction with electrons in the material. The variation of the scattered and diffracted intensity with angle provides information on the electron density distribution and hence atomic position within the material. Depending upon which x-ray technique is used, this yields structural information such as crystallinity values, microphase morphology, interfacial thicknesses and lamellar spacings.

X-rays may scatter coherently or incoherently. With coherent scattering, the electrons are so tightly bound to the atomic nuclei that no energy exchange occurs upon photon collision. However, with incoherent scattering, the photon exchanges energy (change in wavelength) with the electron which in turn is promoted to a higher energy level or is ejected from the atom. Such incoherent scattering gives rise to a continuous background which needs to be subtracted during analysis.

Distinction between WAXS and SAXS is required because the instrumental (especially collimation) requirements and methods of analysing data are often very different, although the basic principles are the same.

6.2. Electron Density Contrast.

For a sample to scatter x-rays it is imperative that an electron density difference exists between individual regions within the sample. As described by Stuhrmann,[1] the electron scattering density, ρ, can be calculated from the following equation:

$$\rho = \frac{\sum b_i}{V} = \frac{\rho_s N_A}{M_w^m} N_e^m L_e \qquad (6.1)$$

where b is the coherent scattering length, V is the volume occupied by the monomer unit, N_A is Avogadro's constant, M_w^m is the monomer molecular weight, N_e^m is the number of electrons in one monomer unit, ρ_s is the sample density and L_e is the scattering length of one electron (0.28×10^{-12} cm).

For crystalline PEO, amorphous PEO and PMMA, the electron scattering densities were calculated to be 11.09×10^{10} cm^{-2}, 10.38×10^{10} cm^{-2} and 10.81×10^{10} cm^{-2} respectively. Consequently, between crystalline PEO and amorphous PMMA, between crystalline PEO and amorphous PEO and between amorphous PEO and PMMA, the differences in ρ are 0.28×10^{10} cm^{-2}, 0.71×10^{10} cm^{-2}and 0.43×10^{10} cm^{-2}. These differences are sufficiently large to provide adequate electron density contrast to scatter x-rays.

6.3. The Wide Angle X-ray Scattering, (WAXS) Determination of the Crystallinity in Polymers.

6.3.1. Introduction.

Wide angle and small angle x-ray scattering can be used to determine the degree of crystallinity, x_c, in polymers. Rabiej[2] has shown that SAXS can not be used as an independent routine method for the determination of the degree of crystallinity. The influence of the transition layer between the crystalline lamellar and the amorphous fraction leads to a value of x_c from SAXS measurements that is greater than that obtained from the more favoured WAXS technique.

A rather simplified view of crystallinity based on the two phase approximation polymer structure is often used. A two phase model consisting of uniform crystalline and amorphous regions with a negligible interface region is assumed, where the scattering capability of the crystalline and amorphous components with the same mass are identical. In principle, this model cannot be applied to block copolymers since the scattering capabilities of the crystalline and amorphous components are clearly different (see section 6.2). Ning has modified this two phase model and applied it to block copolymers of polystyrene-b-poly(ethylene oxide)[3]. Differences in crystallinity values obtained from both models were <1%, and so this more complicated modification can be assumed to be negligible.

The degree of crystallinity is defined as either the weight fraction or volume fraction of the crystalline phase divided by the total (amorphous plus crystalline) weight or volume fraction respectively. If $\mu t>0.5$ (where μ is the linear absorption factor and t the sample thickness), then the influence of x-ray absorption and consequently sample thickness can be ignored.[4]

6.3.2. Theory.

Several methods have been proposed for calculating the degree of crystallinity from WAXS data.[5] They can be generally categorised into two groups:

i) External comparison - the intensity of one component in the sample is compared with the intensity of that component in 100% concentration, and

ii) Internal comparison - the intensities of both components are used and compared.

A variety of different methods from each group has been described in detail elsewhere.[5]

The difficulty in using group i) is that it is rarely possible to obtain either a 100% crystalline or 100% amorphous standard. Mainly for this reason, methods based on the internal comparison group (group ii)), are often used.

6.3.2.1. Hindeleh and Johnson Method[6].

This internal comparison method has been widely used to determine the degree of crystallinity in polymers.

The procedure is based on the resolution of a normalised diffraction pattern into an amorphous background and individual peaks. The diffraction pattern is approximated by:

$$Y_c = \sum_{i=1}^{n} Q_i + B \qquad (6.2)$$

where n is the number of crystalline peaks. The individual crystalline peaks are fitted to a combination of Gaussian and Cauchy (Lorentz) profiles, Q_i:

$$Q_i = f_i A_i \exp\left[-\ln 2\left(\frac{2(x-P_i)}{w_i}\right)^2\right] + \frac{A_i(1-f_i)}{1+\left(\frac{2(x-p_i)}{w_i}\right)^2} \qquad (6.3)$$

where f_i is the profile function parameter (f_i=0 for a Cauchy function, f_i=1 for a Gaussian function and can be any fraction for any combination of functions), A_i is the peak height, w_i is the peak width at half height, P_i is the peak position angle and x is the scattering angle 2θ (the angle subtended by the incident and scattered radiation).

The amorphous background is fitted to a polynomial of the form:

$$B = ax^3 + bx^2 + cx + d \qquad (6.4)$$

Through minimisation of the sum of least squares:

$$S = \sum_{i=1}^{n} (Y_{ci} - Y_{ei})^2 \qquad (6.5)$$

where Y_{ei} and Y_{ci} are the experimental and calculated x-ray scattering intensities respectively, and n is the number of intensity data The WAXS diffraction profile can be resolved into individual crystalline and amorphous fractions. The degree of crystallinity is thus the intensity under the resolved crystalline peaks, divided by the total area under the unresolved WAXS curve.[7]

6.3.2.2. Ruland's Method.

Another group ii) method that has proved successful in determining x_c is that proposed by Ruland[8,10] and later modified by Vonk.[9] This procedure is based on the paracrystal theory,[10] and gives a value for the distortion factor as well as the crystallinity.

The scattered intensity is expressed as:

$$\int_0^\infty I(s)dV_s = 4\pi \int_0^\infty s^2 I(s)ds = 4\pi \int_0^\infty s^2 \bar{f}^2 ds \qquad (6.6)$$

$$\bar{f}^2 = \frac{\sum_i n_i f_i^2}{\sum_i n_i} \qquad (6.7)$$

where f_i is the scattering factor of the atom i, n_i is the number of atoms of type i in the stoichiometric formula, $\bar{f}^2$ is the weighted mean-square atomic scattering factor and s is the reciprocal-lattice vector, $s=2\sin\theta/\lambda$.

The scattered intensity associated with the crystallinity present in the polymer is given by:

$$\int_0^\infty I_c(s)dV_s = 4\pi\int_0^\infty s^2 I_c(s)ds = x_c 4\pi\int_0^\infty s^2\bar{f}^2 Dds \qquad (6.8)$$

where D is a distortion factor, which is related to the loss of intensity due to deviations of the atoms from their ideal positions.

From equations 6.6 and 6.8, the degree of crystallinity, x_c, can be expressed as:

$$x_c = \frac{\int_0^\infty s^2 I_c ds.\int_0^\infty s^2\bar{f}^2 ds}{\int_0^\infty s^2 Ids.\int_0^\infty s^2\bar{f}^2 Dds} \qquad (6.9)$$

This equation is valid provided the scattering angular range, s_1 to s_2 is sufficiently wide. Thus, x_c can be expressed as:

$$x_c = x_c'.K \qquad (6.10)$$

where;

$$x_c' = \frac{\int_{s_1}^{s_2} s^2 I_c(s)ds}{\int_{s_1}^{s_2} s^2 I(s)ds} \qquad (6.11)$$

and

$$K = \frac{\int_{s_1}^{s_2} s^2 f^2 ds}{\int_{s_1}^{s_2} s^2 f^2 D ds} \qquad (6.12)$$

If D is assumed to obey the following relation:

$$D(s) = \exp(-ks^2) \qquad (6.13)$$

then K can be approximated by:

$$\mathrm{K} = 1 + \left(\frac{\mathrm{k}}{2}\right).(\mathrm{s})^2 \qquad (6.14)$$

Using equations 6.10 and 6.14, Vonk[9] found that a plot of y versus $(s)^2$ can be used (see equation 6.15) to determine x_c and k:

$$\frac{1}{x_c'} = y = \frac{1}{x_c} + \left(\frac{k}{2x_c}\right).(s_2)^2 \qquad (6.15)$$

6.3.3. Apparatus.

The WAXS scans were performed using a D5000 Siemens Diffractometer. The sample temperature was controlled using a TTK2-HC Programmer and Heat Controller (supplied by Anton Paar K.G., A-8054 GRAZ, Austria), and a TTK-LNC Liquid Nitrogen Controller (Anton Paar) enabled cooling at rates ranging from 0.1 to 30Kmin^{-1} to sub-ambient temperatures. A Diffrac-At FIT V.3.0. fitting program supplied by Siemens was used to determine the degree of crystallinity for each WAXS scan.

6.3.4. Procedure.

Two internal comparison methods were employed to determine the degree of crystallinity for the unannealed samples and an external method was used to determine the level of induced crystallinity for BC50 and BC55 (see section 6.3.4.3).

The first internal method is extremely simply and quick, and does not require any curve fitting software. It served as a valuable comparison to the more elaborate and accurate second internal method.

6.3.4.1. Internal Method 1.

This procedure has been illustrated in figure 6.1. The 'liquid scattering' background was accounted for by subtracting a linear background from the smoothed (width=1.6, see EVA software package) WAXS data, (see figure 6.1.a). The crystalline peaks were separated from the amorphous component in an arbitrary manner by drawing a straight line between the intensity minima of each crystalline peak, see figure 6.1, b). The total intensity of the sharp crystalline peaks was then calculated by evaluating the total area under the crystalline peaks, i.e., the hatched regions in figure 6.1, b). The degree of crystallinity was determined from the total intensity of the crystalline peak fraction, divided by the total intensity under the background subtracted WAXS pattern (the total area under the WAXS profile in figure 6.1, b).

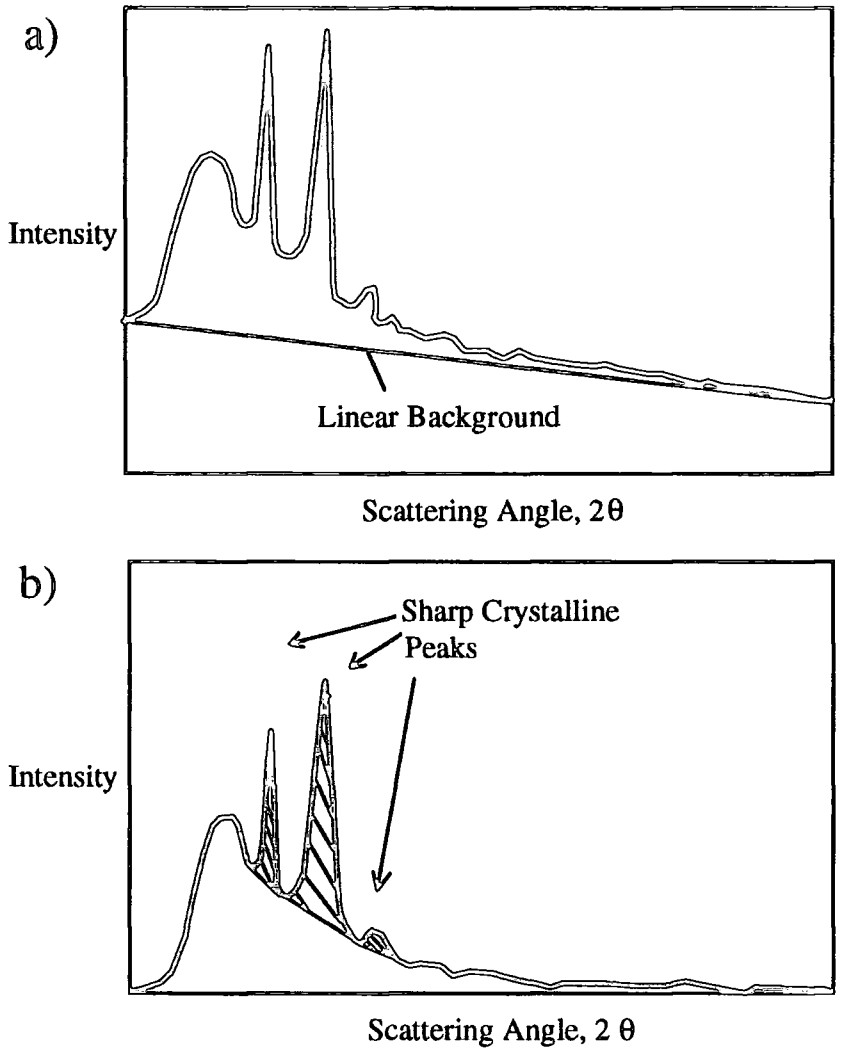

Figure 6.1. Schematic Representation of the Procedure used to Determine the Crystallinity using Internal Method 1.

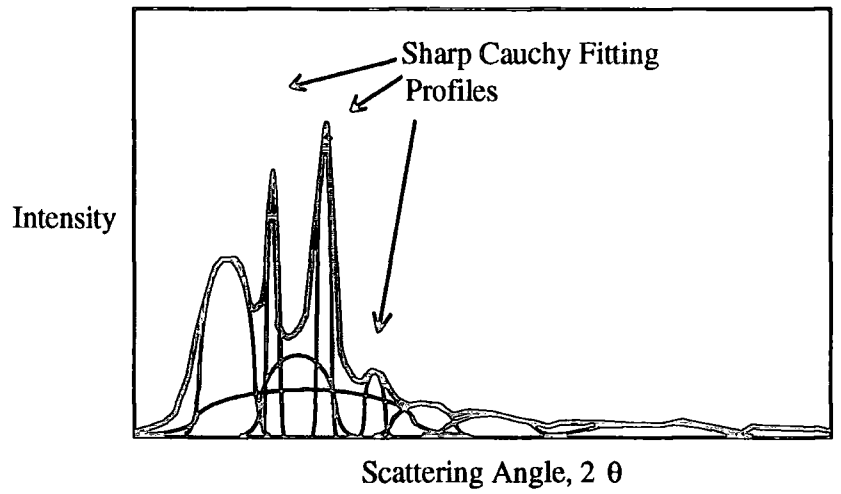

Figure 6.2. Schematic Representation of the Cauchy Curve Fitting Procedure using in Internal Method 2.

6.3.4.2. Internal Method 2.

This method is based on the Hindeleh/Johnson procedure described in section 6.3.2.1. Again, a linear background portion was subtracted from the smoothed (width=1.6) data as in method 1. Ten Cauchy (Lorentz) curves were then fitted to the remaining data using the Diffrac-At FIT software package called, version 3.0, see figure 6.2. This number and type of fitting curves were used so that when added together, the resultant profile closely resembled the total experimental scattering curve. If the fit was found to be unsatisfactory, i.e., the sharp crystalline peaks were not accurately fitted by the Cauchy curves, then the number and type of fitted curves were changed.

Once a close fit to the experimental data had been achieved, the individual peaks were separated into crystalline and amorphous peaks. Those peaks which were narrow enough so that the full width at half maximum (FWHM) < 1.2, were assumed to be crystalline peaks (three sharp crystalline peaks have been annotated in figure 6.2). The remaining peaks were associated with amorphous scattering. The intensity of the crystalline peaks was then summed together and this total, I_c, was equated to the total scattering from the crystalline regions in the sample. Consequently, the degree of crystallinity was evaluated by dividing I_c by the total intensity under the background subtracted curve.

6.3.4.3. External Method.

The cooling/heating stage described in section 6.2.3 was used for the thermal treatment of BC50 and BC55 (see section 6.2.5.2). An alternative external comparison method to calculate the level of induced crystallinity was employed because the amount of amorphous scattered intensity at low scattering angles was dramatically smaller than that observed without the stage. The degree of crystallinity was evaluated by dividing the total intensity under the two main crystalline peaks (at $2\theta=19.1^{o}$ and 23.3^{o}), calculated using method 1, by the total intensity under these two peaks for pure PEO.

6.3.5. Experimental.

6.3.5.1. Crystallinity in Unannealed PEO/PMMA Blends and Block Copolymers.

WAXS scans were recorded for unannealed powdered samples of PEO-b-PMMA block copolymers, PEO and the blends. The x-ray scattering angular range was from 4 to 90^{o} in 0.02 increments. Scattered x-rays were collected for 12 seconds at each angular increment.

6.3.5.2. Phase Separation.

For BC50 and BC55, similar thermal treatments as reported in chapter 4, were performed prior to measurement using the D5000. That is, the polymers were cooled from 423K at two different cooling rates, 10Kmin^{-1} and 30Kmin^{-1}, to various permanence temperatures T', and held at T' for 60 minutes. The samples were then heated at 10Kmin^{-1} to 323K. After 60 minutes at 323K, wide angle x-ray measurements were recorded from 16^{o} to 28^{o} (2θ), in 0.02^{o} increments and for 12 seconds at each scattering angle.

The level of induced crystallinities were calculated using the external method described in section 6.2.4.3.

6.3.6. Results

6.3.6.1. Unannealed Samples.

Figures 6.3, 6.4 and 6.5 display the WAXS scans for PEO, PMMA and unannealed BC50, respectively. The sharp crystalline peaks for PEO reflect the ordered structure of a crystalline polymer whereas the WAXS profile for PMMA consists of a broad amorphous halo. As for all the multicomponent polymer systems investigated, the WAXS profiles are comprised of weighted proportions of the sharp PEO profile and the broader PMMA profile according to the relative fractions of these components.

Tables 6.1 and 6.2 list the crystallinity percentages (±2%) using internal methods 1 and 2 for unannealed PEO-b-PMMA block copolymers and PEO/PMMA blends respectively. The crystallinity indices per gram of PEO are also listed. These values were calculated from method 2's crystallinities.

6.3.6.2. Phase Separation.

Figures 6.6 and 6.7 show the WAXS scans measured at 323K for a variety of permanence temperatures for BC55 and BC50 respectively. It is clear that the degree of induced crystallinity increases as the permanence temperature decreases. For T'=253K for BC50, no crystalline peaks were detected at 323K. The degrees of induced crystallinity at 323K calculated using the external method described in section 6.2.4.3. for BC50, for two different cooling rates to various permanence temperatures, T' are listed in tables 6.3. and 6.4 respectively. Tables 6.5. and 6.6. lists the matching values for BC55.

No shift in the d spacing of the two main crystalline peaks with cooling rate and permanence temperature was observed for both block copolymers. However, the d spacing of these two peaks was found to be slightly larger than the d spacings for pure PEO.

Figure 6.3 WAXS Scan of PEO.

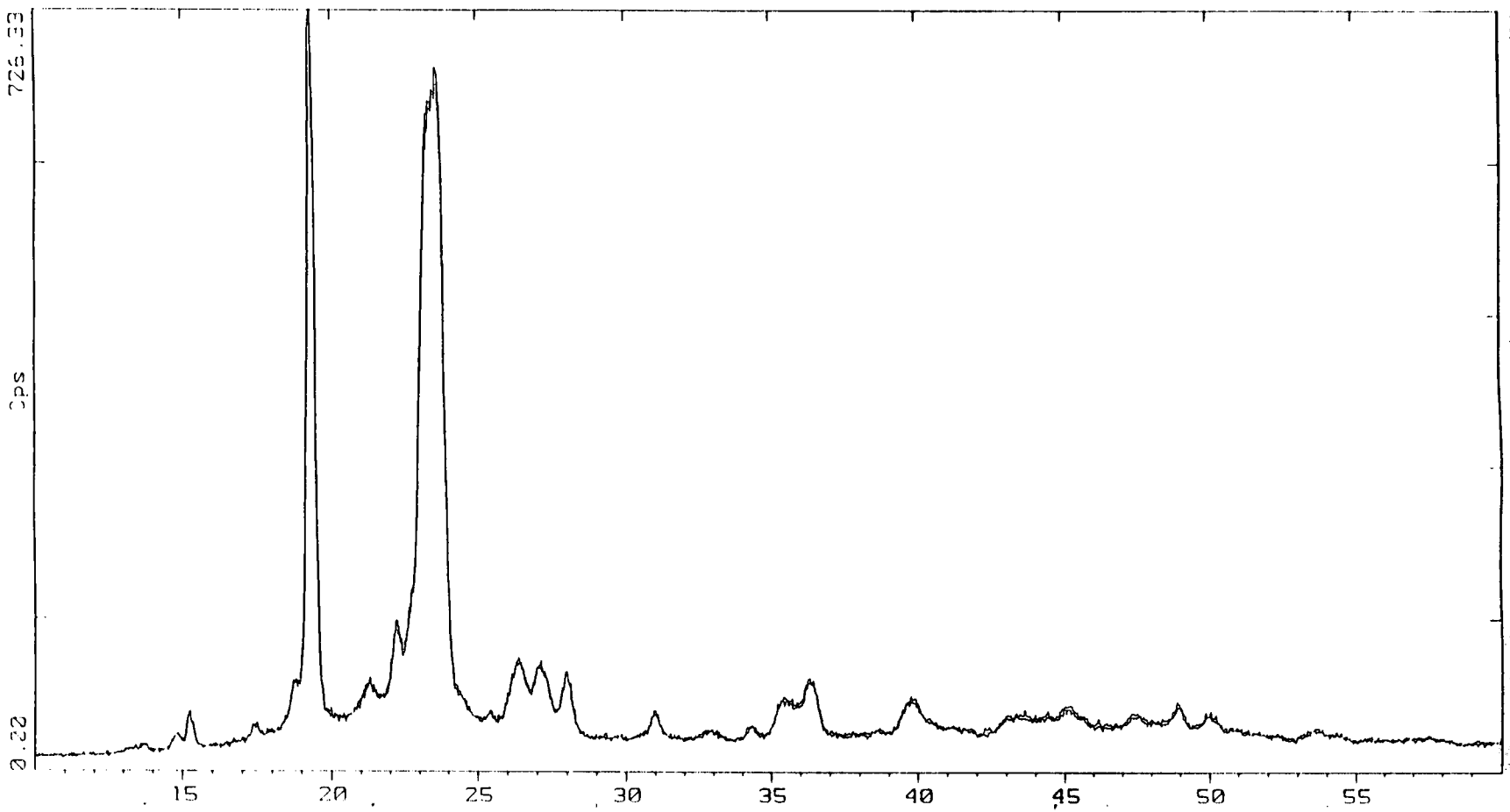

Figure 6.4 WAXS Scan of PMMA.

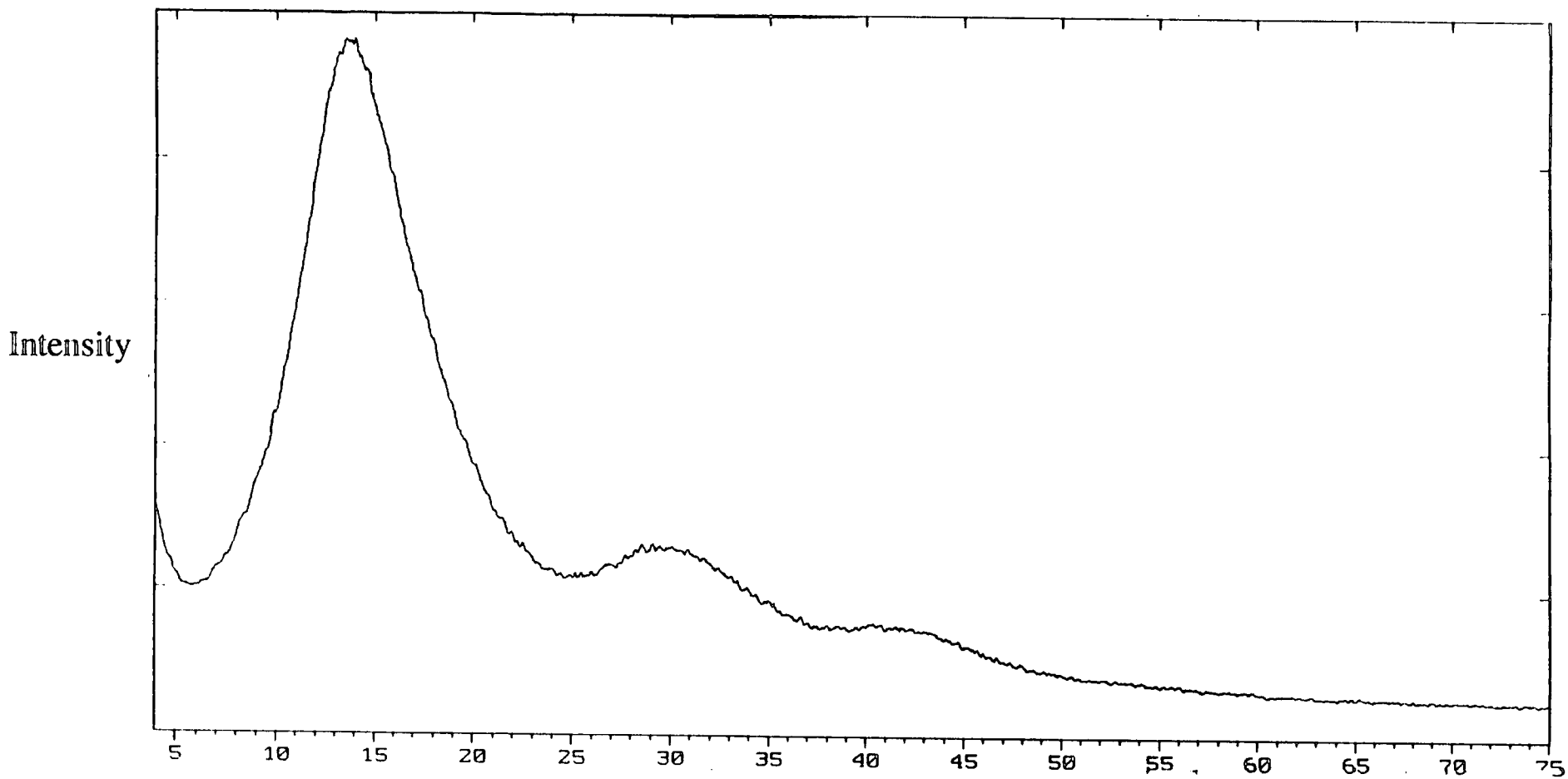

Figure 6.5 WAXS Scan of a PEO-b-PMMA Block Copolymer, BC50.

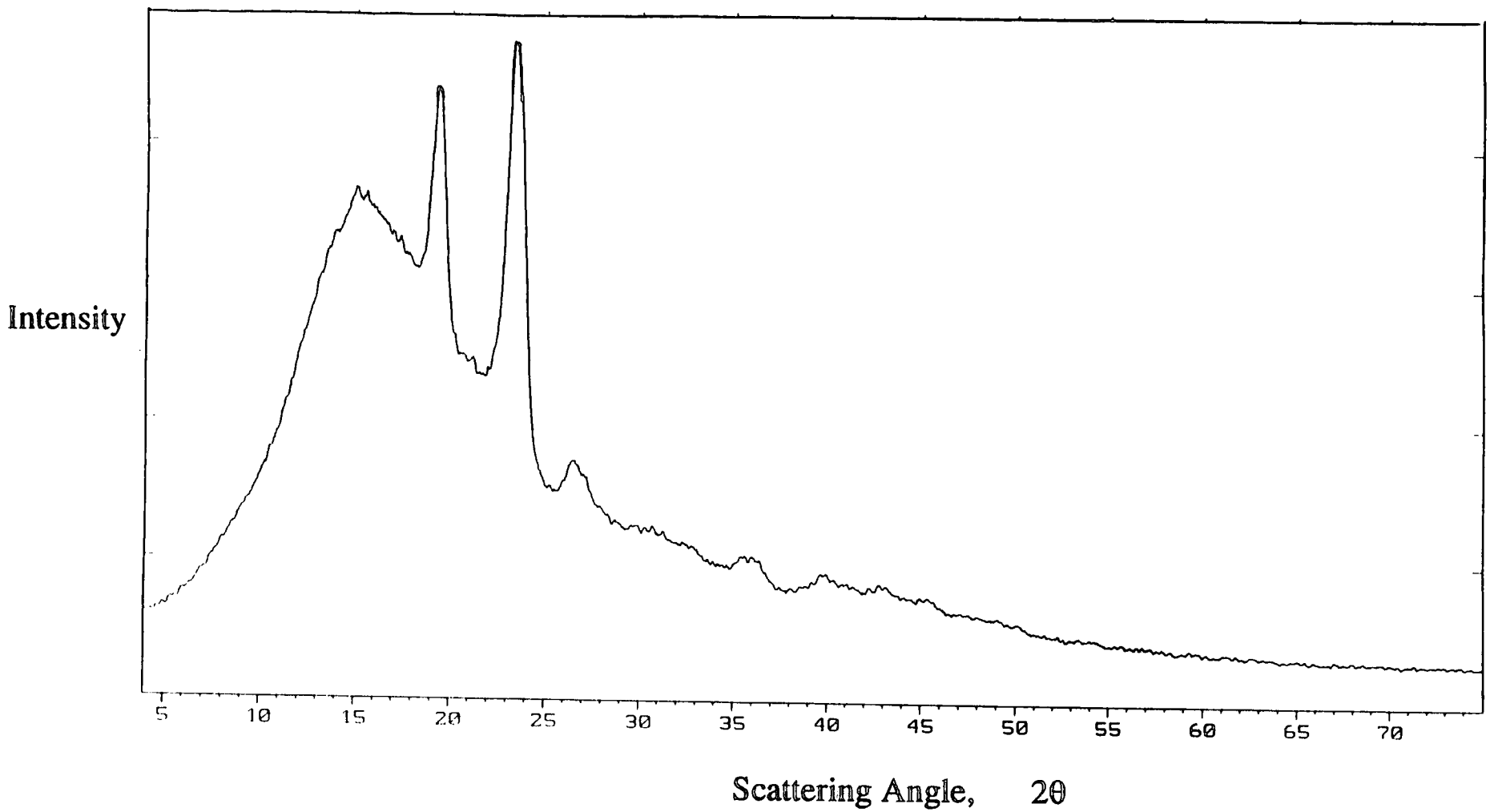

Figure 6.6 WAXS Scans of BC55 at 323K for various T'.

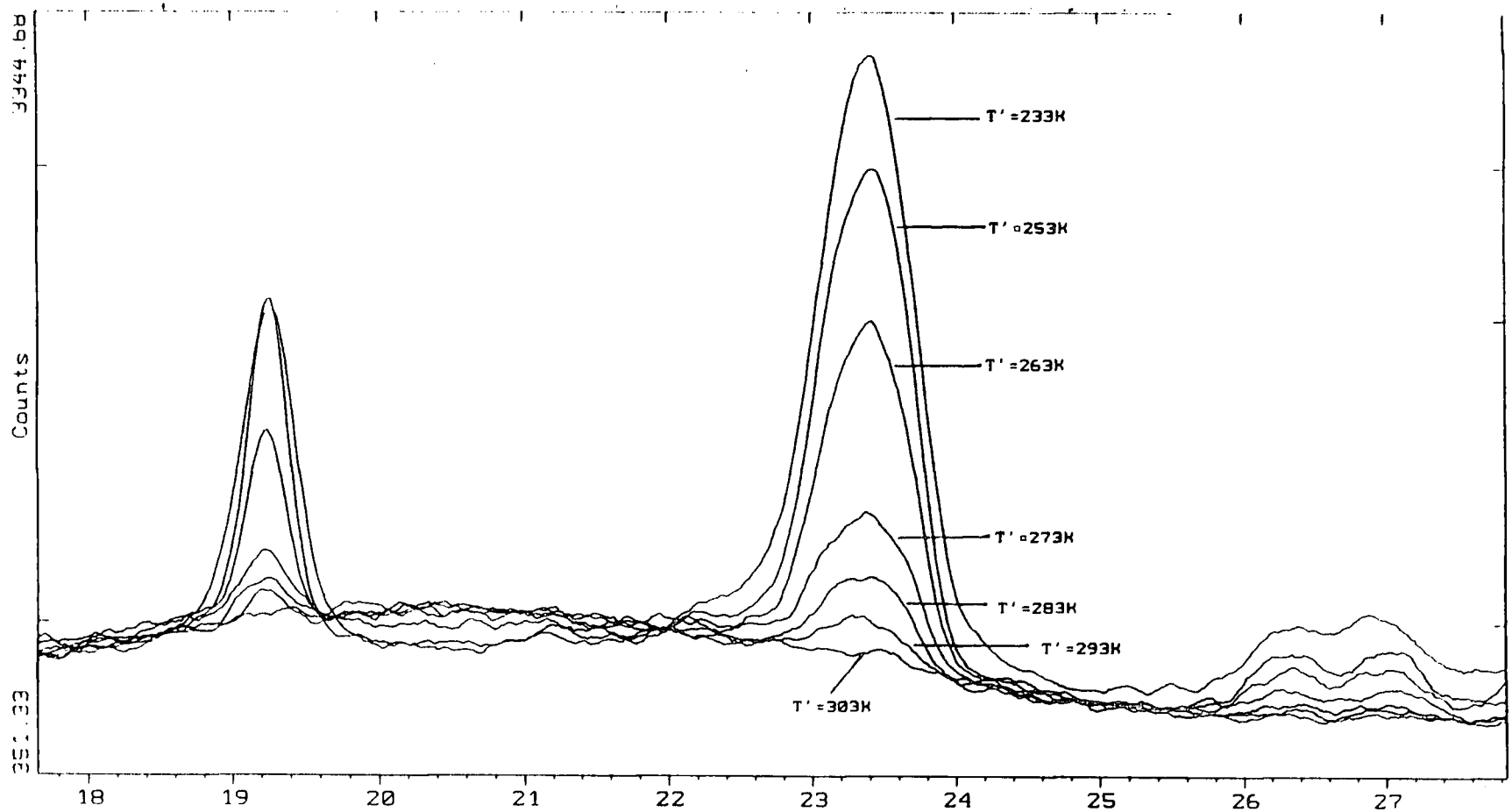

Intensity

Scattering Angle, 2θ

Figure 6.7 WAXS Scans of BC50 at 323K for various T'.

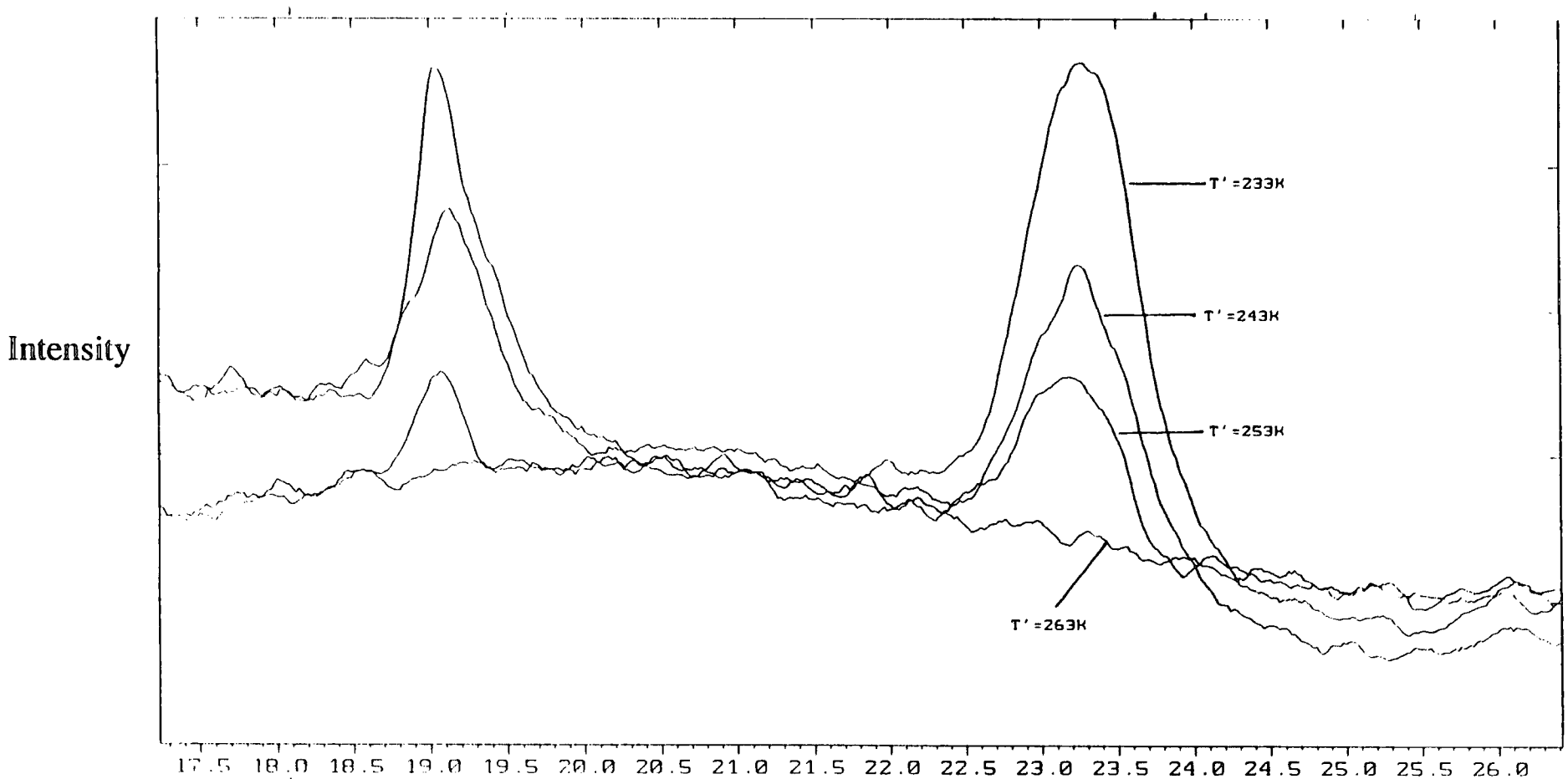

Block Polymer PEO-b-PMMA	Degree of Crystallinity Method 1	Degree of Crystallinity Method 2	Crystallinity Index, x_c
BC76	56.1	55.1	0.73
BC55	24.0	33.6	0.61
BC50	11.4	16.8	0.34
BC31	2.7	3.6	0.12
BC30	2.9	3.3	0.11
BC22	0	0	0
BC16	0.7	0.9	0.06
BC14	0	0	0
BC9	0	0	0
BC9	0	0	0
BC5	0	0	0
BC4	0	0	0

Table 6.1. Unannealed block copolymer percentage of crystallinities.

Blend (w/w)	Degree of Crystallinity Method 1	Degree of Crystallinity Method 2	Crystallinity Index, x_c
100/0 (PEO)	73.5	83.2	0.83
91/9	70.3	83.5	0.92
84/16	64.1	71.5	0.85
70/30	46.3	57.7	0.82
60/40	36.3	44.6	0.74
37/63	13.3	-	-
22/78	7.2	8.5	0.39
18/82	6.0	7.6	0.33

Table 6.2. Percentage of crystallinity of unannealed PEO/PMMA blends and PEO.

Permanence Temperature, T' (K).	Degree of Crystallinity (%).
233	25.2
243	19.4
253	18.1
263	12.7
273	5.3
283	3.2
293	2.0
303	0

Table 6.3. Induced Percentage of Crystallinity, BC55 Quenched to T' ($30Kmin^{-1}$).

Permanence Temperature, T' (K).	Degree of Crystallinity (%).
243	32.9
253	22.7
263	18.6
273	15.6
283	9.4
293	4.9
303	1.1
313	0

Table 6.4. Induced Percentage of Crystallinity, BC55 Cooled to T' ($10Kmin^{-1}$).

Permanence Temperature, T' (K).	Degree of Crystallinity (%).
227	11.1
231	10.2
235	9.1
239	7.7
242	6.3
245	4.2
248	3.9
253	0

Table 6.5. Induced Percentage of Crystallinity, BC50 Quenched to T' ($30Kmin^{-1}$).

Permanence Temperature, T' (K).	Degree of Crystallinity (%).
233	14.9
243	8.4
253	3.8
263	0

Table 6.6. Induced Percentage of Crystallinity, BC50 Cooled to T' ($10Kmin^{-1}$).

6.3.7. Analysis and Discussion.

6.3.7.1. Unannealed Samples.

Figure 6.8 shows the percentage of crystallinity in the unannealed PEO/PMMA blends calculated using internal methods 1 and 2. As shown in this figure, the crystallinity values from method 1 are consistently smaller than those evaluated using internal method 2. This is because method 1 does not account for possible crystalline peak overlap. The difference between the crystallinity values is relatively small (<10%) which suggests that the less rigorous and simpler method, internal method 1, can be utilised to determine the degree of crystallinity from WAXS.

Figure 6.9 compares the degree of crystallinity of the blends with those of the block copolymers. For both systems the degree of crystallinity decreases with decreasing PEO content. This is attributed to the diluent nature of the PMMA amorphous component (see chapters 4 and 5). However, for systems with the same fraction of PEO, the blends exhibited a larger degree of crystallinity with respect to the block copolymers. This reflects the restrictive nature of the chemical joint in the block copolymer. In fact, crystallinity was detected in blends containing 18% PEO (w/w), whereas no crystallinity was detected for a block copolymer containing 22% PEO (w/w).

It is interesting to note the reasonably constant x_c indices for higher PEO contents of both the unannealed blends and unannealed block copolymers. This suggests that as the proportion of PMMA content increases, the relative proportions of both constituents within the crystalline regions remain the same. For lower PEO contents, x_c deceases reflecting the diluent effect of the amorphous fraction, i.e., the relative amount of PMMA trapped in the interlamellar regions of PEO crystallites increases.

Figure 6.8 Percentage of Crystallinity for PEO and Unannealed PEO/PMMA Blends.

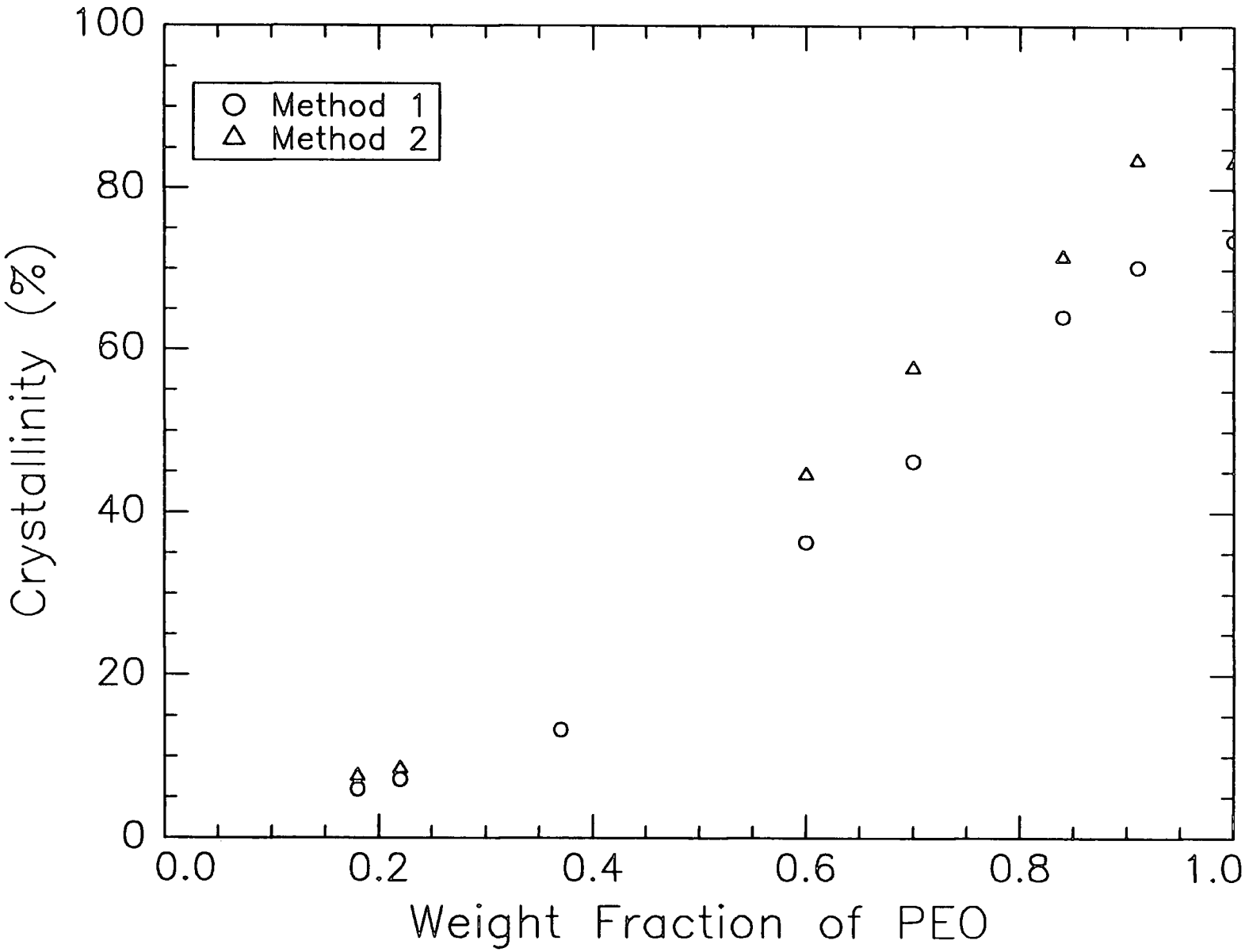

Figure 6.9 Crystallinity (%) for Unannealed Block Copolymers and Blends using Method 2.

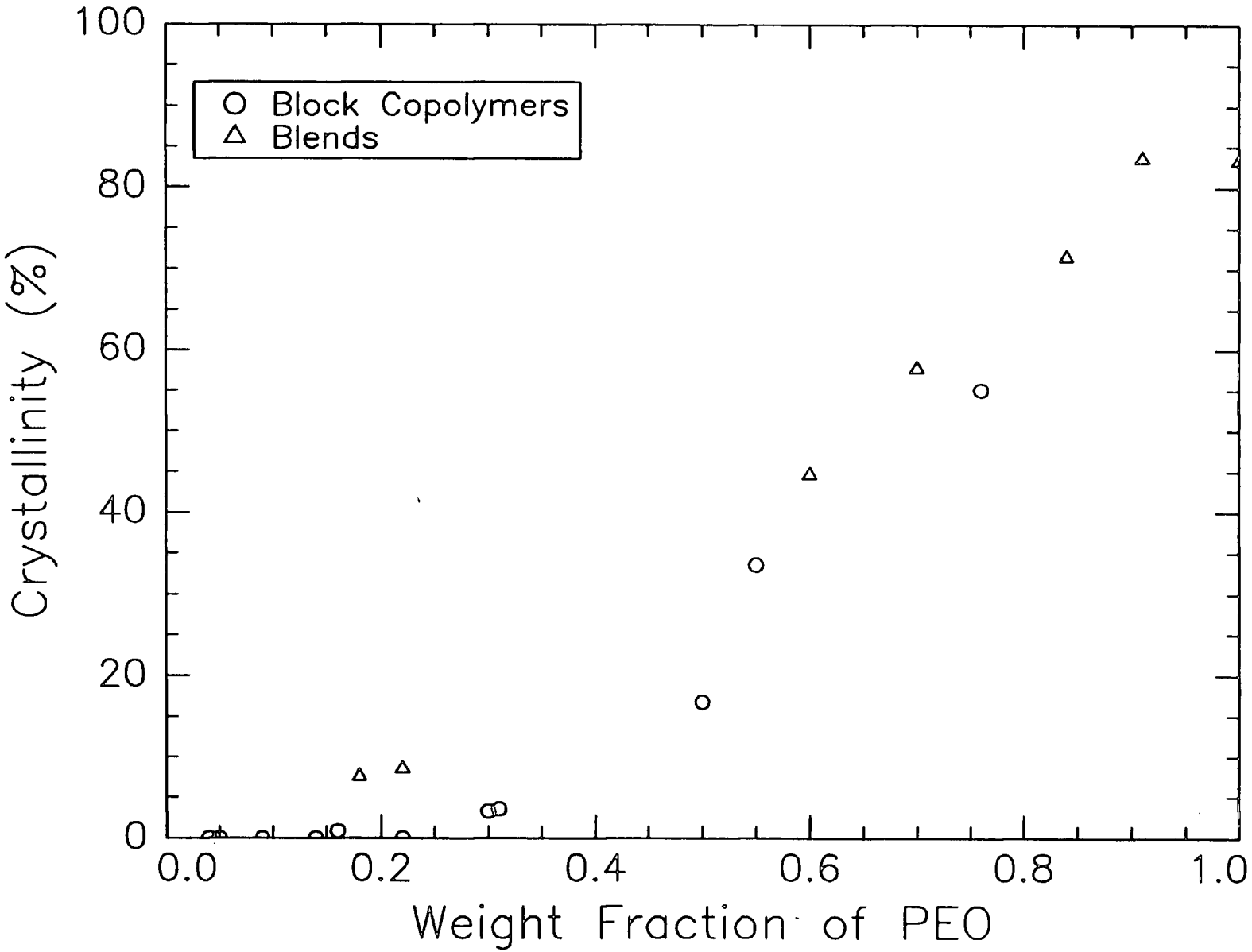

6.3.7.2. Phase Separation.

At the permanence temperatures investigated, no crystallinity was detected. However, for certain thermal regimes, upon heating to 323K, WAXS measurements provided direct evidence of crystallinity at this crystallisation temperature. Thus wide angle x-ray scattering has proved beyond doubt that some form of structural reorganisation such as microphase separation at these low permanence temperatures induces crystallinity at 323K. Figure 6.10 displays the percentage of induced crystallinity for BC55 and BC50 for two cooling rates to T'. For each block copolymer and cooling rate, the values of induced crystallinity tend to level off at the lower and higher limits of the permanence temperatures investigated. Consequently, similar to T_{tr}' in chapter 4, a temperature $T_{1/2}'$, has been assigned to the permanence temperature which half the maximum amount of attainable crystallinity is induced. These values are tabulated in table 6.7.

Polymer and Cooling Rate.	$T_{1/2}'$ (K)
BC50, 30Kmin^{-1}	242
BC50, 10Kmin^{-1}	247
BC55, 30Kmin^{-1}	261
BC55, 10Kmin^{-1}	276

Table 6.7. $T_{1/2}'$ Temperatures for BC55 and BC50 at Two Different Cooling Rates to T'.

The temperature $T_{1/2}'$ listed in table 6.7 show that the structural rearrangement (microphase separation) occurs at a lower temperature for BC50 with respect to BC55. For the higher cooling rates to T', both $T_{1/2}'$ values for BC50 and BC55 are lower than for cooling rates of 10Kmin^{-1}. This suggests that for the lower cooling rates, pre-crystalline nuclei are allowed to form at these higher permanence temperatures. These nuclei facilitate the process of microphase separation.

Figure 6.10 Induced Crystallinity Percentages for BC55 and BC50 for two Cooling Rates to T'.

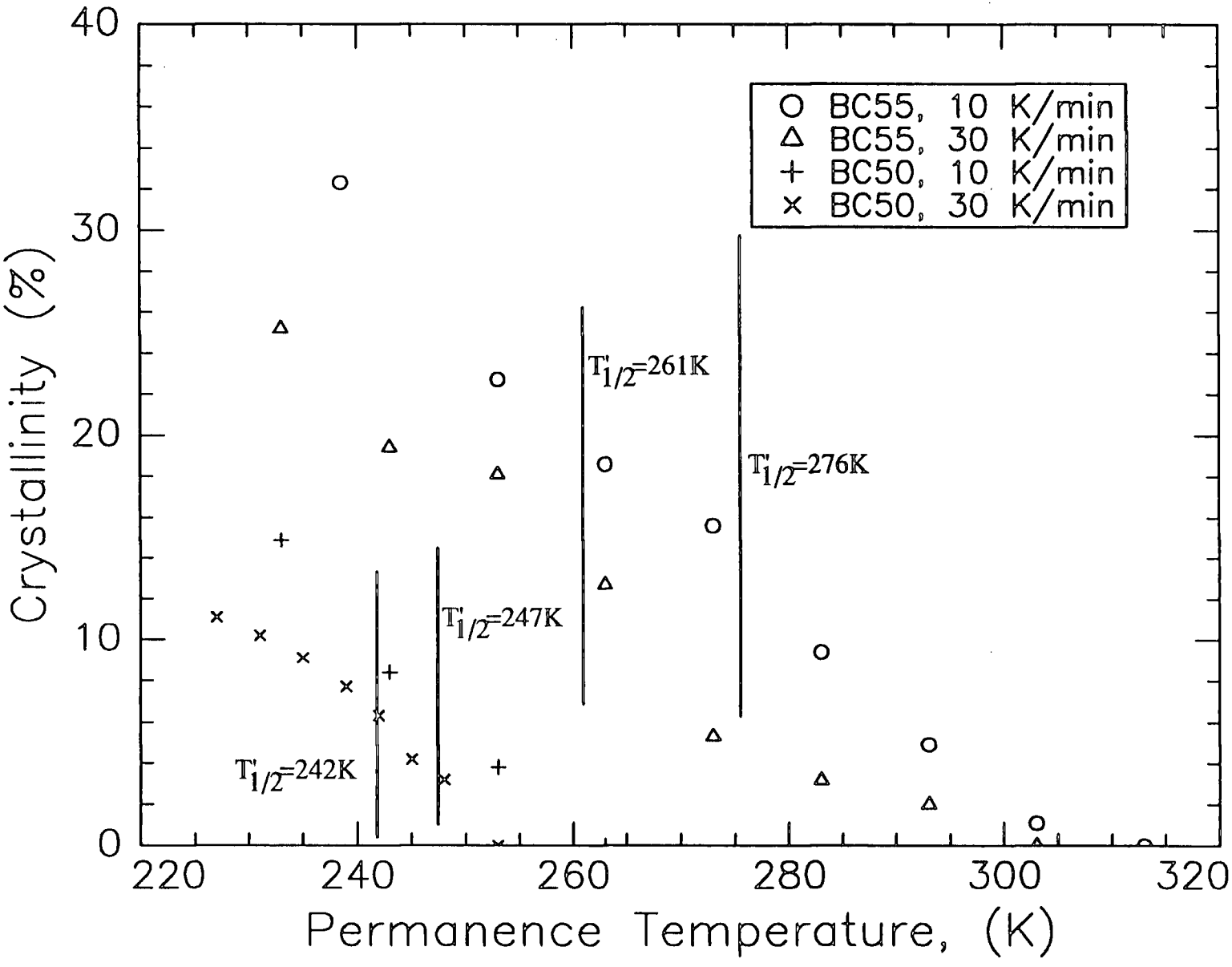

The maximum degree of induced crystallinity were 32.9% and 14.9% for BC55 and BC50 respectively. These values are very similar to the degree of crystallinity obtained from unannealed BC55 and BC50 using internal method 2. The normalised crystalline scattering intensities from the unannealed samples are appreciably higher than for the induced crystalline sample WAXS scans. This indicates that the external method used to determine the level of crystallinity for BC55 and BC50 gives values that are larger than the true values.

The d spacings corresponding to the two main crystalline peaks for both BC55 and BC50 were found to be slightly larger than those for PEO. This suggests that the crystalline regions for these two block copolymers were larger, reflecting the diluent nature of the amorphous PMMA present.

6.4.Small Angle X-ray Scattering, SAXS.

6.4.1. Theory.

As with any scattering process, an inverse relationship between particle size and scattering angle is present. An ordered structure in terms of arrangement and separation of scattering scatters radiation of commensurate wavelength according to the following Bragg equation:

$$n\lambda = 2d\sin(\theta / 2) \qquad (6.16)$$

where the Bragg angle θ is the scattering angle at which the diffraction peak is observed, λ is the wavelength of the incident x-ray radiation and d is the Bragg spacing between adjacent crystalline lamellae for a semi-crystalline polymer. For well defined systems, additional orders of diffraction of lower intensity and at higher scattering angle are observed. These diffraction peaks are equally separated by a distance, d (this spacing usually increases for higher orders of diffraction if the structure is less ordered). In addition to the above interference scattering, the overall scattered intensity is dependent upon the size and shape of the scattering entities. These two contributions to the scattering intensity (see equation 6.17) are often separated during SAXS data analysis, see figure 6.11.

$$I(q) \propto P(q)S(q) \qquad (6.17)$$

where P(q) is the single particle scattering function and S(q) is the interference function. P(q) is determined by the size and shape of the scattering entities and S(q) depends upon the separation and arrangement of these entities.

Detailed texts describing the approaches used to separate these two contributions for a variety of scattering systems have been presented elsewhere.[11-14]

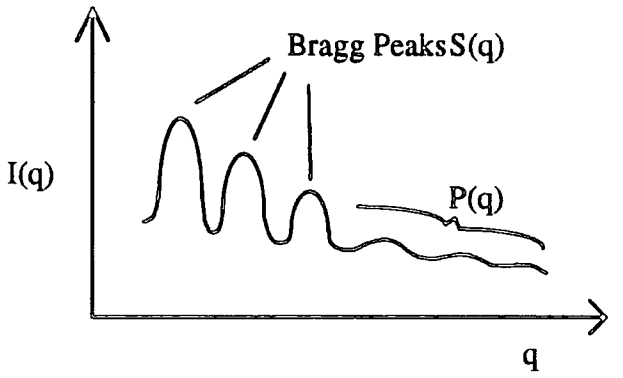

Figure 6.11. Contributions to SAXS Data.

For the work presented in this chapter, 1-dimensional and three-dimensional correlation functions have been calculated. These functions are based on the earlier work by Debye, Anderson and Brumberger[15]. The 1-dimensional correlation function $\gamma(x)$, is related to the experimental scattering intensity by:

$$\gamma(x) = \frac{\int_0^\infty s^2 I(s) \cos 2\pi x s ds}{\int_0^\infty s^2 I(s) ds} \qquad (6.18)$$

where x is the coordinate perpendicular to the layers under investigation and $s=q/2\pi$. It can be visualised as follows: according to Chalkeley et al[16], one considers a measuring rod AB of length x perpendicular to the layers, which moves in the x direction through the layers. In each position within the sample, the product of the electron density deviations, η, at A and B is determined. The correlation function is obtained by averaging overall positions followed by multiplying by $1/\langle\eta^2\rangle$ where $\langle\eta^2\rangle$ is the average obtained for x=0. Hence the value of $\gamma(0)$ is +1 and $-1<\gamma(x)<+1$.

As described more recently by Zachmann et al[17], the 1-dimensional correlation function contains features characteristic of the specific inner surface, the phase volume fractions, the mean domain sizes and the most probable long periods.[18,19]

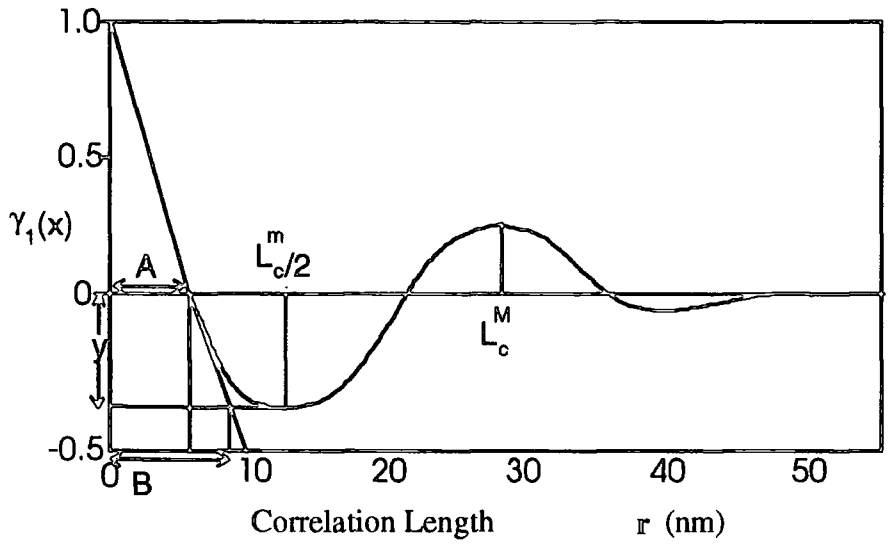

Figure 6.12. Typical Correlation Function Displaying the Main Parameters to be used.

Figure 6.12 displays a typical 1-dimensional correlation function and the parameters that are determined from this function. The position of the first maximum indicates the most probable distance between the centres of gravity between two adjacent crystals or lamellar stacks of the same composition, i.e., the long period, L_c^M (see figure 6.13). L_c^m, the probable distance between the centre of gravity of a crystal and its adjacent amorphous region or between two adjacent lamellar stacks of different composition can be determined from the first minima. The values of L_c^M and L_c^m may vary if the superlattice is not perfect.

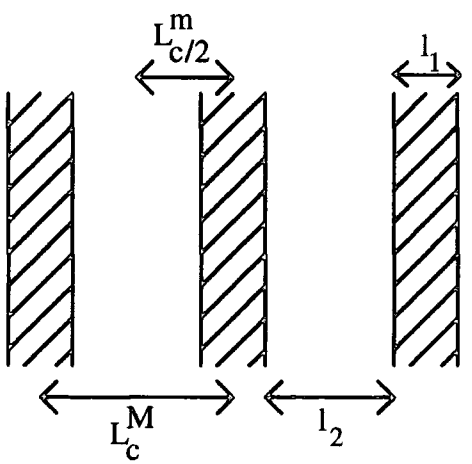

Figure 6.13. Lamellar Model with Evaluated Parameters.

The first intersection of the correlation function with the null line is the product $L_c^M\phi_A\phi_B$ where ϕ_A and ϕ_B are the respective compositions of each lamellar (domain) and any possible interface present leads to a curvature of the correlation function at low r values.

For semi-crystalline polymers, the degree of crystallinity, x_{cl}, within the lamellar stack may be determined from the 1-dimensional correlation function. In fact both lamellar fractions can be determined, but it is not possible to distinguish the degree of crystallinity, x_{cl}, from the amorphous fraction, $1-x_{cl}$, from the correlation function alone. Two methods are given below to determine x_i, x_1 and x_1^o where subscript 1 denotes the larger fraction.

1. $$\frac{1-x_1}{x_1} = cy \qquad (6.19)$$

where y is the value of the correlation function at its first minimum (see figure 6.12), and c is a factor determined in such a way that $c\gamma_1(0)=1$ or c=1, depending upon the definition of x_1 used.

2. $$x_1^o(1-x_1^o)L_c^M = A \qquad (6.20)$$

where A is the first intercept of the correlation function with the abscissa.

The thickness of the crystals, l_c, and that of the amorphous regions, l_a, may also be determined (see equations 6.21). Again, it is not possible to distinguish between l_c and l_a, and so the larger thickness is designated l_1 and the smaller l_2.

$$l_1 = x_1 L \qquad (6.21)$$

$$l_2 = (1-x_1)L \qquad (6.22)$$

Furthermore, l_2 can also be derived using equation 6.23[20]:

$$l_2 = B \tag{6.23}$$

where B is defined in figure 6.12.

If l_2 is determined by equation 6.23, there arises a new possibility to obtain $1-x_1$ using equation 6.22[21]. The value determined using this approach is designated x_{1L}.

For the 3-dimensional correlation function, intersection of this function with $\gamma_1(x)=0$ yields a 3-dimensional correlation length, 3-D. This length is similar the 1-dimensional length but is not restricted to just one direction.

6.4.2. Apparatus.

Small angle x-ray scattering experiments were carried out using a Kratky Compact Small Angle System (Anton Paar K.G. A-8054 GRAZ Austria). The camera is held in a cast brass housing and the whole system can be evacuated to 0.5mbar using the integrated vacuum system connected to a vacuum pump. An XRG 3000 Generator (INEL, Z.A. de Courtaboeuf Av.de.Scandinavie - 91953 LES ULIS) run at 20mA/20kV generates electrons which are fired off a copper target creating a source of x-rays of wavelength 1.54Å. The linear, gas tight (argon/methane 90/10%) detector is a LPS50 model as supplied by INEL, with a beryllium window. A fast analog-to-digital converter (model 8077, Canberra Industries, Inc., One State Street, Meriden CT 06450) converts the detected signal and displays the scattering profile on the screen of an interfaced PC. A temperature controllable sample holder (Anton Paar) enables samples to be heated from room temperature up to 523K. To obtain sufficient scattering intensity, the Kratky camera is fitted with a slit collimation system. The resultant desmeared intensity was corrected to eliminate such collimation effects during the analysis procedure. A moving slit device driven by a synchronous motor attached

to the slit holder facility, supplied by Anton Paar, allowed the measurement of both the absolute scattering intensity and the sample absorption.

Figure 6.14 displays a cross section of the geometrical set-up for the collimated system.

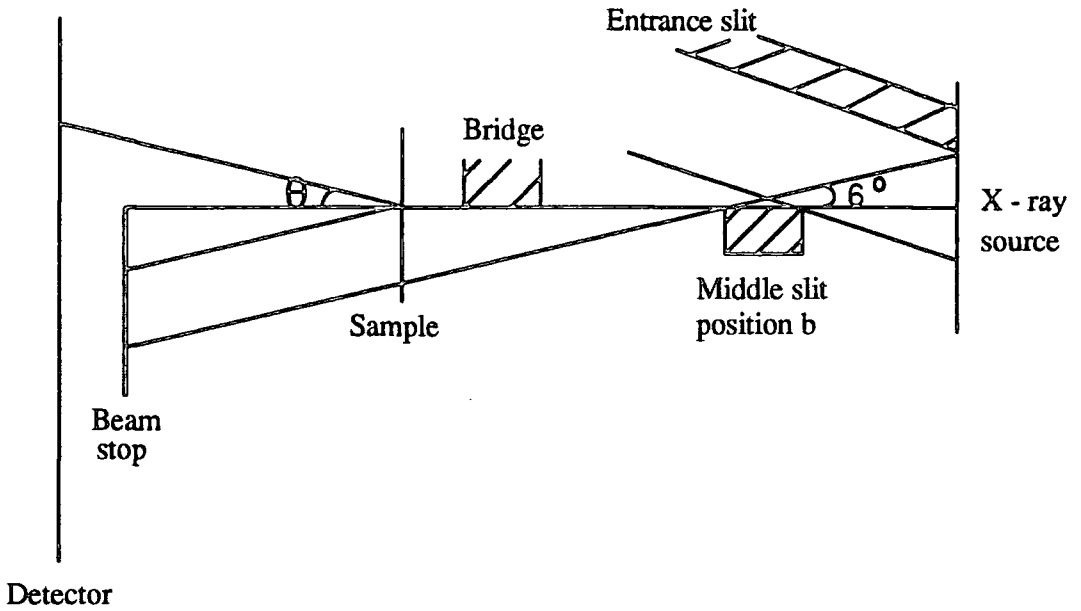

Figure 6.14. Geometrical Set-up of the Collimated Kratky Camera.

The bridge and the middle slit are precisely coplanar, thus minimising the level of parasitic scattering[22]. For the SAXS runs described in this chapter, the middle slit was placed in position b and the system oriented with a projection angle of -6°. This position of the middle slit optimises the set-up in terms of a medium to high resolution, medium incident x-ray intensity and an accessible set-up alignment.[23] The width and intensity of the primary beam are determined by the position of the entrance slit.

6.4.3. Experimental.

6.4.3.1. Sample Preparation.

The polymer samples were molded in a rectangular 26mm x 6mm x 1mm brass holder for the SAXS measurements. A rectangular hole was cut in the brass plate leaving a 1mm perimeter of brass. The brass holder was placed on a piece of aluminium foil, which in turn was placed on a Linkam hotstage. The piece of aluminium foil was large enough to cover both sides of the brass holder. The hotstage was heated to 423K, and the powdered polymer sample was placed in the brass window. A sufficient quantity of sample was molded into the brass holder (1mm deep) and then the sample plus holder was placed in a vacuum oven set at 423K and degassed under vacuum. No glue was used to stick the aluminium window to the brass holder as the melted polymer sample created enough adhesion. Once the polymer sample had been degassed, i.e., the polymer no longer bubbled, the sample was left to cool slowly under vacuum in the vacuum oven. At room temperature, the sample was covered with the attached sheet of aluminium foil forming an aluminium window on both sides of the brass holder. This aluminium window held the polymer sample in place when it was positioned vertically in the SAXS apparatus during the temperature runs.

The polymeric sample was then thermally treated before being placed in the SAXS apparatus. To prevent contact between the sample and the acetone/dry ice coolant (see below) during the thermal treatment, the sample was repeatedly covered with more sheets of aluminium foil. The aluminium wrapped sample was heated to 423K for a further 10 minutes on a Linkam hotstage and then cooled slowly on the hotstage ($-10Kmin^{-1}$) or quenched to a series of low temperatures, T' (see section 6.4.3.2.), by immersing the sample in a dry ice/acetone bath. The temperature of the bath was monitored using a thermostat (Digatron Instrumentation, (3200K) 223K to 1023K) and controlled at a specific temperature by adding more dry ice. The sample was held at T' for various permanence times, t, (see table 6.8). After time t, the sample

was removed from the bath, all of the aluminium covering apart from the initial aluminium window was removed and then placed in the groove of a customised SAXS invar sample holder, which in turn was placed in the Kratky sample heating stage.

6.4.3.2. SAXS Runs.

A number of SAXS runs were performed with different polymer samples, for a variety of permanence temperatures, T', for various permanence times, t and at several SAXS run temperatures, T_{saxs}. The SAXS measurements recorded for BC55 and BC50, quenched to T' and also cooled at $10Kmin^{-1}$ to T', are listed in table 6.8. The permanence time, t, for all runs was 60 minutes.

	Run Temp (K) T_{saxs}							
T' (K)	303	313	318	323	328	333	343	373
289				√				
283				√				
273				√				
263				√				
253				√				
243				√				
233	√	√	√	√	√	√	√	√

Table 6.8. SAXS Measurements for BC50 and BC55.

As well as those SAXS runs shown in table 6.8., the following additional runs were performed:

BC50 and BC55.

Both samples were quenched to T'=233K, and the permanence time at T' was varied (t=5, 15, 30, 120 mins). The samples were then heated in the SAXS apparatus to 323K and SAXS measurements recorded.

BC76, PEO and BL80.

These samples were quenched and cooled slowly ($10Kmin^{-1}$) to room temperature. After 60 minutes at room temperature, the samples were heated in the SAXS apparatus to 323K, and SAXS measurements recorded.

6.4.3.3. Correction and Normalisation of Raw Data.

The raw SAXS data were normalised and corrected using FFSAXS5, which is a collection of FORTRAN routines originally described by Vonk.[24] The following additions to the original FFSAXS operations were included in FFSAXS5:

1) Calculation of the particle size distribution functions[14]

2) Calculation of the 1-dimensional and 3-dimensional interface distribution functions for 2-phase layered structures[25] and

3) Adaptations for the use of film methods[26].

Prior to using FFSAXS5, it was necessary to prepare the raw data using a program called SAXFIL. SAXFIL contains parameters for the routines in FFSAXS5. These parameters have been summarised below.

SCAL - scales the intensity of data set 2 (the parasitic instrumental background) to the level of set 1 (sample data). Values used in SAXFIL: 1 2 1 0 0

SUB - subtracts the intensity values in set 2 (scaled background) from set 1 (sample data). Values used in SAXFIL: 1 2.

BKGR - Calculates the 'sample' background (sometimes called 'liquid scattering') and subtracts this from the set 1 (sample data set) and stores the result in set 1 (smeared background corrected data). Values used in SAXFIL: 1 4 0 700 23000. The sample background was fitted to Porod's Law, as described in more detail in the FFSAXS5 manual.[27]

DESM - The scattered smeared intensities (set 1) were desmeared according to Vonk[28]. Values used in SAXFIL: 1 3 0 0 0. The desmeared intensities are placed on set 3.

CORL - Both 1-dimensional and 3-dimensional correlation functions were calculated by means of Fourier transformations.[29,20] Values used in SAXFIL: 3 1 0 2 600. Using these parameters, the intensity curve was first extrapolated to x=0 using a Gaussian function from R=0 to 600Å with an incremental value of 2.

ANAL - This analysis routine listed the necessary information in an array which were required for the analysis of the scattering curve. These included the channel number, distance along the detector, s and H values (where $H \equiv q = (4\pi/\lambda)\sin(\theta/2)$ and $q = 2\pi s$), and the number of counts. Values used in SAXFIL: 3 0 0 0 0 0 0 0 0 0 0 0 0.

In addition to the parameters listed above, SAXFIL conditions the actual channel contents by providing the following values: wavelength, sample to detector distance, focus to sample distance, calibration factors, transmission factors and values to calculate the height of a channel above the position of the main beam.[30]

FFSAXS5 is a very sensitive data processing program. Small change in the parameters used in this program have a large effect on the desmeared intensity distributions and the correlation functions obtained. Consequently, great care must be taken when determining the values of the parameters to be used in this program.

BKGR - Calculates the 'sample' background (sometimes called 'liquid scattering') and subtracts this from the set 1 (sample data set) and stores the result in set 1 (smeared background corrected data). Values used in SAXFIL: 1 4 0 700 23000. The sample background was fitted to Porod's Law, as described in more detail in the FFSAXS5 manual.[27]

DESM - The scattered smeared intensities (set 1) were desmeared according to Vonk[28]. Values used in SAXFIL: 1 3 0 0 0. The desmeared intensities are placed on set 3.

CORL - Both 1-dimensional and 3-dimensional correlation functions were calculated by means of Fourier transformations.[29,20] Values used in SAXFIL: 3 1 0 2 600. Using these parameters, the intensity curve was first extrapolated to x=0 using a Gaussian function from R=0 to 600Å with an incremental value of 2.

ANAL - This analysis routine listed the necessary information in an array which were required for the analysis of the scattering curve. These included the channel number, distance along the detector, s and H values (where $H \equiv q = (4\pi/\lambda)\sin(\theta/2)$ and $q = 2\pi s$), and the number of counts. Values used in SAXFIL: 3 0 0 0 0 0 0 0 0 0 0 0 0.

In addition to the parameters listed above, SAXFIL conditions the actual channel contents by providing the following values: wavelength, sample to detector distance, focus to sample distance, calibration factors, transmission factors and values to calculate the height of a channel above the position of the main beam.[30]

FFSAXS5 is a very powerful data processing program. Small changes in the parameters used in this program have a large effect on the desmeared intensity distributions and the correlation functions obtained. Consequently, great care must be taken when determining the values of the parameters to be used in this program.

6.4.4. Results.

After normalisation and correction of the raw data files, a desmeared x-ray scattering intensity distribution as a function of s ($s=(2\pi/\lambda)\sin(\theta/2)$) was obtained for each SAXS measurement. Figure 6.15 displays the desmeared intensity distribution for BC55, T'=233K, T_{saxs}=323K. The shape of the intensity profile was found to be very typical for all SAXS runs. The sharp peak at $s=0.00125\text{Å}^{-1}$ is due to a contribution from the main beam spilling over the beam stop, whereas the peaks of lower intensity at higher s are due to sample scattering.

The FFSAXS5 program also evaluated one-dimensional and three-dimensional correlation functions for each SAXS measurement. Figure 6.16 displays an example of the 1-D and 3-D correlation functions for BC50, T'=233K, T_{saxs}=323K. These functions were later analysed according to a procedure used by Zachmann, see section 6.4.1.

For a few data runs, the FFSAXS5 program was unable to desmear the raw data according to the parameters used (see section 6.4.3.3). This can be attributed to the close proximity of the scattering peak to the main beam position and shows a limitation in the applicability of FFSAXS5.

6.4.5. Analysis.

6.4.5.1 Desmeared Intensity.

The Bragg spacings, d (see section 6.4.1), were determined from the desmeared intensity distribution versus s plots for each SAXS run. To facilitate in the evaluation of the scattering peak position, in some cases, log I vs. s was used (see figure 6.17). From figure 6.17, the peak position correspond to the following s values: 0.0015, 0.0034, 0.0056, 0.0078 Å^{-1}. The difference between each peak position is relatively constant, tending to increase with higher orders of diffraction. This indicates a lamellar structure with a degree of disorder and/or a distribution of lamellar spacing. The evaluated d values have been listed in tables 6.9 to 6.17. All the length values listed in these tables have Å units.

Figure 6.15 Desmeared Scattered Intensity vs. s for BC55, T'=233K, T_{SAXS}=323K.

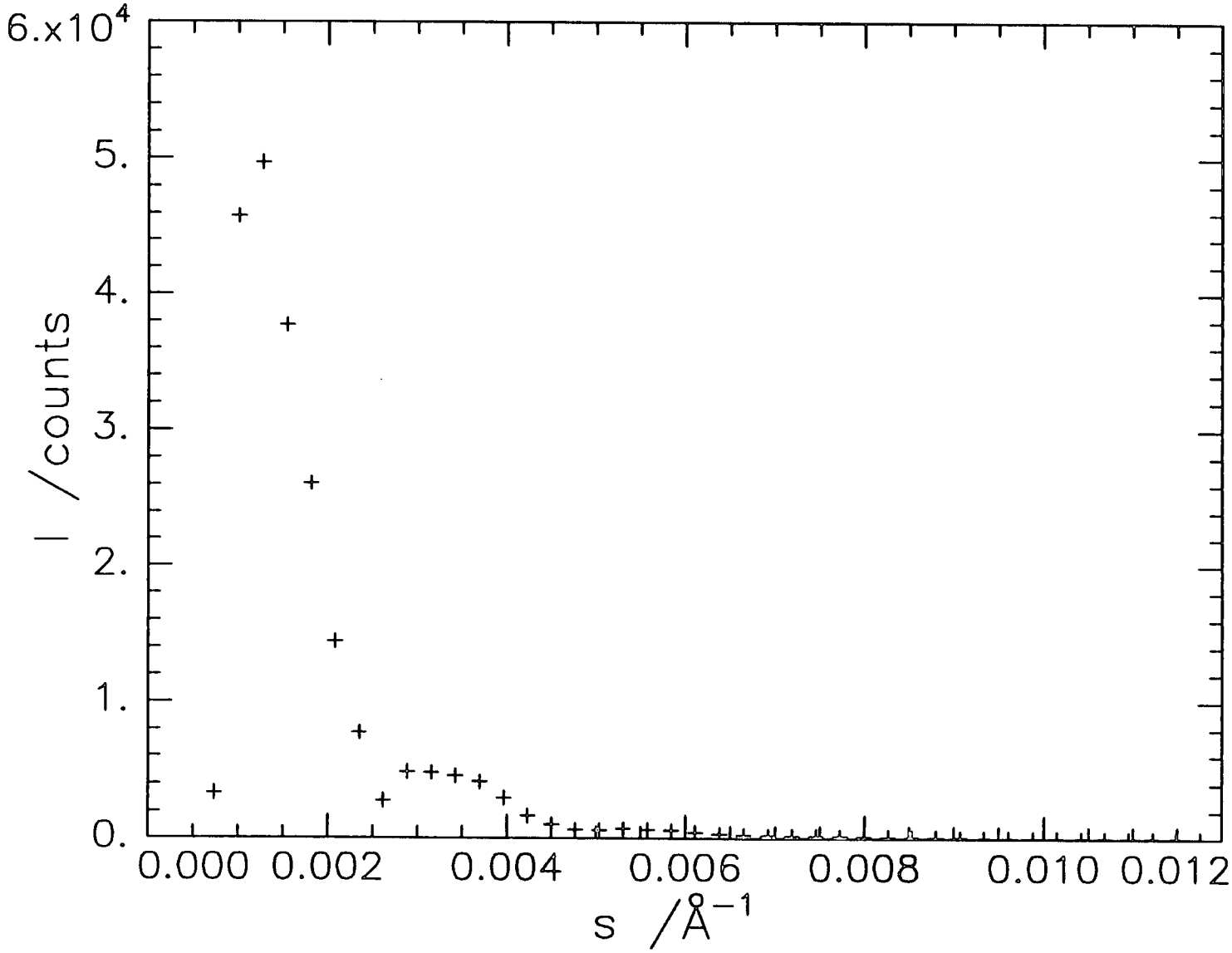

Figure 6.16 1-D and 3-D Correlation Functions for BC50, T'=233K, T_{SAXS} =323K.

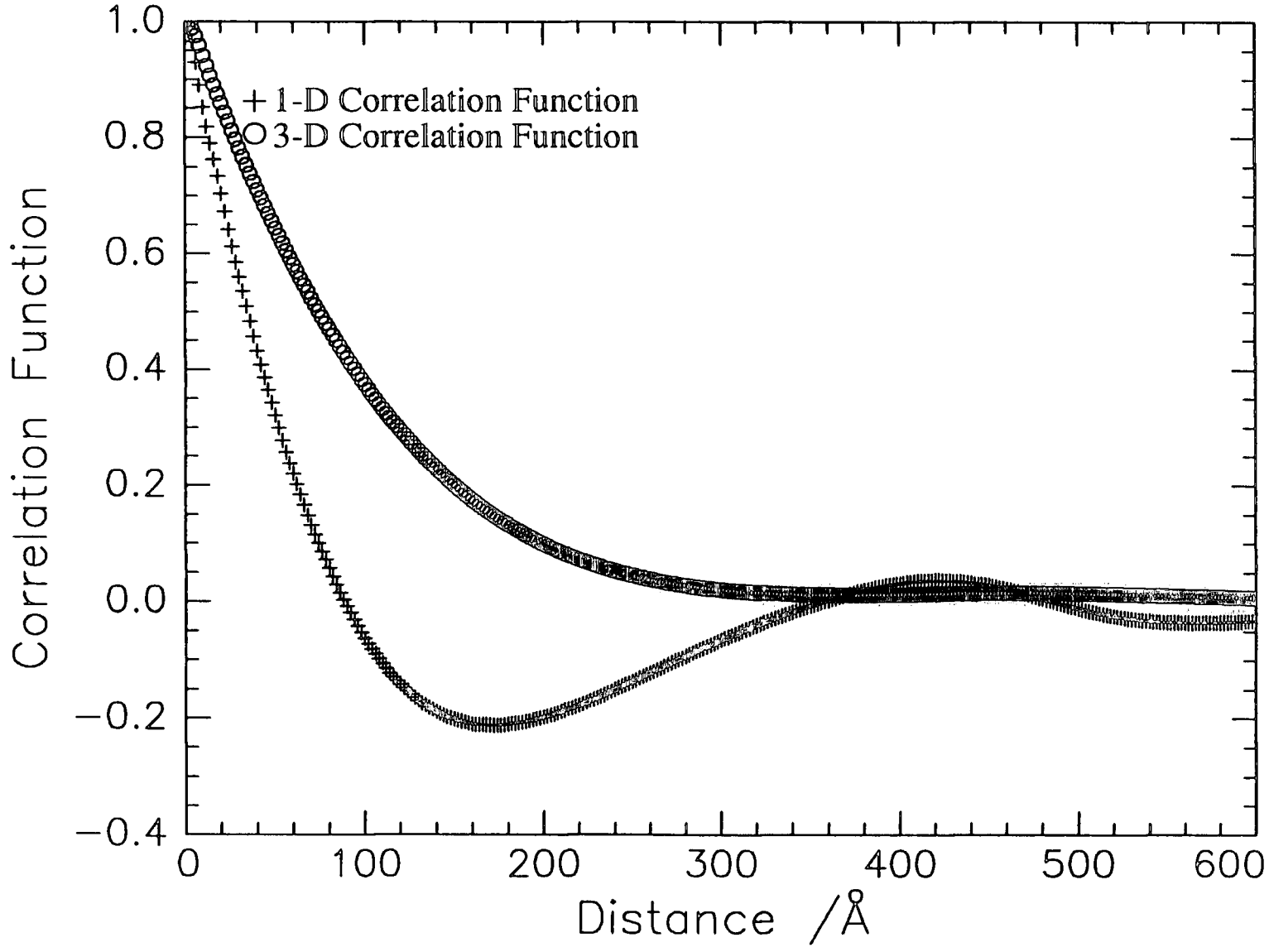

Figure 6.17 Log(I) vs. s for BC55, T'=233K, T_{SAXS}=323K.

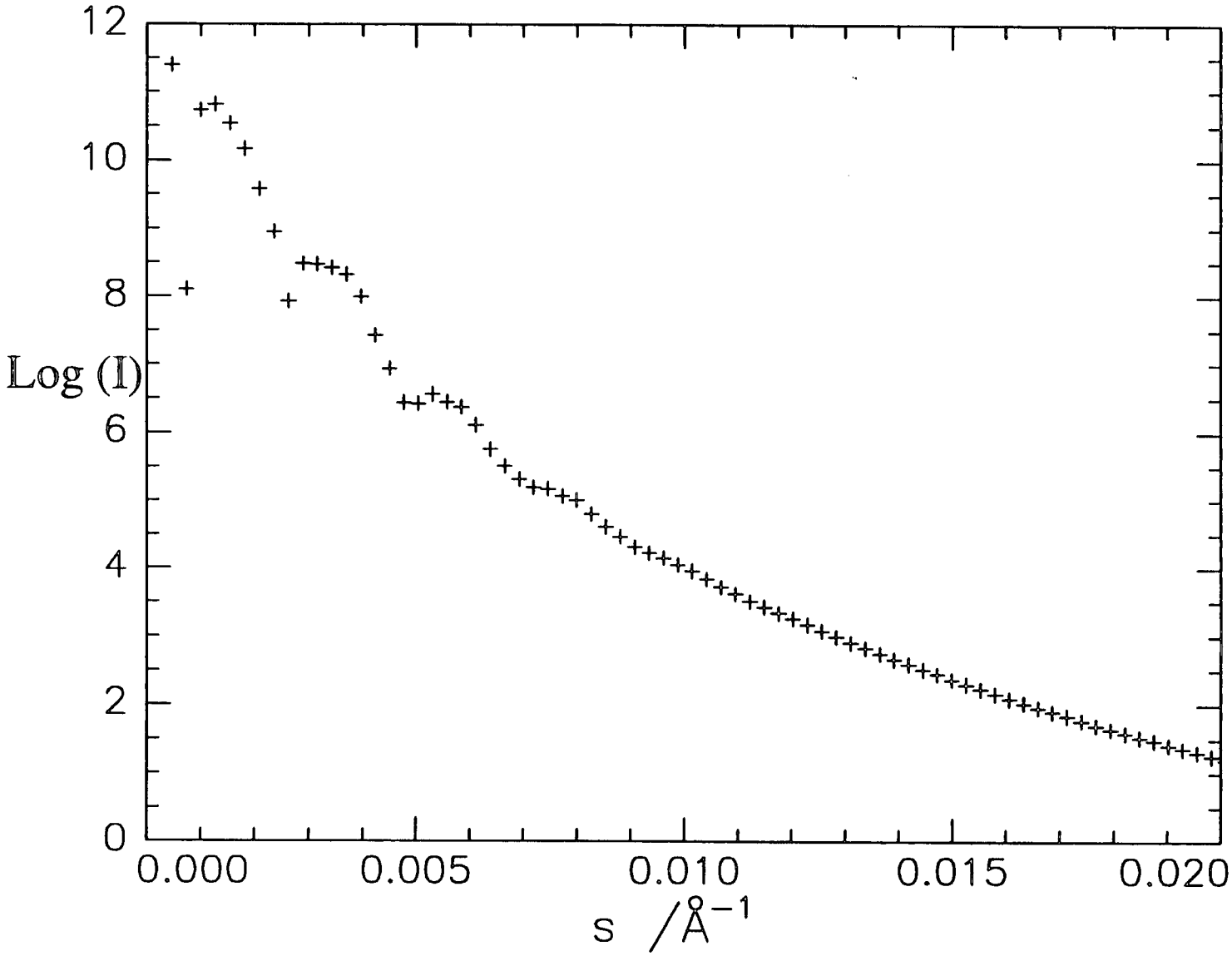

6.4.5.2. Correlation Functions.

The parameters evaluated from the 1-dimensional and 3-dimensional correlation functions are listed in tables 6.9 to 6.17.

T' (K)	A	B (l_2)	y	$L_c^m/2$	L_c^M	3-D	d	l_1	x_1^o	x_1
289	84	99	0.191	222	357	450	494	415	0.62	0.84
283	88	104	0.191	218	338	462	455	382	-	0.84
273	87	110	0.226	228	325	462	455	373	-	0.82
263	86	99	0.187	225	299	477	444	373	-	0.84
253	79	88	0.172	189	360	451	455	387	0.68	0.85
243	72	86	0.187	175	290	442	476	400	0.54	0.84

Table 6.9. BC55 Quenched to T'. Run at T_{saxs} =323K.

T' (K)	A	B (l_2)	y	$L_c^m/2$	L_c^M	3-D	d	l_1	x_1^o	x_1
273	79	88	0.171	200	422	-	472	401	0.75	0.85
263	74	90	0.226	197	427	436	469	385	0.78	0.82
253	72	93	0.26	186	-	420	469	371	-	0.79
243	81	93	0.141	202	345	425	448	394	0.62	0.88
233	72	89	0.23	176	-	379	465	377	-	0.81

Table 6.10. BC50 Quenched to T'. Run at T_{saxs} = 323K.

T' (K)	A	B (l_2)	y	$L_c^m/2$	L_c^M	3-D	d	l_1	x_1^o	x_1
293	96	100	0.003	256	400	-	484	479	0.60	0.99
283	91	107	0.016	224	412	600	476	466	0.67	0.98
273	81	94	0.017	207	no max	540	-	-	-	0.98
263	87	108	0.23	224	no max	386	476	386	-	0.81
253	73	85	0.188	182	no max	510	-	-	-	0.84
243	81	93	0.14	199	376	578	476	419	0.69	0.88
233	66	81	0.215	172	419	372	435	357	0.80	0.82

Table 6.11. BC55 Cooled at 10Kmin^{-1} to T'. Run at T_{saxs}=323K.

T' (K)	A	$B(l_2)$	y	$L_c^m/2$	L_c^M	3-D	d	l_1	x_1^o	x_1
273	113	160	0.09	273	-	-	455	419	-	0.92
263	-	-	-	-	-	-	-	376	-	-
253	73	92	0.268	194	517	320	476	376	0.83	0.79
243	58	77	0.26	163	504	344	444	351	0.87	0.79
233	64	78	0.174	176	-	440	426	362	-	0.85

Table 6.12. BC50 Cooled at $10Kmin^{-1}$ to T'. Run at T_{saxs}=323K.

T_{saxs} (K)	A	$B(l_2)$	y	$L_c^m/2$	L_c^M	3-D	d	l_1	x_1^o	x_1
303	75	84	0.123	210	333	560	426	379	0.66	0.89
313	72	81	0.15	177	299	444	444	386	0.59	0.87
318	63	73	0.155	174	308	439	465	405	0.71	0.87
323	61	71	0.166	161	no max	384	455	391	-	0.86
328	67	82	0.24	171	-	295	-	-	-	0.81
333	91	109	0.2	242	-	436	455	378	-	0.83
343	94	-	-	no min	-	-	462	-	-	-

Table 6.13. BC55 quenched to T'=233K, t=60 minutes.

T_{saxs} (K)	A	$B(l_2)$	y	$L_c^m/2$	L_c^M	3-D	d	l_1	x_1^o	x_1
303	63	72	0.12	165	416	-	476	424	0.81	0.89
313	64	72	0.14	161	419	-	455	400	0.81	0.88
318	61	71	0.149	158	428	-	455	739	0.83	0.87
323	70	86	0.215	173	420	310	465	381	0.79	0.82
328	72	86	0.23	178	473	315	-	-	0.81	0.81

Table 6.14. BC50, quenched to T'=233K, t=60 minutes.

t (min.)	A	$B(l_2)$	y	$L_c^m/2$	L_c^M	3-D	d	l_1	x_1^o	x_1
5	62	80	0.27	164	498	-	455	359	0.86	0.79
15	63	77	0.2	164	525	336	465	386	0.86	0.83
30	64	78	0.22	170	-	337	-	-	-	0.83
120	66	79	0.2	173	537	358	488	405	0.86	0.83

Table 6.15. BC50 Quenched to T'=233K. Run at T_{saxs}=323K.

t (min)	A	$B(l_2)$	y	$L_c^m/2$	L_c^M	3-D	d	l_1	x_1^o	x_1
5	71	79	0.135	175	no max	560	437	385	-	0.88
15	70	81	0.131	179	417	600	476	419	0.79	0.88
30	64	74	0.155	161	422	536	526	458	0.81	0.87
120	62	69	0.12	159	413	-	476	424	0.82	0.89

Table 6.16. BC55 quenched to T'=233K. Run at T_{saxs}=323K.

	A	$B(l_2)$	y	$L_c^m/2$	L_c^M	3-D	d	l_1	x_1^o	x_1
BC76 Quenched to 293K	16	17	0.08	117	-	345	476	443	-	0.93
BC76 Cooled to 293K	64	76	0.14	169	-	421	444	391	-	0.88
PEO Quenched to 293K	86	94	0.10	252	373	-	459	418	0.64	0.91
PEO Cooled to 293K	97	-	-	-	-	-	455	-	-	-
BL80 Cooled to 293K	91	102	0.12	260	358	538	465	414	-	0.89

Table 6.17 Additional SAXS runs, T_{saxs}= 323K.

6.4.6. Discussion.

The values presented in tables 6.9 to 6.17 provide structural information about the crystallinity and microphase separated regions in the polymers studied. It is important to note that the analysis is based upon a lamellar two phase model with sharp interphase boundaries. The diffraction peaks are positioned close to the main beam position (see figure 6.15) and so resolution of the lamellar is relatively low, and the resultant values obtained are slightly dependent upon the parameters used in FFSAXS5, so some caution should be observed when discussing the absolute values of the resultant structural parameters.

As described in section 6.4.1, the Zachmann analysis is unable to distinguish whether l_1, x_1^o and x_1 are associated with the crystalline or amorphous regions. For BC50 and BC55, it is not expected that the all of the PEO component fully crystallises and so it can be assumed that the smaller fraction of the parameters l_i, x_i^o and x_i are associated with the crystalline component.

6.4.6.1. Variation with T' for BC50 and BC55.

6.4.6.1.1. Cooled at 10Kmin^{-1} to T'.

Figures 6.18 and 6.19 plot the length values l_2, l_1, $L_c^m/2$, 3-D and d versus permanence temperature, T', for BC55 and BC50 respectively.

The crystalline thickness, l_2, was evaluated to be 90±10Å for all T' temperatures investigated for BC55 and for T'<253K for BC50. For BC50, T'>273, a much larger value for l_2 was obtained. Similar trends with respect to the permanence temperature were obtained for the amorphous lamellar thickness, l_1 and $L_c^m/2$. This change in length values for BC50 between T'=253K and T'=273K suggests that between these temperatures, a structural transition is present. This difference in behaviour is analogous to the T_{tr}' temperature determined using WAXS (see section 6.3.7.2). The temperature of this transition supports earlier work using WAXS (section 6.3) that shows at T'<253K, microphase separation occurs inducing

Figure 6.18 BC55, Cooled to T', t=60 minutes, Run at 323K.

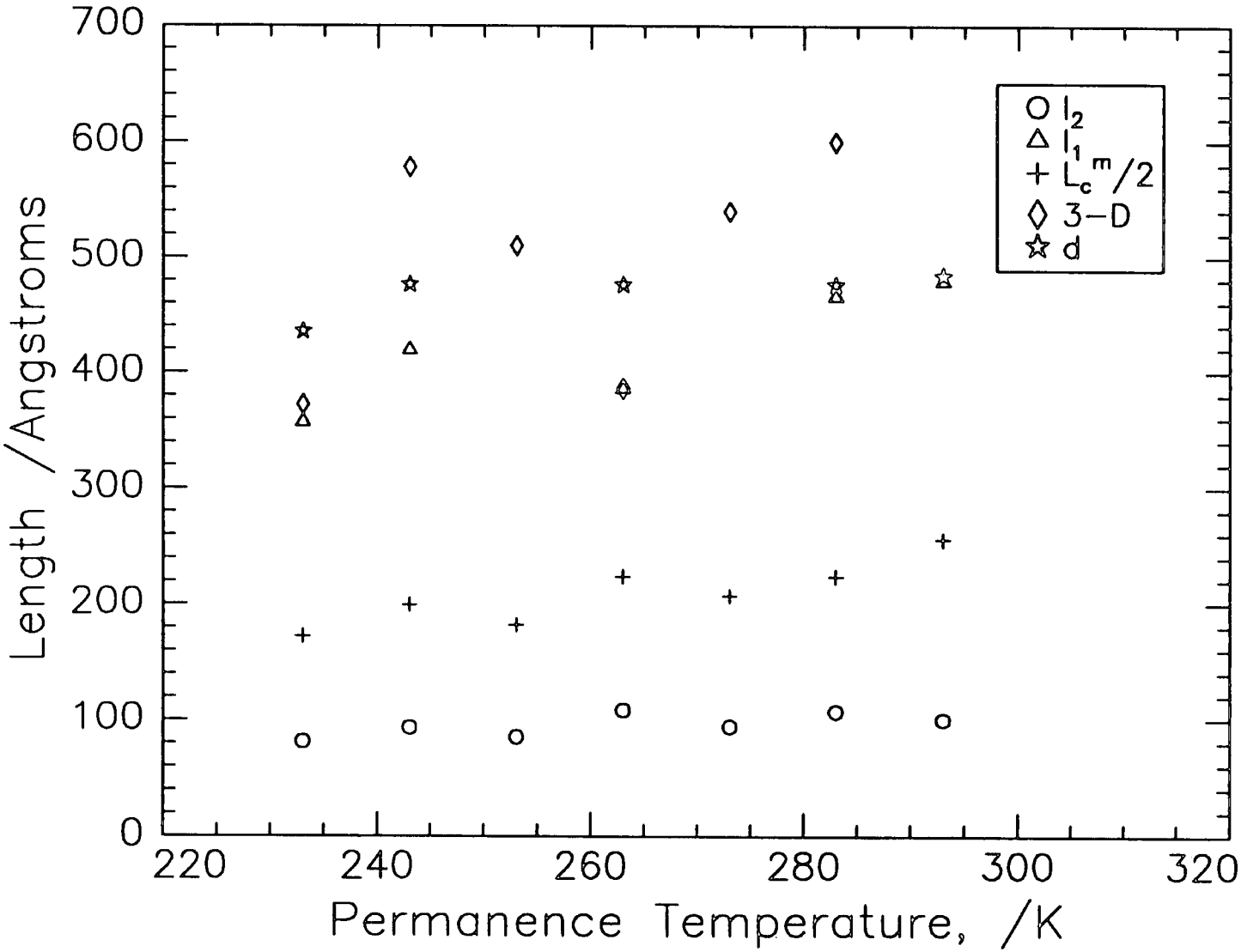

Figure 6.19 BC50, Cooled to T', t=60 minutes, Run at 323K.

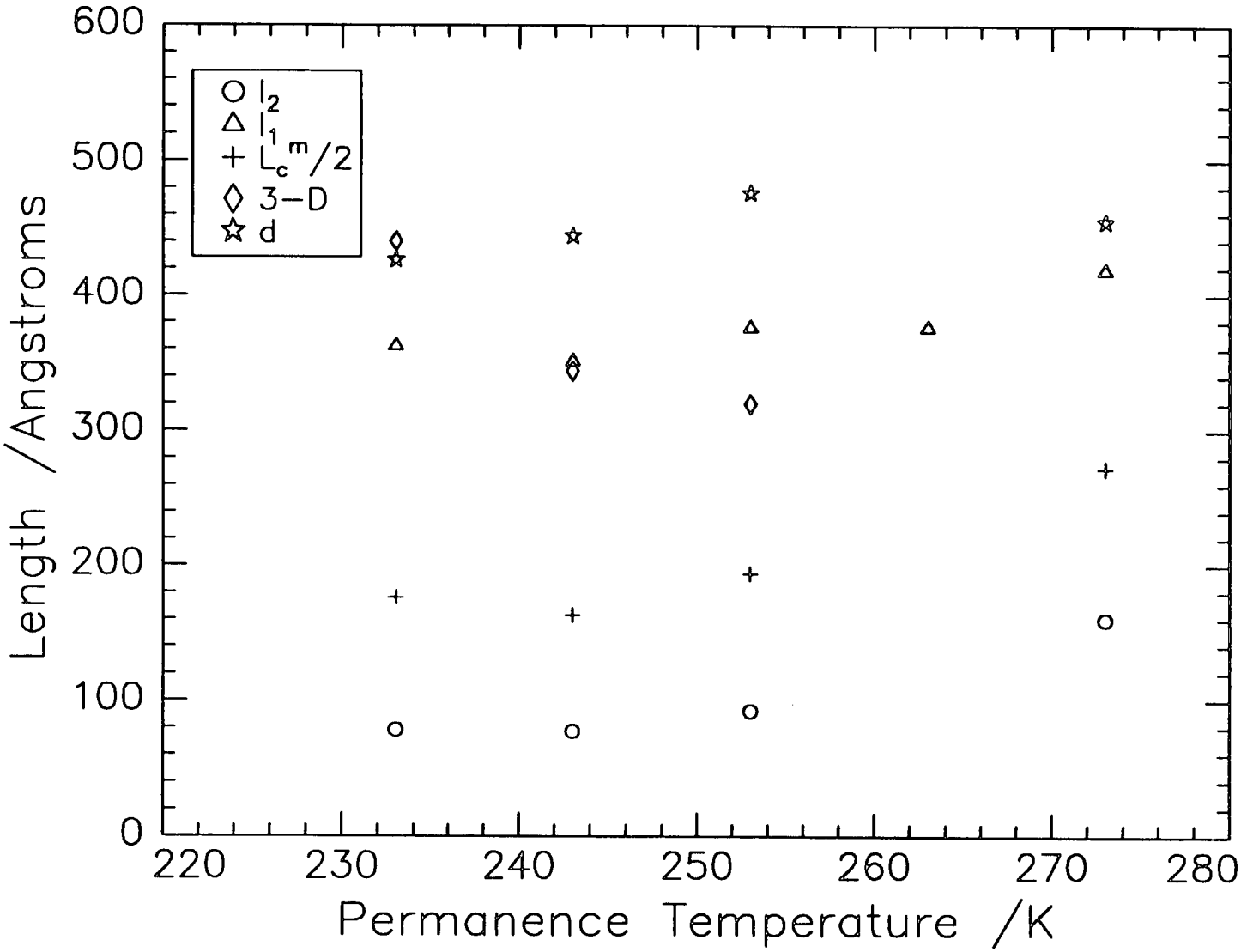

crystallisation at 323K for BC50. In fact, for T'=273K, no crystalline diffraction peak was observed and the amorphous fraction index x_1 increased from 0.79 to 0.92.

For BC55, no variation in length values with T' was detected. This suggests that the slower cooling rate ($10Kmin^{-1}$), allows the PEO component to crystallise directly from the melt without the aid of microphase separated PEO rich regions. This suggestion is supported by previous WAXS experiments (see section 6.3). However, x_1 increased abruptly between T'=263K and T'=273K. These indices above T'=273K are close to 1 indicating the presence of a fully amorphous phase. This behaviour may be attributed to the presence of an ODT transition below T'=263K, where phases comprised of 80% amorphous fraction are formed.

The Bragg spacing, d, was constant for both block copolymers over the complete range of permanence temperatures investigated. A value of d=460±20Å was obtained. It is interesting to note that whereas the values for L_c^M are approximately twice as large as the respective $L_c^m/2$ values for BC55, the ratio L_c^M:$L_c^m/2$ is closer to 2.5 for BC50. This suggests a higher ordered, more well defined structure for BC55 with respect to BC50.

6.4.6.1.2. Quenched to T'.

Only a slight increase in some length values were detected as T' increased, see figures 6.20 and 6.21. On the whole, the values listed in tables 6.9 and 6.10 were relatively constant and no variation between the values for BC55 and those for BC50 were observed.

6.4.6.2. Variation with Run Temperature, T_{SAXS}.

As T_{SAXS} increased to the apparent crystallisation temperature, a small decrease in the length values and an increase in the crystalline fraction was observed, see figures 6.22 and 6.23. This reflects crystallisation of the polymers at temperatures close to 323K. In addition, a slight plateau was observed in the first minimum for the 1-D correlation functions, which is indicative of the presence of crystallinity.[17] Above

Figure 6.20 BC55, Quenched to T', t=60 minutes, Run at 323K.

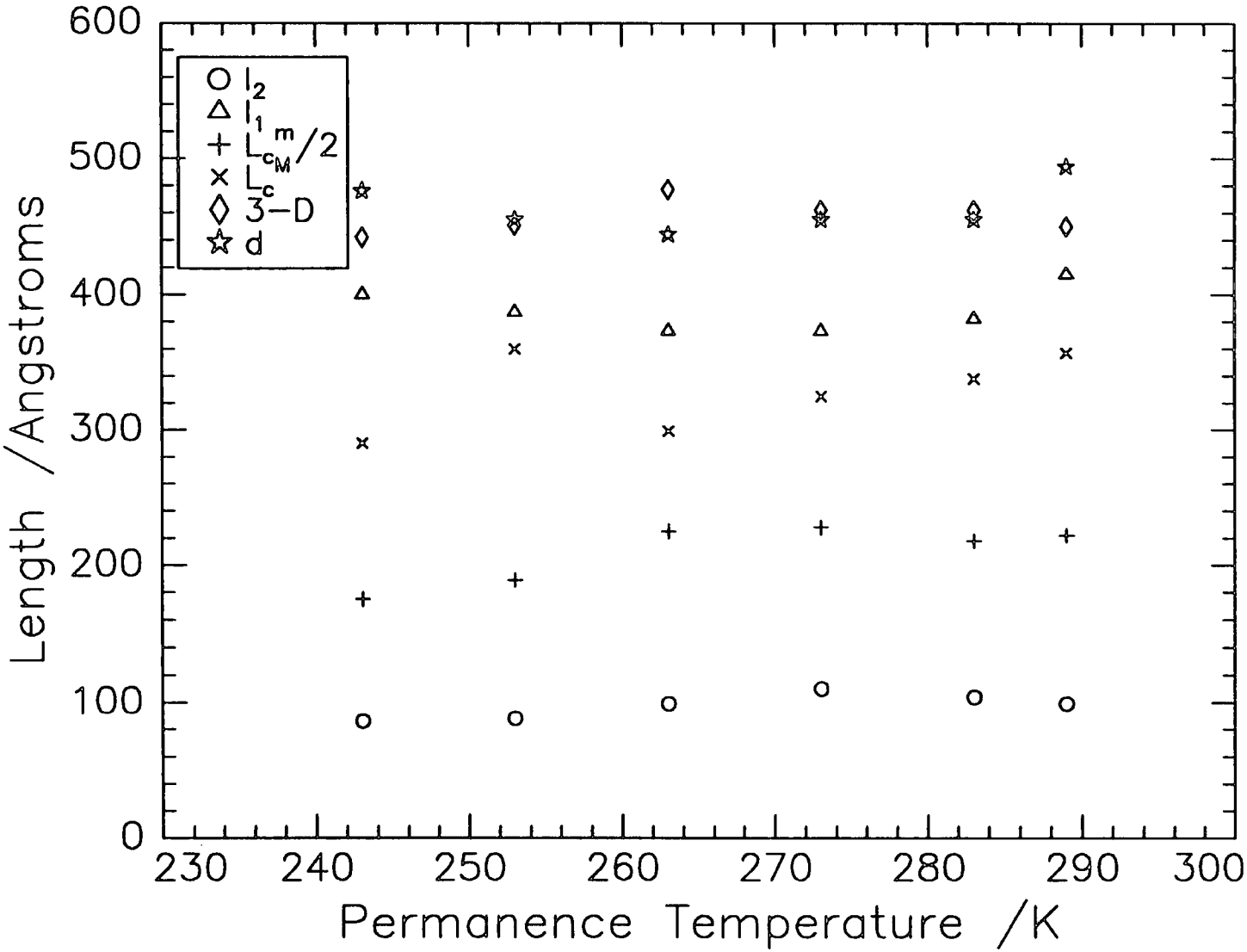

Figure 6.21 BC50, Quenched to T', t=60 minutes, Run at 323K.

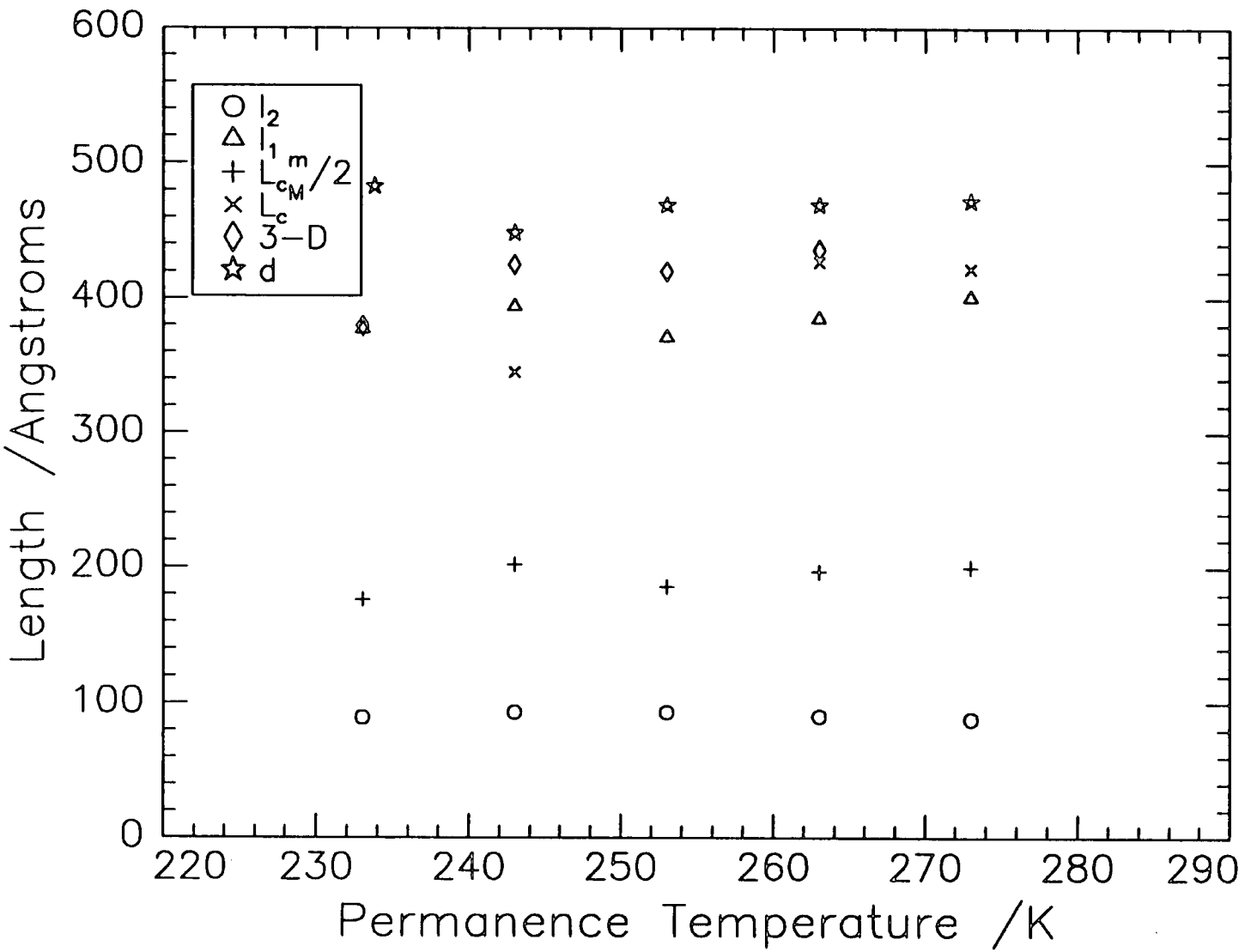

Figure 6.22 BC55, Quenched to T'=233K, t=60 minutes.

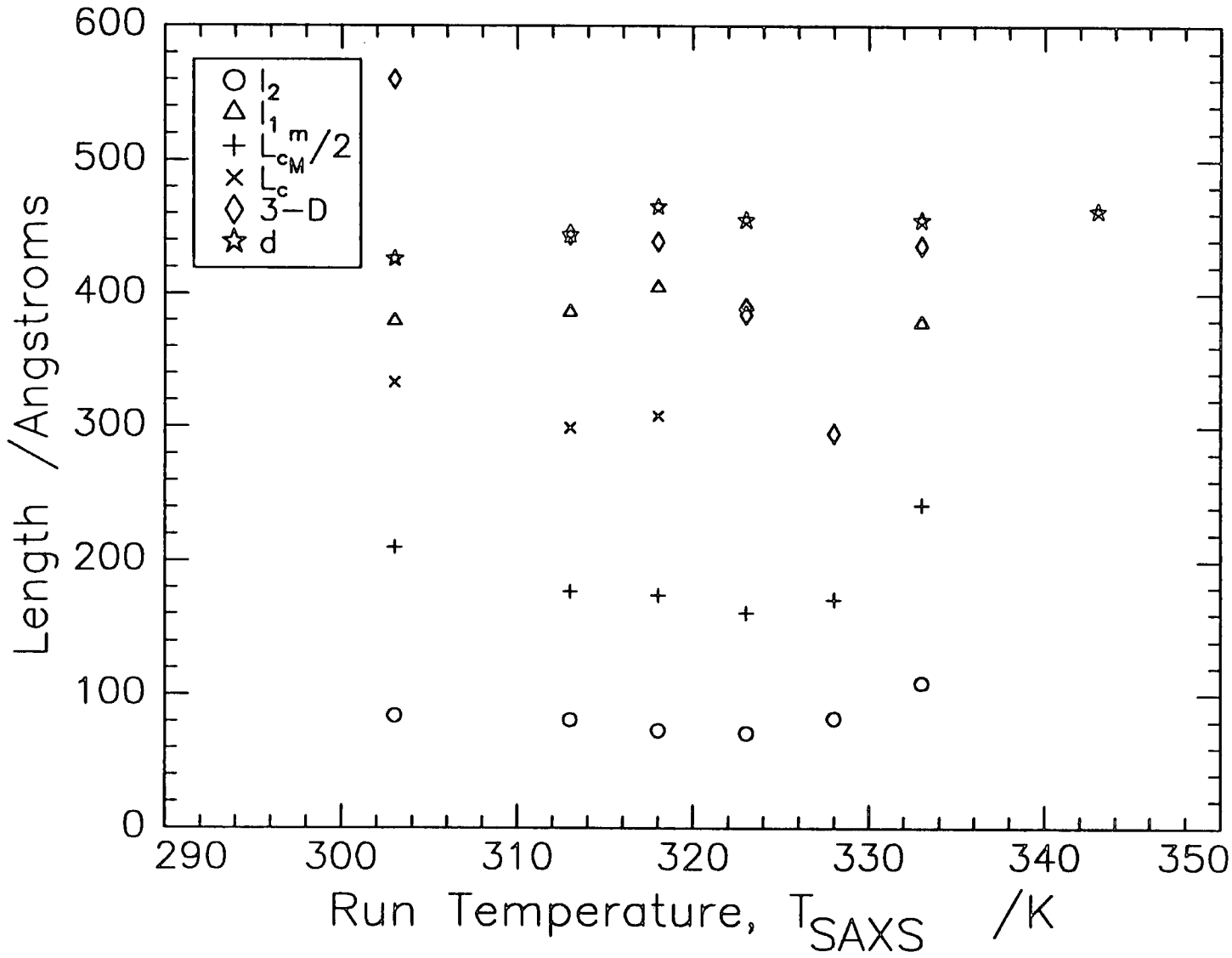

Figure 6.23 BC50, Quenched to T'=233K, t=60 minutes.

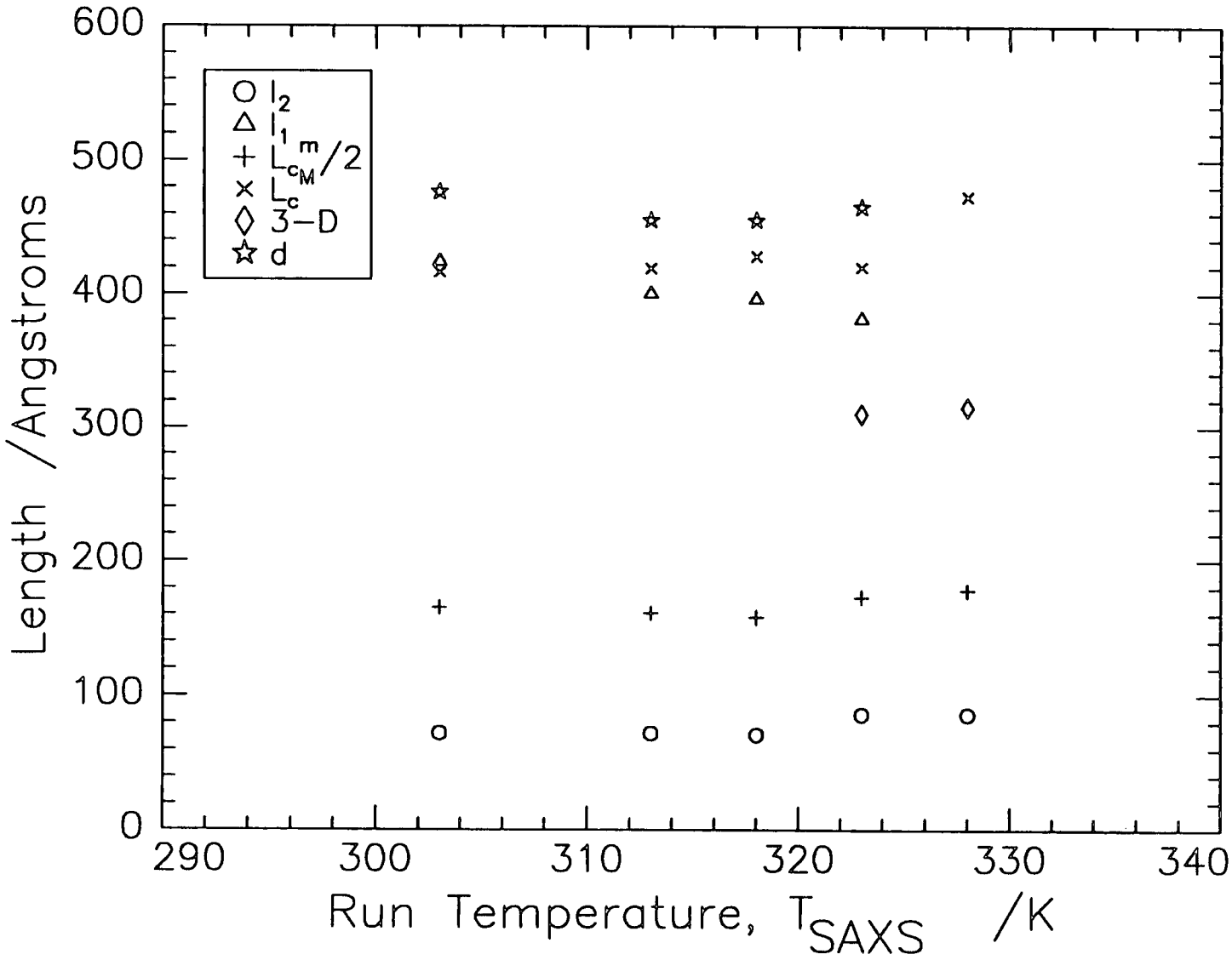

323-328K, an abrupt increase in the values l_2, $L_c^m/2$, 3-D for BC55 and L_c^M, l_2, $L_c^m/2$ for BC50 was observed. These increases reflect a partial breakdown in the polymer structure, i.e., melting. However, the structure is not completely lost. In fact at 343K for BC55, i.e., above T_m', well defined diffraction peaks are observed, see figure 6.24, indicative of ordered lamellar. As shown in figure 6.24, the s positions of these peaks are at 0.0016, 0.0035, 0.0057, 0.0077 and 0.0098 $Å^{-1}$. The difference between each peak is approximately 0.002 $Å^{-1}$, indicating that these peaks are consecutive orders of diffraction from a well ordered lamellar structure. A possible explanation for this behaviour is presented below. The block polymer microphase separates at low permanence temperatures forming lamellar regions rich in either PEO or PMMA. Upon heating to 323K, the PEO rich regions crystallise. Above 323K, the crystals melt, however, the PEO rich fraction is retained in between a hard PMMA rich lamellar latex. The temperature above melting is well below the glass transition temperature of the PMMA rich lamellar.

6.4.6.3. Variation with Permanence Time, t.

No change in length or crystallinity values with permanence time, t, was observed for both BC55 and BC50. This indicates that the structural organisation at T'=233K is complete after 5 minutes.

6.4.6.4. BC76, BL80 and PEO.

The evaluated correlation functions for these three polymer systems were very similar, see figures 6.25 to 6.27. The blend BL80, exhibited similar structural values as those for PEO. For BC76, however, the associated length values were appreciably smaller. This reflects the restrictive nature to crystallisation imposed by the chemical joint in the block copolymer. For these polymer systems, subscript 1 for x_1, x_1^o and l_1 denotes the PEO fraction. It is surprising that for BC76, BL80 and PEO, x_1 is approximately 0.9. Although this value is close to the expected value for these

Figure 6.24 Defined Lamellar Diffraction, BC55 T'=233K, T_{SAXS}=343K.

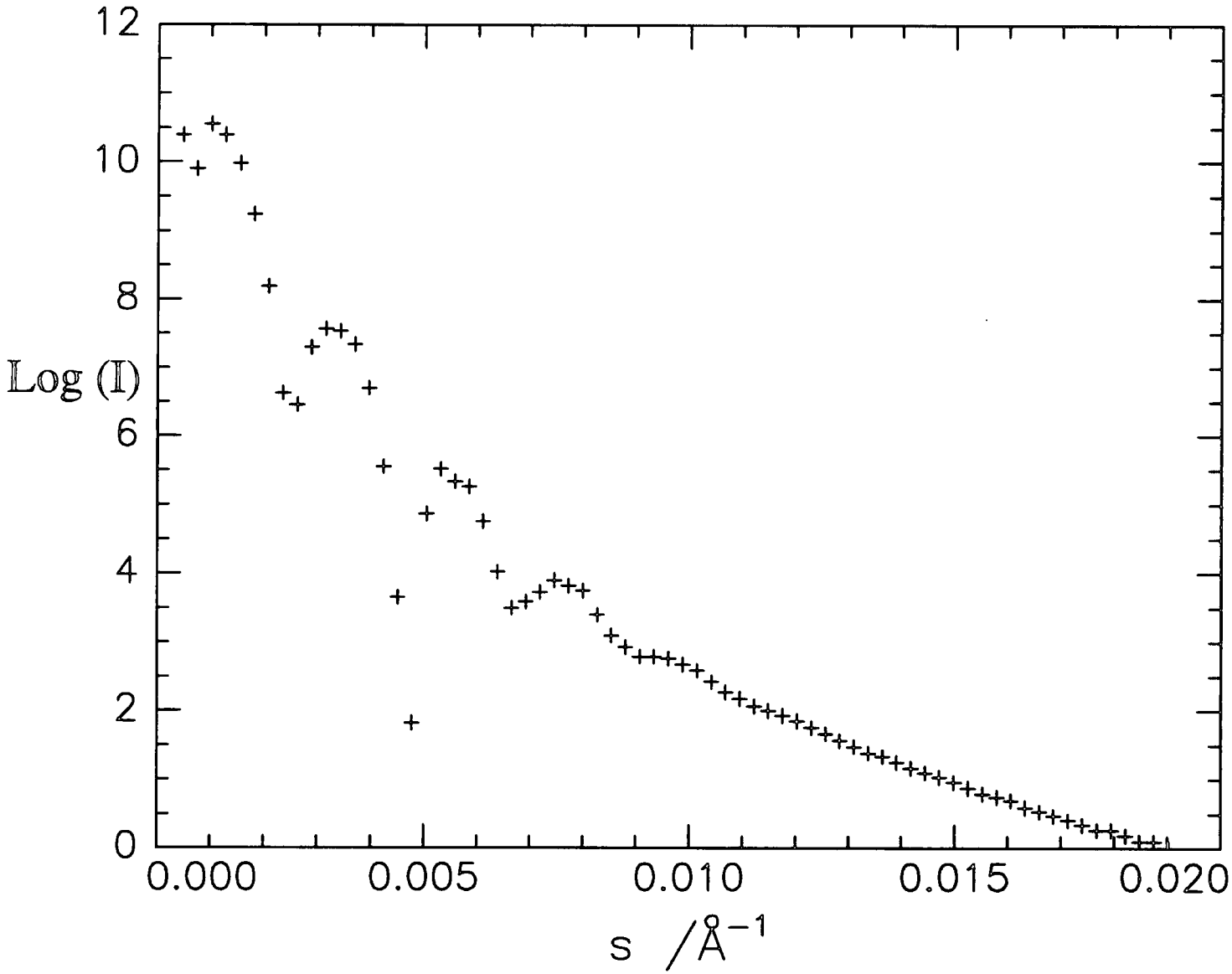

Figure 6.25 Correlation Functions for BC76 (Cooled to Room Temperature).

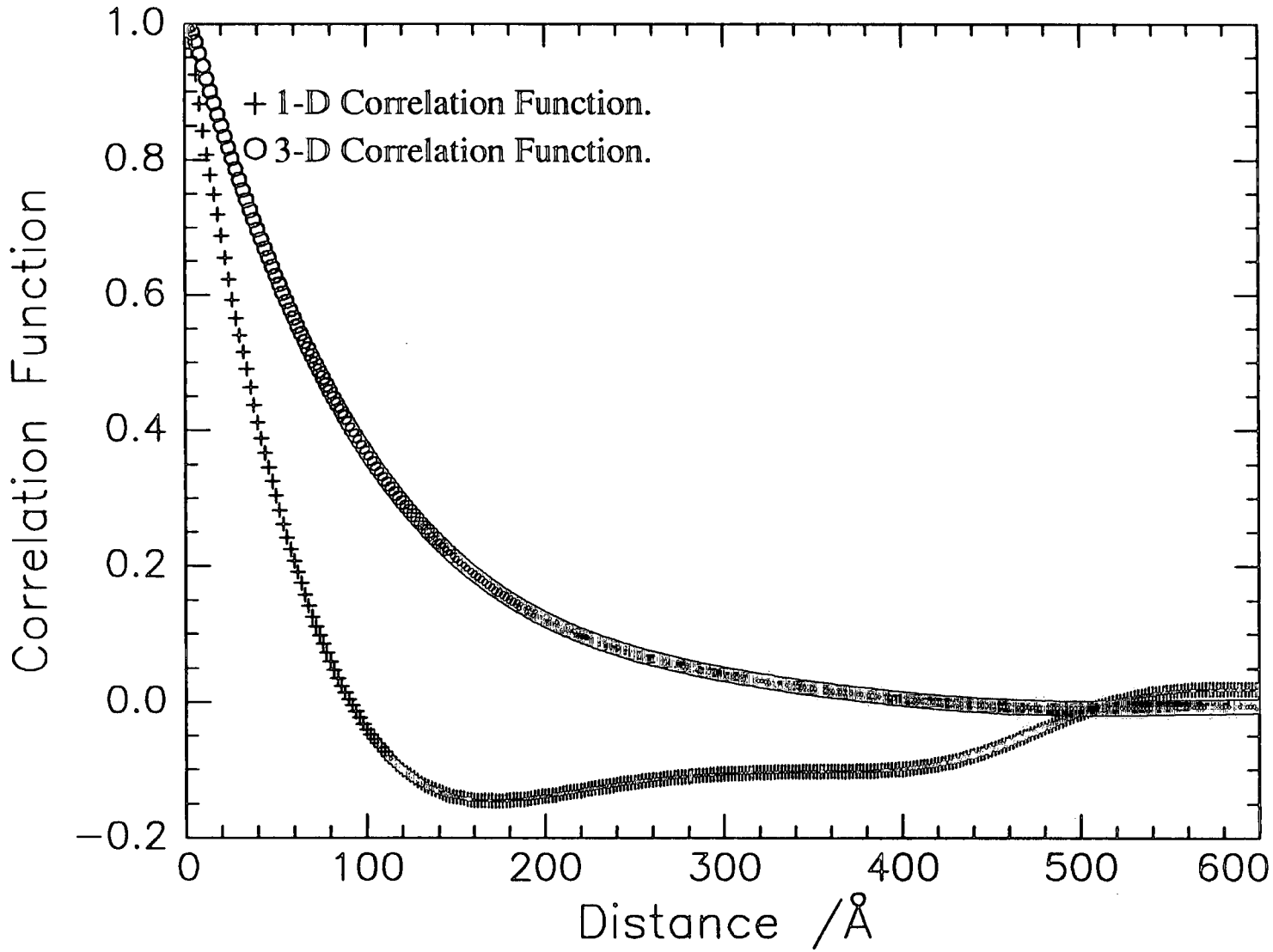

Figure 6.26. Correlation Functions for BL80 (Cooled to Room Temperature).

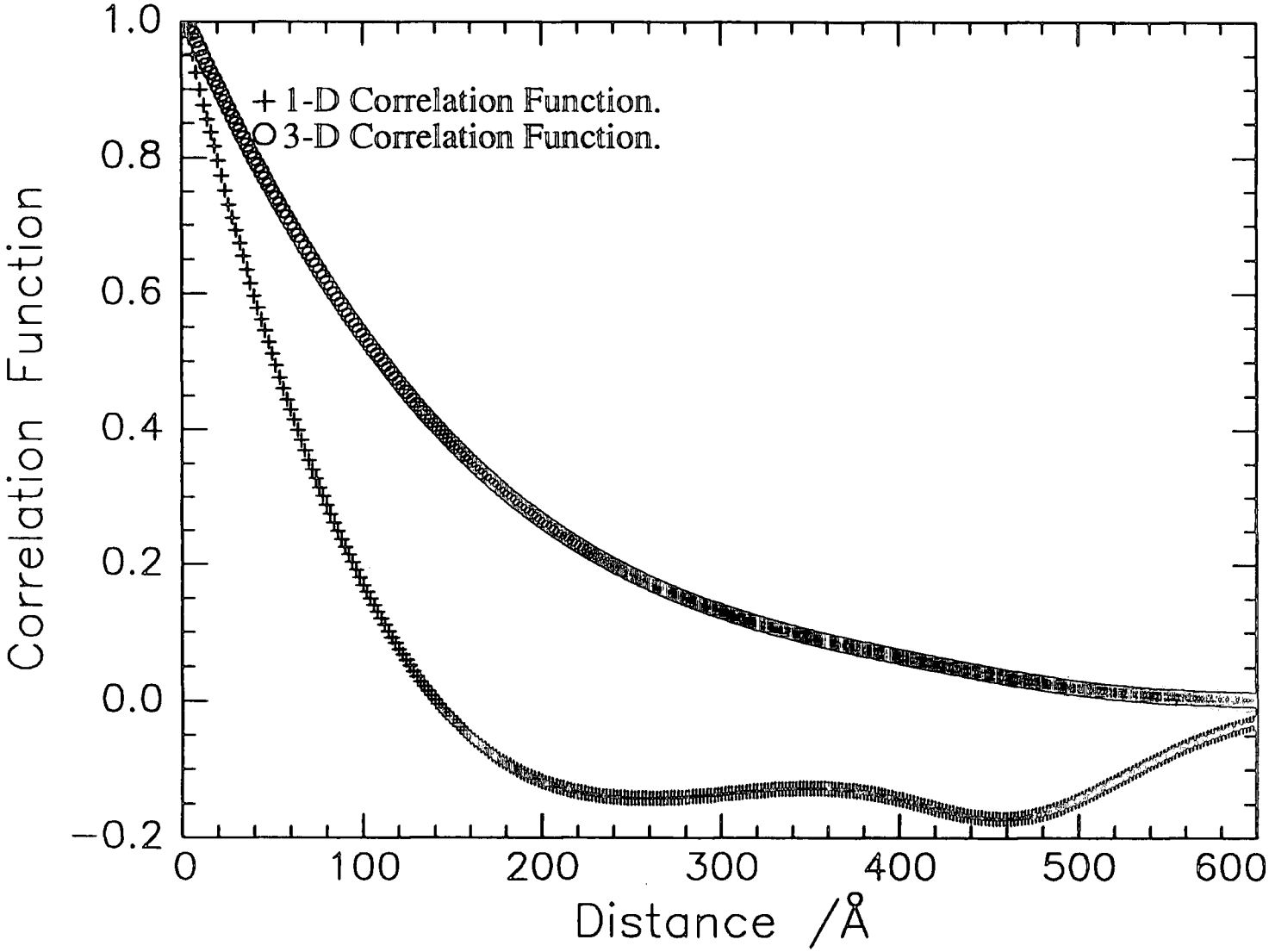

Figure 6.27 Correlation Functions for PEO (Cooled to Room Temperature).

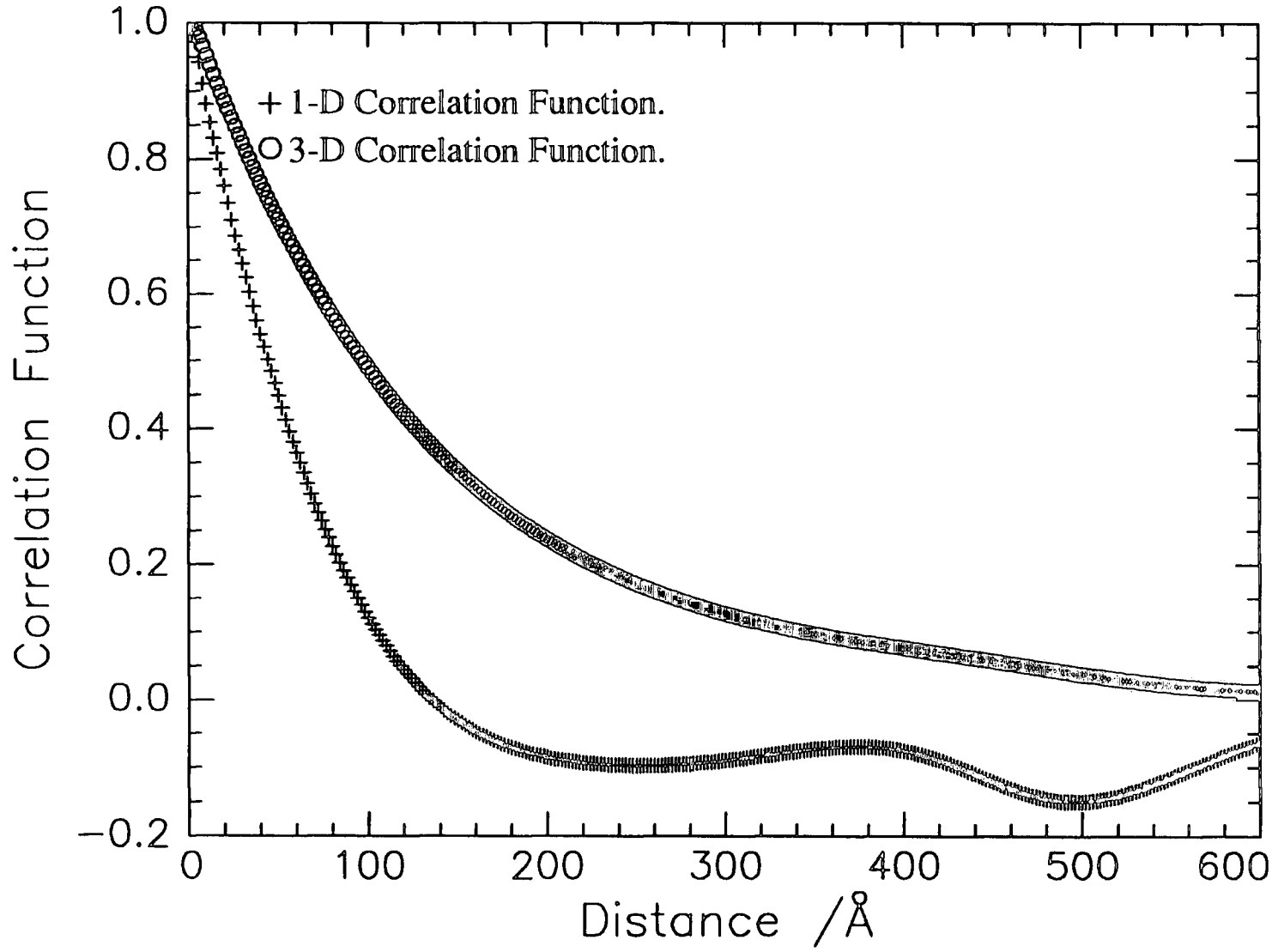

systems, the absence of any variation gives some cause for concern over the applicability of this analysis.

The variation of the desmeared scattered intensity with s for all three systems cooled to room temperature is shown in figure 6.28. The scattering profiles are very similar, each displaying a scattering shoulder at $s=0.0025Å^{-1}$. For PEO, an additional scattering peak can be seen at $s=0.005Å^{-1}$ (see figure 6.28). This suggests that the crystalline structure of PEO is more ordered than that for BC76 and BL80.

$L_c^m/2$ and the 3-D correlation length were even smaller when BC76 was quenched to 293K rather than being cooled at $10Kmin^{-1}$. These smaller values suggest that the quenching process inhibits crystal growth.

Figure 6.28. Desmeared Scattered Intensity vs. s for BC76, BL80 and PEO.

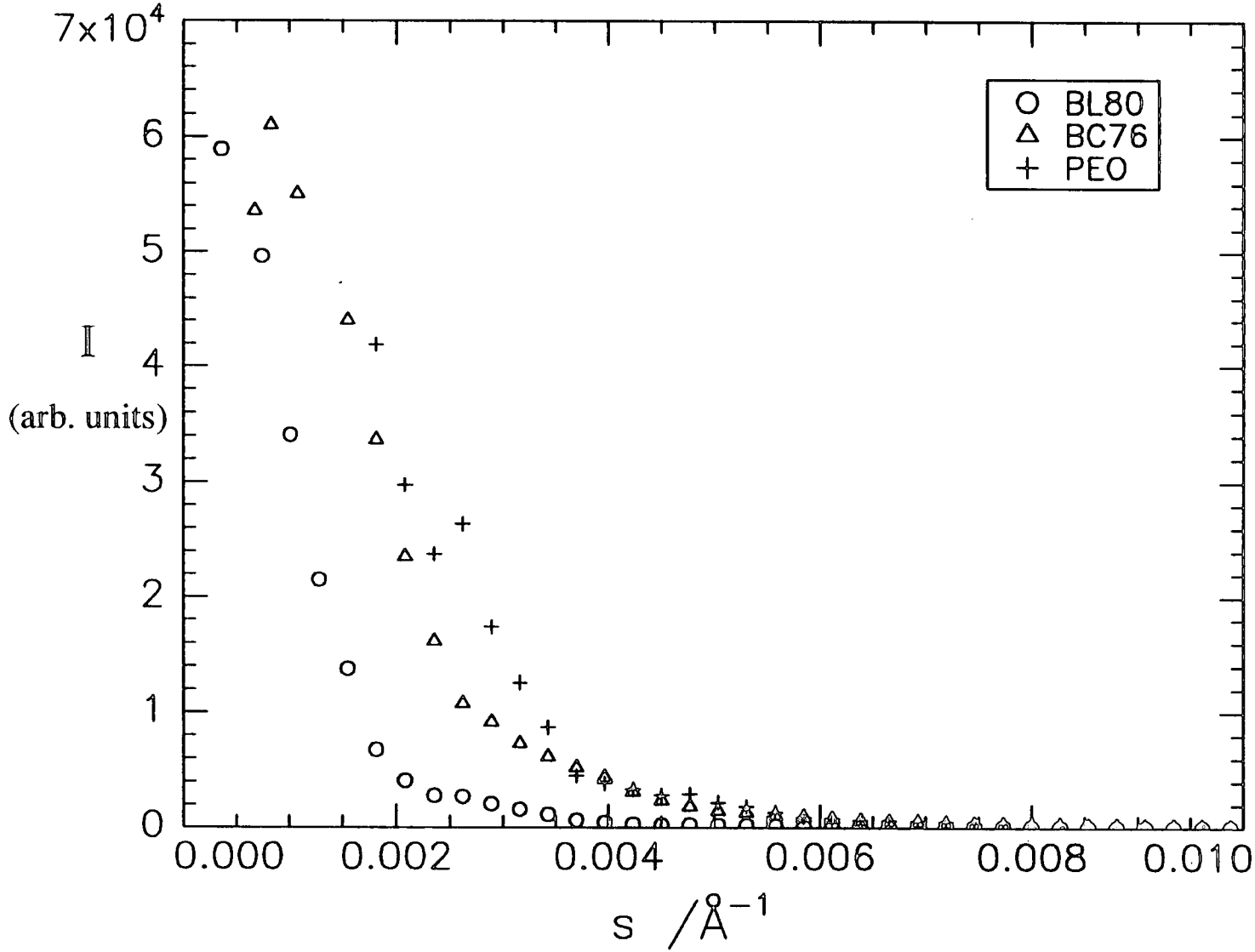

6.4.7. SAXS Conclusions.

For all of the polymer systems investigated using SAXS, the length values were relatively constant. The Bragg spacing, d=460±20Å was found to be systematically larger than the probable distance between the centre of gravity of a crystal and its adjacent amorphous region, L_c^m. As described by Zachmann, this implies that there is a broad distribution of the lamellar thicknesses.[17]

Through analysis of the derived structural parameters, the block copolymers, BC55 and BC50, undergo structural reorganisation at low temperatures. This structural reorganisation can be attributed to microphase separation forming rich PEO microdomains within an amorphous, PMMA rich lamellar matrix. Upon heating, the PEO rich microdomains are able to crystallise at approximately 323K. Above the crystallisation temperature, the crystalline component melts leaving a rigid PMMA lamellar matrix. The induced crystalline regions were 20% crystalline for both block copolymers and no interfacial thickness between PEO rich microdomains and the amorphous PMMA rich lamellar matrix was detected.

6.5. Summary and Conclusions.

The polymers poly(ethylene oxide) and poly(methyl methacrylate) possess sufficient electron density differences between crystalline PEO, amorphous PEO and amorphous PMMA, enabling the crystalline and phase separated structure (2-800Å level) of a mixture of these polymers to be investigated using x-rays.

Wide angle x-ray scattering was used to determine the degree of crystallinity in the blends and block copolymers. Sharp crystalline peaks associated with the crystallinity of PEO were observed, whereas amorphous PMMA gave a much broader scattering halo. The crystallinity in both the unannealed blends and unannealed block copolymers decreased as the percentage of PMMA component increased. This reflects the miscible, diluent nature of the PMMA component inhibiting crystallisation of PEO. The crystallinity of the blends were consistently larger than the corresponding block copolymer in terms of percentage of PMMA component. This was attributed to the chemical joint in the block copolymer restricting crystallisation.

The degree of crystallinities determined for BC55 and BC50 yielded information about the proposed microphase separation process occurring at low permanence temperatures. $T_{1/2}'$, the permanence temperature at which half the maximum amount of attainable crystallinity is induced was evaluated for both BC55 and BC50 for two different cooling rates to T' (see table 6.7). These temperatures were well below the crystallisation temperature and proved to be a useful parameter when describing this process. $T_{1/2}'$ for BC55 was higher than $T_{1/2}'$ for BC50.

Small angle x-ray scattering also proved to be a valuable tool for studying the structural properties of these polymeric systems. SAXS analysis for BC55 and BC50 data supported the conclusions from WAXS. For T'<253K for BC50, crystallinity was induced at approximately 323K. The Bragg spacings were large, d=460±20Å, a broad distribution of lamellar thicknesses was present and no interface between the PEO rich microdomains and the amorphous, PMMA rich surroundings was detected. The well defined diffraction at 343K for BC55 after thermal treatment to low permanence temperatures supports the proposal of microphase separation at T'. This diffraction is

attributed to a rigid PMMA rich lamellar morphology surrounded by melted PEO. The PMMA rich component is rigid at 343K, since this temperature is well below the glass transition temperature of pure PMMA (T_g=398K).

6.6. References.

1. Stuhrmann, H.B. p.199 in 'Small Angle X-ray Scattering', Glatter, O. and Kratky, O., Academic Press, 1982.
2. Rabiej, S. and Wlochowicz, A., Die Angewandte Makromolekulare Chemie, 175, 81-97, Nr.2920, 1990.
3. Ning, Y., Chinese Journal of Polymer Science, Vol. 7, 4, p.315, 1989.
4. Yoa, N., Polymer, 7, 34, 1564, 1993.
5. Baltá-Calleja, F.J. and Vonk, C.G., Chap.5, p.175-204 in 'X-ray Scattering of Synthetic Polymers', Jenkins, A.D. (Ed.), Polymer Science Library 8, Elsevier, 1989.
6. Hindeleh, A.M. and Johnson, D.J., J.Phys. (D), 4, 259, 1971.
7. Hermans, P.H. and Weidinger, A., J.Polym.Sci., 5, 565, 1950.
8. Ruland, W., Acta.Cryst., 14, 1180, 1961.
9. Vonk, C.G., J.Appl.Cryst., 6, 148, 1973.
10. Ruland, W., Polymer, 5, 89, 1964.
11. Glatter, O. and Kratky, O., 'Small Angle X-ray Scattering', Academic Press, 1982.
12. Hall, I.H., p.669, Chapt. 30 in Vol. 1 'Comprehensive Polymer Science', Allen, G., Bevington, J.C., (Eds.), Pergamon Press, 1989.
13. Baltá-Calleja, F.J. and Vonk, C.G., 'X-ray Scattering of Synthetic Polymers', Jenkins, A.D., (Eds.), Elsevier, 1989.
14. Vonk, C.G., J.Appl.Cryst., 9, 433, 1976.
15. Debije, P., Anderson Jr., H.R. and Brumberger, H., J.Appl.Phys., 28, 679, 1957.
16. Chalkeley, H.W., Cornfield, J. and Park, H., Science, 110, 295, 1949.
17. C.Santa Cruz, N. Stribeck, H.G. Zachmann, F.J. Baltá-Calleja, Macromolecules, 1, 24, 5980-5990, 1992.

18. G.R.Strobl, M.J.Schneider and I.G.Voigt-Martin, J.Polym.Sci., Polym. Phys. Ed., 18, 1361, 1980.

19. Y.Tanabe, G.R.Strobl and E.W.Fischer, Polymer, 27, 1147, 1986.

20. Vonk, C.G., Kortleve, G., Kolloid-Z., 220, 19, 1967.

21. Strobl, G.R., Schneider, M., J.Polym. Sci., 18, 1343, 1980.

22. Kratky, O., Z.Elektrochem. 58, 49, 1954; 62, 66 1958, Kratky, O. and Skala, Z., Z.Elektrochem. 62, 73, 1958.

23. Kratky, O. and Stabinger, H., Anton Paar manual 'Kratky, Compact Small Angle System', 1984.

24. Vonk, C.G., J. Appl. Cryst., 8, 340-341, 1975.

25. Ruland, Coll. and Poly. Science, 255, 417, 1977.

26. Vonk, C.G., Pjipers, J.Appl. Cryst. 14, 8-16, 1981.

27. Vonk, C.G., J.Appl. Cryst., 6, 81-86, 1973.

28. Vonk, C.G., J.Appl. Cryst., 4, 340, 1971.

29. Debye, P, Anderson, N.R., Brumberger, H., J.Appl.Phys., 28, 679-683, 1957.

30. Richards, R.W., FFSAXS5 manual 'Data Normalisation and Correction for Small Angle X-ray Scattering Data', University of Durham.

Chapter 7.

Small Angle Light Scattering.

7.1. Introduction.

As part of this project, a small angle light scattering (SALS) set-up has been designed and constructed. This non-destructive technique enables the polymer scientist to investigate changes in the physical nature of polymers on a size scale which is commensurate with the wavelength of light (0.7μm to 1,000μm) in terms of concentration and orientation fluctuations. The speed of data acquisition enables multiple scans to be recorded in rapid succession, allowing the study of fast dynamic processes such as crystallisation and phase separation.

This chapter gives a detailed description of the theory behind SALS, the apparatus used and presents results on the isothermal crystallisation and microphase separation of some of the polymer systems under investigation in this work. The final section presents some results that have been acquired using SALS on other systems which are disconnected with this project, but provide an idea of the range of capabilities that this technique offers.

7.2. Theory.

7.2.1. Interaction with Matter.

Light rays consist of electromagnetic waves in which an electrical and a magnetic field, perpendicular to each other and to the direction of propagation of the wave, vary periodically with position and time. As the wave interacts with matter, the electrical field displaces the positive nucleus and the electrons in opposing directions, thus inducing an electrical dipole moment, a. The dipole moment is a linear function of the electrical field, E, and may be given by;

$$a = \alpha . E \tag{7.1}$$

where the proportionality factor, α is the polarisability. These dipoles oscillate at the same frequency as the incident radiation and radiate secondary light (scattered light). The magnitude of the scattered electric field at a distance r from the scattering object is;

$$E_s = \frac{(\ddot{a} \sin \psi)}{(rc^2)} \tag{7.2}$$

where c is the velocity of light in vacuum, ä is the double differential of a with respect to r, ψ is the angle between the dipole a and the vector r extending from the dipole to the observer. Scattering only occurs if the subregions are optically different, i.e., there is a difference in the local dielectric constant, and if these regions are on a length scale that is commensurate with the wavelength of the incident light.

For the case of Rayleigh scattering in which the frequency of the light is small compared with the natural frequency of the electrons;

$$E_s = (\frac{\alpha E_o \omega^2}{rc^2}) \sin\psi \exp[i(\omega t - \phi)] \tag{7.3}$$

where E_0 is the incident electric field, ϕ is a phase factor accounting for the phase lag experienced by the wave as a consequence of the distance that it travels to the observer.

The scattering may be represented in the form;

$$(E_s)_j = K_j \exp[i(\omega t - \phi)] \tag{7.4}$$

where the subscript j refers to the scattering from the jth object and K is a proportionality constant. For a collection of scattering objects which are sufficiently small and far apart from one another that there is no multiple scattering, the total scattered amplitude can be obtained by summing the amplitudes of the contributors;

$$E_s = e^{i\omega t} \sum_j K_j e^{i\phi j} = e^{i\omega t} F \tag{7.5}$$

where F is referred to as the form factor and is a property of the structure of the scattering system.

Thus, the intensity of the scattered wave is given by

$$I_s = (\frac{c}{4\pi}) E_s E_s^* = (\frac{c}{4\pi}) F F^* \tag{7.6}$$

where the asterisk represents the complex conjugate.

The scattering power may be conveniently expressed in terms of the Rayleigh ratio defined by;

$$\Re = \frac{I_s r^2}{I_o V_s} \tag{7.7}$$

where I_0 is the incident intensity, I_S is the scattered intensity and V_S is the volume of the scattering system. Theoretically, the Rayleigh ratio relates to absolute scattering intensities. Practically, however, due to problems encountered in evaluating the form factor in terms of the geometry of the system, calculating the Rayleigh ratio is often very complicated. Consequently, scattered intensities with arbitrary units are often used.

The dielectric constant[1] is proportional to E_S, and so following on from equation 7.6, the following expression applies;

$$\mathbb{I}_s \propto \left|\mathbb{E}_s\right|^2 \propto \left|d\varepsilon\right|^2 \tag{7.8}$$

where $d\varepsilon$ is the Fourier component of the dielectric constant fluctuation tensor. Using equation 7.8, a relationship between the scattered intensity and concentration fluctuations can be expressed in terms of the local refractive index, n, which is related to the local dielectric constant, ε, via;

$$n = \varepsilon^{\frac{1}{2}} \tag{7.9}$$

In a homogeneous two component polymer system, the average refractive index, n_0, is expressed as;

$$n_o = \phi_1 n_1 + \phi_2 n_2 \tag{7.10}$$

where ϕ_x is the volume fraction of component x in the mixture and n_x is the refractive index of pure component x.

The value of n at a distance r from the centre of the scattering volume is;

$$n(r) = n_o + dn = n_1\phi_1(r) + n_2(1 - \phi_1(r)) \tag{7.11}$$

where dn describes the local deviation in refractive index due to any composition fluctuation.

If the sample is assumed to be isotropic, then;

$$\varepsilon = \varepsilon_0 + d\varepsilon \tag{7.12}$$

Differentiation of equation 7.9 with respect to ε, gives;

$$\begin{aligned} d\varepsilon &= 2ndn \\ &= 2n(n_1 - n_2)d\phi \end{aligned} \tag{7.13}$$

Thus, with reference to equation 7.8,

$$I_s(q) \propto 4(n(n_1 - n_2))^2 S(q) \tag{7.14}$$

where S(q) is defined by:

$$S(q) = < |d\phi q|^2 > \qquad (7.15)$$

and q, the scattering vector is defined by:

$$q = \frac{4\pi n}{\lambda} \sin\left(\frac{\theta}{2}\right) \qquad (7.16)$$

S(q) is the scattering law for the system and q the scattering vector. It is the correlation of the composition fluctuations in the system and is defined to have a value of 1 at q=0.

Two main approaches are employed for analysing the scattering light intensity from a polymer system. The model approach where the total scattering amplitude is evaluated based upon a model of the scattering object. Secondly, for less well defined scattering systems, the statistical approach where the system is defined in terms of mean-squared fluctuations in scattering power and correlation functions. Correlation functions describe the probability that the fluctuation occurring in volume elements separated by a given distance r will be correlated. These fluctuations may arise from concentration and/or orientation fluctuations. The relative contributions may be determined from an analysis of the polarisation of the scattered light.

7.2.2. Light Scattering Theories.

Mie[2,3] provided a rigorous solution for the small angle light scattering from a homogeneous isotropic sphere from the solutions of a series of Maxwell's equations with the appropriate boundary conditions. However, for most applications, the Mie theory proved to be too exact and consequently a number of approximation theories have been used to theoretically describe SALS patterns.

In section 7.2.1, the intensity of scattered light was related to fluctuations in the local refractive index based upon the Rayleigh approximation[4]. A further two light scattering approximate theories are widely used to describe theoretical models. Their application depends upon the size of the refractive index fluctuation and the particle size within the system under investigation, as well as the magnitude of the wavelength of the incident radiation. These theories, which Haudin[5] has presented in detail, are briefly described below.

Three approximations have been widely used; the Rayleigh approximation, the Rayleigh-Gans-Debye (RGD) approximation[3] and the Anomalous Diffraction (AD) approximation[4,6]. The RGD approximation is based upon Rayleigh scattering with the assumption that the scattering from a volume element is independent of the scattering from other volume elements. Table 7.1 lists the conditions under which these approximations are valid.

Approximation	Conditions of validity
Rayleigh	$ka<<1;\|m\|\ ka<<1$
Rayleigh-Gans-Debye (RGD)	$\|m-1\|<<1;\ 2ka\ \|m-1\|<<1$
Anomalous Diffraction (AD)	$\|m-1\|<<1;\ ka>>1$

Table 7.1. Approximations used in light scattering theories.

In table 7.1, a is the characteristic dimension of the scattering units (for spheres a will be the radius), m is the refractive index of the scattering units relative to the medium in which they are embedded and $k=2\pi/\lambda$ where λ is the wavelength of light in the medium.

The Rayleigh approximation is valid for particles of size much less than the optical wavelength, λ, whereas the AD approximation is appropriate for large particles, which scatter strongly in the forward direction. Thus, the RGD approximation tends to be limited to small scattering units. This limitation is expressed by the condition $2ka|m-1|<<1$, which implies that the phase difference between light rays which do and do not pass through the scattering particle must be small. Consequently, the possible size range under investigation is strongly dependent upon $|m-1|$. For example, if $|m-1|$ is 10^{-3}, the RGD approximation is valid for particles of the order of 10μm. If $|m-1|$ is 10^{-2}, the particle size is limited to 1μm.

Both RGD and AD approximations suppose that there is only a small refractive index difference between the scattering units and the surrounding medium, (condition $|m-1|<<1$). This condition holds for semi-crystalline polymers even in the most unfavourable case where a single spherulite is embedded in an amorphous phase.

7.2.3. Model Approaches.

7.2.3.1. Three-dimensional Spheres.

7.2.3.1.1. Isotropic Spheres.

Using the Rayleigh-Gans-Debye approximation, a model of a uniform isotropic sphere of polarisability α_0 and radius R was developed[5]. Based on this model, for small scattering polar angles, the H_V SALS intensity is zero and the scattered V_V intensity is given by[7];

$$I_{Vv} = A(\alpha_o - \alpha_s)^2 V_o^2 [(\frac{3}{U^3})(\sin U - U\cos U)]^2 \qquad (7.17)$$

where A is a proportionality constant, α_S is the polarisability of the medium in which the sphere is embedded, V_0 is the volume of the isotropic sphere and U is given by;

$$U = (\frac{4\pi R_o}{\lambda})\sin(\frac{\theta}{2}) \qquad (7.18)$$

where λ denotes the wavelength of light in the medium and θ is the polar scattering angle, see figure 7.1. Two modes of SALS are possible. Figure 7.1 depicts H_V SALS were the analyser is horizontal and the polariser is vertical with respect to the plane of polarisation of the incident radiation. The other mode of operation is V_V SALS where both the analyser and polariser are vertically polarised.

7.2.3.1.2. Anisotropic Spheres.

Anisotropic spheres (three-dimensional spherulites) e.g. semi-crystalline spherulites, were first considered by Stein and Rhodes[8] and later by Samuels[9] and

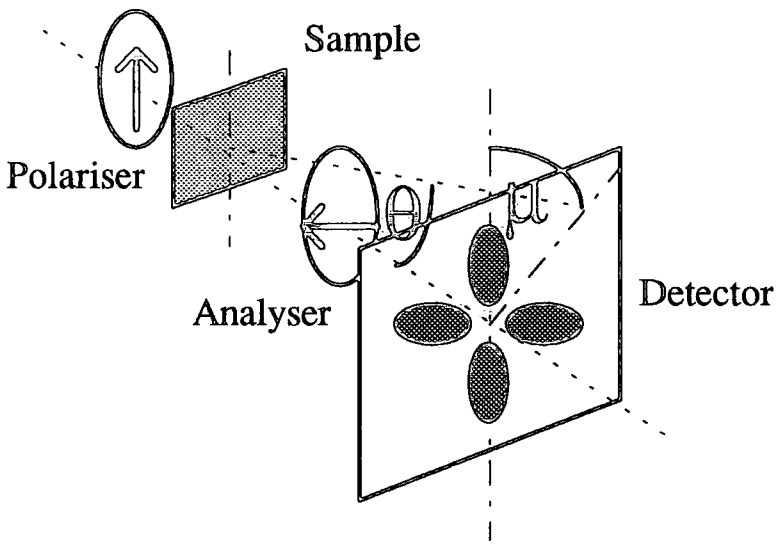

Figure 7.1. Scattering Angles for H_V SALS Set-up.
(μ=azimuthal angle and θ=polar scattering angle).

Clough et al[10]. Using the Rayleigh-Gans-Debye approximation, they calculated the SALS pattern for a homogeneous sphere embedded in an isotropic medium where any volume element of the sphere was uniaxially birefringent with its optic axis in the sphere radius direction. Van Aartsen[11] extended this approach and included the case where the optic axis made an angle β with the sphere radius direction. He considered uniaxial crystals in which α_1 and α_2 are the polarisabilites in the direction of the optic axis and perpendicular to it, respectively. Samuels[9] has shown for the cases where the optic axis is parallel and perpendicular to the sphere radius direction, the I_{Hv} and I_{Vv} equations

are the same. He examined the birefringence of the anisotropic spheres in terms of radial α_r and tangential α_t polarisabilites. The correct form of these equations are;

$$I_{Vv} = AV_o^2 \cos^2 \rho_1 (\frac{3}{U^3})^2 [(\alpha_r - \alpha_s)(Si\ U - \sin U)$$
$$+(\alpha_t - \alpha_s)(2\sin U - U\cos U - Si\ U) \qquad (7.19)$$
$$+(\alpha_r - \alpha_t)[\frac{\cos^2(\theta/2)}{\cos\theta}]\cos^2\mu(4\sin U - U\cos U - 3Si\ U)]^2$$

$$I_{Hv} = AV_o^2 \cos^2 \rho_2 (\frac{3}{U^3})^2 [(\alpha_r - \alpha_t)$$
$$x[\frac{\cos^2(\theta/2)}{\cos\theta}]\sin\mu\cos\mu(4\sin U - U\cos U - 3Si\ U)]^2 \qquad (7.20)$$

where I_{Vv} and I_{Hv} denote the scattered intensities for V_v and H_v scattering respectively. V_o is the volume of the anisotropic sphere, α_s is the polarisability of the surroundings, θ and μ are the polar and azimuthal scattering angles and

$$\cos\rho_1 = \frac{\cos\theta}{[\cos^2\theta + \sin^2\theta\cos^2\mu]^{1/2}} \qquad (7.21)$$

$$\cos\rho_2 = \frac{\cos\theta}{[\cos^2\theta + \sin^2\theta\sin^2\mu]^{1/2}} \tag{7.22}$$

and

$$Si\ U = \int_0^U \frac{\sin x}{x} dx \tag{7.23}$$

Equation 4.20 predicts a four-leaf clover shaped scattering pattern with intensity maxima occurring at azimuthal angles μ=45°, 135°, 225°, 315°, see figure 7.2. The polar scattering angle θ_{max} is represented by the angle subtended by the intensity maximum of one of the lobes and the centre of the pattern (the main beam position). The variation of the scattered intensity with θ is represented by the term $(3/U^3)$(4sinU-UcosU-3Si U). The intensity is zero at zero angle (U=0) and goes through a maximum with increasing θ. The maximum occurs at U_{max}=4.09, however, Peuvrel et al[12] have shown that for the limiting cases of the Rayleigh-Gans-Debye approximation, see table 7.1, U_{max} may vary from 2.8 to 6. The existence of the intensity maximum at μ=45° and U=4.09 enables the determination of an average spherulitic radius, R_o, in a polymer film from the H_v SALS pattern;

$$R_o = \left(\frac{1.025}{\pi n}\right)\frac{\lambda}{(\sin\theta_{max}/2)} \tag{7.24}$$

where n is the averaged refractive index of the spherulite. Since R_o is inversely proportional to $\sin(\theta_{max}/2)$, small spherulites have a four-leaf clover pattern at large polar scattering angles.

Analysis of equation 7.19 shows that the V_V SALS pattern is dependent upon the polarisabilites of both the spherulite and the surrounding environment. Figure 7.3 shows a contour plot the I_{V_V} intensity versus U for anisotropic spheres with radii of 10μm,

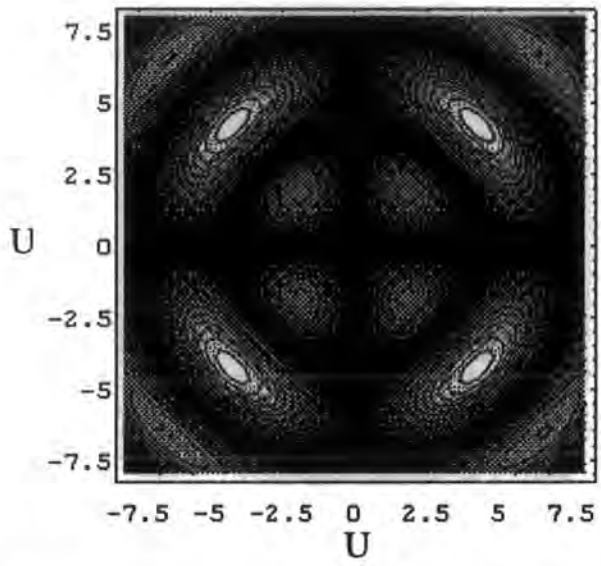

Figure 7.2. Modelled Contour Plot of I_{Hv} versus U for an Anisotropic Sphere (Radius=10μm, Radial Refractive Index=1.54, Tangential Refractive Index=1.5 and Refractive Index of the Surroundings=1.48).

radial refractive index=1.5, tangential refractive index=1.54 and the surrounding refractive index=1.52. Most V_V SALS patterns contain a high level of light intensity at $\theta = 0^o$. Consequently, to protect the detector from exposure to intense light and to restrict the dynamic range, it is often essential to incorporate a beam stop into the SALS set-up to remove this contribution. The V_V SALS pattern is very sensitive to the magnitude and sign of the polarisability of both the spherulite and the surrounding medium. Haudin[5] has looked at the effect of varying polarisabilites for both the spherulite and the

surrounding medium on the V_V SALS pattern in more detail. He observed that positive ($n_r > n_t$) and negative ($n_t > n_r$)[9] spherulites can give the same V_V SALS pattern. However, as the background refractive index is altered, the subsequent change in shape and intensity of the V_V SALS pattern depends upon the sign of birefringence of the spherulite. Based upon this refractive index dependence, Samuels has developed a procedure to determine the sign of a spherulite experimentally[9].

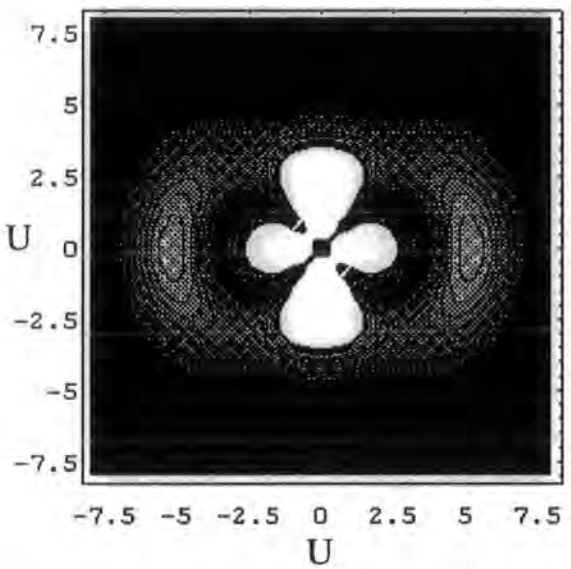

Figure 7.3. Modelled Contour Plot of I_{VV} versus U for an Anisotropic Sphere (Radius=10μm, Radial Refractive Index=1.54, Tangential Refractive Index=1.5 and Refractive Index of the Surroundings=1.48).

Slight anomalies between theory and experiment do exist e.g. $I_{HV} \neq 0$ at $\theta=0$ and the I_{max} (experimental)$<I_{max}$(theory). These discrepancies can be attributed to disorder within the system, see section 7.2.3.4.

Meeten[6,13] calculated the H_V and V_V SALS patterns for isotropic as well as anisotropic spheres using the Anomalous Diffraction Approximation and the results were compared with the RGD approximation. The outstanding difference was that the μ

dependence of the H_V SALS pattern for an isotropic sphere was identical to that of an anisotropic sphere (for RGD approximation, I_{Hv} SALS is zero for an isotropic sphere). The theory predicted an I_{Hv} maximum at U~2.1 for the isotropic case. Thus, using the exact Mie theory or the AD approximation, a spherulite which is isotropic can exhibit a clover-leaf H_V SALS pattern. This prediction has been verified experimentally[14].

7.2.3.2. Two-dimensional Spheres-Disks.

In films where the thickness of the film is less than the spherulitic radius, the sphere must truncate and can be considered to be two-dimensional. Stein and Wilson[15] have derived the SALS equations for an optically anisotropic disk, and Clough et al[16,17] extended them to include such variables as optic axis alignment.

Computer simulations have shown that the theoretical SALS patterns corresponding to a disk model have generally the same appearance as those found for three-dimensional spherulites. For a disk, the following equations apply;

$$I_{Vv} = AA_o^2 \cos^2 \rho_1 [\frac{2}{W^2}]^2 [\{\alpha_t - \alpha_s\}J' + (\alpha_t - \alpha_s)(J'' - J') + (\alpha_r - \alpha_t)\cos^2 \mu (J'' - 2J')]^2 \quad (7.25)$$

$$I_{Hv} = AA_0^2 \cos^2 \rho_2 [\frac{2}{W^2}]^2 [(\alpha_r - \alpha_t)\sin\mu\cos\mu(2J' - J'')]^2 \quad (7.26)$$

where;

$$J' = 1 - J_o(W) \quad (7.27)$$

$$J'' = WJ_1(W) \quad (7.28)$$

and

$$\mathbb{R}_o = (\frac{1.96}{\pi})(\frac{\lambda_m}{\sin\theta_{max}}) \qquad (7.29)$$

where λ_m is the wavelength relative within the medium, A is a proportionality factor, A_o is the area of the disk, α_r and α_t denote the radial and tangential polarisabilites of the scattering particle, α_s is the polarisability of the surroundings and $W=(2\pi R_o/\lambda)\sin\theta$. Equation 7.26 for the calculation of the radius of a disk from the H_v intensity maximum is different to that for a sphere. However, the equations are essentially very similar since the intensity maximum for a particular disk and sphere radius falls in the same angular region.

7.2.3.3. Anisotropic Rods.

A two dimensional model has been derived by Stein and Rhodes[4]. This theory considers the SALS scattering from a distribution of anisotropic rods of length L and infinitesimal thickness. Using this theory, two types of rod orientation distributions have been considered[18]. The theory predicts well the type of H_v scattering experimentally observed. Whether it is of the x-type or the +type, depends upon the orientation of the assembly of rods[9]. This theory has proved useful for interpreting SALS patterns obtained from stretched films with a rod-like morphology.

Kawai and co-workers[20] have successfully extended the two-dimensional theory above to three dimensions. This has been generalised by Van Aartsen[19] and by Hayashi and Kawai[20] who considered rods of finite thickness as well as finite length. Other types of rod shape have been considered, rectangular parallelepipeds[21] and rods with a cross section of lozenge shape[19]. Deviations occur between experiment and theory and modifications to the rod scattering theory have been proposed to take these into account. These have included internal inhomogeneities in orientation of optical axes and

anisotropy[22], polydispersity of rod length[22], lateral rod dimension[21] and more significantly interparticle interference[23].

7.2.3.4. Modifications of the Models for Spherulitic Scattering.

Although the theoretical models predict well many of the features of SALS from spherulites, discrepancies between theory and experimental results have been observed[24-26]. The experimentally determined maximum intensity, I_{max}, is often lower than predicted and shifted to larger polar scattering angle. The theory also predicts zero scattering intensity at $\theta=0^o$ as well as at $\mu=0^o$ and 90^o, whereas a finite scattering intensity is experimentally observed. These discrepancies between theory and experiment are attributed to the internal disorder of spherulites in the polymer sample, different morphological features of real spherulites, distribution of spherulitic sizes, impingement and incomplete growth. In addition, multiple scattering, surface defects produce deviations from the predicted intensity patterns. The models of scattering from individual spherulites have been modified to take into account such effects.

The effects of internal and external disorder have been described in detail previously[27]. Two types of models have been proposed to take internal disorder into account: modifications of the geometrical description of a spherulite as a homogeneous anisotropic sphere or disk[28] and the use of correlation functions to describe the amount of internal disorder.

7.2.3.4.1. Internal Disorder.

The statistical approach for internal disorder in an isotropic sphere was first studied by Stein et al[29]. They used density correlation functions of the sort described by the Debye-Bueche theory[30]. This proved unsuccessful since the Rayleigh-Gans-Debye theory for an isotropic sphere does not predict any H_V pattern and the treatment

considered only density fluctuations. Keijzers et al[31] have proposed a scattering theory in which the scattering intensity is the sum of two terms; the first of which is a perfect spherulite term and the second, a random orientation fluctuation term of the Stein-Wilson type[15]. This proved more successful for spherulites of low order but a limitation of the theory was its treatment of the random contribution as a separate phase, scattering independently. Both contributions are obviously not independent and a more realistic model was proposed by Stein and Chu[32]. They assumed that there is orientational disorder within the spherulites and performed calculations for just two limiting cases; radial disorder in which the optic axis orientation fluctuates depending upon the radial distance r, and angular disorder, where the optic axis orientation fluctuates depending upon it's position at any specific r within the spherulite but is independent of r. From their calculations, they found that an increase in radial disorder leads to an increase in I_{Hv} scattered intensity at higher angles than θ_{max}, whereas angular disorder enhances the relative intensity at angles less than the maximum. In both cases the position of θ_{max} does not change.

The calculations of Stein and Chu[32] were extended to account for the magnitude of the anisotropy, as well as the orientation of the optic axis, by Hashimoto and Stein[33]. The approach of Stein and Chu was further generalised by Yoon and Stein[27] who developed a lattice theory for the orientational disorder in two-dimensional spherulites. Along with those observations by Stein and Chu, they found that I_{max} was appreciably reduced by disorder. Similar conclusions have been observed by Bartczak et al[25], i.e. internal disorder lowers the scattering intensity at the maximum and increases it at larger and smaller scattering angles. This type of disorder is partly responsible for the finite scattering at $\theta=0^{o}$.

considered only density fluctuations. Keijzers et al[31] have proposed a scattering theory in which the scattering intensity is the sum of two terms; the first of which is a perfect spherulite term and the second, a random orientation fluctuation term of the Stein-Wilson type[15]. This proved more successful for spherulites of low order but a limitation of the theory was its treatment of the random contribution as a separate phase, scattering independently. Both contributions are obviously not independent and a more realistic model was proposed by Stein and Chu[32]. They assumed that there is orientational disorder within the spherulites and performed calculations for just two limiting cases; radial disorder in which the optic axis orientation fluctuates depending upon the radial distance r, and angular disorder, where the optic axis orientation fluctuates depending upon it's position at any specific r within the spherulite but is independent of r. From their calculations, they found that an increase in radial disorder leads to an increase in I_{Hv} scattered intensity at higher angles than θ_{max}, whereas angular disorder enhances the relative intensity at angles less than the maximum. In both cases the position of θ_{max} does not changed.

The calculations of Stein and Chu[32] were extended to account for the magnitude of the anisotropy, as well as the orientation of the optic axis, by Hashimoto and Stein[33]. The approach of Stein and Chu was further generalised by Yoon and Stein[27] who developed a lattice theory for the orientational disorder in two-dimensional spherulites. Along with those observations by Stein and Chu, they found that I_{max} was appreciably reduced by disorder. Similar conclusions have been observed by Bartczak et al[25], i.e. internal disorder lowers the scattering intensity at the maximum and increases it at larger and smaller scattering angles. This type of disorder is partly responsible for the finite scattering at $\theta=0^{o}$.

7.2.3.4.2. External Disorder.

External disorder includes incomplete spherulitic development, interspherulitic interference, size distribution and spherulitic truncation.

7.2.3.4.2.1. Polydispersity.

For polydisperse spherulites, the geometrical models have been modified by assuming the scattered light intensity can be regarded as the sum of the intensities scattered by individual spherulites[34]. As the polydispersity increases, a shift of θ_{max} and some skew of the intensity distribution to lower scattering angles was observed.

7.2.3.4.2.2. Interspherulitic Interference.

Interspherulitic interference gives rise to a sinusoidal modulation of the scattering profile. This contributes to the coarseness of the experimental SALS pattern. A model for interspherulitic interference has been derived by Stein and Picot[35] and Prud'homme and Stein[36]. Calculations of I_{Hv} show that these modulations are more significant for a smaller number of illuminated spherulites and that the position of the H_v scattering maximum is not effected. Kawai and co-workers treated the model above in terms of a paracrystal of the Hosemann type [23,37] and applied it to two types of scattering particles, rods[23] and sheaves[37]. Using this approach, fluctuations of particle orientation and distance between adjacent particles were introduced. In the case of rod-like particles, it was found that the scattering patterns were very dependent upon interparticle interference. For oriented sheaf-like textures, the theory accounts for the four inner lobes observed in the experimental H_v patterns, unaccounted by earlier scattering theory from isolated sheaves[38]. The capability of this theory to incorporate fluctuations in particle orientation has proved valuable for polymer specimens that have been industrially processed. Yoon and Stein[39] have also accounted for interparticle interference using a statistical approach.

7.2.3.4.2.3. Truncation.

Stein and Picot[40] considered single, double and a few cases of multiple truncation for random assemblies of two-dimensional spherulites. The case of multiple truncation was further developed by Prud'homme and Stein[41]. It was observed that as the amount of truncation increased, the spherulitic 'four-leaf-clover' pattern tended towards the 'four-tennis-racket' pattern and became very disordered for higher degrees of truncation. The effect of truncation also shifted θ_{max} towards smaller scattering angles. However, it was concluded that since high amounts of truncation are necessary to cause a significant amount of disorder, truncation only accounts for part of the departure from the perfect spherulite pattern[42].

More recently, Tabar et al[43] have presented a generalisation of the theory of Prud'homme and Stein[41] to account for the effect of impingement of growing spherulites on their H_V SALS patterns. Their theory is based on computer simulated results for two-dimensional spherulites and they observed that impingement caused a lowering in intensity of the intensity scattering maxima and diminishment of the overall sharpness of the scattering peak as well as an intensity contribution at $\theta=0^o$ [46-48]. Truncation also altered the meaning of the average spherulitic radius as determined from SALS. Tabar et al[47,48] showed that the average spherulitic radius is the quotient of averages of the nth and (n-1)th order, where n varies in the range from 4-6 depending upon the dimensionality of the spherulites and the mode of primary nucleation.

7.2.3.4.2.4. Incomplete Development.

Incompleteness of development is another cause that accounts for experimental discrepancies form theory and can account for the observed 'four-tennis-racket' type pattern. Spherulites nucleate from bundle-like crystals which evolve into sheaves and eventually into complete spherulites. Such an evolution has been idealised by the fan model[28,44]. As a consequence, Motegi et al suggested that the more sheaf-like the

crystalline textures, the more the H_V pattern approaches the four-tennis-racket pattern and also displays strong scattering intensity at low scattering angles. Such phenomena are often found in low-density polyethylene films[28].

7.2.3.4.2.5. Geometrical Deviations.

A general theory accounting for deviations from circular two-dimensional spherulites has been proposed by Tatematsu et al[45]. The general expression for intensity I_{Hv} is;

$$I_{Hv}(\theta,\mu) = \frac{4\delta^2 E_0^2 R_0^4}{4}[A_1(\theta) - A_2(\theta)\cos 4\mu] \qquad (7.30)$$

where E_0 is the incident electric field, R_0 is some characteristic particle radius and $\delta=\alpha_r-\alpha_t$ is the optical anisotropy of the scattering element. $A_1(\theta)$ and $A_2(\theta)$ are coefficients depending on the external shape of the disk. For perfect disks, these coefficients are equal and the scattering equations reduce to those for perfect two-dimensional spherulites. Three types of crystalline textures were discussed by Tatematsu[45]; sheaf-like, N-regular polygonal and eccentric circular. Such deviations from the perfect two-dimensional circular spherulite involved I_{Hv} intensities at zero polar scattering angle, $\theta=0$ and I_{Hv} intensities along the polarisation axes.

The effect of different types of internal and disorder on I_{Hv} SALS patterns have been summarised in tables 7.2 and 7.3 below.

Type of Disorder	Influence on H_v Scattering for an Anisotropic Three-dimensional Spherulite.
Internal disorder	
Radial disorder	Increase in I_{Hv} at angles greater than θ_{max}. Reduction in I_{Hv} at θ_{max}.
Angular disorder	Increase in I_{Hv} at angles less than θ_{max}. Reduction in I_{Hv} at θ_{max}.
External disorder	
Polydisperse spherulites	Shift in θ_{max} to lower scattering angles. Intensity distribution skewed.
Interspherulitic interference	Sinusoidal modulation of the SALS pattern (this coarseness increases as the number of illuminated particles increases).
Truncation and Impingement	Change from the four-leaf-clover to the four-tennis-racket pattern. Shift of θ_{max} to lower scattering angles. Lowering and broadening of I_{Hv} at θ_{max}. Finite scattering at $\theta=0$ and along the polarisation axes ($\mu=0^o$ and 90^o).
Incomplete development	Tendency towards the four-tennis-racket pattern. Stronger scattering at lower scattering angles.
Geometrical deviations	Finite scattering at $\mu=0$ and along the polarisation axes.

Table 7.2. The Effect of Disorder on the H_v SALS Four-leaf Clover Pattern for a Three-dimensional Anisotropic Spherulite.

Model Geometry	H_v SALS Pattern	Radius Determination.
Isotropic		
Three-dimensional sphere	x-type four-leaf-clover Low intensity (AD approx.)	U≈2.1
Anisotropic		
Three-dimensional sphere	x-type four-leaf-clover for optic axes perpendicular or parallel to the radius direction +-type four-leaf-clover for optic axes at 45^o to the radius direction.	$R_o=(1.025/\pi)(\lambda/(\sin\theta_{max}/2))$
Two-dimensional sphere, disk	As for three-dimensional anisotropic sphere.	$R_o=(1.96/\pi)(\lambda/\sin\theta_{max})$
Rod	x-type or +-type four-leaf-clover depending upon the orientation of the rod assembly.	No θ_{max}. Length of rod calculated from overall scattering pattern.
Sheaf-like	x-type or +-type four-tennis-racket depending upon the orientation of the optic axes within the sheaves.	N/A

Table 7.2. Theoretical H_v SALS Patterns for Various Isolated Geometries.

7.2.4. Statistical Approach.

In real systems when the degree of disorder is large, it is convenient to describe the system in terms of statistical functions rather than in term of size, shape and distribution of particles. A statistical theory of the scattering from a locally isotropic medium having only fluctuations in density was proposed by Debye and Bueche[30]. They defined a correlation function, $\gamma(r)$;

$$\gamma(r) = \frac{< \eta_1 \eta_2 >_r}{\tilde{n}} \tag{7.31}$$

where $\tilde{n}$ is the average refractive index, $\eta_1=\alpha_1-\alpha$ is the fluctuation in polarisability at point 1 and α is the spatial average polarisability for the medium. The symbol $<>_r$ designates an average over all points separated by distance r. When r=0, $<\eta_1\eta_2>_r=\tilde{n}$ and $\gamma(r)=1$. Thus $\gamma(r)$ decreases from unity towards zero with increasing r in a manner dependent upon the geometry of the system and represents the probability of correlation in polarisability fluctuations for pairs of volume elements separated by r. For the case of a rationalised system of units, the scattered intensity in terms of the Rayleigh ratio:

$$\Re = (\frac{\pi^2}{\lambda_o^4})\bar{n}^2 \int_V \gamma(r) \exp[-ik(r.s)]dr \tag{7.32}$$

where V is the volume element. It has been found experimentally and shown theoretically[49] that the correlation function is exponential;

$$\gamma(r) = \exp(\frac{-r}{a}) \tag{7.33}$$

where a is a correlation distance and is a measure of the spatial size of the fluctuation.

The Debye-Beuche theory was generalised by Goldstein and Michalik[50] to apply to anisotropic systems. Stein and Wilson[51] then proposed a less general but more easily applied model for random orientation fluctuations. Based upon the random fluctuation model, a more rigorous derivation of the scattered intensities, I_{Hv} and I_{Vv}, in terms of Rayleigh ratios have been proposed[5];

$$\Re_{Vv} = \frac{\pi^2}{\lambda_0^4}[\bar{n}^2 \int_V \gamma(r)\exp[-ik(r.s)]dr + \frac{4}{45}\bar{\delta}^2 \int_V \mu(r)f(r)\exp[-ik(r.s)]dr \tag{7.34}$$

$$\Re_{Hv} = \frac{\pi^2}{\lambda_o^4} \times \frac{1}{15}\bar{\delta}^2 \int_V \mu(r)f(r)\exp[-ik(r.s)]dr \tag{7.35}$$

where f(r) is a correlation function for orientation defined as;

$$f(r) = \frac{1}{V}\int_V [\frac{3\cos^2\theta'(R,r)-1}{2}]\, dR \tag{7.36}$$

and $\theta'(R,r)$ is the angle between the optic axes. When r tends to infinity, there is no correlation in orientation of the optical axes and so f approaches zero.

It follows from equation 7.34 and 7.35 that;

$$\Re_{Vv} - \frac{4}{3}\Re_{Hv} = \frac{\pi^2}{\lambda_o^4}\overline{\eta}^2 \int_V \gamma(r)\exp[-ik(r.s)]dr \qquad (7.37)$$

Thus, the density correlation function $\gamma(r)$ can be obtained from Fourier inversion of equation 7.37 while $f(r)\mu(r)$ is obtained from Fourier inversion of equation 7.35. If there are no orientation correlations, i.e. $I_{Hv}=0$, then equation 7.37 reduces to the Debye-Bueche equation.

Models have been proposed for non-random correlations where the probability of having two optical axes with correlated orientation depends upon the angle that an axis subtends with the interconnecting vector r, β, as well as the separation of these axes. This problem has been treated in two dimensions by Stein et al[52], in three dimensions by van Aartsen[53] and generalised to describe oriented systems[54]. However, a large number of parameters are necessary which are often difficult to evaluate and so this approach has limited use.

7.3. Apparatus.

7.3.1. Set-up.

Based upon earlier papers by Stein et al[55,56], the small angle light scattering set-up schematically represented in figure 7.4 and shown in figure 7.5, was constructed.

Housed in a large, light-tight box, solidly fixed to the wall, the main profile was vertically positioned. Excess space was purposefully left around the sample stage area for the potential incorporation of additional equipment such as electrical and magnetic poling apparatus, shear or deformation equipment, etc... Each optical component was designed to have two, sometimes three, degrees of lateral movement, and positioned at a constant height above the main profile (appendix I for a list of the each optical component).

A helium/neon laser (vertically polarised with reference to the analyser, wavelength, λ =632.8nm) was mounted on a shorter profile, orthogonally positioned at the base of the main profile. Approximately 90% of the laser radiation was reflected vertically upwards onto the sample area and the remaining 10% focused onto a small diode. This diode was connected to the detector and the signal obtained used to monitor any extraneous fluctuations in the incident beam.

Prior to scattering from the sample, it is necessary to attain a satisfactory main beam in terms of collimation, appearance, intensity and width. The main beam can be collimated using a beam expander, however, it was found that the original laser beam is suitably collimated. Addition of a beam expander not only reduces the incident beam intensity but also diminishes the optical clarity of the set-up. As a general rule, it is important to minimise the number of optical components prior to the sample stage in order to improve optical clarity. Neutral density filters and pinholes are used to adjust the intensity and the width of the main beam respectively. A range of neutral density filters are available (see appendix I). It is important that the intensity of the scattered light falling on the detector does not exceed 262×10^6 counts per pixel, otherwise the detector floods

and the image is distorted. In addition, excessive light may cause permanent damage to the active array in the CCD detector. Usually no neutral density filters are needed when the marata plate is incorporated in the SALS set-up since this plate dramatically reduces the overall scattering intensity. The diameter of the main beam is normally defined by a 150μm pinhole, although smaller pinholes are available if the experimenter wants to probe a smaller area of the sample. Unwanted Fresnel diffraction[57] of the main beam by the pinhole is removed by placing a second pinhole (500μm) approximately 5cm from the first, so only the primary portion falls on to the second pinhole.

The Linkam hotstage contains a 2mm aperture, allowing incident radiation to pass through a sample placed over this hole. The hotstage can be controllably cooled to liquid nitrogen temperatures and heated to 573K at a maximum rate of $100Kmin^{-1}$ (up to 873K if cooling water is circulated around the stage). For temperatures below 273K, to minimise the effect of condensation on the hotstage's windows, additional glass windows and/or thicker quartz windows are incorporated in the stage. This, however, reduces the optical quality of the SALS set-up. Problems are only encountered when using the V_V SALS mode (see later), in terms of extraneous scattering. This is overcome by increasing the size and/or changing the shape of the beam stop. Practically, care must be taken when filling the dewar with liquid nitrogen since the thin, black connecting tube to the hotstage becomes very brittle and may snap.

Two polarisers are placed either side of the sample stage and two different modes of operation are available; either H_V SALS or V_V SALS (see section 7.2). The higher case letter denotes the plane of polarisation of the incident light before the sample hotstage, and the subscript indicates the plane of polarisation after the sample hotstage (figure 7.1. illustrates H_V mode). The polariser placed between the sample hotstage and the detector is appreciably larger than the other polariser, allowing polar scattering angles, θ, up to 50^o to be attained when it is placed close to the sample hotstage.

The scattered light falls onto a marata plate, which is essentially a frosted plate. The resultant image is then focused onto the 1cm-1cm, 512x512 pixel CCD detector array using a telephoto lens attached to the detector. An 8 Mbyte detector controller board enables rapid data acquisition and storage, and a three stage Peltier cooler cools the photo active element to 193K, virtually eliminating the effects of dark current noise. A more detailed description of the OMA CCD detector can be found in appendix I.

7.3.2. Alignment.

Initial alignment involves removal of all the optical components apart from the laser, prism, coarse diaphragm and detector (with lens cap). A beam that is parallel with the vertically mounted stage and at uniform distance from the stage is desired. This is attained by adjusting the height position of the He/Ne laser, the orientation of the prism and by viewing the beam's position on the detector's lens cap. Vertically shifting the position of the coarse diaphragm proves to be a useful alignment tool.

Once aligned, the main beam can be refined by introduction of various optical components. A beam expander is available, however the collimation of the laser beam is satisfactory and such an addition proves only to lower the optical purity of the set-up and decrease the beam's intensity. Several neutral density filters are available to alter the intensity of the incident beam, and two pinholes are placed directly in front of the hotstage defines the incident beam's diameter and removes unwanted Fresnel diffraction. This diameter is smaller than the hotstage's aperture, usually 500μm in diameter. An absorbing sheet placed just before the hotstage removes any unwanted internal reflection.

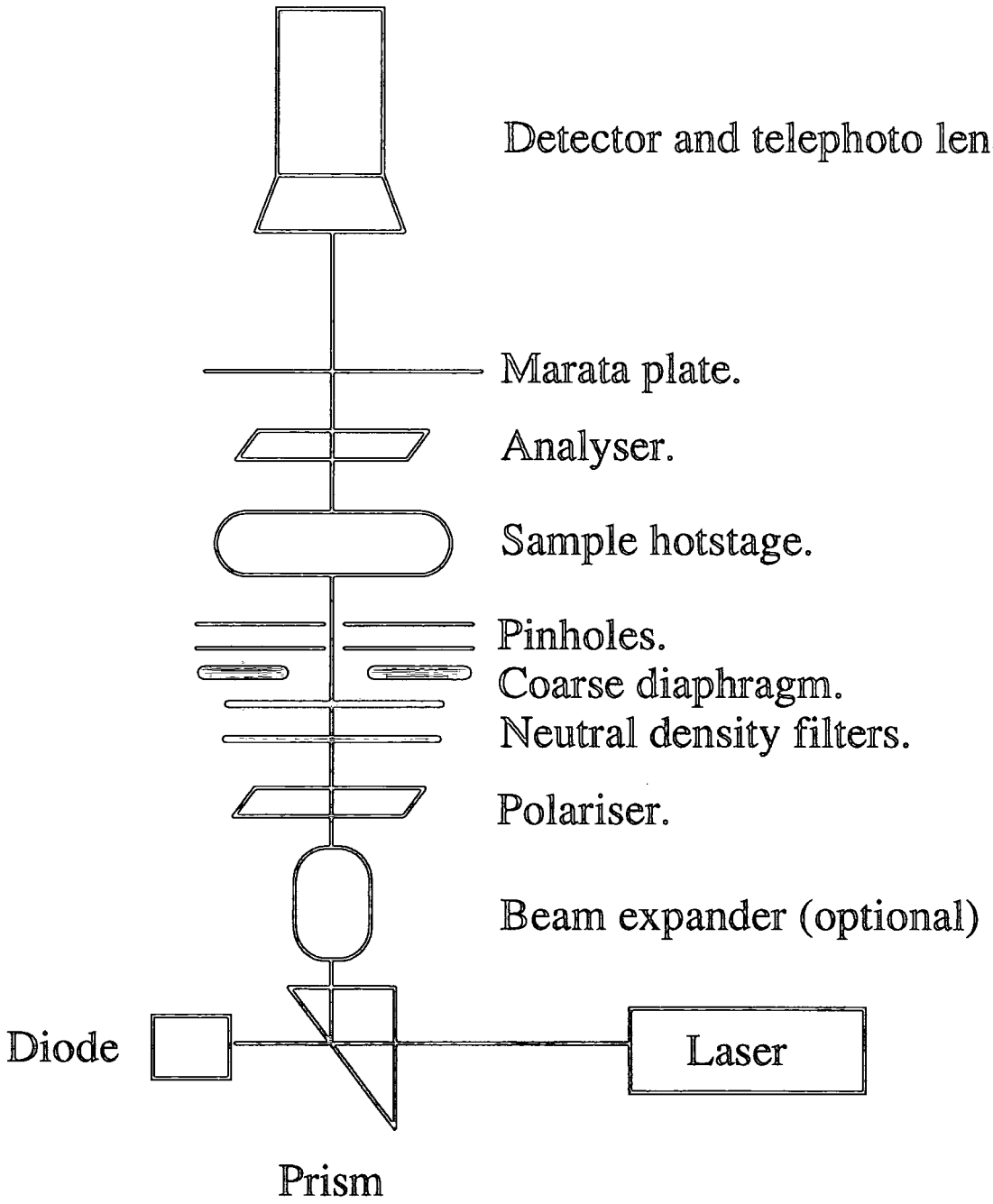

Fig.7.4. Schematic Representation of SALS Set-up.

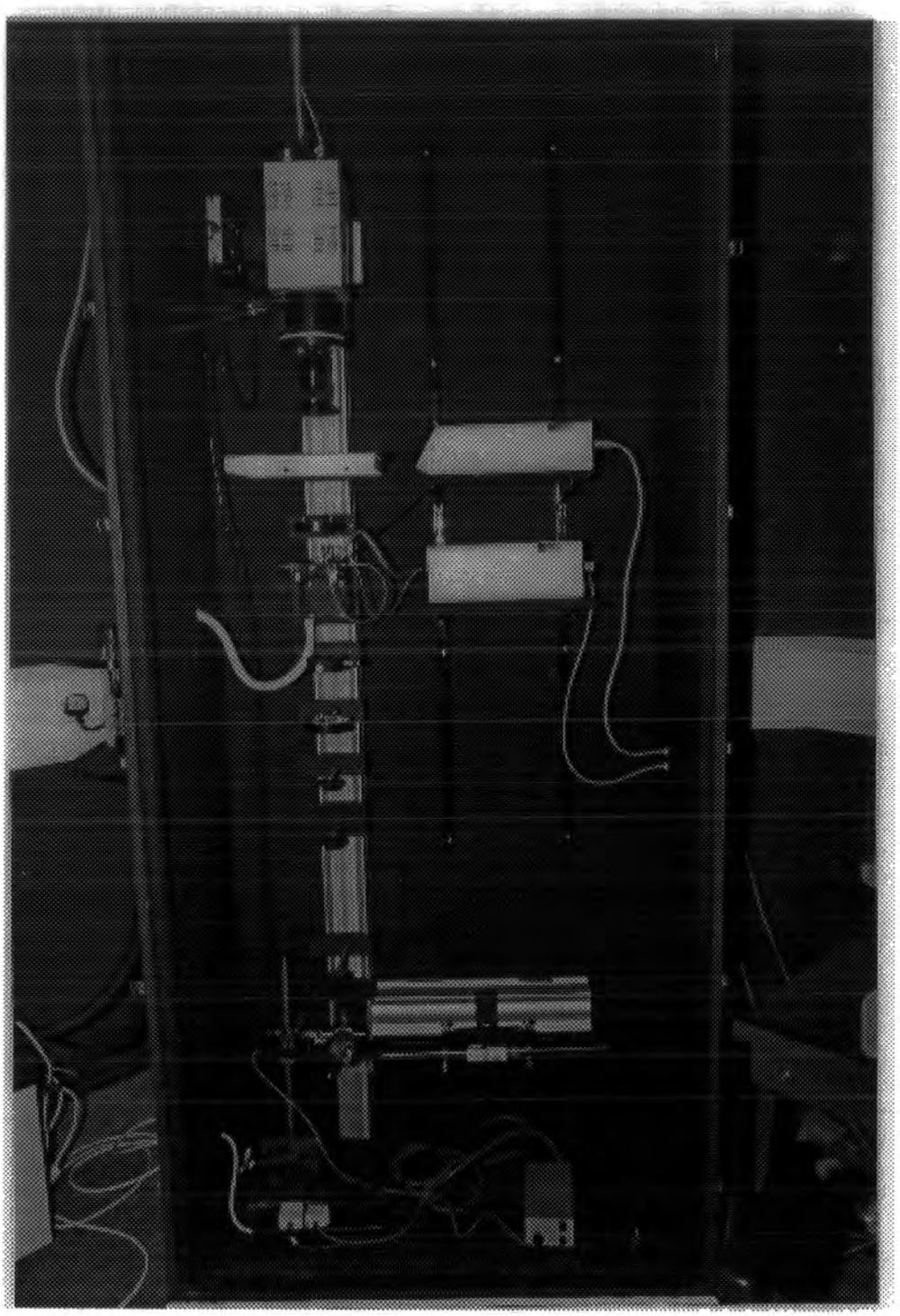

Figure 7.5. Small Angle Light Scattering Set-up.

7.3.3. Calibration.

The SALS set-up was calibrated using a 150 graduations per millimeter diffraction grating. The diffraction grating scattered light according to the expression: $d\sin\theta=m\lambda$, where d is the diffraction grating spacing, λ is the wavelength of the Helium/Neon laser, θ is the scattering angle related to the diffraction principle maximum, see figure 7.6 and m is the order of the principle diffraction maxima. Thus, the pixel value difference between each maxima is related to θ ($\theta=0.2417^{o}$ for $d=150\mu m$ and $\lambda=632.8nm$).

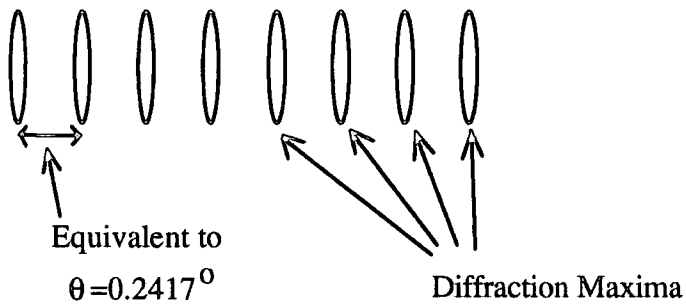

Figure 7.6. Image of Diffraction Pattern on Photo Active Element.

The polar scattering angular range was defined by the relative positions of the hotstage and the marata plate and also their positions along the vertical profile (see calibration table 1).

The values in table 7.4 represent the number of pixels on the detector's surface which is equivalent to a polar scattering angle, θ, of **0.2417°**. For example, for marata plate and hotstage positions, 65 and 25 respectively (M.P.=65, H.S.=25), and for a scan set-up of 512 X (50 x10) (see later), $\theta = 0.2417^{o}$ is equivalent to 5.22 columns (5.22 pixels) along the x axis, and 0.522 rows (5.22 pixels) along the y axis. The relationship between the number of pixels and polar scattering angle can assumed to be linear. Thus, 100 columns along the x axis (equal to 100 pixels) is equivalent to $\theta = 4.63^{o}$.

H.S.	M.P. 65	Max. θ	Max.q (μm^{-1})	M.P. 55	Max. θ	Max.q (μm^{-1})	M.P. 75	Max. θ	Max. q (μm^{-1})
4.7	8.14	7.6°	1.316	4.46	13.87°	2.40	16.01	3.86°	0.67
15	6.63	9.33°	1.615	4.14	14.95°	2.58	-	-	-
25	5.22	11.85°	2.05	-	-	-	-	-	-
35	3.62	17.09°	2.951	1.63	38.08°	6.48	-	-	-

Table 7.4. SALS Calibration Table with Marata Plate

(Number of Pixels Equivalent to θ=0.2417°).

Key:

H.S. = hotstage position using the scale on the vertical profile, (positions are read from the top of each component's carrier).

M.P. = Marata plate position.

Max. θ = maximum polar scattering angle possible.

q = scattering vector, $q = 4\pi n/\lambda \sin(\theta/2)$ (here λ=632.8nm, n=1), where n is the refractive index of the sample.

The maximum scattering angle has been calculated by assuming that the main beam position is at the centre of the detecting array i.e. at pixel co-ordinate (256,256) for a 512 X 512 set-up. Thus, the maximum polar scattering angle for M.P.=65 and H.S.=25 is, max. θ = 256/5.22 x 0.2417 = 11.85°.

Initial experiments suggests M.P.=65 provides good SALS resolution and a convenient range of θ (see calibration graph for M.P.=65, figure 7.7.a). As shown in figure 7.7.a, the number of pixels per θ=0.2417° increases as the diffraction grating is moved further away from the detector, i.e., as the M.P. position decreases. This is an expected trend as the diffraction maxima fan out at larger distances. Without the marata

plate, the intensity of the incident beam is greatly increased. Consequently it is necessary to lower the intensity using neutral density filters. The maximum polar scattering angular range attainable without the use of a marata plate is 3.75^{o} to 4.64^{o} (see figure 7.7.b). In this case, there is a slight decrease in the number of pixels per $\theta=0.2417^{o}$ as the diffraction grating is moved to lower M.P. values. This is an unexpected trend and may reflect a slight divergence in the incident radiation.

The telephoto lens on the detector has three adjustment parameters, focal length, aperture size and depth of field. These alter the size (scattering angle) and shape of the scattered light falling on the plane of the detector. To minimise the complexity of the optical set-up, these have been set at the following values, focal length = ∞, depth of field = 12.5 and aperture size = 1.6.

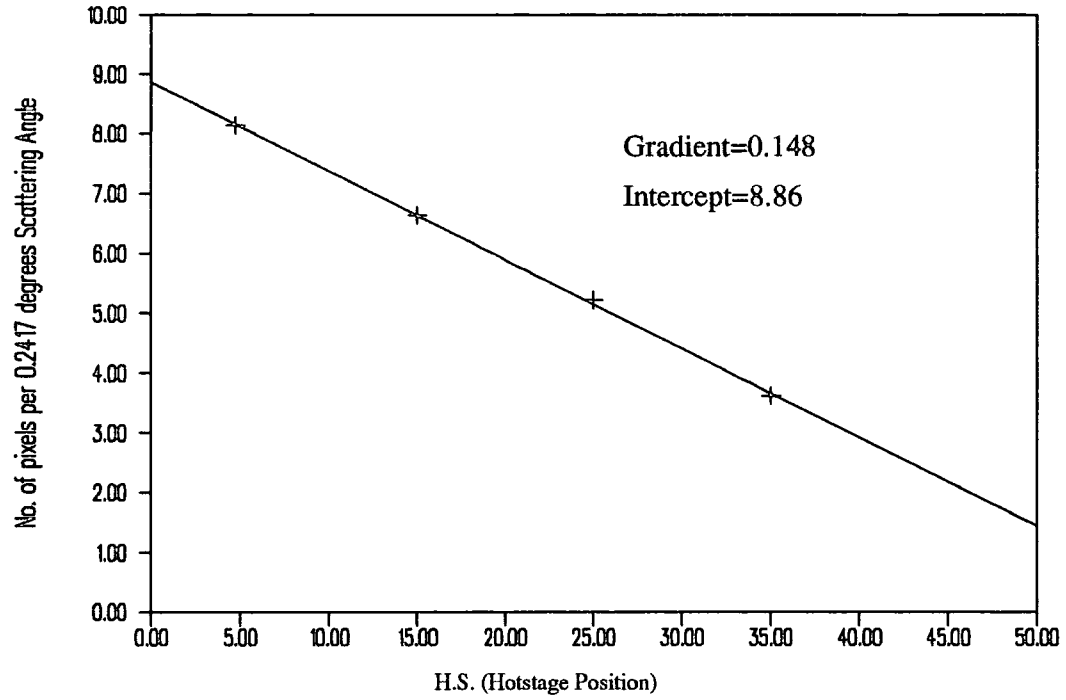

Figure 7.7.a SALS Calibration with Marata Plate at M.P.=65.

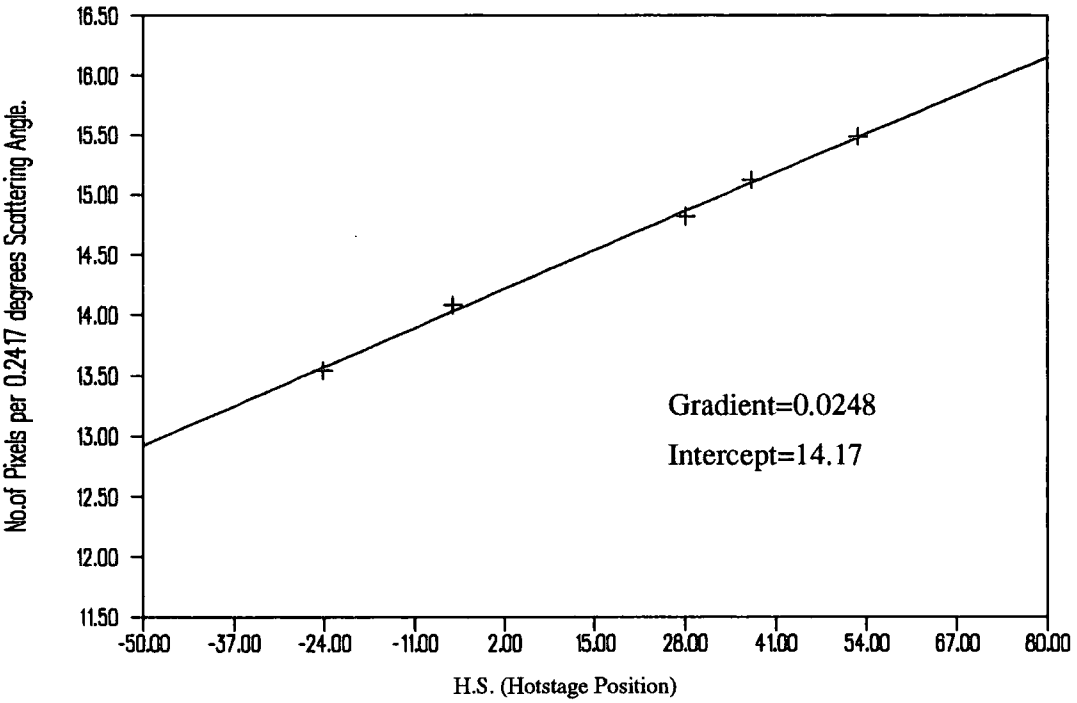

Figure 7.7.b SALS Calibration Without Marata Plate.

7.4. Data Acquisition.

7.4.1. Sample Preparation.

Samples are usually prepared as thin films placed between two glass cover slips (two glass cover slips aid in the formation of a thin film with uniform thickness). The type of substrate used is often assumed to have little effect on the properties of the sample under investigation. However, Edel et al[58] have shown that using glass and gold substrates, that the phase behaviour of thin films of polystyrene and poly(methyl methacrylate-co-cyclohexylmethacrylate) is dependent upon both sample thickness and substrate. The thickness of each film varies according to the nature of the polymer under investigation, however, it is important due to modelling considerations that the light scattered remains in the single scattering regime[55] (no multiple scattering) i.e. approximately 80% of the incident radiation is transmitted by the sample. If the sample is too opaque, then multiple scattering becomes excessive and corrective procedures during analysis are necessary[59,60]. However, if the sample is too thin, then surface effects become dominant. This contribution can be minimised by melting the polymer between two glass slides or by immersing the sample in a suitable refractive index matching fluid[61].

Sample films were either cast from solution or melted onto the glass substrate. Solution concentrations vary normally from 5 to 20% weight by weight, and it was essential to remove all of the solvent prior to measurement. An important practical point to note is that if thick substrate slides are used, then a temperature gradient may be present between sample and hotstage.

7.4.2. Run Set-up.

The following practical/software points have been described in more detail in the OMA4000 manuals (ref. no. 221535-A-MNL-B, 221534-Z-MNL-A and UK4000SW-A-MNL-A supplied by EG&G) and in a SALS manual[62]. For the text below, bold type refers to labelled fields in the OMA4000 software.

With the computer turned on, the laser beam and the detector's cooling water supply (set at 283K), and then the detector's power block are turned on. The OMA4000 detecting software is then initialised using the 4000.bat file in the OMA4000 directory.

The OMA4000 software has two display menus, each containing a horizontal information bar at the top of the screen displaying several fields. Prior to data acquisition, the parameters in each field need to be customised according to the criteria of the SALS experiment i.e., number of scans, time between each scan, exposure time, scan set-up (see below).

Firstly, the **detector/temperature on/off** field in the **run, set-up** menu is turned on and allowed to cool to a specified temperature, usually 213K, for at least thirty minutes. This reduces background noise (dark current). A green 'locked' information bar in the top right hand corner of the main menu indicates that the detector is at the specified temperature.

7.4.2.1.Set-up

Data acquisition mode - pre-defined data acquisition (DA) mode (DA 1 can be customised if necessary - see OMA4000 software manual).

Memories/ Data scans/ Ignored scans/ Prep. scans - for **Go Live**, needs to be 1 1 0 0. For **Go Accum**, defines the number of scans and the time between each scan (see section 7.4.3).

Exposure time - exposure time of the detecting array - time between open and closed shutter.

Detector temperature on/off - normally set at 213K for at least thirty minutes prior to data acquisition- reduces dark current contributions. This temperature is attained using a Peltier cooler and an accompanying water supply (Haake F3 and GH, Mess-Technik GmbH u. Co., Dieselstr. 4, 7500, Karlsruhe 41, Germany).

7.4.2.2. Scan

This field defines the scan set-up. The maximum number of scans possible in any one experiment using Go Accum is dependent upon the scan set-up used. For example, for a scan set-up of 512X512 pixel array (no binning of pixels), owing to the restriction of available RAM on the OMA control board, the maximum number of scans possible is 8. For a 512x50 set-up (i.e. ten pixels binned into one data point), the maximum number of scans is 81).

The time required for data processing and storage also depends upon the scan set-up (as well as Pixel Time and Anti-Bloom). Table 7.5 lists the times taken for data acquisition and storage for a series of scan set-ups (100% anti-bloom).

Array	512x1, 512x1	512x1, 50x10	50x10, 512x1	100x5, 100x5	100x5, 512x1	100x1, 100x1
Normal Pixel Time (s)	4.808	0.511	1.255	0.360	1.636	1.014
Fast Pixel Time (s)	2.706	0.307	1.044	0.282	1.226	-

Table 7.5. Time Required to Process and Digitise One Data Scan (Excluding Exposure Time).

7.4.3. Data Acquisition.

There are two modes of data acquisition - Go Live and Go Accum - selected from the run menu.

Go Live - data is acquired according to the scan set-up. Each scan overwrites the previous scan and only the last data scan is stored in the temporary data curve called 'Lastlive'. This mode is primarily used as an visual aid to determine the nature of the SALS data.

Go Accum - a series of scans are acquired and stored on the OMA control board inserted inside the Dell 333D (up to 8MBytes). The number of scans is defined by the memories field and the frequency by the ignored scans field.

For example;

Scan set-up - 512X50, from table 7.5, processing and data storage time for one scan is 0.511 seconds.

Exposure time = 300ms.

Memories = 3 (20 data scans are recorded when Go Accum is initiated).

Data Scans = 1 (1 scan is performed, the data stored and then the number of ignored scans performed).

Ignored Scans = 3 (after performing each data scan, 10 scans are performed but no data is stored).

Prep. Scans = 2 (Prior to the first data scan, two scans are performed but no data is recorded. This acts as a time delay before data acquisition and also removes any built up charge on the detecting array).

Thus, for the parameters used above, the following time sequence for data acquisition using Go Accum applies;

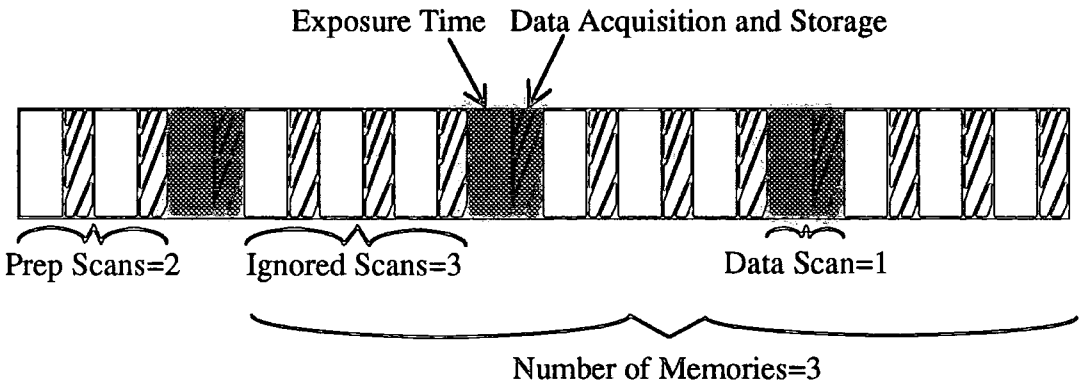

Figure 7.8. Schematic Representation of the Time Sequence for Data Acquisition using Go Accum.

A decrease in the anti-bloom percentage results in only a small reduction in processing time, e.g. for array 512x1,50x10, data processing and digitisation time = 0.511 seconds (100% anti-bloom) and 0.487 seconds (0% anti-bloom).

7.4.4. Data Storage and Manipulation.

Once data has been acquired, prior to storing the data permanently onto the hard disk, it is good practice to inspect the quality of the data in the temporary data file (called 'lastlive' by default). Each data scan is partitioned into curves. The number of curves depends upon the type of scan set-up used and is equivalent to the number of rows used in the scan set-up. To inspect the data file, select **Files**, **Directory**, and then the curve (s) from the curve directory to be inspected. The value associated with the **curve** field is the number of data scans multiplied by the number of rows in the scan set-up, e.g. scan set-up is 512x50 and the number of memories for Go Accum is 60, then the total number of curves in 'lastlive' is 50 x 60 =3000. To inspect the 10th scan, you need to load that part of 'lastlive' into the temporary curve directory. Once lastlive has been selected, change the function field to **load curve set**, enter the number of the curve at which the 10th scan starts in the **start** field i.e.10 x 50 =500 and the number of curves to be counted in the

count field i.e. 50 for a 512x50 scan set-up, rename the file and execute Go. Enter the plot set-up required, normally 1 (this is accomplished by entering a cross in the plot set-up field whilst in the curve directory display), and then return to the graphics display by either pressing F10 or Escape. The data can be autoscaled to view the full range of intensities by pressing F8. If another curve set is present in the curve directory with the same plot set-up, then this will also be autoscaled.

The file can then be renamed (an appropriate sub directory if chosen if necessary) and then saved to the hard disk by executing the 'save as' field. The Dell 333D has approximately 200MBytes of memory available for data storage. Since each data uses a large quantity of memory on the hard disk, it is necessary to save the data files to tape when the hard disk is nearly full using the tape operating software package SYSTOS.

The OMA4000 software can be used to analyse and manipulate the SALS data, however a more powerful computing package is PV-Wave (ideal for large data sets). PV-Wave has been loaded onto the VAX and so it is necessary to down load the acquired data to the VAX. Firstly, the format of the data needs to be changed (simplifies data manipulation when using PV-Wave). Whilst the acquired data is in the curve directory (if not it can be re-loaded using the load curve set field), select Files and Translate. Enter the name of the data in the curve directory as the input file ('lastlive' or filename), and then an output filename (c:\filename). Select the format OMA1460 (ASCII type) and execute.

After the data file has been formatted, it is transferred to the VAX via the Rainbow ethernet. Exit the OMA4000 software, and enter Rainbow using the rainbow.bat file in the rainbow directory. Once in Rainbow, select transfer file option, single file transfer and enter the following;

c:\filename dur.ircvax::[user name.directory]filename (user name password).

e.g. c:\lastlive dur.ircvax::[phr.bc13]lastlive.dat phr password

Once transferred, to save space on the computers hard disk, delete the formatted data file. A 'disk quota exceeded' message appears if there is insufficient space on the VAX when file transfer is in progress.

7.4.5. Data Analysis.

After the data has been down loaded onto the VAX station, it can be analysed using PV-Wave. The software is initialised using the command 'wave'.

Prior to data manipulation, the data sets need to be formatted. At the start of each data set there is a four line header describing the size of the data file. This is followed by a single column of data values. In order to read the data values, it is necessary to position the 'cursor' at the start of the single column of data values. This is accomplished by creating a string array that is four lines long, ob, and then reading this array. Firstly, however, the data set is opened for reading by entering; **openr,1,'filename.dat;1'**, where 1 denotes the Logical Unit Number, LUN. Each LUN number represents is a defined area of computing space where operations are performed. Each LUN needs to be opened and closed when necessary.

The four string array is created and named ob; **ob=strarr(4)**

The header is read into ob and so now the cursor is positioned at the start of the single column of data values; **readf,1,ob**

If the data scan was in a 512x50 format, then a floating point array of size 512x50 is created, **a36=fltarr(512,50)**.

Read in the data; **readf,1,a36**

If more than one data scan is present in the data file, then this additional data can be subsequently read into either the existing variable, a36, or another variable. All variables are temporary, and so may be overwritten and are lost when the software is exited. Additional variables need to be defined prior to use.

Once the data has been read into a defined variable, it can be manipulated accordingly. For SALS, it is often necessary to perform routine manipulations repeatedly. Consequently, several macros have been written (see appendix II). They may be edited using the VMS editor ($edit), compiled by entering the command, .run macroname.pro and executed using, macroname,data array name. For example if a36 is the array name and int.pro is the macro for determining the overall intensity of a series of scans, then the following commands apply; .run int.pro followed by int,a36. VMS commands can be executed whilst in PV-Wave by placing a $ sign in front of each command.

7.5. Experimental.

7.5.1. Introduction.

Using small angle light scattering, the isothermal crystallisation kinetics of BC76 and BL80 and the proposed microphase separation of BC55 and BC50 at low permanence temperatures (see Chapters 4 and 6) were investigated.

7.5.2. Sample Preparation.

The polymer samples in powdered form were melt cast between two glass cover slips on a Linkam hotstage. Thin homogeneous films, approximately 4μm thick, were formed. Preliminary experiments found that solution cast films were inhomogeneous.

7.5.3. Isothermal Crystallisation.

The isothermal crystallisation kinetics of BC76 and BL80 were evaluated by monitoring both the amount of depolarised light (H_V mode) and the variation in the spherulitic radius, R, as a function of time for a series of crystallisation temperatures (range 295K to 311K). The polymer films were heated to 423K for 10 minutes in the SALS Linkam hotstage, and then quenched ($100Kmin^{-1}$) to a series of crystallisation temperatures, T_C. Once at T_C, the time during isothermal crystallisation, t, was initiated. The number of scans and the time between each scan at T_C depended on the run set-up in Go Accum mode as described in section 7.4.3.

7.5.4. Microphase Separation.

For the block copolymers BC50 and BC55, the overall V_V intensity was recorded as a function of permanence time for a series of low permanence temperatures, T'. As with the DSC and x-ray experiments (see chapters 4 and 6), the samples were heated at 423K for 10 minutes and then quenched ($100Kmin^{-1}$) to the permanence temperature, T'.

7.6. Results.

7.6.1. Isothermal Crystallisation.

7.6.1.1. Depolarised Intensity.

Figure 7.9 shows the overall depolarised light intensity (arbitrary units), I_{Hv}, as a function of time for a series of crystallisation temperatures for BC76. Similar sigmoidal crystallisation isotherms were observed for BL80, for a series of crystallisation temperatures.

7.6.1.2. Spherulitic Radius.

Figure 7.10 shows a typical H_v SALS four-leaf-clover pattern for BC76. The x-type pattern is indicative of a semi-crystalline spherulitic morphology whose crystalline molecular axis is either parallel or perpendicular with respect to the spherulitic radius (see section 5.4).

Using the macro SALS.PRO (appendix II), the intensities of the four lobes were added together, averaged, and then a slice was taken from the main beam position through the intensity maximum of this averaged lobe. This was repeated for each SALS scan. Figure 7.11 shows the resultant H_v SALS intensities for BC76 as a function of polar scattering angle, θ, for a series of time at T_c =308K.

Owing to the relatively large spherulitic size of the semi-crystalline polymers under investigation, with respect to the diameter of the incident radiation, four-leaf clover images were not obtained for all data runs. That is, for most of the SALS runs, the incident radiation only illuminated parts of the whole spherulites. The subsequent extinction patterns were poorly developed and did not give form four-leaf clover H_v SALS patterns. The number of non four-leaf clover patterns increased at higher T_c as at these crystallisation temperatures, the spherulites were larger.

Figure 7.9 Overall Depolarised Intensity vs. Crystallisation Time for BC76.

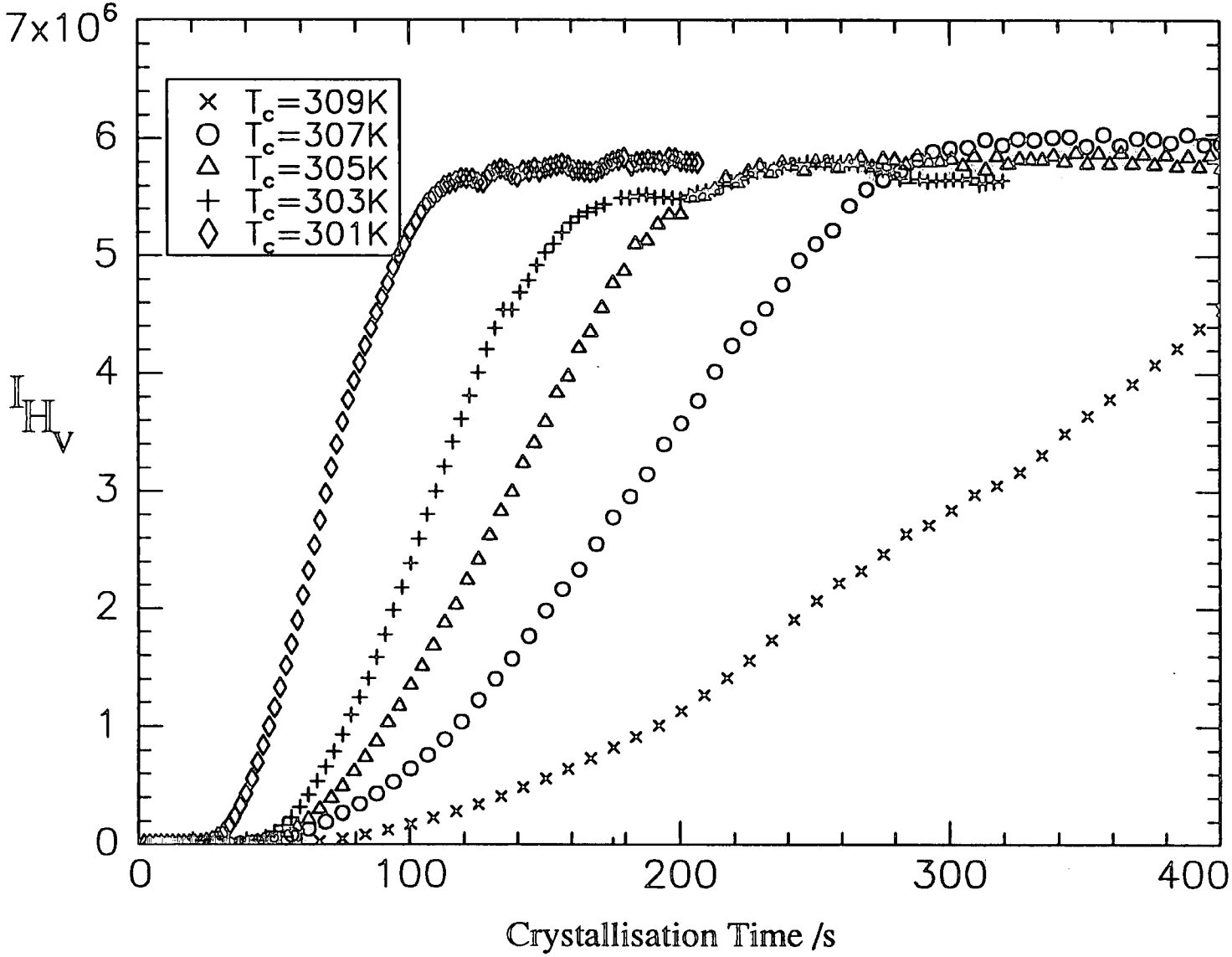

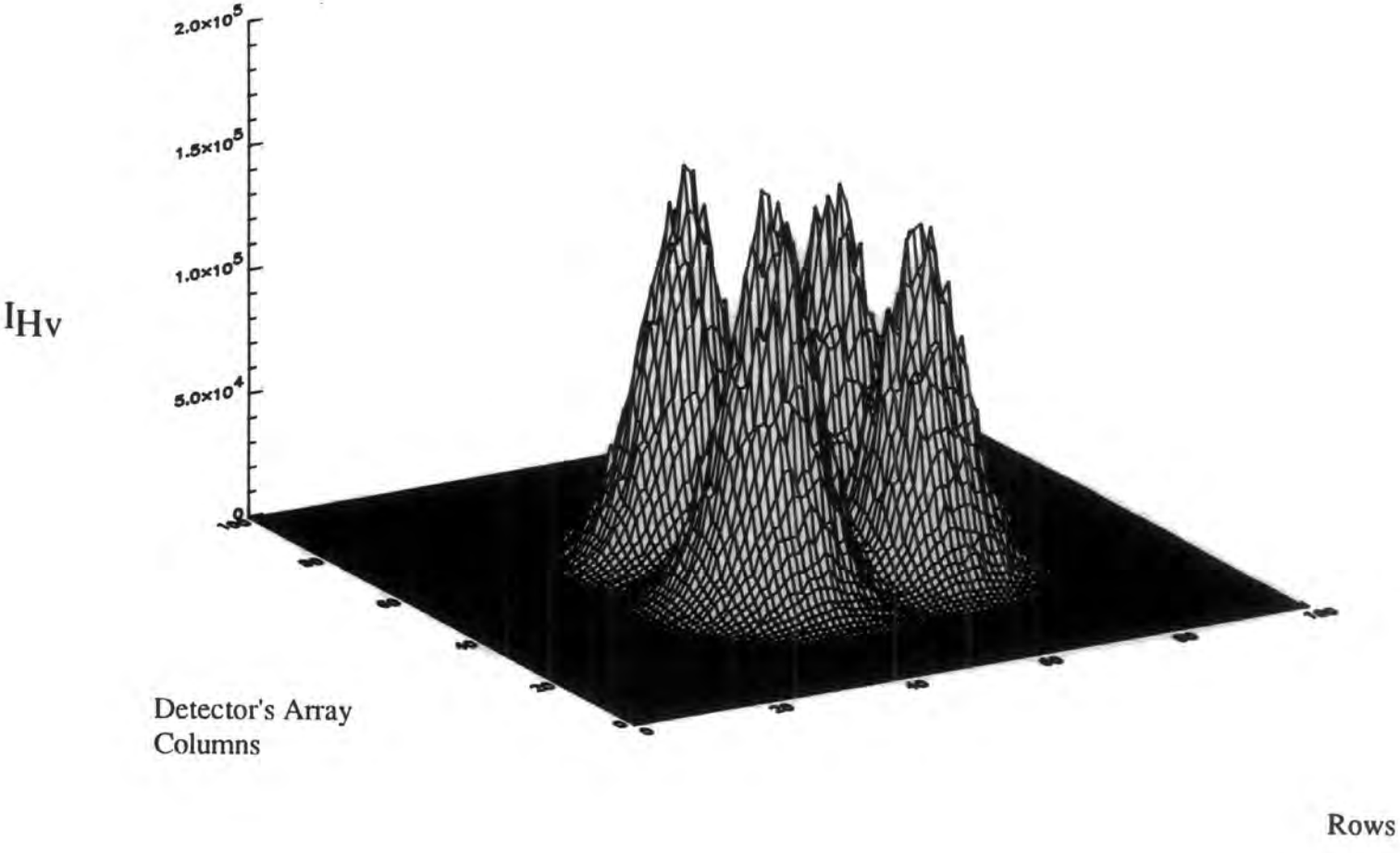

Figure 7.10. 3-D Four-leaf Clover H_v SALS Pattern of Semi-crystalline BC76.

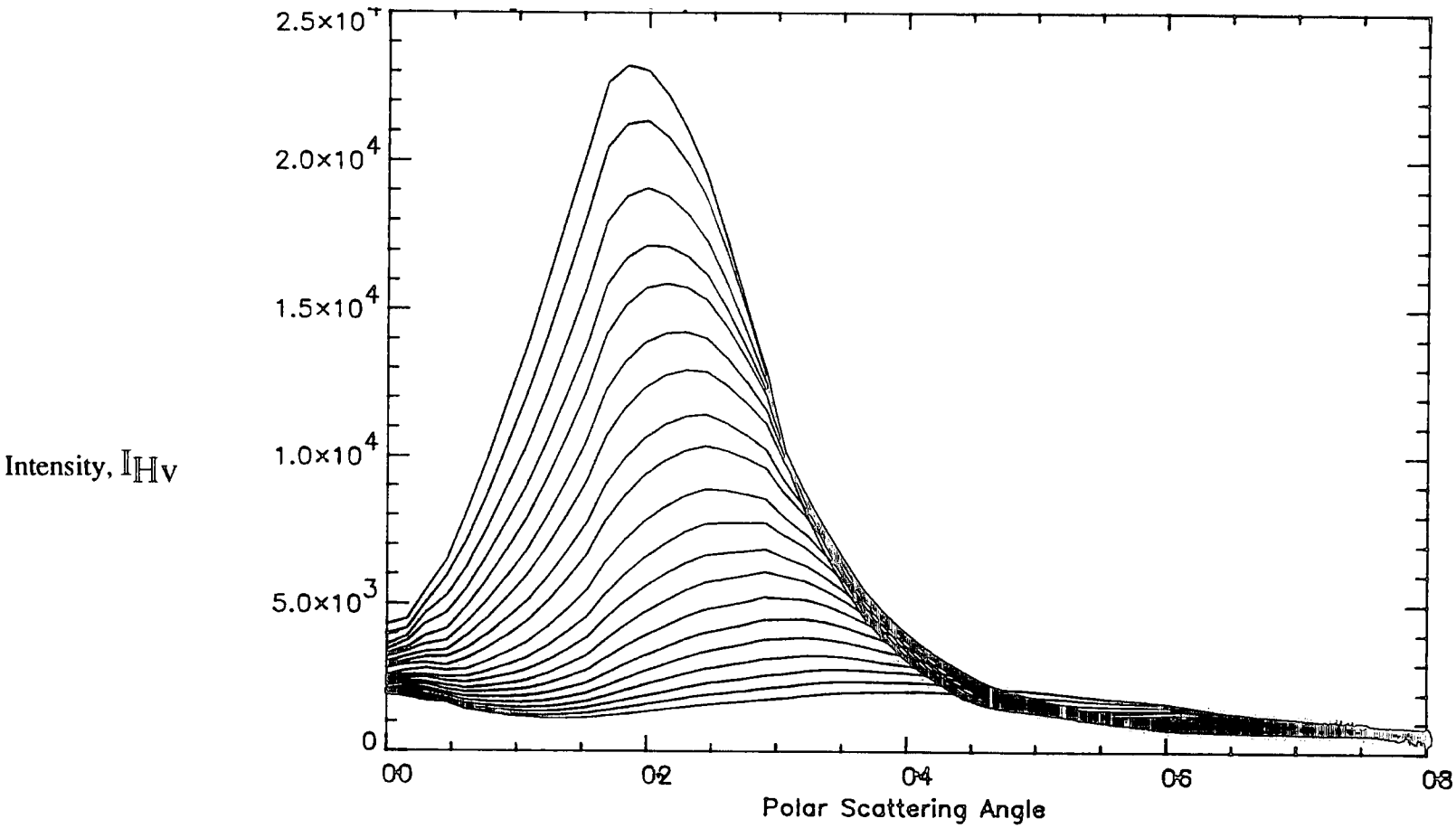

Figure 7.11. H_v SALS Intensities Taken from the Main Beam Position Through I_{max} for BC76 at T_c=308K for a series of Crystallisation Times..

7.6.2. Microphase Separation.

For temperatures below T'=239K for BC50, the V_V intensity varied sigmoidally with permanence time, t. Whereas above T'=245K, the overall V_V intensity did not vary with time, see figure 7.12. Similar intensity variations were detected for BC55 for permanence temperatures, T'<253K.

7.7. Analysis and Discussion.

7.7.1. Isothermal Crystallisation.

7.7.1.1. Depolarised Intensity.

Assuming that the depolarisation intensity of plane-polarised light I_{Hv}, is directly proportional to the quantity of crystalline material[93], then it is possible to monitor the overall crystallisation kinetics using SALS by means of an Avrami analysis;

$$\theta = \exp\left(-K_n t^n\right) \tag{7.38}$$

where θ, the fraction of untransformed material, is of the form $(I_C-I_t)/(I_C-I_O)$[93], I_O and I_C are the initial and final intensities and I_t the intensity at time t. K_n is related to the isothermal crystallisation rate constant and n is the Avrami exponent. Equation 7.38 is easily transformed into the double logarithmic form used for experimental analysis;

$$\log(-\ln\theta) = n\log t + \ln K_n \tag{7.39}$$

Figure 7.13 shows the subsequent Avrami analysis of BC76 for a series of isothermal crystallisation temperatures. Owing to the double logarithmic nature of

Figure 7.13 Avrami Analysis of the Overall Depolarised Intensity Data for the Isothermal Crystallisation of BC76.

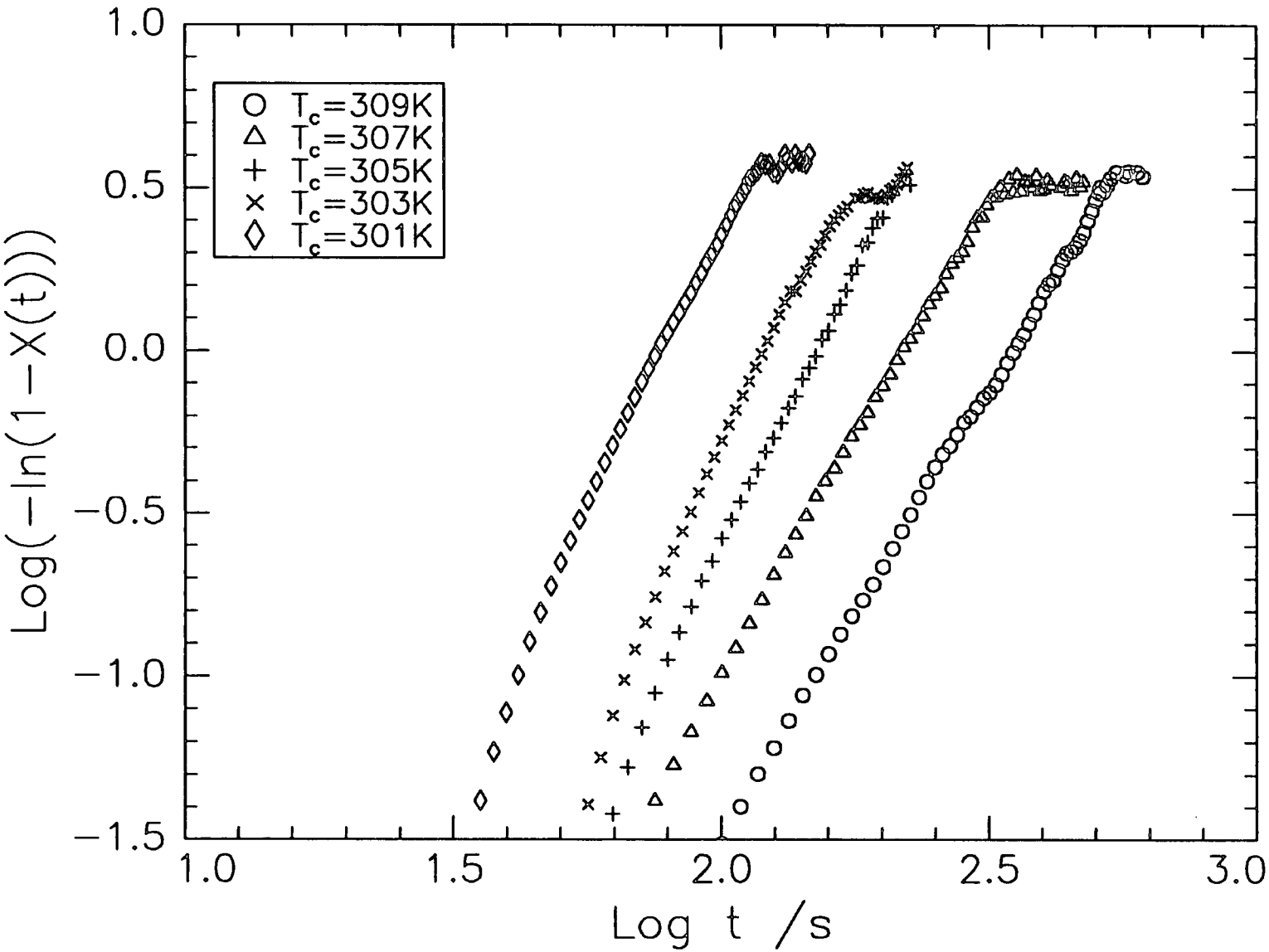

Figure 7.12 Vv SALS Intensity vs. Permanence Time, t at Two Permanence Temperatures for BC50

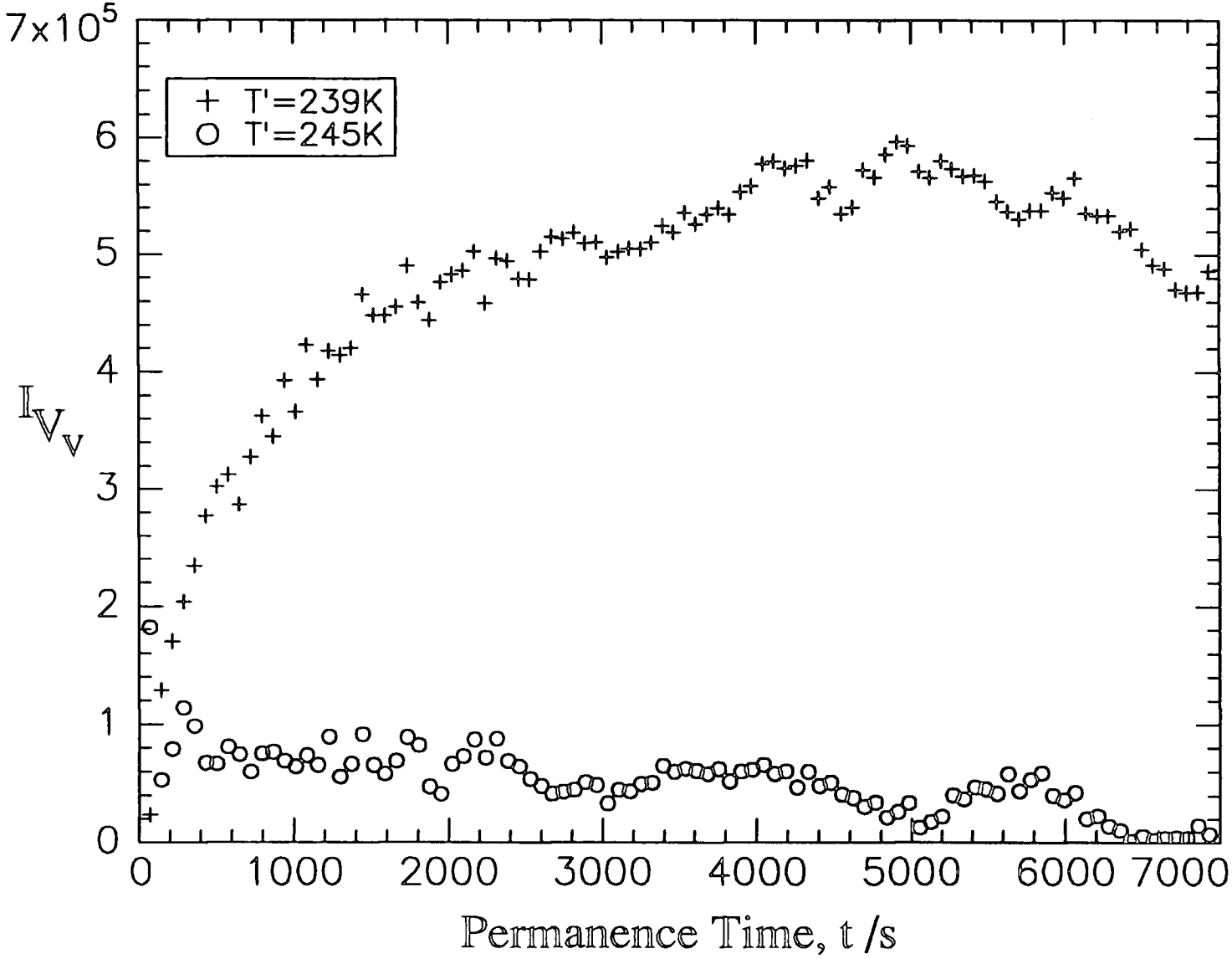

equation 7.39, the linear fit is weighted towards higher values of log(t) to encompass the majority of data points. Tables 7.6 to 7.7 lists the evaluated Avrami parameters for BC76 and BL80 respectively. The standard deviations for n and $\log K_n$, calculated from repeated measurements, were 0.2 and 0.3 respectively.

The Avrami exponents for BC76 and BL80 as a function of isothermal crystallisation temperature are plotted in figure 7.14. Both BC76 and BL80 (for isothermal crystallisation temperatures greater than 303K), showed a slight increase form approximately n=2.5 to n=3.0 as the crystallisation temperature decreased. For BL80 at T_c <303K, n increased abruptly to approximately n=4. From table 1.2, n=2.5 relates to homogeneous nucleation with a spherical growth geometry which is diffusion controlled. However, since the spherulitic radii are far greater than the film's thickness, then it is already known that the growth geometry is disc-like. Thus, n=2.5 suggests homogeneous nucleation where the rate determining steps are approximately equal. As n increases to n=3, the rate governing step in the overall isothermal crystallisation process tends towards one that is interfacially controlled. This change in crystallisation mechanism as T_c decreases can be related to the degree of undercooling. As the degree of undercooling increases, then there is a concomitant increase in the free energy of the system to crystallise. This manifests itself as an increase in the rate of crystallisation. There is, however, the opposing factor of mobility at large undercoolings. As T_c decreases, the temperature tends towards the glass transition temperature of the system and so the mobility of the crystallisable units also decreases. When this factor dominates, the rate of crystallisation decreases. For the crystallisation temperatures studied, this is not the case. Thus, the rate of diffusion increases as T_c decreases and so as observed experimentally, attachment of the crystallisable units to the crystal interface tends to be the slowest, rate determining step.

Figure 7.14 Avrami Exponent versus Crystallisation Temperature for BC76 and BL80.

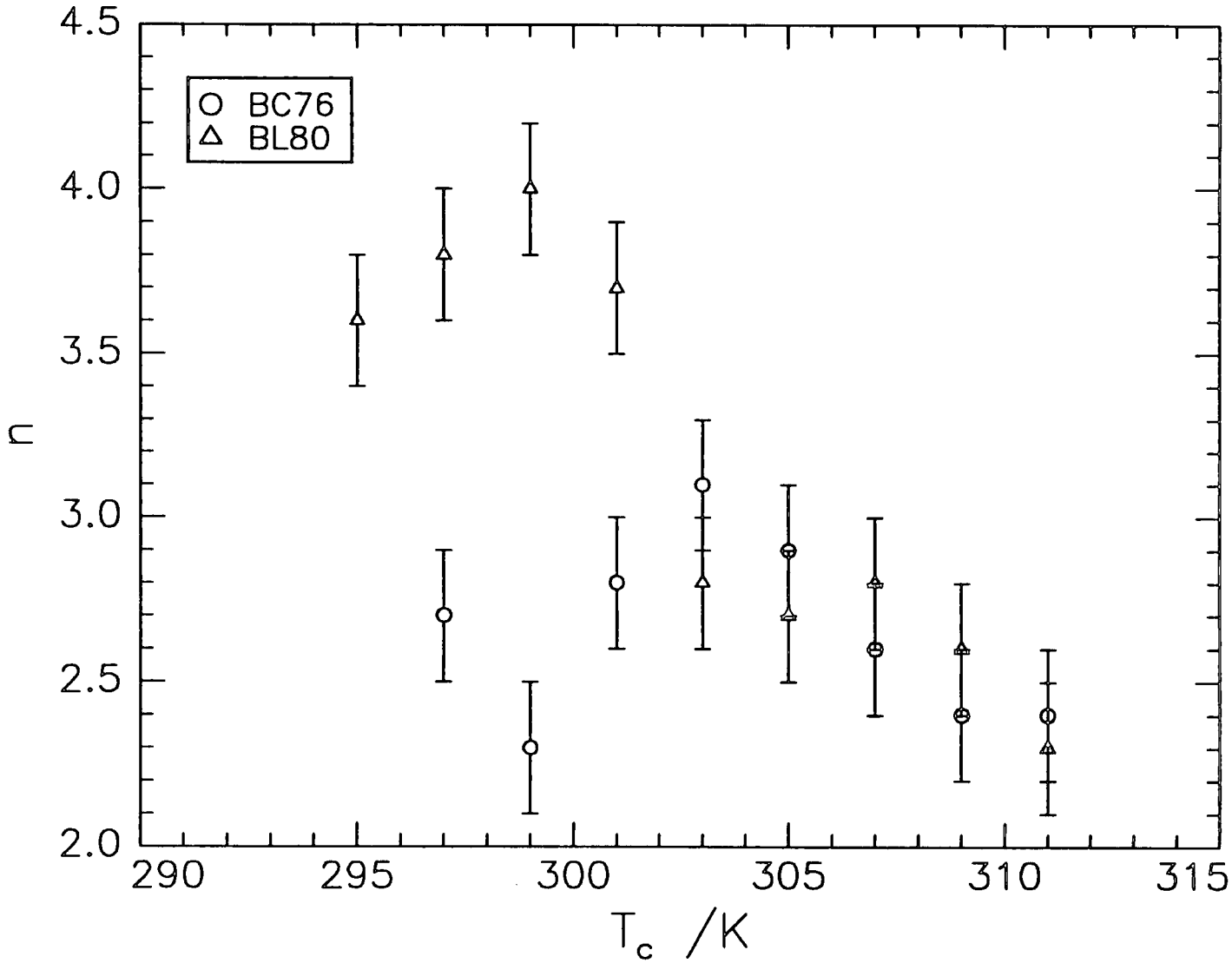

T_c (K)	n	$Log(K_n)$
297	2.7	-4.4
299	2.3	-3.9
301	2.8	-5.0
303	3.1	-6.3
305	2.9	-6.2
307	2.6	-5.8
309	2.4	-6.0
311	2.4	-6.3

Table 7.6. Evaluated Avrami Parameters for BC76 from Depolarised Light Scattering Data.

T_c(K)	n	$Log(K_n)$
295	3.6	-4.6
297	3.8	-4.8
299	4.0	-5.7
301	3.7	-5.2
303	2.8	-4.3
305	2.7	-4.3
307	2.8	-4.4
309	2.6	-4.9
311	2.3	-5.1

Table 7.7. Evaluated Avrami Parameters for BL80 from Depolarised Light Scattering Data.

(Error term for n= ±0.2).

At n=4, there is no corresponding interpretation for a disc-like growth geometry. A possible explanation may be that at these low T_c for BL80, the spherulites grow so quickly that the spherulites truncate forming spherical crystalline entities with radii commensurate with film thickness.

Figure 7.15 shows the $\log K_n$ versus crystallisation temperature for BC76 and BL80. This graph clearly shows that the rate of crystallisation of BL80 is greater than that of BC76 at the same crystallisation temperature i.e. $\log K_n$ is less negative for BL80. For BC76, $\log K_n$ becomes less negative as T_c decreases indicating an increase in crystallisation rate. For BL80, however, after an initial increase in crystallisation rate, $\log K_n$ becomes more negative at lower T_c suggesting that the lower mobility of the crystallisable units is beginning to dominate the crystallisation process.

7.7.1.2. Spherulitic Radius.

Using equation 7.29, averaged radii of the crystalline disc morphology were evaluated from the polar scattering angle position of the maximum H_v intensity as a function of time at T_c. The refractive indices of the polymeric sample were calculated from the relative fractions of the homopolymer constituents. The refractive indices of the homopolymers PEO and PMMA were calculated from the molar refraction group contributions, R_{LL}[63], using equation 7.40;

$$n = \left(\frac{1 + \frac{2R_{LL}}{V_m}}{1 - \frac{R_{LL}}{V_n}} \right)^{1/2} \qquad (7.40)$$

Figure 7.15 $LogK_n$ versus Crystallisation Temperature for BC76 and BL80.

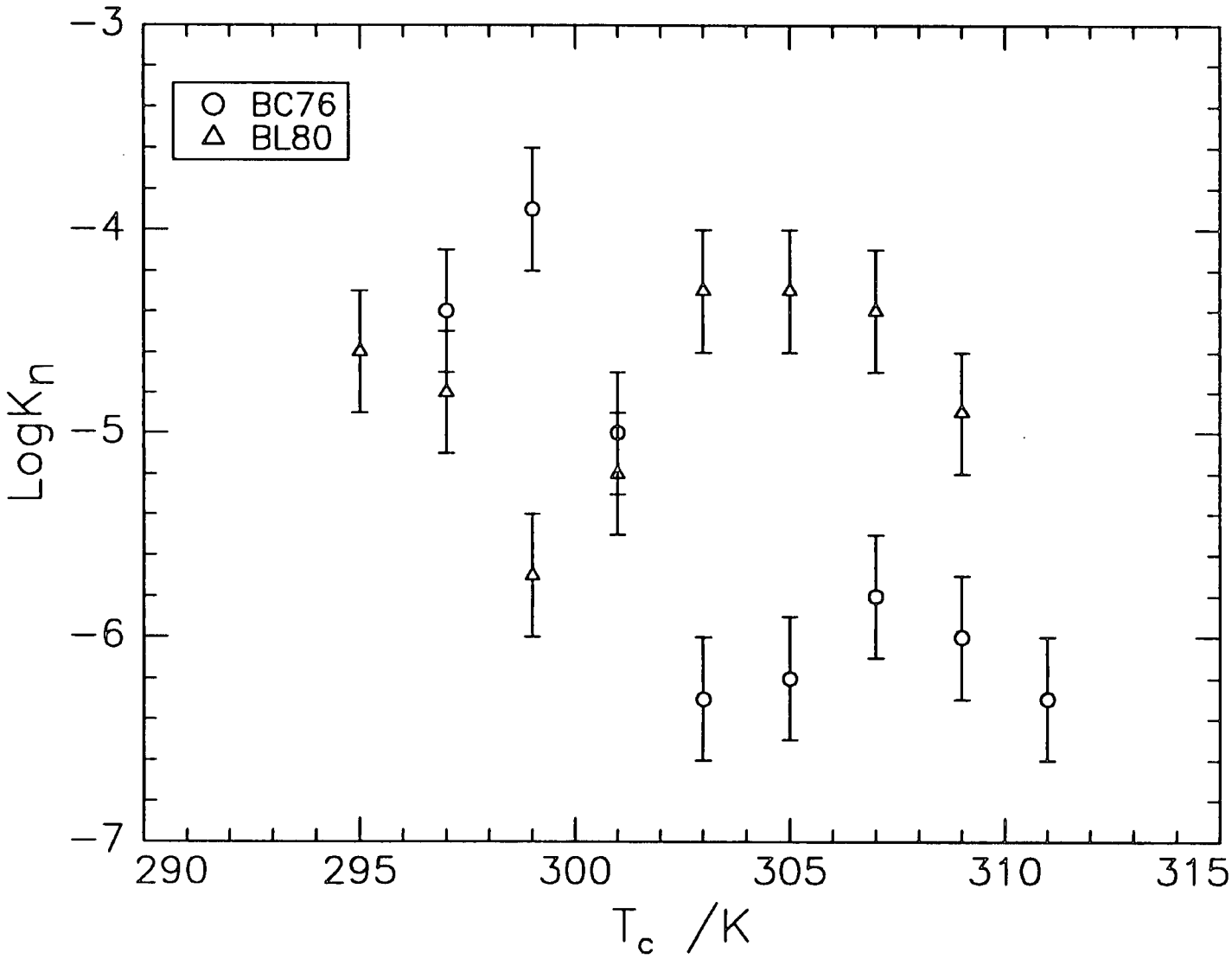

where V is the homopolymer molar volume, $V=86.5cm^3mol^{-1}$ for PMMA, $V=34.5cm^3mol^{-1}$ for crystalline PEO and $V=38.9cm^3mol^{-1}$ for amorphous PEO. The refractive index for a specific wavelength was evaluated through extrapolation of a Cauchy plot, n vs. λ^{-2}.

For all data sets which displayed four-leaf clover H_V SALS patterns, the evaluated disc radius increased linearly with time until the spherulites truncated, see figure 7.16. As in chapter 5 using optical microscopy, through modification of the Avrami analysis (see equation 5.4), the change in spherulitic radius as a function of time was analysed and provided information about the isothermal crystallisation mechanism, see figure 7.17. Table 7.8 lists the evaluated Avrami parameters along with the evaluated spherulitic growth rates for BC76 and BL80.

Polymer and T_c (K)	n	Log K_n	G ($\mu m min^{-1}$)
BC76, 309	2.9	-6.6	58.5
BC76, 307	3.0	-7.1	82.3
BC76, 305	2.8	-7.3	97.4
BL80, 297	2.7	-4.1	383
BL80, 295	2.9	-3.5	414

Table 7.8. Evaluated Avrami Parameters Describing the Isothermal Crystallisation of BC76 and BL80.

The evaluated $\log K_n$ and G values increase as T_c decreases as expected. They also compare favourable with values determined using optical microscopy.

The associated errors for n and log K_n were ± 0.3 and ± 0.4 respectively. All the evaluated Avrami exponents were approximately equal to n=3. From table 5.4, this represents an interfacially controlled growth mechanism with a spherical geometry. This is

Figure 7.16 Spherulitic Radius, R vs. Crystallisation Time for BC76.

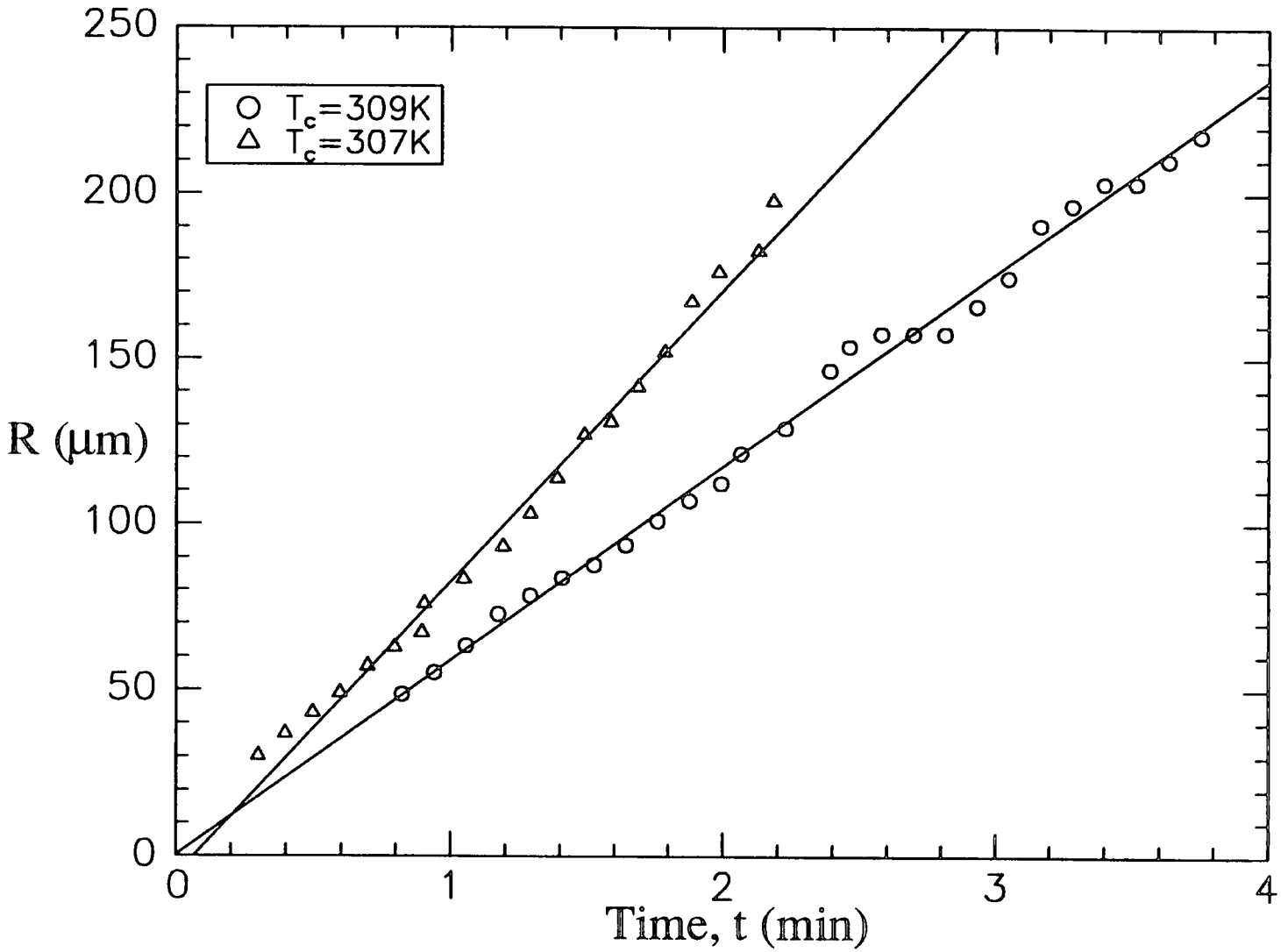

Figure 7.17 Avrami Analysis of the Isothermal Crystallisation of BC76 using R vs. t Data.

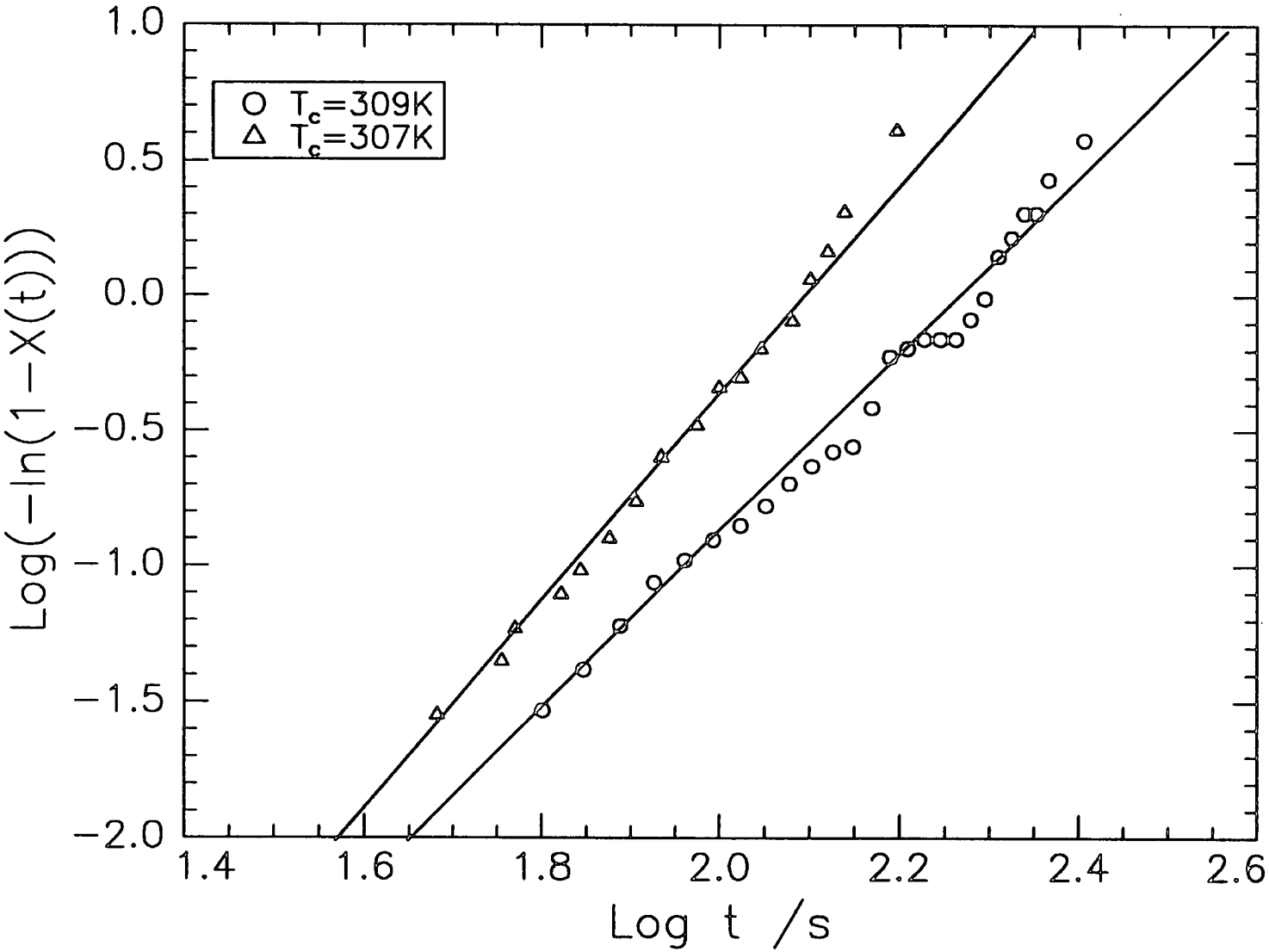

a surprising result since owing to the relative size of the spherulitic radii with respect to the film thickness, the growth geometry is disc-like.

Using optical microscopy, the Avrami exponent were found to be n=2.2±0.2 data for both BC76 and BL80. As from the SALS data above, this value of n represents a growth mechanism which is interfacially controlled but correctly predicts a disc-like growth geometry. Thus, the values of n form SALS are too large. There is no obvious rationalisation for this difference in n values and so caution should be adhered to when using this approach to calculate n.

7.7.2. Microphase Separation.

Owing to the size of the wavelength of the incident radiation, scattering entities must be of the order of a micron and above in size (see section 7.2). Thus, the observed variation in V_V intensity indicates that the scattering entities are $\geq$ 0.7μm. This is surprising since the expected size of the microdomains for block copolymers are normally of the order of 100Å[64]. A possible explanation for this behaviour is that the PEO microdomains are joined together through amorphous tie molecules forming an aggregate which is $\geq$ 0.7μm. This hypothesis is supported by the acquisition in V_V mode of a 'Fraunhofer type' ring of very low intensity when the block copolymers BC50 had crystallised at 323K prior to quenching to T'=233K, t=60 minutes. The position of the ring corresponds to scattering entities of approximately 3μm in diameter. Observation of sporadic highly disordered birefringent entities (approx. 3μm in diameter) using optical microscopy when viewed through crossed polars for BC50 at 323K after the same thermal treatment supports this SALS measurement. The morphology of this crystalline entity requires further investigation.

The V_V intensity variation with permanence time was analysed using the Avrami equation where;

$$1 - \mathbb{X}(t) = \frac{(\mathbb{I}_{Vv,\infty} - \mathbb{I}_{Vv,t})}{(\mathbb{I}_{Vv,\infty} - \mathbb{I}_{Vv,0})} \tag{7.41}$$

and $I_{Vv,\infty}$ is the final V_v intensity after microphase separation, $I_{Vv,t}$ is the V_v intensity after time t and $I_{Vv,0}$ is the V_v intensity at the t=0. The intensity values were corrected so that $I_{Vv,0}$=0 at t=0.

Figure 7.18 shows the subsequent Avrami analysis for BC50 at T'=239K. The evaluated Avrami parameters for both BC55 and BC50 are listed in tables 7.9 and 7.10.

T' (K)	Log K_a	n_{ms}
253	N/A	N/A
242	N/A	N/A
239	-1.79	0.65
235	-1.26	0.80
233	-0.85	1.03

Table 7.9. Evaluated Avrami Parameters for BC50 at various Permanence Temperatures, T'.

T'(K)	LogK_a	n_{ms}
258	N/A	N/A
253	-2.2	0.66
250	-1.6	0.71
243	-1.03	1.02

Table 7.10. Evaluated Avrami Parameters for BC55 at various Permanence Temperatures, T'.

Figure 7.18 Avrami Analysis of Vv SALS Intensity vs. Permanence Time, t at T'=239K for BC50.

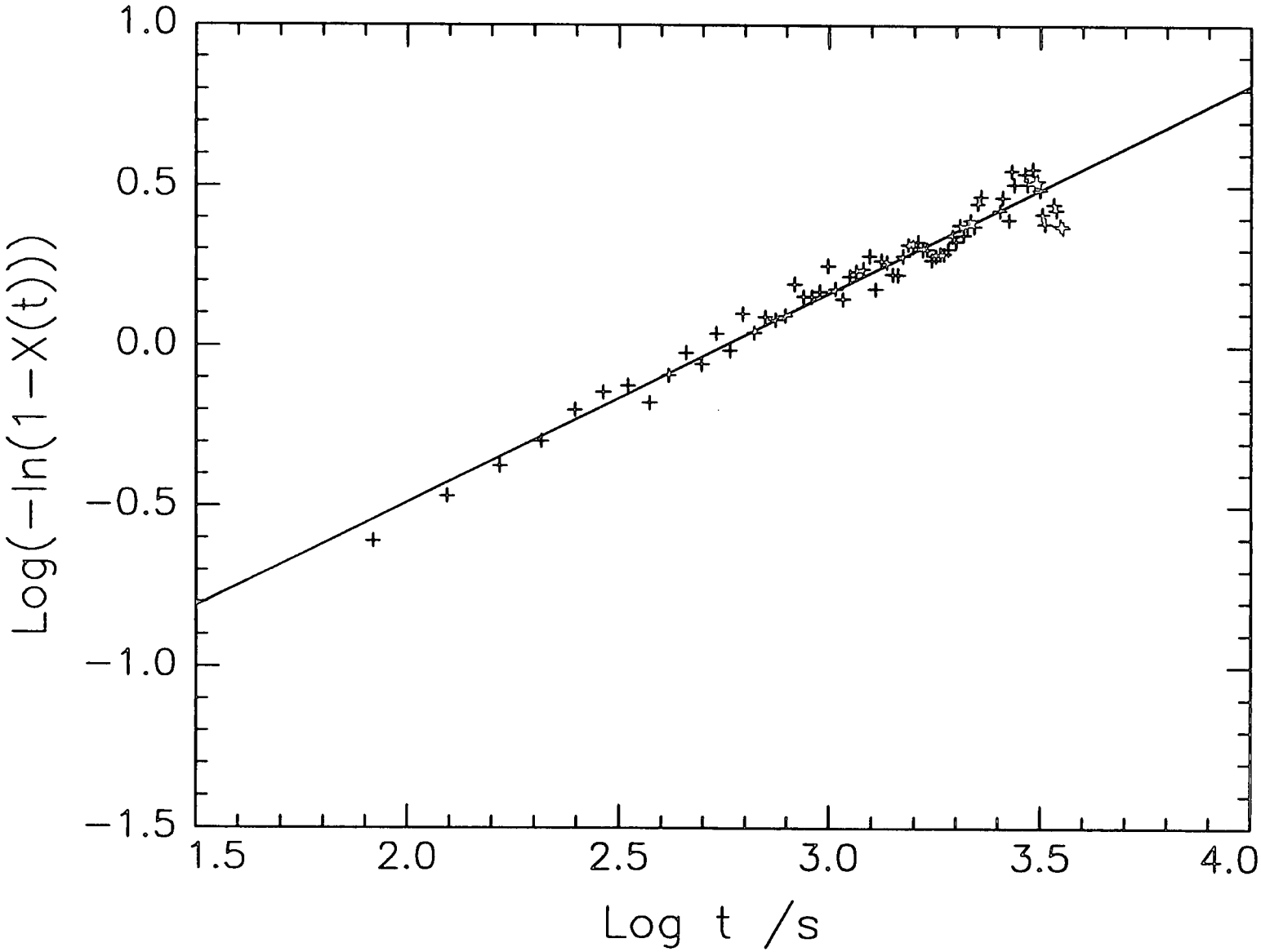

For BC50 and BC55, no V_V intensity variation with permanence time was detected for T'>242K and T'>258K respectively. For the other lower permanence temperatures investigated, the sigmoidal variation of I_{V_V} with time is clear evidence of structural reorganisation at these low temperatures. The shape of this intensity variation is characteristic of microphase separation according to a nucleation and growth type mechanism, see 1.1.3.2.2. The evaluated Avrami parameters listed in tables 7.9 and 7.10 indicate that the rate of microphase separation increases at lower T' and the Avrami exponent is ranges form 0.5 to 1. This represents a nucleation and growth microphase separation mechanism with an instantaneous nucleation process, diffusion controlled with a growth geometry which is either disc-like or rod-like. Similar Avrami exponents were determined using differential scanning calorimetry, see chapter 4.

7.8. Conclusions.

7.8.1. Isothermal Crystallisation.

The isothermal crystallisation kinetics of BC76 and BL80 were investigated by monitoring the overall depolarised intensity, I_{Hv}, and the spherulitic radius, R_o for various crystallisation temperatures. The evaluated rate constants were appreciably lower for the block copolymer with respect to the corresponding blend and decreased as the crystallisation temperature increased.

From the depolarised intensity data, the Avrami exponent for both polymeric systems tended to increase from n=2.5 to n=3 as the crystallisation temperature decreased. This represented a slight change in the crystallisation mechanism at lower temperatures, where the growth rate tended to be interfacially controlled. The growth geometry remained disc-like and the process was homogeneously nucleated. Whereas the Avrami analysis of the change in spherulitic radii with crystallisation time does not provide any information about the type of nucleation (modified analysis, see chapter 5), the evaluated Avrami exponent was approximately 3. Using table 5.4, as for the analysis above, this value of n represents an interfacially controlled growth mechanism, but indicates a spherical growth geometry. Owing to the size of the spherulitic radii being greater than the film thickness, this is clearly not the true physical picture.

7.8.2. Microphase Separation.

For the permanence temperatures, T'<239K for BC50 and T'<253K for BC55, a sigmoidal variation of V_v intensity with permanence time was detected. This is indicative of a microphase separation process governed by a nucleation and growth mechanism. Analysis of this behaviour gave an Avrami exponent ranging from 0.5 to 1 indicating instantaneous nucleation with a disc-like or rod-like growth geometry and a growth

mechanism which is diffusion controlled. Similar results, including the magnitude and variation of $\log K_n$ values with T', were obtained from DSC data, see chapter 4.

The fact that a variation in V_V scattering was detected suggests that the scattering entities are larger than 0.7μm. Since it is unfeasible for block copolymers to form microdomains in this size range, then a possible rationalisation is the formation of an aggregate. Such an explanation is supported by: the observation of sporadic, highly disordered, 3μm crystalline entities at 323K when viewed through crossed polars using optical microscopy and a Fraunhofer ring representing 3μm scattering entities using V_V SALS.

7.9. Additional SALS Results.

7.9.1. Introduction.

Small angle light scattering data was acquired for a variety of other polymeric systems. A brief description of the results obtained, along with experimental procedures, data acquisition and processing and methods of analysis are presented below. It is not the purpose of this section to analyse and quantify the results for each system in detail, but to highlight the wide range of possible applications that this technique offers.

7.9.2. Macroscopic Phase Separation in Poly(carbonate) / Poly(methyl methacrylate) (PC/PMMA) Blends.

7.9.2.1. Introduction.

Blends of PC/PMMA (50/50, 40/60, 30/70, w/w) undergo phase separation of the LCST type when heated to temperatures greater than 473K. This work was conducted in collaboration with Dr. S.Kotomin, University of Liverpool.

7.9.2.2. Experimental.

Thin films (approx. 10μm thick) of three different compositions of PC/PMMA blends (50/50, 40/60 and 30/70, w/w), were solution cast between two glass cover slips. Each sample was placed on the sample hotstage and the relative positions of the marata plate and sample hotstage were adjusted to optimise the polar scattering angular range to be studied. The samples were temperature jumped to 503K, and V_V scans were acquired at constant time intervals over a specified period of time using the 'Go Accum' data acquisition mode. Prior to data acquisition, to block out any contribution from the unscattered main beam, a small beam stop (circular piece of black card) was placed on the surface of the horizontally held marata plate.

7.9.2.3. Data Processing.

Each data set was transferred to a VAX terminal and analysed using PV-Wave. The first data scan was used as a background scan and subtracted from all subsequent data scans. Once the central main beam position had been determined, the background subtracted data was radially averaged using the macro RADAV.PRO (see appendix II). The results were saved in a file in an array format of V_V intensity versus track number. This file was later restored and the results presented as V_V intensity versus polar scattering angle, θ.

7.9.2.4. Results.

Phase separation of the polymer blend at 503K produced a well defined 'Fraunhofer' type ring, see figure 7.19, which increased in intensity and shifted towards lower polar scattering angles as the phase separation process proceeded. Figure 7.20 shows the scattered V_V intensity as a function of the scattering vector, q (m^{-1}), at 503K for the 30/70 PC/PMMA blend.

7.9.2.5. Method of Analysis.

As previously stated in the introduction (7.9.2.1.), it is not the purpose of this section to analyse the data in detail, but to indicate the possible range of structural and dynamic information that can be obtained using SALS. Consequently, a brief description of the potential parameters that can be obtained from the analysis of the light scattering data of macroscopic phase separation in binary polymeric systems.

The V_V light scattering data of the early stages of spinodal decomposition can be treated by the Cahn-Hilliard linearisation theory[65,66] for small molecules. This has been extended by de Gennes[67] for polymers. Cook[68] noticed that the linearised theories did not take into account thermal fluctuations and so provided a modified form of the Cahn-Hilliard equation;

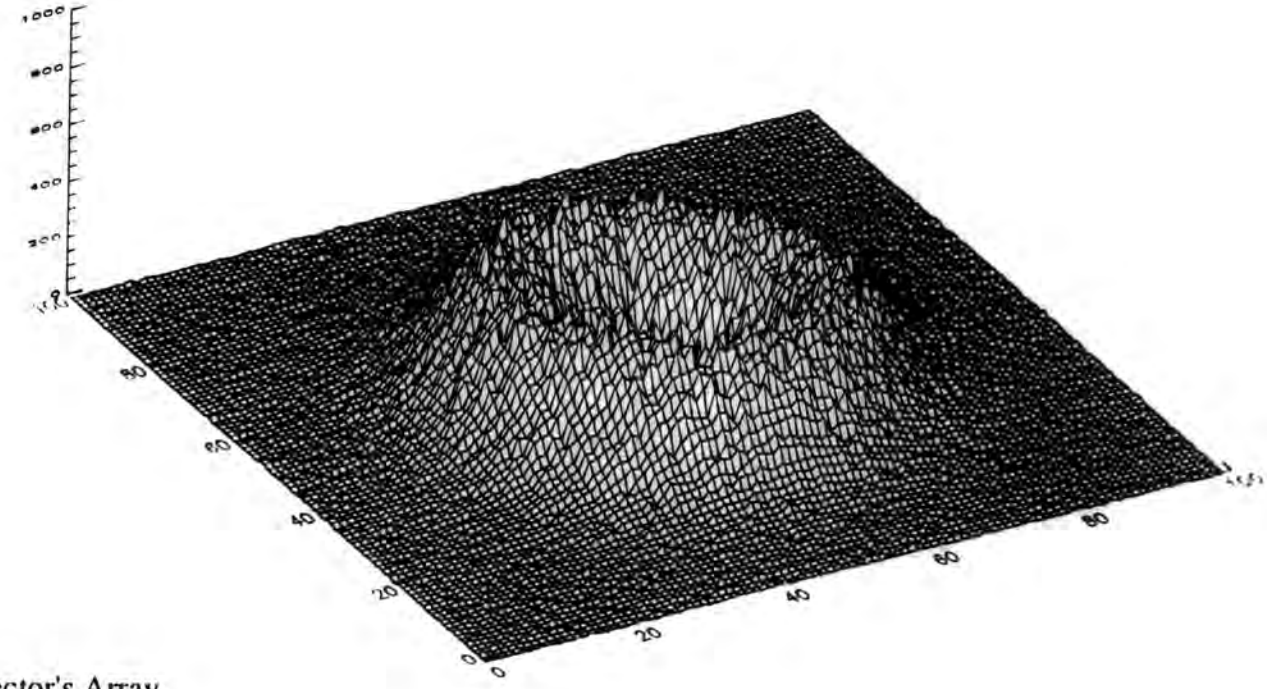

Figure 7.19. 'Fraunhofer Type' Ring From V_v SALS of a Phase Separated 30/70 PC/PMMA Blend at 503K.

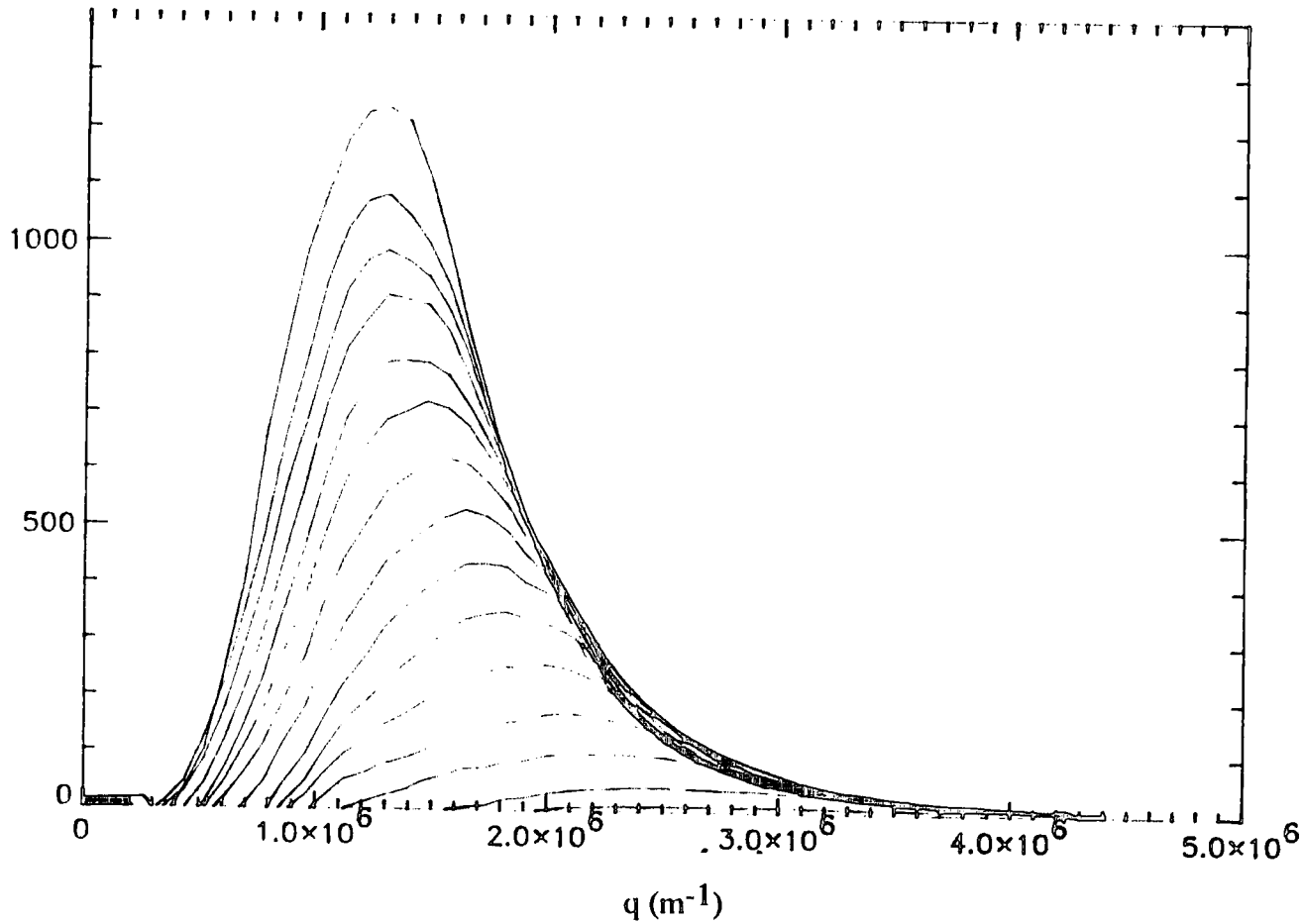

Figure 7.20 Radially Averaged V_v Intensity as a Function of q for the Phase Separation of a 30/70 (w/w) PC/PMMA Blend at 503K.

$$S(q,t) = S_s(q) + [S(q,t=0) - S_s(q)]\exp[2R(q)t] \quad (7.42)$$

where $S_s(q) \sim I_{Vv}(q)$[69,70],

i.e.
$$I_{V_v} \propto \exp[2R(q)t] \quad (7.43)$$

where

$$R(q) = -Mq^2\left\{\left(\frac{\partial^2 G}{\partial \phi^2}\right) + 2\kappa q^2\right\} \quad (7.44)$$

and q is the scattering vector (see equation 7.16). R(q) is the amplification factor which represents the growth rate of concentration fluctuations, M is the mobility constant of the molecules, κ the concentration gradient coefficient and G is the free energy of the mixture. If R(q) is determined from the slope of a plot of lnI(q,t) versus t, then the apparent diffusion coefficient D_{app}, can be evaluated from a plot of $R(q)/q^2$ vs. q^2. This parameter provides the opportunity to determine the spinodal temperature. In the nucleation and growth regime, $\delta^2G/\delta\phi^2$ is positive and so according to equation 7.44, R(q) must be negative. In the spinodal temperature regime, however, $\delta^2G/\delta\phi^2$ is negative and hence R(q) is positive for values of q smaller than the critical q. Therefore, a plot of D_{app} versus temperature (temperature jumped to different temperatures) gives the spinodal temperature through extrapolation of D_{app} to zero. This temperature dependence has been described in more detail by Hashimoto et al[71].

At late stages of spinodal decomposition, the scattered intensity deviates away from the exponential behaviour and the scattering maximum shifts towards smaller q. This corresponds to the onset of a coarsening process called Ostwald ripening. Information

regarding the later stages of spinodal decomposition can be obtained by analysing the shift in peak position towards lower scattering angles. The intensity peak position gives an approximate size of the phase separated domains from the following expression;

$$d_m \cong \lambda / 2n \sin\left(\frac{\theta}{2}\right) \tag{7.45}$$

The maximum scattering vector magnitude, q_m, is often fitted to a power law expression proposed by Langer et al[72] and Binder et al[73];

$$q_m \approx t^{-\beta} \tag{7.46}$$

where the value of β is used to compare the phase separation kinetics with various models describing phase separation e.g. the Lifshits and Slyzov evaporation-condensation model[74] where the droplet size grows with β=1/3. The scaling concept proposed by Furukawa[75] allows numerous data sets at different temperatures to be superimposed onto a master curve. The resultant structure function indicates the self-similarity (similar geometrical domain shapes and size distribution) of phase separation for different temperatures (and different compositions) and provides a general description of this process in the late-stage regime.

Numerous studies have been published regarding the investigation of macroscopic phase separation in binary polymeric systems using light scattering. These publications include work on polystyrene/poly(vinyl methyl ether) (PS/PVME)[76-80], polyisoprene/poly(ethylene-propylene) (PI/PE-b-PP)[81], polycarbonate/isotactic poly(methyl methacrylate) (PC/i-PMMA)[82] and the effect of adding a styrene-butadiene diblock copolymer to the blend[83].

7.9.3. Phase Separation Prior to Polymerisation in Segmented Polyurethane Block Copolymers.

7.9.3.1. Introduction.

This section reports results aimed at the investigation of macroscopic phase separation prior to polymerisation in segmented polyurethane block copolymers. Earlier studies have investigated the microdomain morphology using small angle x-ray scattering[84] and the macroscopic phase structure using SALS[85].

7.9.3.2. Experimental.

The diisocyanate and diol monomers were mixed together, immediately placed between two glass cover slips and positioned on the sample hotstage between two vertically polarised polarisers. V_V SALS scans were than acquired as a function of time during polymerisation. After polymerisation, a single V_V SALS background scan was acquired using the same experimental set-up but with no sample present.

7.9.3.3. Data processing.

Each background subtracted, isotropic data scan was then radially averaged about the main beam position using PV-Wave.

7.9.3.4. Results.

No distinct 'Fraunhofer' type halo's were observed, contrary to the phase separation in section 7.9.2. The V_V intensity increased exponentially as θ decreased.

7.9.3.5. Analysis and discussion.

The V_V SALS data was analysed on the basis of the Debye-Bueche two phase model[30] i.e., $I(q)^{-1/2}$ vs. q^2 was plotted, where I(q) is the V_V intensity (arbitrary units)

Figure 7.21. Density Correlation Length, a, vs. Time after the Beginning of Polymerisation of the Segmented Polyurethane Block Copolymer.

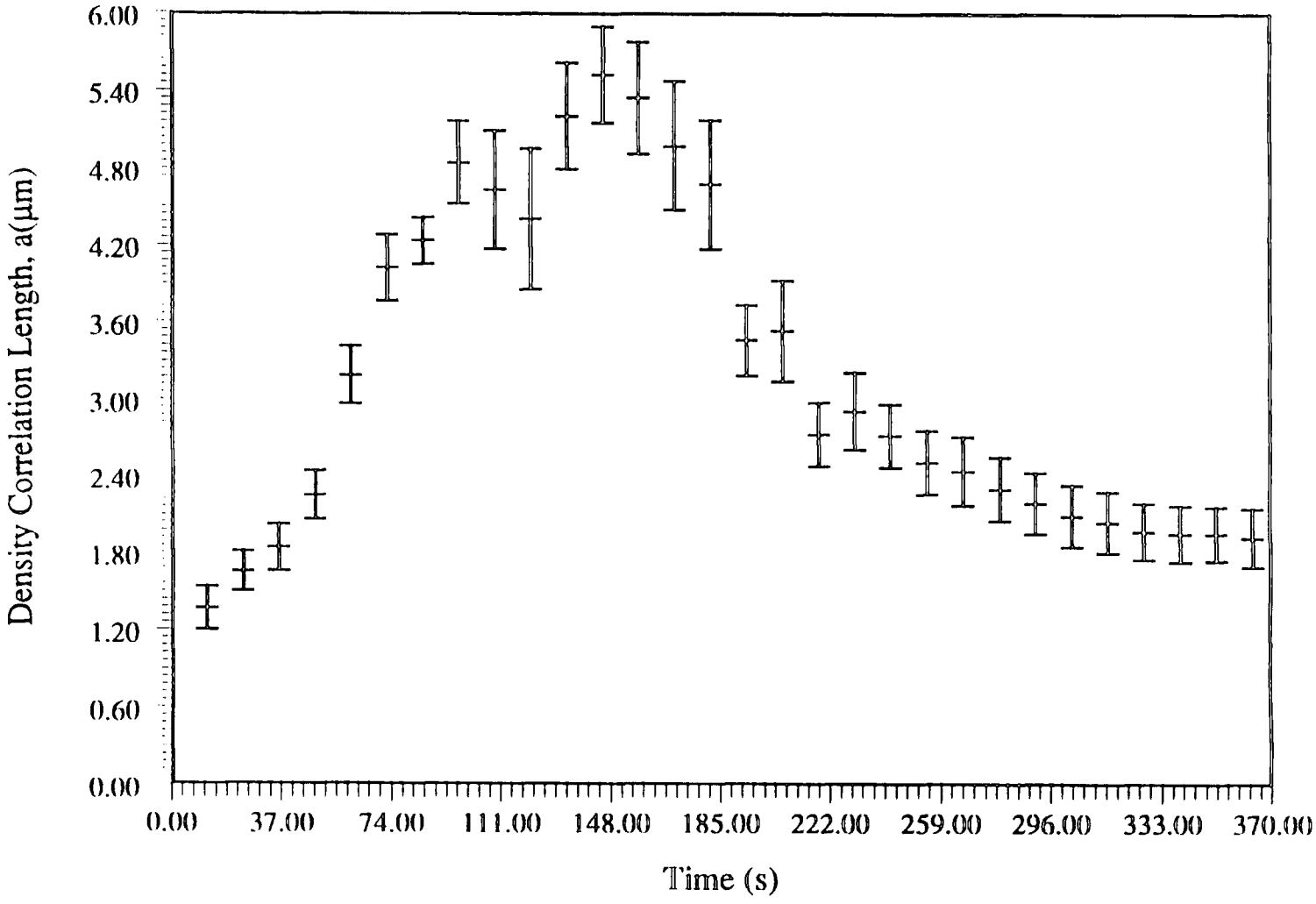

Figure 7.22. Mean Square Fluctuation in Polarisability, $\langle \eta^2 \rangle$ vs. Time after the Beginning of Polymerisation of the Segmented Polyurethane Block Copolymer.

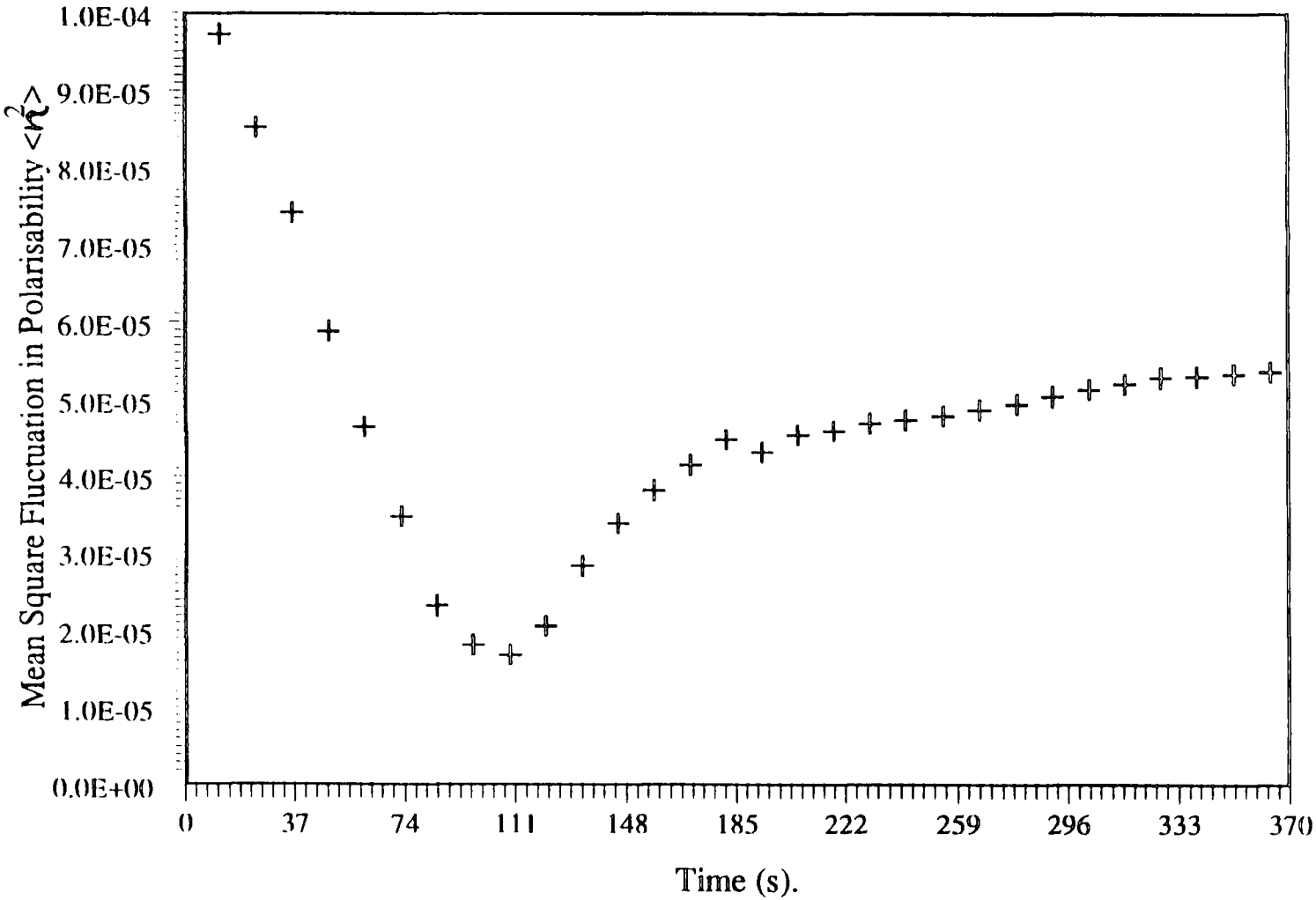

and q is the magnitude of the scattering vector (see equation 7.16). From this analysis, a correlation length, a, and the mean square fluctuation in polarisability, $\langle\eta^2\rangle$, were calculated using the following expressions;

$$a = \left(\frac{\text{gradient}}{\text{intercept}}\right)^{\frac{1}{2}} \tag{7.46}$$

$$\langle \eta^2 \rangle = \frac{(\text{intercept})^{-2}}{(8\pi(\omega c)^4 a^3)} \tag{7.47}$$

where ω is the angular frequency of the incident radiation and c is the speed of light. Figures 7.21 and 7.22 displays the correlation length, a, and $\langle\eta^2\rangle$, respectively, as a function of time after initial mixing of the two monomers. The maximum correlation length of approximately 5μm after 140 seconds supports the proposed onion morphology by Castro[93] based on SAXS measurements.

To conclude, these results have indicated an additional method of quantifying phase separation when the V_V SALS pattern does not display a 'Fraunhofer' type scattering halo.

7.9.4. Spherulitic Deformation Studies.

7.9.4.1. Introduction.

Several authors have investigated the effect of deformation in relation to spherulitic crystalline textures for a variety of semi-crystalline polymers using H_V and V_V SALS[86-89]. These results have been theoretically interpreted using various model approaches. Information regarding the spherulitic size and shape, the change in orientation of the optic axes of the scattering volume elements, the change in deviation of the optic axis orientation angle from it's average value and the change in the distance over which this deviation is correlated has been obtained as a function of extension ratio.

Here, results from H_V and V_V SALS patterns illustrating the effect of deformation and subsequent relaxation for a semi-crystalline polyurethane are reported.

7.9.4.2. Experimental.

An approximate 3mm thick strip of a semi-crystalline polyurethane, clamped in a deformation rig, was attached to the SALS main profile, situated between the two polarisers. H_V and V_V SALS scans of the undeformed polyurethane were acquired prior to subsequent H_V and V_V scans of the same sample under a series of extensions. At 389% extension, the polymer sample was allowed to relax, and H_V and V_V SALS scans were recorded for relaxation extensions commensurate with earlier stretched extension percentages.

7.9.4.3. Results and Discussion.

Figure 7.23 shows the H_V SALS deformations patterns for the semi-crystalline polyurethane. As the percentage of extension increased, the 'four-leaf-clover' H_V pattern for the undeformed polyurethane elongated orthogonally to the stretching direction along with an overall decrease in depolarised intensity and dihedral angle, μ, see diagram 7.1.

Figure 7.23. H_v SALS Spherulitic Deformation of a Semi-crystalline Polyurethane.

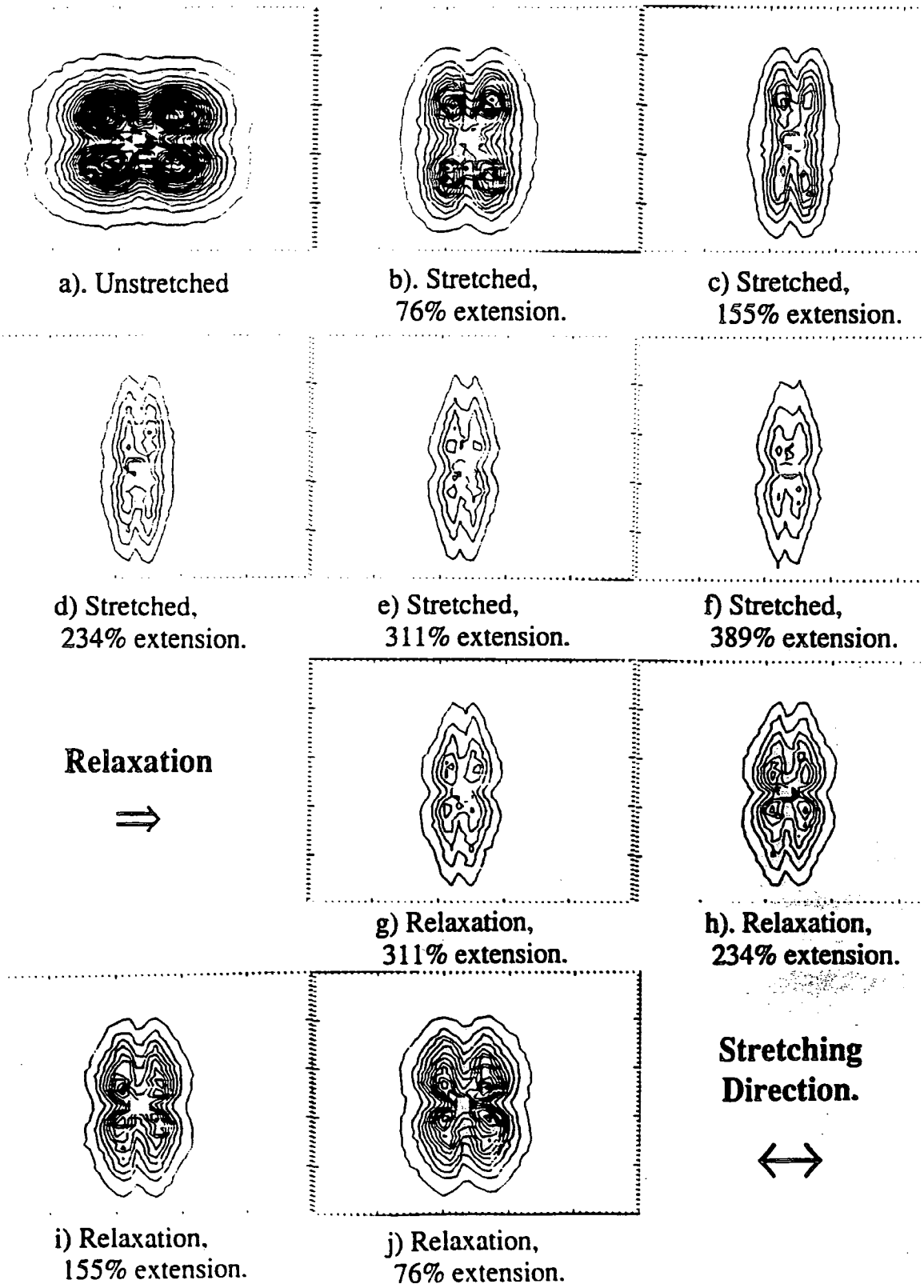

This elongation and change in dihedral angle indicated a change in the undeformed spherulitic morphology to one that is more rod-like. The decrease in polarised intensity can be attributed to an increase in disorder within the spherulite.

Upon relaxation, the SALS patterns increased in intensity and returned to their original shape. However, the position of the intensity maximum and thus the dihedral angle relaxed in a manner unrelated to the change in μ during stretching. Figures 7.23 b), and 7.23 j), clearly illustrate the difference in position of intensity maxima for the stretched and relaxed polyurethane sample at the same extensions. The change in the intensity and shape of the scattering pattern, and the variation of dihedral angle suggest that two distinct deformation processes are present. An overall macroscopic spherulitic deformation and an internal, optical axis deformation. Figures 7.24 and 7.25 show the variation of dihedral angle, μ, and the average spherulitic radius respectively as a function of elongation ratio.

The V_V SALS patterns also showed variations in intensity and angle (θ, μ), however, these patterns are far more complex than the H_V SALS case. Thus, difficulties are inherently present in any form of quantitative evaluation. To conclude, H_V and V_V SALS can provide quantitative information regarding the deformation of semi-crystalline morphologies and their internal structure.

Figure 7.24. Variation of Dihedral Angle, μ, at I_{max} vs. Elongation Ratio.

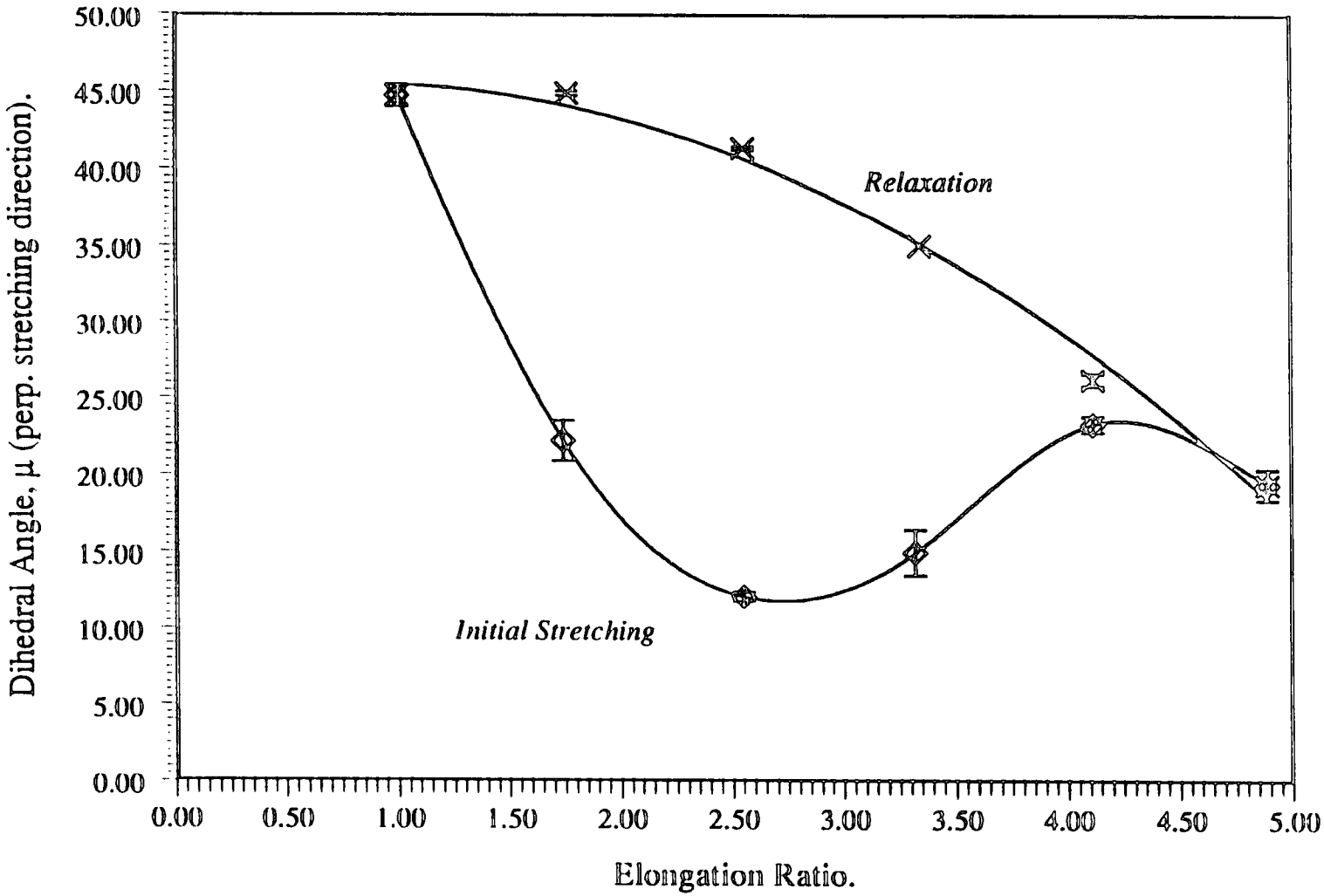

Figure 7.25 Variation of Averaged Spherulitic Radius, $R_{<4>}$, vs. Elongation Ratio.

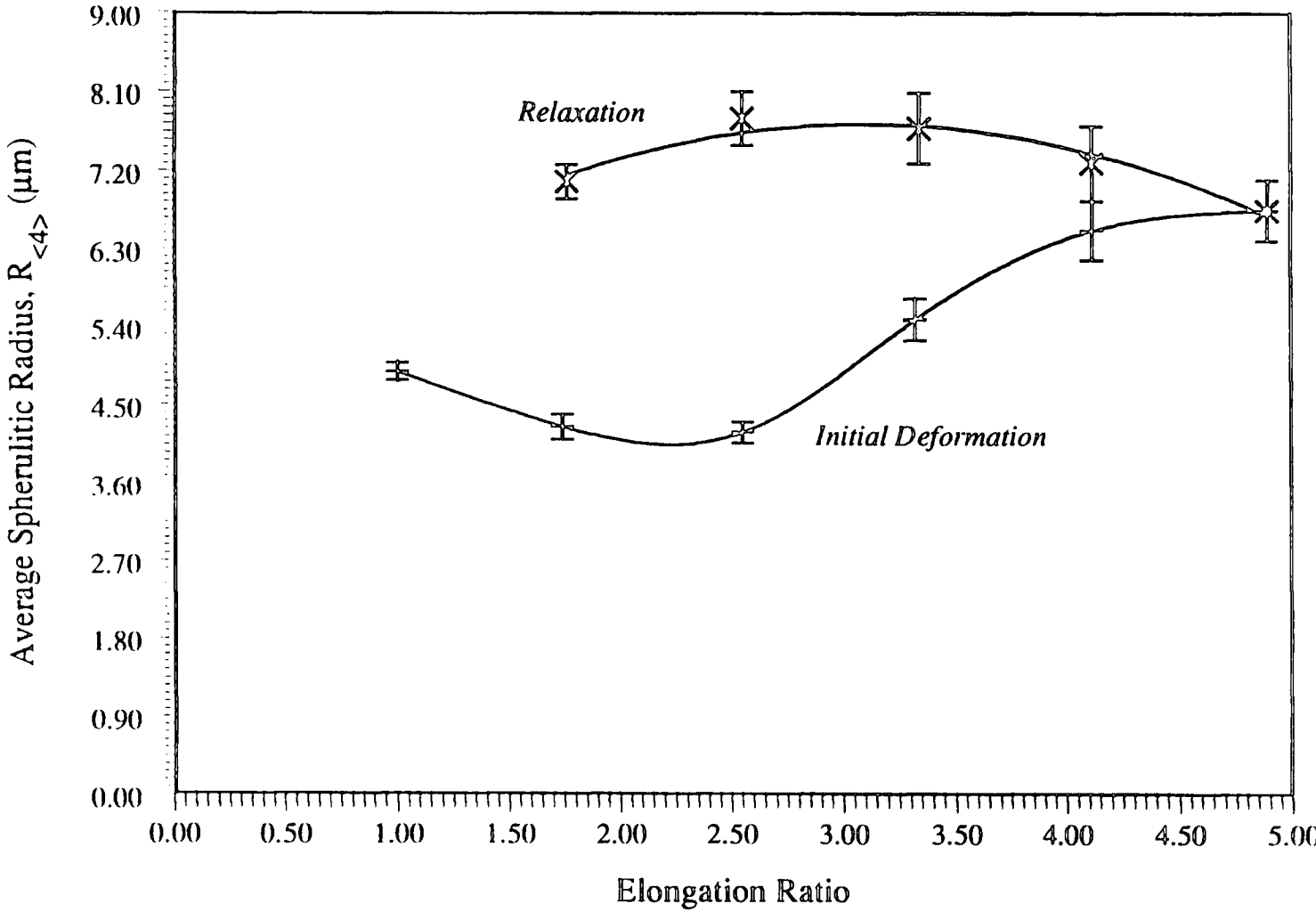

7.9.5. SALS from a Liquid-Crystalline Polymer.

7.9.5.1. Introduction.

The H_V SALS intensities as a function of temperature from a thermally treated liquid-crystal polymer are reported below. The liquid-crystal polymer has a non-centrosymmetric arrangement of electrical dipoles which ought to possess low scattering characteristics. Coupled with the capability of forming thin films with long term stability, this type of polymer may be utilised in the fabrication of non-linear optical devices[90]. The following results have been reported elsewhere in more detail[91].

7.9.5.2. Experimental.

Thin films (10μm thick) were solution cast between two glass cover slips and placed on the sample hotstage. The total H_V SALS intensity was recorded as a function of temperature for samples which were subjected to two thermal treatments;

i) heated to 493K at 40Kmin^{-1}, and then immediately cooled to room temperature at the same rate, and

ii) heated to 493K at 40Kmin^{-1}, cooled to 423K and annealed at this temperature for 45 minutes, and than cooled to room temperature at 40Kmin^{-1}.

7.9.5.3. Data Processing.

The total depolarised intensity for each scan was evaluated using the software package PV-Wave. The macro INT.PRO (see appendix II), subtracts a dark-noise background value from the calculated overall intensity for a series of scans. The results are stored in an array, which can be presented as a plot of total depolarised intensity as a function of temperature.

7.9.5.4. Results and Discussion.

Figures 7.26 and 7.27 show the overall depolarised light intensity variation as a function of temperature for samples subjected to treatment i) and ii) respectively. An increase in intensity is observed as the well ordered liquid-crystal passes through it's mesophases towards the isotropic state during heating for the sample subjected to treatment i). Usually, as the amount of disorder increases, a concomitant decrease in the total depolarised intensity is expected for liquid crystalline polymers[92].

This unusual variation in intensity indicated that the ordered liquid-crystals at low temperatures were monotropic at low temperatures i.e. all the optical axes in the polymer are aligned parallel to the incident vertically polarised light. For this arrangement of mesogens, under crossed polars, the depolarised scattering intensity would be approximately zero. As the monotropic system becomes more disordered, the optical axes deviate from their parallel alignment with the plane of polarisation of the incident light, resulting in an increase in depolarised scattering intensity.

The low depolarised light intensity observed from room temperature up to 533K for a sample prepared according to treatment ii), is indicative of a highly monotropic system. This suggest the annealing process at 423K for 45 minutes and the subsequent cooling to room temperature at $40Kmin^{-1}$ has effectively 'frozen in' this well ordered structure.

To conclude, whereas the total depolarised intensity can not detect individual transitions between adjacent mesophases, it clearly can provide useful structural information within liquid-crystalline systems. Further analysis in terms of correlation lengths can be used to describe the degree of order in different liquid-crystalline mesophases[92].

Figure 7.26 Treatment i), Heated From 373K to Onset of Degradation.

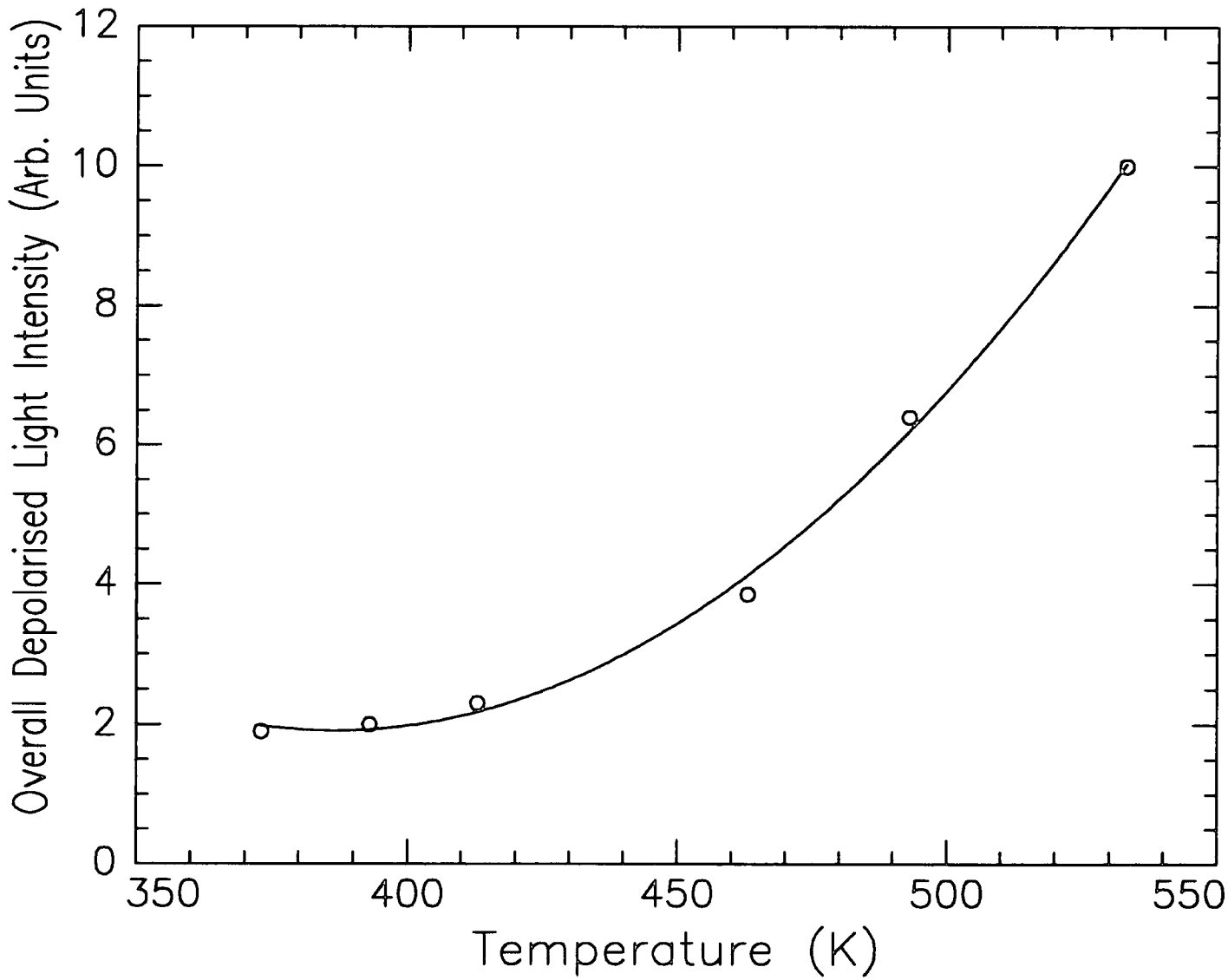

Figure 7.27 Treatment ii), Heated to 533K and Cooled to Room Temperature at 10K/min.

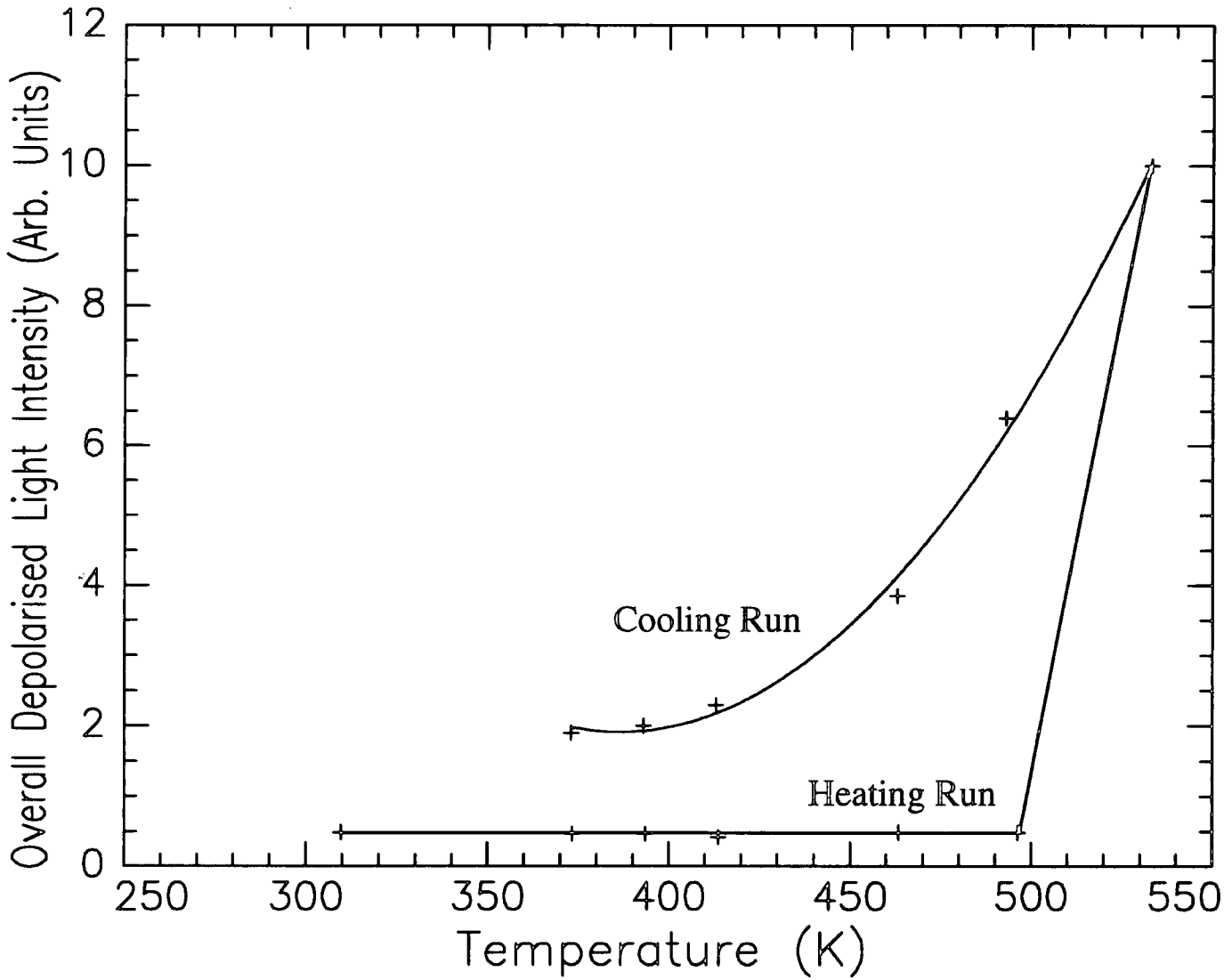

7.10. SALS Conclusions.

For systems that possess sufficiently large refractive index differences, small angle light scattering can be used to provide structural information on the micron level and above. Two different modes of operation, V_V and H_V scattering, enable the scattering contributions: concentration and orientation fluctuations, to be distinguished. This allows the investigation of systems which alter the plane of polarisation of polarsied light, i.e. crystalline systems, as well as systems that possess concentration fluctuations, i.e. phase separated systems.

The technological advancement of fast digitised detectors have improved the applicability of SALS. The technique can be used to monitor fast processes such as crystallisation at high undercoolings and spinodal decomposition.

7.11. References.

1. Berne, B.J. and Pecora, R., 'Dynamic Light Scattering', Wiley, New York, 1976.
2. Mie, G., Ann.Physik, 25, 377, 1908.
3. Van De Hulst, H.C., 'Light Scattering by Small Particles', John Wiley and Sons, New York, 1957.
4. Stein, R.S. and Rhodes, M.B., J.Polym.Sci., Part A-2, 7, 1539, 1969.
5. Haudin, J.M., Chapt. 4 in 'Optical Properties of Polymers', G.H.Meeten, Ed., Elsevier, London, 1986.
6. Meeten, G.H., Optica Acta, 29, 759, 1982.
7. Guinier, A., Fournet, G., Walker, C. and Yudowich, K., 'Small Angle Scattering of X-rays', Wiley, New York, 1955.
8. Stein, R.S. and Rhodes, M.B., J. Appl. Phys., 31, 1873, 1960.
9. Samuels, R.J., J. Polym. Sci., Part A-2, 9, 2165, 1971.
10. Clough, S.B., Stein, R.S. and Picot, C., J. Polym. Sci., Part A-2, 9, 1147, 1971.
11. Van Aartsen, J.J., Office of Naval Research Technical Report No. 83, Project NR 056-378, Contract No 33 57 (01), March 1966.
12. Peuvrel, E., Siegert, D., Navard, P. and Meeten, G.H., J.of Polym.Sci., Part B, Polym.Phys., Vol.30, 865-869, 1992.
13. Meeten, G.H. and Navard, P., J.of Polym.Sci., Part B., Polym.Phys., Vol.27, 2023, 1989.
14. Desbordes, M., Meeten, G.H. and Navard, P., J.of Polym.Sci., Part B., Polym.Phys., Vol.27, 2037, 1989.
15. Stein, R.S. and Wilson, P.R., Office of Naval Research Technical Report No. 35, Project NR 356-378, Contract No 33 57 (00), August 1961.
16. Clough, S., Van Aartsen, J.J. and Stein, R.S., J. Appl. Phys., 36, 3072, 1965.

17. Stein, R.S., Erhardt, P., Van Aartsen, J.J., Clough, S. and Rhodes, M., J. Polym. Sci., Part C, 13, 1, 1966.

18. Samuels, R.J., J Polym. Sci., Part A-2, 7, 1197, 1969.

19. Van Aartsen, J.J., Eur.Polym.J., 6, 1095, 1970.

20. Hayashi, N. and Kawai, H., Polym. J. (Japan), 3, 140, 1972.

21. Matsuo, M., Nomura, S., Hashimoto, T. and Kawai, H., Polym. J. (Japan), 6, 151, 1974.

22. Hashimoto, T., Murakami, Y., Hayashi, N. and Kawai, H., Polym. J. (Japan), 6, 132, 1974.

23. Hashimoto, T., Ebisu, S. and Kawai, H., J. Polym. Sci., Polym. Phys. Ed., 19, 59, 1981.

24. Rego Lopez, J.M. and Gedde, U.W., Polymer, 30, 22, 1989.

25. Bartczak, Z. and Galeski, A., Polymer, 31, 2027, 1990.

26. Tabar, R.J., Leite-James, P. and Stein, R.S., J.of Polym.Sci., Polym.Phys.Ed., 23, 2085-2107, 1985.

27. Yoon.D.Y., and Stein,R.S. ,J.Polym.Sci., Polym.Phys.Ed., 12, 763, 1974.

28. Motegi, M., Oda, T., Moritani, M. and Kawai, H., Polym. J. (Japan), 1, 209, 1970.

29. Stein, R.S., Wilson, P.R. and Stidham, S.N., J. Appl. Phys., 34, 46, 1963.

30. Debye, P. and Beuche, A.M., J. Appl. Phys., 20, 518, 1949.

31. Keijzers, A.E.M., Van Aartsen, J.J. and Prins, W., J. Am. Chem. Soc., 90, 3107, 1968.

32. Stein, R.S. and Chu, W., J. Polym. Sci., Part A-2, 8, 1137, 1970.

33. Hashimoto, T. and Stein, R.S., J. Polym. Sci., Part A-2, 9, 1747, 1971.

34. Stein, R.S., Stidham, S.N. and Wilson, P.R., Office of Naval Research Technical Report No.36, Project NR 356-378, Contract No 33 57 (01), 1961.

35. Stein, R.S. and Picot, C., J. Polym. Sci., Part A-2, 8, 1955, 1970.

36. Prud'homme, R.E. and Stein, R.S., J. Polym. Sci., Polym. Phys. Ed., 11, 1357, 1973.

37. Hashimoto, T., Todo, A. and Kawai, H., Polym. J. (Japan), 10, 521, 1978.

38. Hashimoto, T., Todo, A., Murakami, Y. and Kawai, H., J. Polym. Sci., Polym. Phys. Ed., 15, 501, 1977.

39. Yoon, D.Y. and Stein, R.S., J. Polym. Sci., Polym. Phys. Ed., 12, 735, 1974

40. Stein, R.S. and Picot, C., J. Polym. Sci., Part A-2, 8, 2127, 1970.

41. Prud'homme, R.E. and Stein, R.S., J. Polym. Sci., Polym. Phys. Ed., 11, 1683, 1973.

42. Stein, R.S. and Wilkes, G.L., in 'Structure and Properties of Oriented Polymers', Ward, I.M. (Ed.), Applied Science Publishers, London, 85-133, 1975.

43. Tabar, R.J., Stein, R.S. and Rose, D.E., J.Polym.Sci., Polym.Phys.Ed., 23, 10, 2059-2084, 1985.

44. Picot, C., Stein, R.S., Motegi, M. and Kawai, H., J. Polym. Sci., Part A-2, 8, 2115, 1970.

45. Tatematsu, S., Hayashi, N., Nomura, S. and Kawai, H., Polym. J. (Japan), 3, 488, 1972.

46. Ishikawa ,T. and Stein, R.S., Polym.J., 8, 369, 1976.

47. Tabar,R.J., Wasiak,A., Hong,S.D., Yuasa,T. and Stein, R.S., J.Polym.,Sci., Polym., Phys., Ed., 19, 49, 1981.

48. Tabar ,R.J., Stein,R.S., and Rose, D.E., J.Polym., Sci., Polym., Phys., Edn., 23, 2059, 1985.

49. Rhodes, M.B., Keedy, D.A. and Stein, R.S., J. Polym. Sci., 62, S73, 1962.

50. Goldstein, M. and Michalik, E.R., J. Appl. Phys., 26, 1450, 1955.

51. Stein, R.S. and Wilson, P.R., J. Appl. Phys., 33, 1914, 1962.

52. Stein, R.S., Erhardt, P.F., Clough, S.B. and Adams, G., J. Appl. Phys., 37, 3980, 1966.

53. Van Aartsen, J.J., in 'Polymer Networks, Structural and Mechanical Properties', Chompff, A.J. and Newman, S. (Eds.), Plenum Press, New York, p.307, 1971.

54. Hoffman, J.D., Frolen, L.J., Ross, G.S. and Lauritzen, J.I., J. Res. Nat. Bur. Std., 79A, 671, 1975.

55. Pethrick, R.A., Richards, R.W., 'Static and Dynamic Properties of the Polymeric Solid State', p.109-125, D.Reidel Publishing Company, 1982.

56. Tabar, R.J. and Stein, R.S., J.Polym. Sci., Polym. Phys. Ed., Vol. 20, 2041-2049, 1982.

57. Born, M. and Wolf, E., p.383, 386 in 'Principles of Optics - Electromagnetic Theory of Propagation Interference and Diffraction of Light', Sixth Edition, Pergamon Press, 1987.

58. Edel, V., Abetz, V. and Fischer, E.W., poster presented at the 4th European Polymer Federation Symposium on Polymeric Materials, 1992.

59. Stein, R.S., Keane, J.J., J.Polym. Sci., 17, 21, 1955.

60. Prud'homme, R.E., Bourland, L., Natarajan, R.T. and Stein, R.S., J. Polym. Sci., Polym. Phys. Ed., 12, 1955, 1974.

61. Samuels, R.J., J. Polym. Sci., Part A-2, 9, p.2183, 1971.

62. Richardson, P.H., 'Small Angle Light Scattering Manual', January 1993.

63. Van Krevelen, D.W., p.292-296, 'Properties of Polymers'. 3rd Edition, Elsevier, 1990.

64. Noshay, A., McGrath, J.E., 'Block Copolymers Overview and Critical Survey', Academic Press, New York, 1977.

65. Cahn, J.W., J.Chem.Phys., 42, 93, 1965.

66. Cahn, J.W., Trans.Met.Soc.AIME, 242, 166, 1968.

67. De Gennes, P-G.,J.Chem.Phys., 72, 4756, 1980.

68. Cook, H.E., Acta.Metall., 18, 297, 1970.

69. Binder, K.J., Chem.Phys., 79, 6387, 1983.

70. Okada, M. and Han., C.C., J.Chem.Phys., 85, 5317, 1986.

71. Hashimoto, T., Kumaki, J. and Kawai, H., Macromolecules, 16, 641, 1983.

72. Langer, J.S., Bar-on, M., Miller, H.S., Phys.Rev., A, 11, 1417, 1975.

73. Binder, K. and Stauffer, D., Phys.Rev.Lett., 33, 1006, 1974.

74. Lifshits, I.M. and Slyozov, V.V., J.Chem.Phys.Solids, 19, 258, 1961.

75. Furukawa, H., Phys.Rev.Lett., 43, 136, 1979.

76. Snyder, H.L. and Meakin, P., J.Chem.Phys., 79, 11, 1983.

77. Hashimoto, T., Kumaki, J. and Kawai, H., Macromolecules, 16, 641, 1983.

78. Santore, M.M., Han, C.C. and McKenna, G.B., Macromolecules, 25, 3416, 1992.

79. Hashimoto, T., Itakura, M. and Shinidzu, N., J.Chem.Phys, 85, 11, 6773, 1986.

80. Yang, H., Shibayama, M., Stein, R.S., Shimizu, N. and Hashimoto, T., Macromolecules, 19, 1667, 1986.

81. Cumming, A., Wiltzius, P., Bates, F.S. and Rosedale, J.H., Phys.Rev.A, 45, 2, 1992.

82. Kyu, T. and Lim, D-S., Macromolecules, 24, 3645, 1991.

83. Roe, R-J. and Kuo, C-M., Macromolecules, 23, 4635, 1990.

84. Koberstein, J.T. and Stein, R.S., J. Polym. Sci., Polym. Phys. Edn., 21, 1439, 1983.

85. Koberstein, J.T. and Stein, R.S., Polymer, Vol. 25, 171-177, 1984.

86. Samuels, R.J., J. of Polym. Sci.; Part A-2, Vol. 6, 1101-1139, 1968.

87. Stein, R.S., Hashimoto, T., J. of Polym. Sci., Part A-2, Vol. 9, 517-529, 1971.

88. Van Aartsen, J.J. and Stein, R.S., J. of Polym. Sci., Part A-2, Vol. 9, 295-311, 1971.

89. Kimura, I., Ishihara, H., Ono, H., Yoshihara, N., Nomara, S., Kawai, H., 88. Macromolecules, Vol. 7, No.3, 355-363, 1974.

90. Warner, M, Materials Research Soc., Proc. Conf. Boston, 134, 61, 1989.

91. Tsibouklis, J., Richardson, P.H., Richards, R.W., Feast, W.J., Polymer Bulletin, 30, 595-601, 1993.

92. Hahn, P.E., Ph.D. Thesis, Polymer Science and Engineering Graduate School of the University of Massachusetts, 1987.

93. Castro, J.M., Lopez-Serrano, F., Macosko, C.W. and Tirrell, M., J.Appl.Polym.Sci., 26, 2067, 1981.

94. Magill, J.H., Polymer, 2, 221, 1961; 3, 25, 1962.

Chapter 8.

8. Summary and Conclusions.

8.1. Synthesis of PEO-b-PMMA Block Copolymers.

A successful synthetic procedure was employed to synthesise series of PEO-b-PMMA block copolymers with varying ethylene oxide percentages and constant PMMA molecular weight. This involved the high vacuum, anionic polymerisation of methyl methacrylate monomer using diphenyl methyl potassium initiator. The ethylene oxide monomer was then added to the 'living' PMMA.

8.2. Poly(ethylene oxide)/Poly(methyl methacrylate) Blends.

8.2.1. Phase Behaviour.

Experimental evidence supporting miscibility over the whole composition range for the poly(ethylene oxide)/poly(methyl methacrylate) blends studied in this work was found. Single glass transition temperatures for higher PMMA concentration blends were observed using DSC which agreed well with those predicted by Fox for a miscible system on a molecular level. For blends with lower PMMA volume fraction, a single T_g was detected, however, this temperature remained at a constant value reflecting the T_g for an 80% by weight PEO crystalline lamellar.

Further evidence for the diluent nature of the amorphous fraction, based upon apparent and equilibrium melting point depression, and the decrease in the crystallinity indices x_t and x_c, as the concentration of PMMA increased was observed using DSC and optical microscopy. Analysis of the melting point depressions gave the χ values listed in table 8.1.

Technique	χ (at 336K)
DSC, unannealed blends.	-0.16
DSC, annealed blends	-0.08
Optical Microscopy	-0.52

Table 8.1. Evaluated Flory-Huggins Interaction Parameters.

The χ values in table 8.1 are all negative indicating miscibility at temperatures close to the melt temperature of PEO.

For the blend BL60, however, irregular Avrami parameters from DSC data and irregular apparent melting points using optical microscopy were observed. These irregularities were attributed to the presence of a UCST-type phase boundary at the crystallisation temperatures studied. Other investigators have proposed a similar explanation for the rather unusual crystalline behaviour observed for the intermediate blend composition range (see chapter 2).

8.2.2. Isothermal Crystallisation.

Analysis of the isothermal crystallisation of the blends, resulted in an evaluated rate constant that decreased as the concentration of PMMA increased and as the crystallisation temperature decreased. Once again this shows the diluent nature of amorphous PMMA retarding the crystallisation of the PEO component. In fact the PMMA retards the crystallisation of PEO to such an extent that no re-crystallisation was observed for blends containing less than 40% PEO fraction by weight. From DSC, where a powdered form of the polymer sample is investigated, a reasonably constant value for the JMA exponent of 3.8±0.2 was determined for all blend compositions (with the exception of BL60). This value refers to an isothermal crystallisation mechanism of spherical growth geometry, nucleation that occurs at a constant rate throughout the crystallisation process (homogeneous nucleation) and an interfacially controlled rate determining step. From optical microscopy data, where the

polymer sample is now a thin film, a modified JMA exponent of 2.2±0.2 was evaluated for all blend compositions. Since the radii of the spherulites observed are much greater than the film thickness, then this JMA exponent can be interpreted in terms of a disc-like growth geometry which is interfacially controlled. By comparing the value of n from DSC (n=3.8±0.2) with that from optical microscopy (n=2.2±0.2), due to the relative analyses used, the difference in n gives an indication of the contribution from the 'type of nucleation'. With homogeneous nucleation, where nucleation occurs at a constant rate throughout the time scale of the experiment, there is a contribution of 1 towards the JMA exponent. Whereas for instantaneous nucleation, where nuclei form instantaneously at the start of the transformation, there is a zero contribution to n[20]. The difference in n for BC76 and the blends is 0.6 ± 0.2. This indicates that a large proportion of the nuclei form instantaneously and the majority nucleate at a rate that decays exponentially throughout the time scale of the experiment, see figure 8.1.

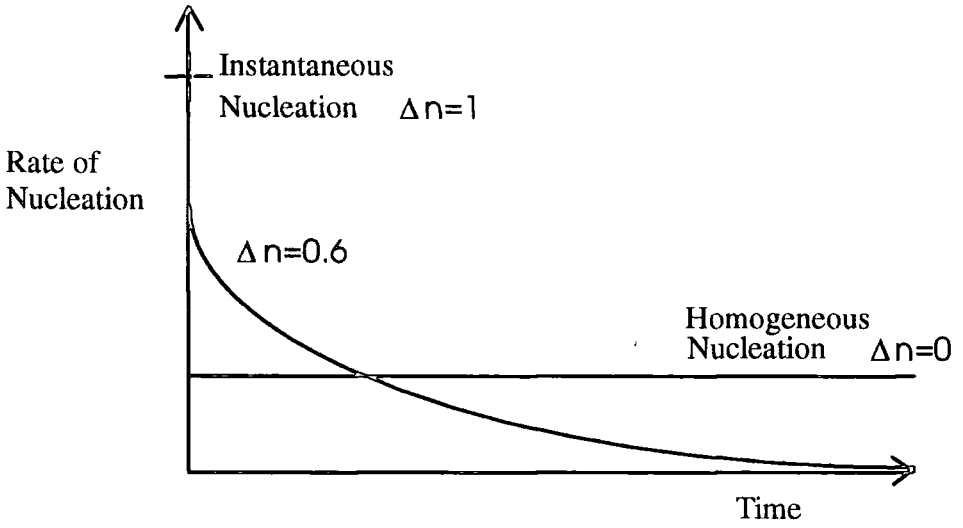

Figure 8.1. Interpretation of the Contribution to the JMA Exponent from the 'Type of Nucleation'.

SALS results from investigation of the overall crystallisation process gave an Avrami exponent from n=2.5 to 3, which abruptly increased to n=4 at T_c<303K for BL80. Since thin films are used for SALS experiments, then the growth geometry is

disc-like. The Avrami exponents are not the same as those determined from the growth of the spherulitic radius as viewed using depolarised light microscopy, however, as these exponent values contain a contribution from the 'type of nucleation', The difference between Avrami exponent values from SALS and optical microscopy is very similar to Δn, see figure 8.1.

Thus, using three different techniques, it can be concluded that the isothermal crystallisation mechanism of PEO/PMMA blends is nucleated as schematically shown in figure 8.1., interfacially controlled, with a spherical growth geometry in the bulk and a disc-like growth geometry in thin films.

8.3. PEO-b-PMMA Block Copolymers.

8.3.1. Phase Behaviour.

In accordance with the Fox and Pochan analyses, single T_g's were detected using DSC. However, the presence of additional T_g's associated with phases rich in either homopolymer suggests that the block copolymers are only weakly miscible.

Whereas the block copolymer BC76 contained sufficient PEO to crystallise directly when cooled to temperatures below the melt, this was not true for BC55, BC50 and BC30. For these block copolymers, as detected using DSC, SALS, WAXS and SAXS, thermal treatment was necessary to induce crystallinity. Figure 8.2. shows schematically the stages of microphase induced crystallinity. At 423K, the block copolymer is completely miscible, figure 8.2a). From DSC and SALS data, it was deduced that BC55 and BC50 phase separated according to a nucleation and growth mechanism at relatively low temperatures forming microdomains rich in PEO, figure 8.2b). The PEO chains did not crystallise at these low temperatures, but were present in a 'supercooled' state. Upon heating to 323K, the PEO chains in the PEO rich microdomains become more mobile, allowing the PEO chains to align and consequently crystallise, figure 8.2c). Above the crystallisation temperature, the

crystalline component melts leaving a rigid PMMA lamellar matrix. This matrix is rigid since the melt temperature is well below the glass transition temperature of PMMA.

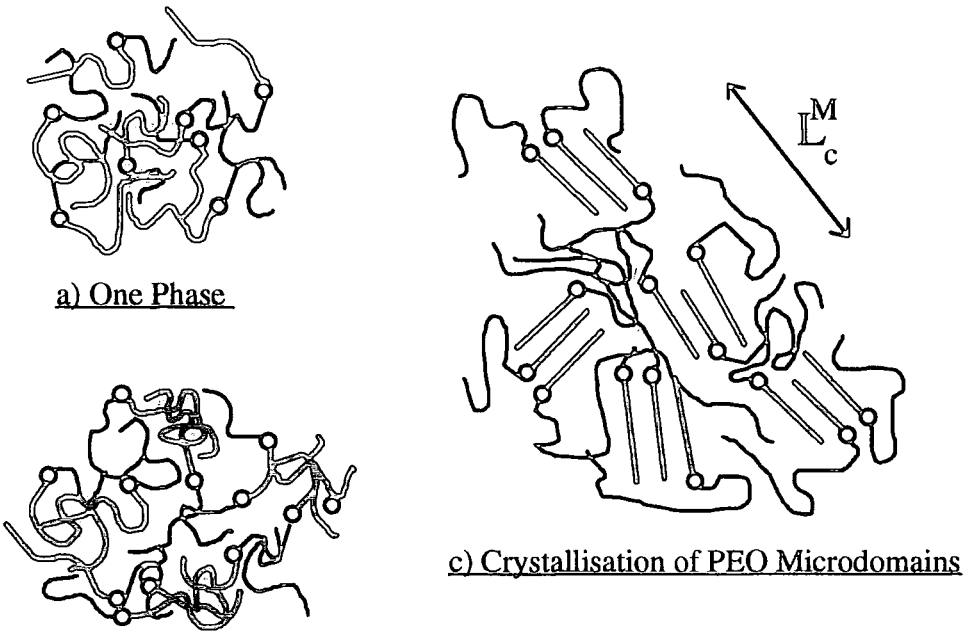

a) One Phase

b) Microdomains of PEO

c) Crystallisation of PEO Microdomains

Figure 8.2. Stages of Microphase Separation Induced Crystallinity.

From SALS data, the block copolymers crystallised forming highly disordered sporadically placed regions of the order of 3μm diameter. Since, the microdomains scattered light at the microphase separation temperatures, T', this implied that the scattering entities were larger than 0.7 μm. A possible explanation for this behaviour, owing to the small microdomain size is the formation of microdomain aggregates. SAXS data indicated that the crystalline regions were disordered and most probable distance between the centres of gravity between two adjacent lamellar crystals, L_c^M was 520±20Å, see figure 8.2c.

From the evaluated Avrami exponents using SALS and DSC data, the nucleation of the microphase separation mechanism was instantaneous, the growth diffusion controlled and the growth geometry was disc-like changing to rod-like at lower permanence temperatures. It was not possible to distinguish at what temperature the order-disorder transition temperature occurred, however, two

informative permanence temperatures were defined, T_{tr}' from DSC and $T_{1/2}'$ from WAXS. T_{tr}' is the permanence temperature at which the rate of microphase separation is highest and $T_{1/2}'$, is the permanence temperature at which half the maximum amount of attainable crystallinity is induced. These values are tabulated in table 8.2.

Polymer and Cooling Rate.	Transition Temperature (K)
BC50, 100Kmin^{-1}	T_{tr}'=240.5
BC55, 100Kmin^{-1}	T_{tr}'=254
BC50, 30Kmin^{-1}	$T_{1/2}'$=242
BC55, 30Kmin^{-1}	$T_{1/2}'$=261
BC50, 10Kmin^{-1}	$T_{1/2}'$=247
BC55, 10Kmin^{-1}	$T_{1/2}'$=276

Table 8.2. Transition Temperatures Describing the Microphase Separation of PEO-b-PMMA Block Copolymers.

As shown in table 8.2. the transition temperatures imply that the ODT of BC50 (ODT<240.5K) is lower than that for BC55 (ODT<254K). The values in table 8.2. also show that the defined transition temperatures are highly dependent upon cooling rate. The lower the cooling rate the higher the transition temperature.

The unequivocal detection of microphase separation at these low temperatures is totally surprising if one takes into account the glass transition temperatures of BC55 (T_g=279K) and BC50 (T_g=273K) as observed using DSC. A possible explanation is that the heterogeneity within the system is too small to be detected using DSC, i.e., <70Å. This is supported by preliminary 2-D diffusion nmr experiments[1] which detected mobility of PEO rich regions at the low permanence temperatures and a microdomain size of 25Å.

Thus, for BC55, BC50 and BC30, via specific thermal treatment, microphase separation induces crystallinity in these block copolymers upon heating. This unusual property has a potential commercial applications as a heat sensitive packaging film. For example, if the crystallisable component within the film packaging crystallises just above ambient temperatures, then owing to these crystalline regions, the film becomes mechanically stronger and opaque. This visible change in film properties would be highly informative. Such a packaging would be ideal for heat sensitive biological products.

8.3.2. Isothermal Crystallisation.

As the thermal routes to crystallisation for BC76 compared to BC55 and BC50 were different, then it is not surprising to find that the degrees of crystallinity and the apparent melting points for these two sets of block copolymers were different. Even though BC76 contains over 20% more PEO by weight than BC55 and BC50, this difference does not account for the appreciably higher crystallinity values (53% for BC76 compared to 34% and 10% for BC55 and BC50 respectively), and a 4K larger apparent melting point temperature. Consequently, it is deduced that the crystalline regions for BC55 and BC50 are far more disordered than those for BC76.

The block copolymers with less than 30% by weight PEO were unable to crystallise even after undergoing thermal treatment at low permanence temperatures.

8.4. Blends vs. Block Copolymers.

BC76 and the blends exhibit similar crystallisation behaviour. The polymers crystallise directly when cooled to temperatures below the melt according to the same crystallisation mechanism in the bulk: spherical growth geometry where the nucleation is mainly homogeneous and the spherulitic growth is diffusion controlled. The chemical joint connecting the constituent homopolymers in BC76, however, dramatically reduces and the degree of crystallinity, the melting point temperature and the rate of crystallisation, a 3-4 fold decrease was observed in the latter. This reduced

rate of crystallisation can be explained using an approach used by Donth et al[2]. They showed the necessity for mobile free crystallisable chain ends during crystallisation. Since the block copolymer has only one free chain end compared to two for the blends, then the rate of crystallisation for BC76 is lower. No appreciable variation in the lateral surface free energies, σ_e, or the Avrami exponents, n, was observed.

The thermal treatment necessary to induce crystallisation for BC55 and BC50 was not needed for BL60. However, this blend composition displayed some unusual crystallisation features which were ascribed to the presence of phase separation processes competing with crystallisation. Therefore, it can be concluded that for both the blend and the block copolymers at these intermediate compositions, phase separation processes are present at low temperatures. In the case of the block copolymers, the crystallisation has been retarded to such an extent that a composition 'window' has been created, where the polymers can be quenched into a metastable region without the block copolymers crystallising.

The conclusions reached above for the phase behaviour of poly(ethylene oxide) poly(methyl methacrylate) blends and block copolymers are schematically shown in figure 8.3.

The double-hatched region denotes the two phase region for the block copolymer. The phase diagram for the blends supported earlier work on the phase behaviour for this system, see figure 2.1.

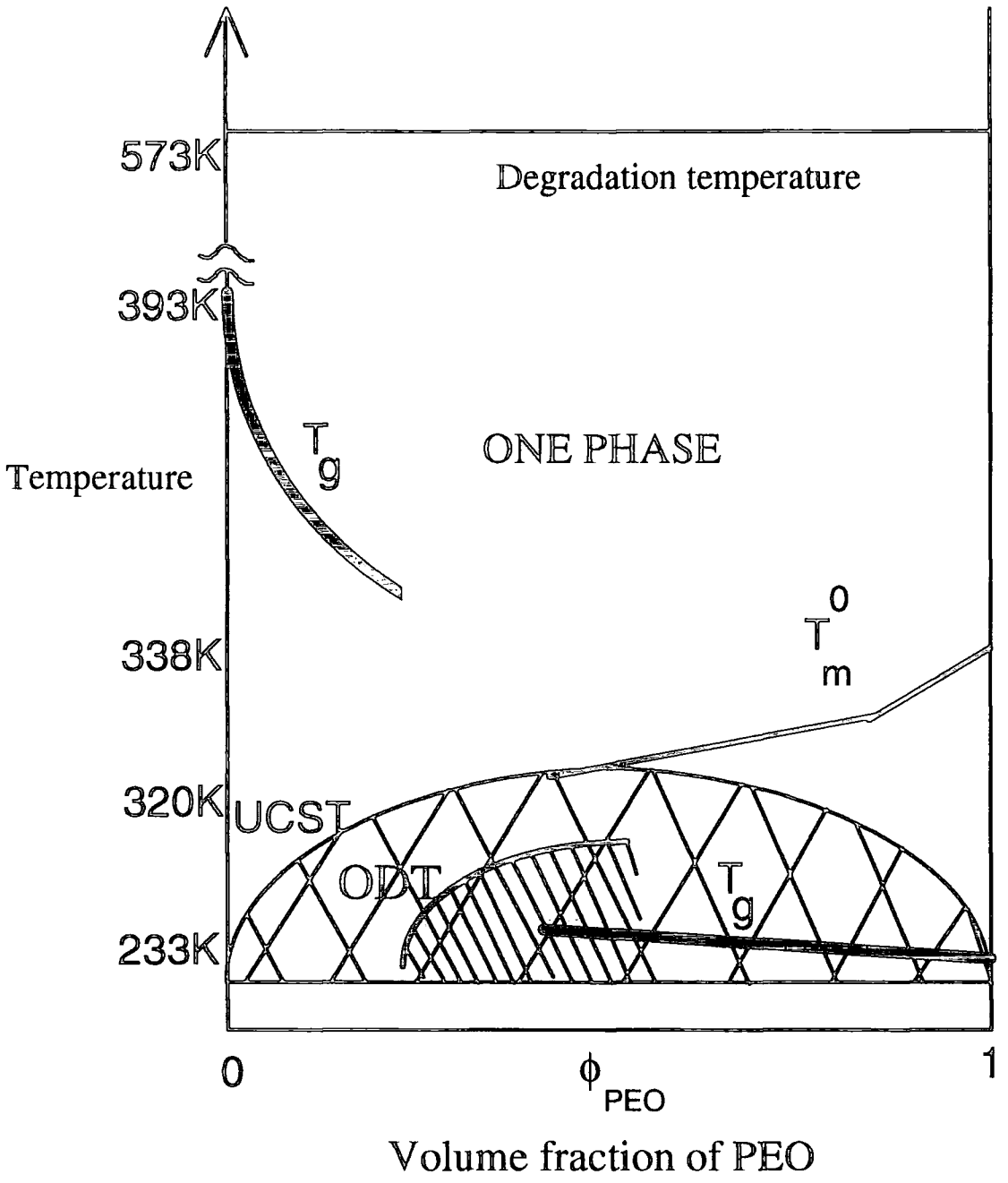

Figure 8.3. Phase Diagram for PEO/PMMA Blends and PEO-b-PMMA Block Copolymers.

8.5. Comparison of Techniques Used.

Through recent technological advancements in the design of CCD detectors, the faster speed of data collection has enhanced the potential capabilities that small angle light scattering offers. Along with theoretical developments in modelling SALS data, this technique has begun to attract wide spread interest from both academia and industry.

The Avrami analysis of the isothermal crystallisation of the crystallisable polymers using SALS, OM and DSC shows how well these techniques can complement one another. Although the principles of SALS and OM are the same, however, SALS data is far more quantitative and can monitor the overall crystallisation process through summing the overall scattered depolarised light. This capability, along with DSC data, allowed the mechanistic contributions to the Avrami exponent to be differentiated.

8.6. Future Work.

Further investigation of the phase behaviour of the intermediate compositions of both PEO/PMMA blends and PEO-b-PMMA block copolymers at the lower UCST temperatures would be interesting. Using SALS, Tomura et al[3] have recently studied the UCST type phase behaviour for an amorphous/semi-crystalline binary blend, poly(vinylidene fluoride)/poly(methyl methacrylate). A similar approach could be used for PEO/PMMA. The proposed aggregation of microdomains for the block copolymers in the two phase region as well as the structure and morphology of the microphase separated and crystalline phases would also be of particular interest.

In water, the block copolymer, BC76, appeared opalescent suggesting the formation of micelles. Micellular studies have not been conducted on this type of block copolymer and consequently this research would prove to be very useful and potentially fruitful.

8.7. References.

1. S.Lehmann, S., Max-Planck Institut für Polymerforschung, Prof. Spiess's Group, unpublished data, 1993.
2. Donth, E., Kretzschmar, Schulze, G., Garg., D., Höring, S. and Ulbricht, J., Acta Polymerica, 38, 261, 1987.
3. Tomura, H., Saito, H. and Inoue, T., Macromolecules, 25, 1611-1614, 1992.

Appendix II

Supplier - Micro-Controle

Code	Description.
170226	X95 Profile (2m long) x 1
179221	X95 Profile (0.5m long) x 1
178232	CX95.50 Carriage x 10
178233	CX95.80 Carriage x 6
178235	CX95.120 Carriage x 1
N/A	CX95.120 Modified Carriage x 1
133133	P080 BD PO Prism table with differential adjustors x 1
178196	90° Reflection Prism x 1
178196	SB19.18 Adaptor Support ϕ12 Rod Mounting (Beam Expander) x 1
S311302	Biconvex lens ϕ10mm, focal length 20mm x 1
178343	B10 Adaptor
338066	MR5.16 linear stage x 1
338283	Intermodular Adaptor Plate, MR5.16 ϕ12 pillar x 1
133201	SB18YZ Support x 2
081424	30 micron Pinhole with mount for SB18YZ (Beam Expander) x 1
178199	SB32.31.5 Adaptor Support ϕ12 rod mounting (Beam Expander) x 1
S311306	Biconvex lens ϕ31.5, focal length 200mm x 1
178349	B31.5 Adaptor Mount x 1
081425	Microscopic Pinhole 50 micron dia. with mount x 1
081426	Microscopic Pinhole 80 micron dia. with mount x 1
081427	Microscopic Pinhole 100 micron dia. with mount x 1
081428	Microscopic Pinhole 150 micron dia. with mount x 1
081429	Microscopic Pinhole 200 micron dia. with mount x 1
338224	EQ8.02 Support Bracket x 1
178144	Rod Mounted Iris Diaphragm x 1
178197	SB19.22.4 Adaptor Support ϕ12 rod mounting (Neutral Density Filter)
178347	B22.4 Adaptor x 1
S371140	50% Transmission Neutral Density Filter x 1
S371141	20% Transmission Neutral Density Filter x 1
S371142	10% Transmission Neutral Density Filter x 1
S371143	5% Transmission Neutral Density Filter x 1
N/A	MRT120.63 setting unit with lockable carriage x 2 (Detector bracket)

N/A	Bracket CCD-MRT x 1 (Detector bracket)
N/A	Bracket MRT-MRT x 1
N/A	Modified PI 50.02 with central counterbore 6mm hole (P080 Table) x1
N/A	12mm diameter Pillars (various lengths)

Supplier - **Linkam**

THMS 600	Heating Freezing Stage with X,Y manipulators.
CS 196	Cooling System (including a liquid nitrogen dewar with 1m tubing)
TMS 91	Temperature Control System
VTO 232	Video Text Overlay

Supplier - **EG&G Instruments**

OMA - Vision CCD.

Optical multichannel analyser - charge coupled device (CCD) detector.

Specifications:

Fibre optic link between PC and detector.
High quantum efficiency; over 40% at 700nm.
Low noise; 4 electrons of system noise.
High gain; 1 count per 4 photoelectrons.
Photon conversion; 10 photons per count.
High dynamic range; over 5 orders of magnitude.
New ADC Technology; 18 bits.
Fast digitisation; 5 microseconds per pixel; effective rate.
Versatile scan patterns; 512 x 512 pixel scientific grade CCD.
Vacuum sealed housing; provides maximum cooling efficiency.
Visible or UV enhanced detectors.
8 MB RAM located on the OMA control board.
Obtain 512 x 512 pattern in 1.34 seconds.

Supplier - **Dell Computers.**

Dell 333D PC with 486DX i.e. with math coprocessor.
200 MB hard disk.
Tag No. 09RBU; ref. no. 288735.
Extended warranty to 10/93.

Appendix II.

II.1. SALS.PRO, Quadrant Averaging with μ=45º Data Slice for X-type Pattern.

```
pro sals, a36                          name of macro
a36=fltarr(512,50)                     define a floating-point array called a36
a36a=congrid(a36a,200,200)             change a36 to an array with an equal
                                       number of rows and columns.
a36b=fltarr(98,98)                     defining an array for each quadrant.
a36c=fltarr(98,98)
a36d=fltarr(98,98)
a36e=fltarr(98,98)
a36b=a36a(0:97,99:196)                 main beam at (97,99). placing data form
                                       a36a, rows 0 to 97 and columns
                                       99 to 196 into a36b.
a36c=a36a(97:194,99:196)
a36d=a36a(97:194,2:99)
a36e=a36a(0:97,2:99)
a36f=rotate(a36e,2)                    rotate 180º anti-clockwise.
a36g=rotate(a36d,1)                    rotate 90º anti-clockwise
a36h=rotate(a36b,3)
a36i=(a36f+a36g+a36h+a36c)/4           average the four quadrants.
x=indgen(200)                          create a vector called x with consecutive
                                       integer values from 1 to 200
y=indgen(200)
f=a36i(x,y)                            a diagonal slice (μ=45º) through the
                                       quadrant averaged data.
save,filename='data.res',f             save f in a file called data.res.
end; sals                              end of the macro.
```

For +-type SALS pattern, replace bold text with; f=a36i(0,*).

II.2. RADAV.PRO, Radially Averaging

```
pro radav,data
data1=congrid(data,200,200)
x=intarr(200,200)
y=intarr(200,200)
```

```
for i=0,199 do x(i,*)=i                    a 200x200 array; 1 2 3 4 5
for i=0,199 do y(*,i)=i                    of the type →    2 3 4 5 6
a=(x-100)          subtract 100 form                       3 4 5 6 7
c=(y-100)          each value in x and call a              4 5 6 7 8
b=double(a)        a doubled.                              5 6 7 8 9
f=b^2              b squared.
d=double(c)
g=d^2
e=f+g
z=sqrt(e)                                  square root e and call z
p=fltarr(100)
i=0
for i=0,99 do begin                        starts 100 x loop
index=where(z le (i+1) and z gt i)
p(i)=avg(data1(index))                     average all data values which have an
endfor                                     index value between i and i+1 i.e.
save, filename='radav.res',p               at a distance i from the main beam
end;radav                                  position.
```

II.3. INT.PRO, Overall Intensity for a Series of Scans.

```
pro int,a36
z=fltarr(80)
i=0
for i=0,79 do begin                        loop for 80 scans
a36=fltarr(512,50)
readf,1,a36
y=total(a36)                               adds up all intensity values in a36.
z(i)=y-(512*50*467)                        subtract a constant background value
endfor                                     and store each total intensity
save, filename='intense.res',z             in vector z.
end; int
```

II.4. AVRAMI.PRO, Avrami Analysis.

```
pro avrami, y                              raw intensity (or radii) data in y
aa=fltarr(50)                              50 data values to be analysed.
.run                                       all of the following commands are
```

i=0	executed in one batch at the end command.
for i=0,48 do begin	
aa(i)=(y(49)-y(i))/y(49)	$(I_{max}-I_t)/I_{max}$ [1-X(t)] placed in aa.
endfor	
end	
e=-alog(aa)	-ln (1-X_t)
f=alog10(e)	$\log_{10}$(-ln (1-X_t)
a=indgen(48)+1	set-up an integer string 1 to 48
b=a*3*0.541	string of times for each scan
c=alog10(b)	$\log_{10}$(t)
plot,c,f	
save,filename='result.av',c,f	
end; avrami	

Appendix III.

Colloquia, Lectures and Seminars Given by Invited Speakers from 1st August 1990 to 31st July 1993.

Attendance at a lecture is denoted by an asterisk.

REVISED VERSION

UNIVERSITY OF DURHAM

Board of Studies in Chemistry

COLLOQUIA, LECTURES AND SEMINARS GIVEN BY INVITED SPEAKERS 1ST AUGUST 1990 TO 31ST JULY 1991

ALDER, Dr. B.J. (Lawrence Livermore Labs., California) — 15th January, 1991
Hydrogen in all its Glory

BELL†, Prof. T. (SUNY, Stoney Brook, U.S.A.) — 14th November, 1990 ✳
Functional Molecular Architecture and Molecular Recognition

BOCHMANN†, Dr. M. (University of East Anglia) — 24th October, 1990 ✳
Synthesis, Reactions and Catalytic Activity of Cationic Titanium Alkyls

BRIMBLE, Dr. M.A. (Massey University, New Zealand) — 29th July, 1991
Synthetic Studies Towards the Antibiotic Griseusin-A

BROOKHART, Prof. M.S. (University of N. Carolina) — 20th June, 1991 ✳
Olefin Polymerizations, Oligomerizations and Dimerizations Using Electrophilic Late Transition Metal Catalysts

BROWN, Dr. J. (Oxford University) — 28th February, 1991 ✳
Can Chemistry Provide Catalysts Superior to Enzymes?

BUSHBY†, Dr. R. (Leeds University) — 6th February, 1991 ✳
Biradicals and Organic Magnets

COWLEY, Prof. A.H. (University of Texas) — 13th December, 1990 ✳
New Organometallic Routes to Electronic Materials

CROUT, Prof. D. (Warwick University) — 29th November, 1990
Enzymes in Organic Synthesis

DOBSON†, Dr. C.M. (Oxford University) — 6th March, 1991 ✳
NMR Studies of Dynamics in Molecular Crystals

GERRARD†, Dr. D. (British Petroleum) — 7th November, 1990
Raman Spectroscopy for Industrial Analysis

HUDLICKY, Prof. T. (Virginia Polytechnic Institute) — 25th April, 1991
Biocatalysis and Symmetry Based Approaches to the Efficient Synthesis of Complex Natural Products

JACKSON†, Dr. R. (Newcastle University) — 31st October, 1990
New Synthetic Methods: α-Amino Acids and Small Rings

KOCOVSKY†, Dr. P. (Uppsala University) — 6th November, 1990
Stereo-Controlled Reactions Mediated by Transition and Non-Transition Metals

LACEY, Dr. D. (Hull University) — 31st January, 1991 ✳
Liquid Crystals

LOGAN, Dr. N. (Nottingham University) — 1st November, 1990
Rocket Propellants

MACDONALD, Dr. W.A. (ICI Wilton) — 11th October, 1990 ✳
Materials for the Space Age

MARKAM, Dr. J. (ICI Pharmaceuticals) — 7th March, 1991 ✳
DNA Fingerprinting

PETTY, Dr. M.C. (Durham University) — 14th February, 1991 ✳
Molecular Electronics

PRINGLE[+], Dr. P.G. (Bristol University) — 5th December, 1990
Metal Complexes with Functionalised Phosphines

PRITCHARD, Prof. J. (Queen Mary & Westfield College, London University) — 21st November, 1990
Copper Surfaces and Catalysts

SADLER, Dr. P.J. (Birkbeck College London) — 24th January, 1991 ✳
Design of Inorganic Drugs: Precious Metals, Hypertension + HIV

SARRE, Dr. P. (Nottingham University) — 17th January, 1991 ✳
Comet Chemistry

SCHROCK, Prof. R.R. (Massachusetts Institute of Technology) — 24th April, 1991 ✳
Metal-ligand Multiple Bonds and Metathesis Initiators

SCOTT, Dr. S.K. (Leeds University) — 8th November, 1990 ✳
Clocks, Oscillations and Chaos

SHAW[+], Prof. B.L. (Leeds University) — 20th February, 1991
Syntheses with Coordinated, Unsaturated Phosphine Ligands

SINN[+], Prof. E. (Hull University) — 30th January, 1991 ✳
Coupling of Little Electrons in Big Molecules. Implications for the Active Sites of (Metalloproteins and other) Macromolecules

SOULEN[+], Prof. R. (South Western University, Texas) — 26th October, 1990
Preparation and Reactions of Bicycloalkenes

WHITAKER[+], Dr. B.J. (Leeds University) — 28th November, 1990
Two-Dimensional Velocity Imaging of State-Selected Reaction Products

[+] Invited specifically for the postgraduate training programme.

UNIVERSITY OF DURHAM

Board of Studies in Chemistry

COLLOQUIA, LECTURES AND SEMINARS FROM INVITED SPEAKERS

1991 – 1992 (August 1 – July 31)

1991

October	17	Dr. J.A. Salthouse, University of Manchester ✳ Son et Lumiere – a demonstration lecture
October	31	Dr. R. Keeley, Metropolitan Police Forensic Science ✳ Modern forensic science
November	6	Prof. B.F.G. Johnson†, Edinburgh University ✳ Cluster–surface analogies
November	7	Dr. A.R. Butler, St. Andrews University Traditional Chinese herbal drugs: a different way of treating disease ✳
November	13	Prof. D. Gani†, St. Andrews University ✳ The chemistry of PLP–dependent enzymes
November	20	Dr. R. More O'Ferrall†, University College, Dublin Some acid–catalysed rearrangements in organic chemistry
November	28	Prof. I.M. Ward, IRC in Polymer Science, University of Leeds ✳ The SCI lecture: the science and technology of orientated polymers
December	4	Prof. R. Grigg†, Leeds University Palladium–catalysed cyclisation and ion–capture processes
December	5	Prof. A.L. Smith, ex Unilever ✳ Soap, detergents and black puddings
December	11	Dr. W.D. Cooper†, Shell Research ✳ Colloid science: theory and practice

1992

January	22	Dr. K.D.M. Harris†, St. Andrews University ✳ Understanding the properties of solid inclusion compounds
January	29	Dr. A. Holmes†, Cambridge University Cycloaddition reactions in the service of the synthesis of piperidine and indolizidine natural products

January	30	Dr. M. Anderson, Sittingbourne Research Centre, Shell Research ✳ Recent Advances in the Safe and Selective Chemical Control of Insect Pests
February	12	Prof. D.E. Fenton†, Sheffield University Polynuclear complexes of molecular clefts as models for copper biosites
February	13	Dr. J. Saunders, Glaxo Group Research Limited ✳ Molecular Modelling in Drug Discovery
February	19	Prof. E.J. Thomas†, Manchester University Applications of organostannanes to organic synthesis
February	20	Prof. E.Vogel, University of Cologne *The Musgrave Lecture* Porphyrins: Molecules of Interdisciplinary Interest
February	25	Prof. J.F. Nixon, University of Sussex *The Tilden Lecture* Phosphaalkynes: new building blocks in inorganic and organometallic chemistry
February	26	Prof. M.L. Hitchman†, Strathclyde University Chemical vapour deposition
March	5	Dr. N.C. Billingham, University of Sussex ✳ Degradable Plastics – Myth or Magic?
March	11	Dr. S.E. Thomas†, Imperial College Recent advances in organoiron chemistry
March	12	Dr. R.A. Hann, ICI Imagedata ✳ Electronic Photography – An Image of the Future
March	18	Dr. H. Maskill†, Newcastle University Concerted or stepwise fragmentation in a deamination–type reaction
April	7	Prof. D.M. Knight, Philosophy Department, University of Durham ✳ Interpreting experiments: the beginning of electrochemistry
May	13	Dr. J–C Gehret, Ciba Geigy, Basel ✳ Some aspects of industrial agrochemical research

† Invited specially for the postgraduate training programme.

UNIVERSITY OF DURHAM

Board of Studies in Chemistry

COLLOQUIA, LECTURES AND SEMINARS FROM INVITED SPEAKERS

1992 - 1993 (August 1 - July 31)

1992

October 15 — Dr M. Glazer & Dr. S. Tarling, Oxford University & Birbeck College, London ✳
It Pays to be British! - The Chemist's Role as an Expert Witness in Patent Litigation

October 20 — Dr. H. E. Bryndza, Du Pont Central Research
Synthesis, Reactions and Thermochemistry of Metal (Alkyl) Cyanide Complexes and Their Impact on Olefin Hydrocyanation Catalysis

October 22 — Prof. A. Davies, University College London
The Ingold-Albert Lecture The Behaviour of Hydrogen as a Pseudometal

October 28 — Dr. J. K . Cockcroft, University of Durham ✳
Recent Developments in Powder Diffraction

October 29 — Dr. J. Emsley, Imperial College, London
The Shocking History of Phosphorus

November 4 — Dr. T. P. Kee, University of Leeds
Synthesis and Co-ordination Chemistry of Silylated Phosphites

November 5 — Dr. C. J. Ludman, University of Durham ✳
Explosions, A Demonstration Lecture

November 11 — Prof. D. Robins, Glasgow University
Pyrrolizidine Alkaloids : Biological Activity, Biosynthesis and Benefits

November 12 — Prof. M. R. Truter, University College, London ✳
Luck and Logic in Host - Guest Chemistry

November 18 — Dr. R. Nix, Queen Mary College, London
Characterisation of Heterogeneous Catalysts

November 25 — Prof. Y. Vallee. University of Caen
Reactive Thiocarbonyl Compounds

November 25 — Prof. L. D. Quin, University of Massachusetts, Amherst
Fragmentation of Phosphorous Heterocycles as a Route to Phosphoryl Species with Uncommon Bonding

November 26 — Dr. D. Humber, Glaxo, Greenford ✳
AIDS - The Development of a Novel Series of Inhibitors of HIV

December 2 — Prof. A. F. Hegarty, University College, Dublin
Highly Reactive Enols Stabilised by Steric Protection

December 2 — Dr. R. A. Aitken, University of St. Andrews
The Versatile Cycloaddition Chemistry of $Bu_3P.CS_2$

December 3 — Prof. P. Edwards, Birmingham University
The SCI Lecture - What is Metal?

December 9 — Dr. A. N. Burgess, ICI Runcorn ✳
The Structure of Perfluorinated Ionomer Membranes

1993

January 20	Dr. D. C. Clary, University of Cambridge Energy Flow in Chemical Reactions
January 21	Prof. L. Hall, Cambridge NMR - Window to the Human Body
January 27	Dr. W. Kerr, University of Strathclyde Development of the Pauson-Khand Annulation Reaction : Organocobalt Mediated Synthesis of Natural and Unnatural Products
January 28	Prof. J. Mann, University of Reading ✳ Murder, Magic and Medicine
February 3	Prof. S. M. Roberts, University of Exeter Enzymes in Organic Synthesis
February 10	Dr. D. Gillies, University of Surrey NMR and Molecular Motion in Solution
February 11	Prof. S. Knox, Bristol University *The Tilden Lecture* Organic Chemistry at Polynuclear Metal Centres
February 17	Dr. R. W. Kemmitt, University of Leicester Oxatrimethylenemethane Metal Complexes
February 18	Dr. I. Fraser, ICI Wilton ✳ Reactive Processing of Composite Materials
February 22	Prof. D. M. Grant, University of Utah Single Crystals, Molecular Structure, and Chemical-Shift Anisotropy
February 24	Prof. C. J. M. Stirling, University of Sheffield Chemistry on the Flat-Reactivity of Ordered Systems
March 10	Dr. P. K. Baker, University College of North Wales, Bangor 'Chemistry of Highly Versatile 7-Coordinate Complexes'
March 11	Dr. R. A. Y. Jones, University of East Anglia ✳ The Chemistry of Wine Making
March 17	Dr. R. J. K. Taylor, University of East Anglia ✳ Adventures in Natural Product Synthesis
March 24	Prof. I. O. Sutherland, University of Liverpool Chromogenic Reagents for Cations
May 13	Prof. J. A. Pople, Carnegie-Mellon University, Pittsburgh, USA *The Boys-Rahman Lecture* Applications of Molecular Orbital Theory
May 21	Prof. L. Weber, University of Bielefeld Metallo-phospha Alkenes as Synthons in Organometallic Chemistry
June 1	Prof. J. P. Konopelski, University of California, Santa Cruz Synthetic Adventures with Enantiomerically Pure Acetals
June 2	Prof. F. Ciardelli, University of Pisa Chiral Discrimination in the Stereospecific Polymerisation of Alpha Olefins
June 7	Prof. R. S. Stein, University of Massachusetts ✳ Scattering Studies of Crystalline and Liquid Crystalline Polymers

June 16 Prof. A. K. Covington, University of Newcastle
Use of Ion Selective Electrodes as Detectors in Ion Chromatography

June 17 Prof. O. F. Nielsen, H. C. Ørsted Institute, University of Copenhagen
Low-Frequency IR - and Raman Studies of Hydrogen Bonded Liquids

File Ref. CG137/E(CH)

Appendix IV

Research Conferences Attended.

March 26-28th, 1991

Macro Group UK Meeting, Aspects of Contemporary Polymer Chemistry, University of Lancaster.

Poster presented.

April 3-5th, 1991

Polymer Physics, A Conference to mark the retirement of Andrew Keller, FRS, University of Bristol.

July 22-26th, 1991

Polymer Surfaces and Interfaces II, University of Durham, Durham

Poster presented.

September - October 2nd, 1992

4th European Polymer Federation Symposium on Polymeric Materials, Baden-Baden, Germany.

Oral and poster presentation: 'Small Angle Light Scattering from Solid Films of PEO-b-PMMA Block Copolymers'

April 6-8th, 1993

Macro Group, Aspects of Contemporary Polymer Chemistry, University of Lancaster.

Presented Lecture: 'Phase Transitions in PEO-b-PMMA Block Copolymers'.

July 20-22nd, 1993

The Polymer Conference, Robinson College, University of Cambridge, Cambridge.

Poster presented.

September 22-23rd, 1993

IRC Industrial Club Seminar, University of Durham

Poster presented.

Publications.

Tsibouklis, J., Richardson, P.H., Richards, R.W. and Feast, W.J., Polymer Bulletin, 30, 595-601, 1993.

Tsibouklis, J., Richardson, P.H., Ahmed, A., Richards, R.W., Feast, W.J., Martin, S.J., Bradley, D.D.C. and Warner, M., Synthetic Metals, 61, Vol 1-2, 159-162, 1993.

Richardson, P.H. and Richards, R.W., Polymer (in press), 1993.

Kotomin, S., Richardson, P.H. and Richards, R.W., (to be published).